ISSN 0370—8691

NATIONAL ACADEMY OF SCIENCES OF THE REPUBLIC OF ARMENIA

Communications of the Byurakan Astrophysical Observatory

1

Erevan 2023

Communications of BAO, Vol. 70, Issue 1, 2023, pp. 1-6

Iron in Armenian really means *a Sky Drop*?

A. Yeghikyan *

Byurakan Astrophysical Observatory, Byurakan, Aragatzotn Province, Armenia

Abstract

In the languages of the ancient Hittites and Egyptians, and later the Greeks, iron was called *celestial metal* or by the close in meaning word. A browse review of iron names in several languages shows that with the exception of the mentioned three languages, in other languages the name of the iron reflects its function (hard, cutting, superpower, iron-stone, etc.) but not origin. According to the Hittite sources, iron was produced by the masters of the *Hatti* kingdom controlled by Hittities, located, by the way, next to the kingdom of *Hayasa*. *Hatti* adjoins the region on the southeastern coast of the Black Sea, where, according to Aristotle, the *Halibs* lived - craftsmen who produced *the best iron*. It is known that the mountain rivers of this area brought sand and accumulated in the mouths sand with a high content of magnetite, an iron-containing mineral with a lower melting point (compared to other rocks). It is this circumstance, according to geologists, that the beginning of the *iron* century takes place in this area in the XV-XIII centuries BC. On the basis of all of the above, the literal translation of the Armenian name of iron *erkat* = *dropped from the sky* does not seem to be meaningless. But academic philologists categorically disagree with this. In this report, a more convincing (from the astrophysicist point of view) etymology of the Armenian word *erkat* = *er-ka* = *heavenly metal* is proposed.

1. Introduction

There is an intricate and unsolved problem of the meaning of the Armenian word *erkat* which literally is *iron*, but also means *a Sky Drop*. This is of course the task for philologists and historians but at least astrophysicists may have some contribution into the statement of the problem, may ask and hope to get from professionals clear answers for the simple questions listed in this work. All data below are from academic and easily verifiable sources.

As is known, etymology of Armenian twin words "yerkinq" and "yerkir" ("sky" and "earth", correspondingly) is very uncertain (e.g. Acharian (1935) especially if one would like to connect them with "iron-yerkat" by means of the debatable common root "yer" and decode the word as a "sky drop = yer-kat". Modern philologists (e.g. Martirosyan (2011)) refuse any such a relation and announce as a coincidence the spelling of the modern Armenian word resulted with the mentioned meaning. Historians probably also will decline that explanation because according to the usually accepted point of view when the Iron Age has started in the Hittities Kingdom or to be more correct, in the northern part of the Empire (the Hatti Kingdom) around XV-XIII B.C. (e.g. by Bryce (2007)) there were no carriers of (pre)Armenian: (pre)Armenians have leaved their Balkan ancestral land and have entered into the mentioned area now known as the Armenian Highland no earlier than at XII B.C. as was shown by Dyakonov (1968).

But let us discuss all the known facts carefully. First of all it should be highlighted here that in some very old languages the ancient name for iron was "Metal of Heaven": a well-known example is coming from the hieroglyphic language of the ancient Egyptians where it was pronounced as "ba-en-pet" (in other sources, "ba-ne-pe"), meaning either stone or metal ("ba") of Heaven "ne-pe" as referred e.g. by Bayun (2011) and Giorgadze (1988). A basic idea, expressed in ancient religious texts, was that the firmament of Heaven was of iron. This belief probably arose from the occasional fall of meteoric iron from the sky. It is interesting to note that the "iron from heaven" hieroglyphs which look like as presented below (Fig. 1 left, Bayun (2011)), they also were displayed on the Meteoritical Society Journal cover from 1969 to 1987 (Fig. 1, right).

Examples of placement of figures are given below.

*ayarayeg@gmail.com

doi: https://doi.org/10.52526/25792776-23.70.1-1

Figure 1. "Iron from heaven" hieroglyphics *Left:* Bayun (2011). *Right:* A known cover of the Journal.

2. Iron in Armenian, the location of carriers of that term and all that

It should be stressed that iron in Egypt as in some other countries was obtained from meteorites long before the Iron Age set in (about XXV-XX B.C.), but such iron things (e.g. knifes) were very rare. Now we distinguish between meteoritic and ore iron by at first their Nickel abundance which in the former is larger by a magnitude and more (Ni is about 5-10 % in meteoritic iron providing a good quality of resulting iron while only about 0.5 % in ore iron) and at second, as is mentioned, by their quality: meteoritic iron things are of course, better thanks to the known minor contributions like Ni etc. Knifes from meteoritic iron were known ca XXX BC. Earlier as some kind of a stone awl and later on the base of an meteoritic iron awl. They were used in Egypt, ca XXV BC for ritual sacrifice. What is interesting in some texts such awls were named as "biz" as was described by Wainwright (1938) (see also GizaPyramid (2017)) while "biz" in (modern) Armenian also means an (iron) awl (unfortunately with unknown etymology).

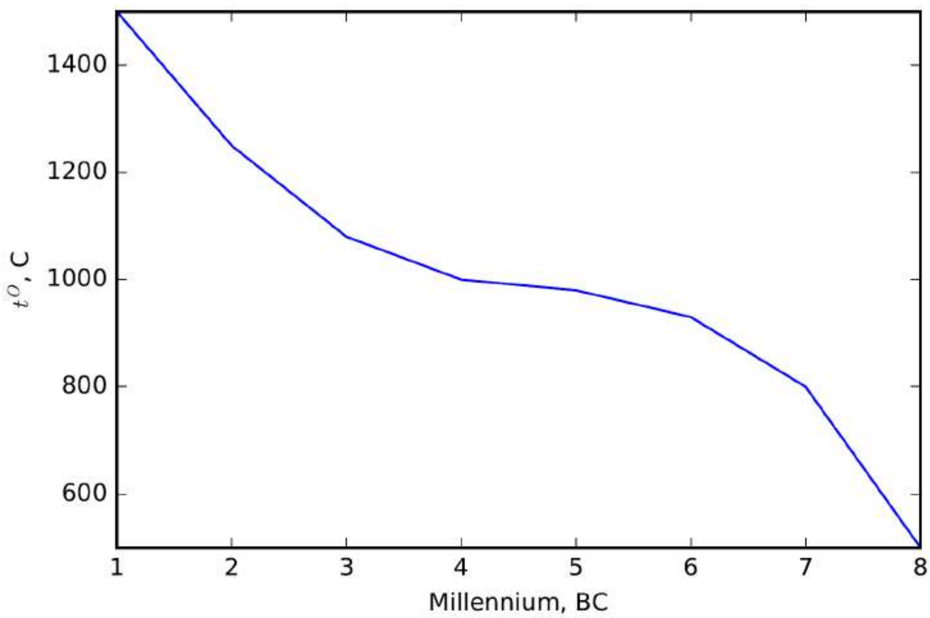

Figure 2. Rise of industrial thermal ability by Ivanov (1983).

Concerning the origin of first iron things a question is rose how much meteoritic iron was dropped on

doi: https://doi.org/10.52526/25792776-23.70.1-1

the area of Near East during ancient times? According to careful assessments of Ivanov (1983) up to 1 mln tonn is estimated a mass of iron meteorites accumulated on the area of Ancient Near East. Transition to rocky iron production has taken place in XV-XIV BC thanks to an increased industrial thermal ability described by Ivanov (1983) and shown in Fig 2. Later Egyptians lost the ability to get iron things and began to import them from the Hatti Kingdom, controlled by the Hittites Empire. The most important point for us is that people in that country have distinguished between the meteoritic and rocky iron and have been named them differently ("ha-pal-ki", the more later form is "ha-wal-ki"), "heaven iron", "good iron" - probably steel that is iron with important dopants, "black iron" - Bayun (2011).

But who were in fact first iron makers? As is well documented by Ancient Greek sources the first industrial production of iron was done by Halibs, who lived at the South-Eastern Black Sea coast and their dominant occupation was iron melting and fabrication (first mentioned by Aeschylus (VII BC), Herodotus (VII BC), Xenophon (IV BC). It is generally accepted now that the dating of the process is about XV-XIII B.C. The magnetite sands of the river deposits in that area with a lesser melting point than other iron-containing rocks, about 1300-1400 C as compared with 1530 C. Well known now minor dopants of that iron-contained sand played the important role and provided a good quality of iron. Aristoteles claims that "halib iron is the best one in the world, because Halibs produce it in their own secret way". He calls it "white Halib iron" (cited by Kosidowsky (1963)). Now it should be stressed that there is a point of view that "halib" means an occupation ("iron maker" according to Harutiunyan (1998)) and it is interesting to note that Pliny the Elder (I AD) (and Strabon (I AD)) marked them as armenohalibs, see below, in Fig 3.

Figure 3. Location of Armenohalibs according to Pliny the Elder (I AD) and Strabon (I AD).

In fact, of course, geographically the area of halibs is located on the part of the Armenian Highland at the coast of Black Sea, as shown in Fig 4. One can see that the Hayasa country is located between the Hatti Kingdom and the Halibs area Bayun (2011) (see Fig. 4). In such a case it is worthy to note that Hittitologists discuss long time about a possible relation of Hayasa country with Armenians because Hayasa name is dated earlier than XV BC. In such a relation it is interesting to note that both "Hayasa" and "Hayk" mean self-name of Armenians in Armenian. On the other hand Dyakonov (1968) insists on the coincidence of two names while Ivanov (1983) rejects Dyakonov's speculations and supports their close connection. What is interesting some modern academic sources e.g. Redgate (2000), Russel (2004) both refer to earlier work of Dyakonov (1968) but not mention much more modern work of Ivanov (1983). In short, according to Dyakonov (1968) such a connection is linguistically impossible while the Armenian point of view about origin of "hay" is supported by Ivanov (1983).

It is out of scope of this note to reveal pro and contra concerning the problem of the Armenian nature of

doi: https://doi.org/10.52526/25792776-23.70.1-1

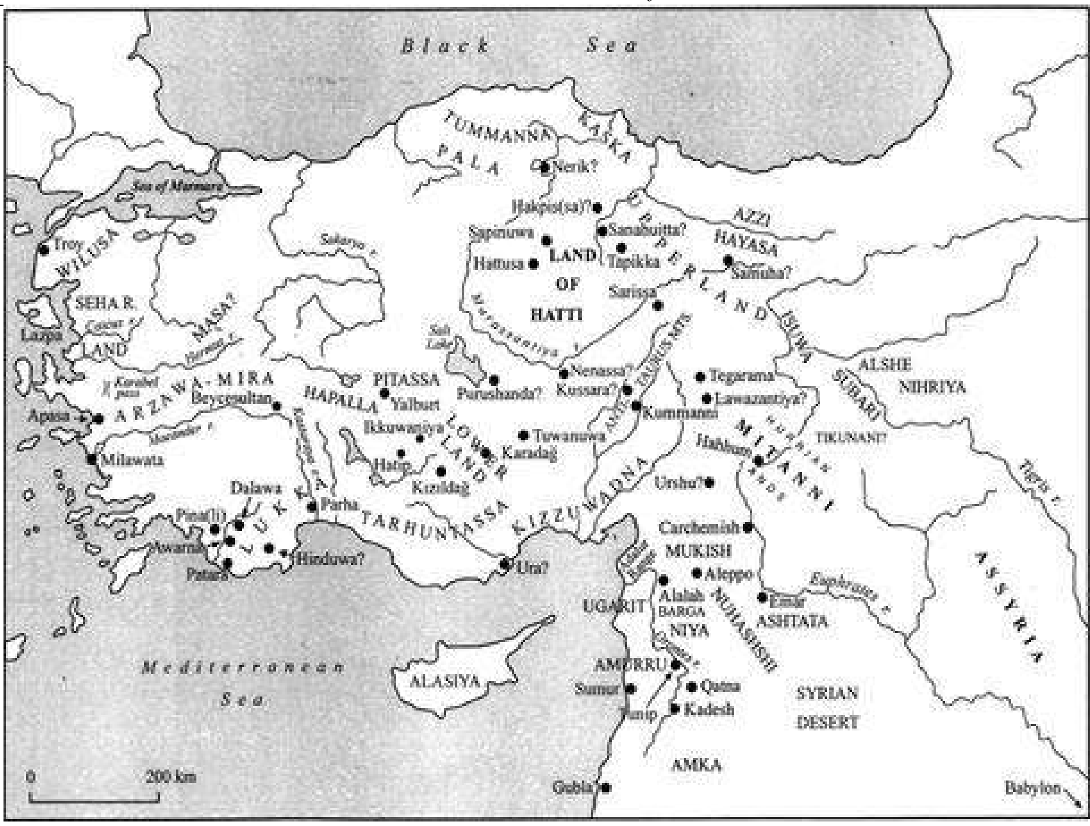

Figure 4. The map of the Hatti Kingdom, controlled by the Hittites Empire by Bryce (2007).

the Hayasa country but one should stress that there is a good geographical coincidence between Hayasa and the territories of (Armeno)Halibs according to comparison of mentioned Fig 3 and Fig 4 (Pliny the Elder (I AD), Bryce (2007)). It is worthy to note also that it is an area of Hamshen Armenians for whom iron in their dialect is "ergat" (Acharian (1935)). At last but not least technologically more convenient production of iron on the area of historical Armenia (e.g. Metsamor) is dating at XIV-XIII B.C. and what is more important there is close archeological (technological) connections between the Hatti (Hayasa) and Metcamor melting furnaces (Ivanov (1983)). At last but not least a much more early production of iron-containing paints for ornaments demanding on less than 1000 C was revealed in Metcamorian cultural layers and described by Ivanov (1983).

It should be stressed also that authors of many academic publications avoid the mentioned possible link between "Hayasa" and "Hayastan", like Walbaum (1980), Giorgadze (1988), Grigoryev (2000) but just reveal details of industrial production of first iron things. These authors describe that the texts of Hittites clearly distinguish between different kinds of iron: "iron" - (AN.BAR, also in Sumerian), "black iron" - (AN.BAR GE 6), "good clean iron" - (AN.BAR SIG 5), "sky iron" - (AN.BAR nepissass) but nowhere mention the similarity with that of in Armenian. On the other hand a modern Russian language internet folklore is saturated with such a findings equating the name of iron in Armenian "yerkat" with the mentioned term of the "sky drop". For example, "...first its (meteoritic iron) names come from Egypt, Mesopotamia and Armenia and mean sky metal..." Encyclopedia of Petrol (2017). Or, "... the iron name in ancient languages - e.g. in Ancient Armenia means "dropped from the sky..." by Gribanov (2011).

I am not going here to present a complete decoding of the questioned Armenian term "erkat" by reasons described above but just try to underline a following - in Greek, iron is known by 3 names: 1) " $\sigma\iota\delta\eta\rho o\zeta$ ", - "sederial" which probably reflects possible communications between Greeks and first "iron makers" at the Early Iron Age; 2) " $\chi\alpha\lambda\kappa o\sigma$ " - which means "metal, copper, steel"; 3) " $\chi\alpha\lambda\upsilon\psi$" - "iron, steel", coming from mentioned halibs as was shown by Ivanov (1983). Interestingly, " $\chi\alpha\lambda\kappa o\sigma$" is connected with more earlier term "ka-ko", coming from Mycenaean and meaning general name of metal in the pre-Iron Age as was mentioned by Ivanov (1983).

Let now browse in the Wiki Dictionares: it is easy to check following meanings: Persian (Farsi) - pulad (polat) - cast steel, Arabic - Fulad, Parzillu - iron stone - Assyrian, Akkadian - PAR.ZILLU, Aramaic - PAR.ZEL, bar-zel - Hebrew - as cutting, Ferrum - in all Romanian languages, also as hard (connected with bars - thicken - Sanskrit), Apkhazian - aikha (iron) - hard, German - Eisen (adopted from Keltic=Celtic

doi: https://doi.org/10.52526/25792776-23.70.1-1

- isara) - also old English - superpower, Georgian - rkina (probably adopted from Armenian). At last but again not least, one should mention the name Timur=Temur=Tamerlane=iron - as hard as iron (Timur, Meaning of name (2017)).

One can easily see that "sky drops" meanings were absent in the list above. One can see also that among existing languages (skipping Greek, Egyptian and Hittite) only Armenian name of iron (if directly translating from modern Armenian as "a sky drop") is connected with its nature and source of the origin while other languages stressed the function. Thus one comes to the final question, concerning interpretation of the term "yerkat - iron" in Armenian: is it correct to connect "yer-kat" with "sky iron" or not ? The answer is positive but bear in mind objections of phylologists one can suggest a new simple and evident idea: iron in Armenian means "sky metal" but not the "sky drop", that is yer - ka - (t) should be translated as sky metal. Here "yer" is "sky" in Armenian and "ka" is "metal" from oldest Micenian=IndoEuropian.

Thus it looks like that all the names of iron reflects the functions while Greek, Egypt and Hittite names and probably Armenian are connected also with the origin, meaning the "sky metal".

3. Conclusion

A probable connection between "Iron" in Armenian as concerned to its origin is discussed. On the base of data from easily verifiable sources is shown that all the names of "iron" in ancient and more modern languages reflect the "functions" while those in Hittite, Egypt, Greek and probably Armenian relate the origin. So "yer-ka (t)" in Armenian means "the sky metal"!

The author understand how complicated is the problem from the philological and historical points of view, on the other hand if all the mentioned above is impossible and is a mere coincidence then one should hope for unbiased explanation of that from the professionals in the subject. Also it would be not bad to understand first of all why so many coincidences are announced by academic sources concerning the History of Armenia, like, 1. Aratta = Ararat, 2. Hayasa = Hayastan, 3. Er-ka-t = the Sky Metall. One should remind that all of them (and some others) are announced as coincidences. So it would be much appreciated if one may explain such coincidences (at least what is concerned with "yerkat") in the way different from described above. Finally the author anticipates that the best scientific solution of the problems would be just simply to equate the names with their meanings in the list above.

Acknowledgements

This work was made possible by a research grant number No 21AG-1C044 from Science Committee of Ministry of Education, Science, Culture and Sports RA.

References

Acharian, H. 1935, Armenian Root Dictionary

Aeschilus, VII BC, Prometheus enchained

Bayun, L. 2011, Hittities and their contemporaries in the Ancient Near East, in: (A. Chubaryan, ed.), The World History, v. I, 184, M

Bryce, T. 2007, The Hittities Kingdom, Oxford University Press

Dyakonov, I. 1968, Prehistory of Armenians, Yerevan

Giza Piramid: The use of meteorites by Ancient Egyptians, 2017, "gizapyramid.com/meteorite.htm"

Giorgadze, G. 1988, Production and use of iron in central Anatoly by Hitities cuneiform texts, The Ancient East: ethno-cultural contact

Gribanov, A. 2011, The world history of mining

Grigoryev, S. 2000, Proceedings of Chelyabinsk Scientific Center, Issue 1

Harutiunyan, B. 1998, On the ethnicity of the Chorokh river areal population in VII-IV centuries BC, Hist.-Philolog. J. 1-2, 233

Herodotus, VII BC

Ivanov, V. 1983 History of Slavonic and Balkan names of metalls, M., Nauka

Ivanov, V. 1983 ...About haya..., Hist.Phyl.J., 4, Yerevan

Kosidowski, Z. 1963, Bible stories, Warsaw

Martirosyan, H. 2011, private message

doi: https://doi.org/10.52526/25792776-23.70.1-1

The Large Encyclopedia of Petrol and Gas, ”ngpedia.ru/id017038p2.html”

Pliny the Elder, I AD, The Natural History, VI, 4, 11-12

Redgate, A. 2000, The Armenians, WB

Russell J.2004, The Formation of the Armenian Nation, ULA, The Armenian People from Ancient to Modern Times, NY, St. Martin?s Press, p.19

Strabon, I AD, XII, 3, 19

Timur, Meaning of name, ”first-names-meanings.com”

Waldbaum, Y., 1980, The First Archeological Appearance of Iron and the Transition to the Iron Age. In: The Coming of the Age of Iron. Yale University Press, New Haven, London

Wainwright, G. 1938, The Sky-Religion in Egypt, Cambridge UP

Xenophon, IV BC, Anabasis

doi: https://doi.org/10.52526/25792776-23.70.1-1

Communications of BAO, Vol. 70, Issue 1, 2023, pp. 7-8

Introduction

Editorial board *

NAS RA V. Ambartsumian Byurakan Astrophysical Observatory (BAO)

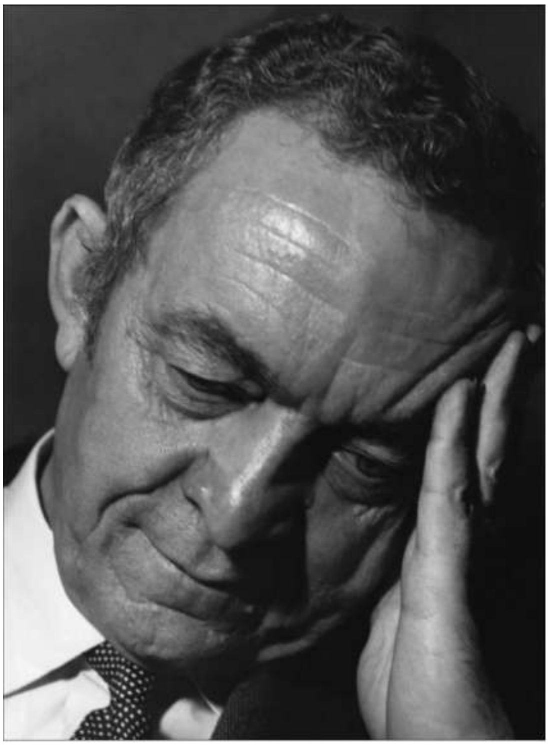

Ludwik MIRZOYAN (1923-1999)

Ludwik V. Mirzoyan is one of the beneficents of the Armenian astronomy whose whole life and scientific activity were devoted to the Byurakan Observatory and to the development of Armenian astronomy. His scientific, pedagogical, editorial, scientific-organizational and scientific-administrative works are colossal and invaluable. Mirzoyan has always been beside V. A. Ambartsumian and played one of the main roles in the formation and prosperity of the Byurakan Observatory, in the acquisition of the great scientific fame.

L. Mirzoyan's main scientific results are the proposing of a new method of determination of interstellar selective absorption, the working out of the method of "synthetic" stellar association and the demonstration of the expansion of OB-association, the determination of the value of A constant of the Galactic rotation, the investigation of the problem of K effect, the discovery and the investigations of hundreds of flare stars in Orion, Pleiades, and in other systems, as well as in Solar neighborhood, the spectrophotometric investigation of unusual objects, such as V1057 Cyg, FG Sge, RW Aur and SS Cyg, the investigation of Shahbazian compact groups of compact galaxies, etc. Altogether, *L. Mirzoyan* has 271 scientific publications, including 171 scientific papers (128 of them in scientific journals and 43 of them in proceedings of conferences), 15 books and booklets, 65 popular scientific articles and information materials. If we add the organization of a number of conferences, the editing of the journal "Astrofizika", 20 books and the proceedings of conferences, the teaching at the Yerevan State University, the training of a dozen of academic personnel (including foreign scientists) to all above mentioned, *L. Mirzoyan's* great merit in Armenian astronomy becomes clear.

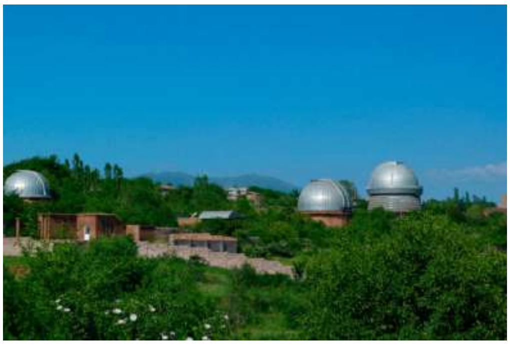 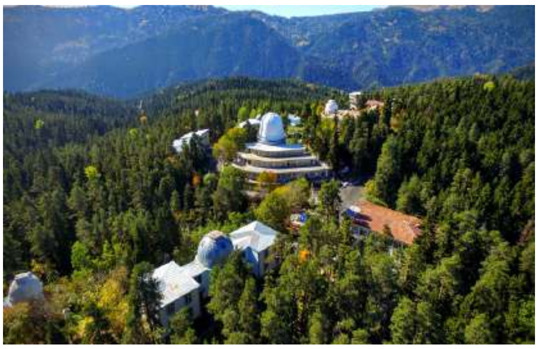

Byurakan Astrophysical observatory Abastumani Astrophysical Observatory

*combao@bao.am

The scientific collaboration and friendship between the Armenian and Georgian astronomers were established since 1930s due to *V. Ambartsumian's* (1908-1996) and *E. Kharadze's* (1907-2001) efforts. Many Armenian and Georgian astronomers collaborated and published joint papers. Among them, it is necessary to note the articles of *L. Mirzoyan* and *G. Salukvadze*, who jointly worked on stellar associations, T Tau and flare stars, etc. It was this topic that was devoted to a whole series of PhD and Doctoral theses of researchers from both Byurakan and Abastumani observatories. Such close cooperation was largely facilitated by regular joint Byurakan-Abastumani colloquiums, which began in 1974.Taking into account the significant contribution of *L. Mirzoyan* to the Armenian-Georgian cooperation several colloquia (1998, 2003, 2013) were dedicated to Lyudwik Mirzoyan's anniversaries.

On May 1-5, 2023, the **XV Joint Byurakan-Abastuman colloquium** was organized in Byurakan. It is also dedicated to *Lyudwik Mirzoyan's* anniversary (100*th*). 27 Armenian and 11 Georgian astronomers were participating. Works covering a wide range of astrophysical problems were presented at the colloquium. Active scientific discussion of the presented tasks will undoubtedly serve as a guarantee for further fruitful cooperation.

This issue of "Communications of BAO" includes the proceedings presented on the XV Joint Byurakan-Abastumani Colloquium. All the papers passed relevant peer-review.

Byurakan Astrophysical Observatory (BAO): current activities and statuses

A. M. Mickaelian *

NAS RA V. Ambartsumian Byurakan Astrophysical Observatory (BAO), Byurakan 0213, Aragatzotn Province, Armenia

Abstract

We review the current activities and statuses of the Byurakan Astrophysical Observatory (BAO), one of the most active research institutes of the Armenian National Academy of Sciences. BAO was founded by the outstanding scientist, National Hero of Armenia Viktor Ambartsumian in 1946 as an institute of the Armenian Academy of Sciences. Its main scientific research field is the instability phenomena of the Universe. It is recognized as an Armenian National Value in 2013, IAU Regional Centre in 2015, IAU Outstanding Astronomical Heritage in 2021, Registered UNESCO documentary heritage item (Markarian Survey) in 2011 and has a number of other statuses. BAO has two major instruments; 2.6m classical reflector and 1m Schmidt telescope. A number of research projects are active at BAO and its scientists are rather active at international level. Since 1998, BAO bears the name of V. A. Ambartsumian.

Keywords: *observatories – telescopes – observations – databases – meetings – summer/winter schools.*

Introduction

Byurakan Astrophysical Observatory (BAO) is one of the famous and most active research institutions of the Armenian National Academy of Sciences (NAS RA), as well as one of the most important astronomical centres in Eastern Europe and Middle East region, both by its scientific instruments and achievements. The Observatory was founded in 1946 on the initiative of Viktor Ambartsumian (1908-1996), the famous Armenian scientist of the 20th century. BAO is situated at an altitude of 1405m on the southern slope of Mt. Aragatz (with highest peak at 4090 m altitude), near village Byurakan, some 30 km Northwest to Yerevan, the capital of Armenia. V.A. Ambartsumian became the first director of the observatory, and main directions of astrophysical investigations were determined by him. First studies at BAO related to the instability phenomena taking place in the Universe, and this trend became the main characteristic of the science activity in Byurakan. Scientific results came just after the foundation of BAO. In 1947 stellar systems of new type, stellar associations were discovered by V.A. Ambartsumian. It was proved that at present star-forming processes are going on in the Universe, and stars are being formed by groups. Ambartsumian put forward an idea of star-forming in stellar associations together with gas and dust. In the mid-50s V.A. Ambartsumian gave a new explanation for radiogalaxies radiation and proposed a new conception on the activity of galactic nuclei. By the time, it was accepted by all the astronomers, and at present most of the astrophysical observatories have the subject of Active Galactic Nuclei (AGN) as one of their main research areas. The discovery of stellar associations and Ambartsumian's idea about activity of galactic nuclei, as well as investigations on radiation transfer theory, based on Ambartsumian's principle of invariance, elucidated the further development of the research activities in BAO. Among the observing studies, Markarian Survey on Active (UV-Excess) Galaxies may be mentioned, carried out in 1965-1980. After the disintegration of the Soviet Union, the Byurakan astronomers underwent difficult situation in economy and science, however, in a few years a new activity began in mid-90s with some re-organizational process and new international collaborations. Due to French astronomers, the 2.6m telescope was equipped with new instrumentation and started to giving new interesting results. Later on, in 2015, the 1m Schmidt was also renovated and started observations. Due to obtained results the Byurakan Observatory is recognized by the scientific community as one of the main centres for astrophysical research. The conceptions and ideas proposed in Byurakan have found their further elaboration in many observatories, a few thousands of new objects discovered in

*aregmick@yahoo.com

doi: https://doi.org/10.52526/25792776-23.70.1-9

Byurakan are observed worldwide by famous astrophysicists. Since 1998 the Byurakan Observatory bears the name of V.A. Ambartsumian – its founder and scientific leader for many years. It is now more than 75 years that the Byurakan Observatory is among the world astronomical centers and successfully continues its new discoveries and high-level research.

BAO telescopes

The ZTA-2.6 telescope (installed in 1975) is the largest observational instrument of the Byurakan Astrophysical Observatory and one of the 10 biggest telescopes of Europe, Asia, Africa and Australia. It is included in the list of the largest scientific equipment of the former USSR territory. At the time of its installation, it was the 7th largest telescope in the world.

Figure 1. 2.6 m telescope of BAO.

BAO's 1m Schmidt Telescope (installed in 1960) is one of the world's 10 largest telescopes of this type and one of the most effective telescopes in general. Markarian Survey (FBS), observations of stellar clusters and associations and discoveries of thousands of flare and T Tau stars were carried out by this telescope.

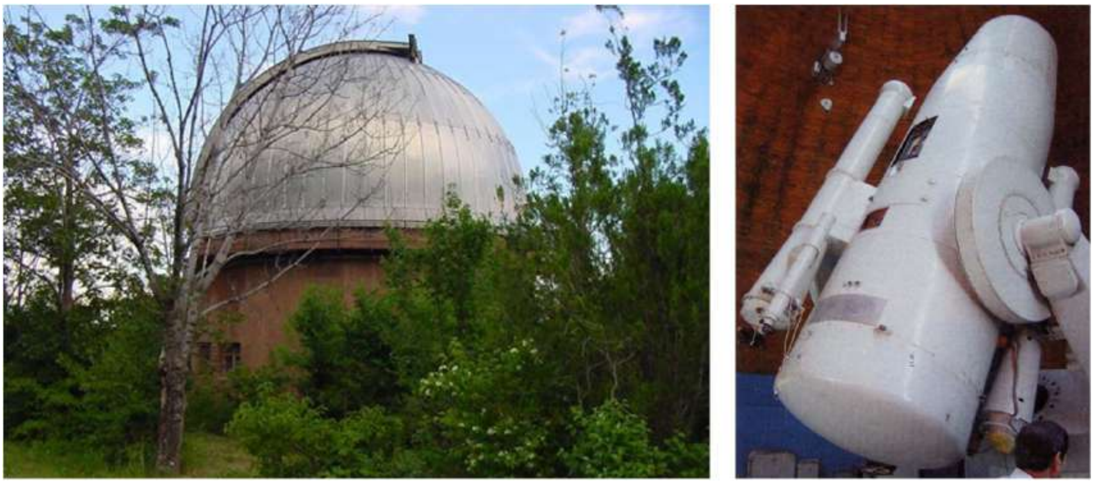

Figure 2. 1m Schmidt Telescope of BAO.

Research Activities

BAO is one of the rarest observatories in the world where many new cosmic objects have been discovered. About 14,500 cosmic objects have Armenian names. It is famous by its surveys. Stellar Associations were discovered in 1947 by Viktor Ambartsumian in BAO. The formation of the stars in groups and the continuous processes of star formation currently occurring in the Galaxy have been proved. In the middle of 1950s,

doi: https://doi.org/10.52526/25792776-23.70.1-9

Viktor Ambartsumian put forward the hypothesis of the activity of galactic nuclei, as a result of which a new direction of astrophysics has been developed. The main directions of research at BAO are:

- Star-Formation phenomena, Star-Formation regions, young stars and young stellar objects.
- Nebulae, their connection with stars, mechanism of formation and evolution.
- Nuclear and Star-Formation activity of galaxies, groups and clusters of galaxies.
- Theoretical studies: radiative transfer theory, interpretation of spectra.
- New directions: astrochemistry, astrobiology, High Energy Astrophysics (HEA) and others.

BAO basic program is called A-3: The role of non-stable phenomena in the evolution of cosmic objects.

Research Departments

Currently, BAO has 9 research departments covering broad aspect of astronomical/astrophysical topics, from stars to galaxies and from observations to theory. They are:

- *Astronomical Surveys*, Head: *Dr.* Areg Mickaelian
- *Non-Stable Phenomena*, Head: *Dr.* Haik Harutyunian
- *Young Stellar Objects (YSOs)*, Head: *Dr.* Tigran Magakian
- *Active Galaxies*, Head: *Dr.* Ruben Andreasyan
- *Astrochemistry, Astrobiology and Exoplanets*, Head: *Dr.* Ararat Yeghikyan
- *Theoretical Astrophysics*, Head: *Prof.* Arthur Nikoghossian
- *High Energy Astrophysics (HEA)*, Head: *Dr.* Gagik Ter-Kazarian
- *Cosmic Compact Objects and Relativistic Gravity*, Head: *Dr.* Armen Sedrakian (Germany)
- *Archaeoastronomy and Cultural Astronomy*, Head: *Dr.* Hayk Malkhasyan

In addition, *Prof.* Elma Parsamian is BAO Director's scientific advisor. BAO also has foreign scientific advisors:

- Vladimir Airapetian (GSFC, NASA, USA)
- Georges Alecian (Paris-Meudon, France)
- Tigran Arshakian (Koeln, Germany)
- Valeri Hambaryan (Jena, Germany)
- Garik Israelian (IAC, Spain)
- Michel Dennefeld (IAP, France, Project Advisor)
- Lex Kaper (Amsterdam, Netherlands, Project Advisor)

Research Projects

Along with their regular research work, BAO scientists have a number of projects, including:

- RA Science Committee Advanced Research Grant 21AG-1C044 (2021-2026): Star Forming Regions: *Origin and Evolution*, PI Elena Nikoghosyan

doi: https://doi.org/10.52526/25792776-23.70.1-9

- RA Science Committee Advanced Research Grant 21AG-1C053 (2021-2026): *Revelation of Early Stages of Gal. Evolution by Means of Multiwavelength Study of Active Galaxies*, PI Areg Mickaelian
- RA Science Committee Thematic Grant 21T-1C031 (2021-2024): *Young Stellar Objects with Extreme Outbursting Activity*, PI Tigran Magakian
- RA Science Committee Remote Laboratories Establishment Grant 22RL-039 (2022-2027): *Search and identification of high-velocity stars by means of dynamical ejections from multiple stars and Supernova explosions*, PI Valery Hambaryan (Jena, Germany), Co-PI Satenik Ghazaryan
- Volkswagen Foundation Research Grant (2021-2023): *Equation of State and Composition of Proto-Neutron Stars and Merger Remnants with Hyperons*, PI Armen Sedrakian
- ANSEF grant PS-astroex-2597 (2022-2023): *Search and studies of luminous X-ray galaxies*, PI: Areg Mickaelian

Digitized First Byurakan Survey (DFBS)

The First Byurakan Survey (FBS) has been created by Beniamin Markarian and colleagues in BAO in 1965-1980. The survey is the largest ever astronomical spectroscopic survey of the northern sky and is considered as one of the most important achievements of the Astrophysics in 20th century. This was a new method of search for active galaxies. The first digitalization project of Armenia was carried out in BAO in 2002-2007 by Areg Mickaelian and his team, the digital version of 2000 plates of Markarian Survey (FBS) was created and reserved in the largest Armenian astronomical database. This digitized version is called DFBS, the largest low-dispersion spectroscopic database in the world (https://www.aras.am//Dfbs/dfbs.html).

Armenian Virtual Observatory (ArVO)

The Armenian Virtual Observatory (ArVO) was created in 2005 and is one of the 22 national VO projects of the International Virtual Observatories Alliance (IVOA). The Astrophysical Virtual Observatories (AVOs) have been created in a number of countries using their available databases and current observing material as a collection of interoperating data archives and software tools to form a research environment in which complex research programs can be conducted. Among all these data, a large spectroscopic database for all objects will be especially useful. ArVO has being created to utilize the Digitized First Byurakan Survey (DFBS) as an appropriate spectroscopic database. ArVO is a project of the Byurakan Astrophysical Observatory (BAO) aimed at construction of a modern system for data archiving, extraction, acquisition, reduction, use and publication. ArVO is based on the Digitized First Byurakan Survey (DFBS). One of the ArVO's main tasks is to create and utilize a global Spectroscopic Virtual Observatory, which will combine data from DFBS and other low-dispersion spectroscopic databases, as well as provide the first understanding on the nature of any object up to B=18m. In frame of the ArVO, BAO collaborates with the Institute of Information Technologies (IIT) of the Armenian National Academy of Sciences to develop software for ArVO corresponding to the IVOA standards. Beside the DFBS, ArVO is being complemented by the Digitized Second Byurakan Survey (SBS) database, the Byurakan photographic archive, and BAO 1m and 2.6m telescopes observations.

Space Debris Monitoring project

Since 2014, the Roscosmos station has been operating under contract at BAO, which monitors Space debris. The collaborator is the Astronomical Scientific Centre (Russia). A new monitoring project started at the observational base "Saravand" of BAO. This project initiated for revealing natural and artificial objects at the near-Earth Space. This is a kind of continuation of earlier observational projects implemented at the Observatory prior the collapse of Soviet Union. This time, near-Earth space monitoring is carried out at the request of the Russian agency "Roskosmos". For observations, the EOP-1 module is used, which includes small telescopes with a mirror diameter of 40cm, 25cm and 19cm.

Collaborations

doi: https://doi.org/10.52526/25792776-23.70.1-9

BAO has always been very active in international collaborations and also collaborations with local (Armenian) scientific organizations.

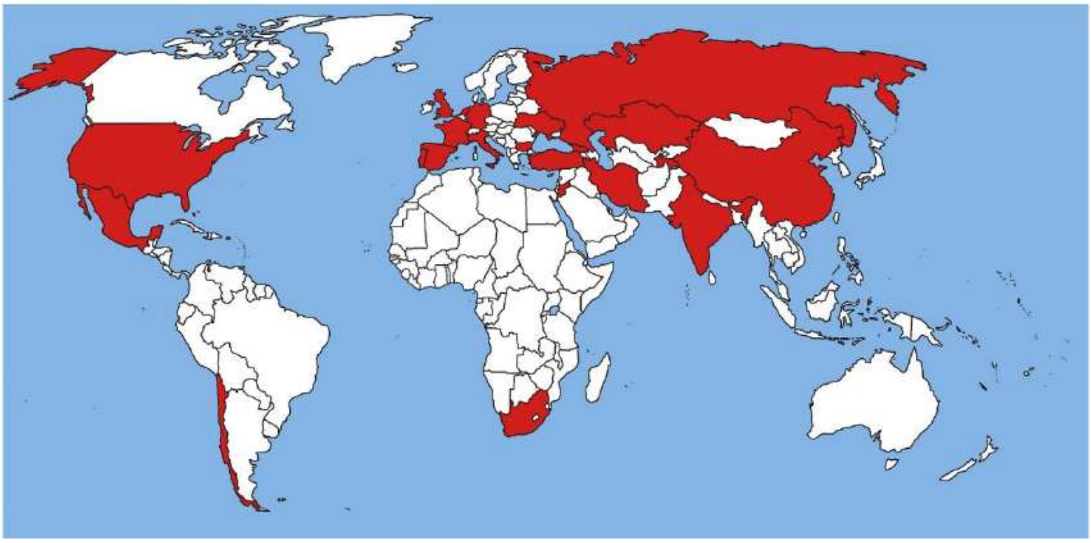

Figure 3. The world map of BAO collaborations. In total, 23 countries are involved.

Scientific Organizational Activities

BAO seminars

BAO is very active in organizing seminar. We have 4 types of seminars: Scientific, including also review seminars, Technical, Information, and Reports. During 2017-2023, 182 seminars, including 41 by foreign speakers were organized. The seminars by outstanding scientists were given by: Nobel Prize Winners John Mather (NASA/GSFC, USA), Reinhard Genzel (MPE, Germany), and Michel Mayor (Geneva Observatory, Switzerland), IAU President Ewine van Dishoeck (Leiden Observatory, Netherlands), ESO Director General Xavier Barcons (ESO, Germany), outstanding scientists Joseph Silk (IAP/JHU, France), Jill Tarter (SETI Institute, USA), Edward P.J. van den Heuvel (University of Amsterdam, Netherlands), Vahé Petrosian (Stanford University, USA), Daniel Kunt (IAP, France) and others.

European Annual Astronomical Meeting 2007

One of the European Astronomical Society (EAS) Annual Meetings was organized by BAO in 2007 in Armenia (JENAM-2007, Joint European and National Astronomy Meeting). It was the largest ever scientific event in Armenia by both its significance and the number of participants. It had 14 parallel sessions and hundreds of talks and posters.

IAU Symposia and Colloquia

Six IAU Symposia and an IAU Colloquium have been organized by BAO: 1966, 1986, 1989, 1998, 2001, 2016 and 2023. Due to BAO, Byurakan village appears in the list of 10 "cities", such as Paris, Rome, Vienna, Prague, Beijing, Honolulu, Rio de Janeiro, where the International Astronomical Union's (IAU) meetings took place most frequently. The Proceedings were published by Cambridge University Press (CUP) and the Astronomical Society of the Pacific (ASP) Conference Series.

First International Conference on CETI 1971

The world's first international (in fact, Soviet-American) conference on the search for extraterrestrial intelligence (SETI) and communication with them (CETI) was held at BAO in 1971. Many famous scientists were present, including 3 Nobel Prize Winners. At that time the exoplanets were not yet discovered and

doi: https://doi.org/10.52526/25792776-23.70.1-9

the scientists believed that the only way of revelation of extraterrestrials is the communication with them by sending and receiving radio signals. But the meeting encouraged many further studies in this area.

UNESCO Conference 2017

A UNESCO Regional Conference, the only such one in Armenia was organized by BAO in 2017 entitled "Astronomical Heritage of the Middle East". It covered many aspects of Archaeoastronomy and Cultural Astronomy and was rather important for the Armenian science representing many talks and posters on various heritage items, including the Armenian calendars, the Armenian (astronomical) rock art, ancient observatories, names of constellations, medieval Armenian astronomy, Anania Shirakatsi's heritage, etc. The Proceedings were published by the Astronomical Society of the Pacific (ASP).

Meetings on Interdisciplinary and Multidisciplinary Sciences

In 2015 and 2020, we have organized Symposia on "Astronomical Surveys and Big Data" (ASBD and ASBD-2) with the participation of astronomers and computer scientists. Many leaders and/or other representatives from the International Virtual Astronomy Alliance (IVOA) and national VO projects were present. In 2014, we organized one of the first meetings of such type "Relation of Astronomy to other Sciences, Culture and Society" (RASCS) with wide participation of astronomers, physicists, computer scientists, chemists, biologists, historians, archaeologists, philosophers, linguists, and others. A number of meetings on Archaeoastronomy and Cultural Astronomy were organized as well.

Byurakan International Summer Schools (BISS)

The Byurakan International Summer Schools (BISS) for Young Astronomers (founded in 2006) are among the World's top-3 Astronomical Schools. In 2018, Byurakan International Summer School (BISS), which is being held once per 2 years, was announced one of the world's best astronomical schools by the International Astronomical Union. The school is intended for young astronomers, MSc and PhD students in Astronomy. Until now, 8 summer schools have been held: 2006, 2008, 2010, 2012, 2016, 2018, 2020 and 2022. The 2010 school was combined with the IAU International School of Young Astronomers (ISYA).

BAO Official Statuses and Initiatives

BAO as RA National Value

BAO was granted the status of "National Value" of the Republic of Armenia in 2013, by the decree of the RA government. BAO is one of the 3 RA National Values together with Matenadaran and Armenian Genocide Museum-Institute. Its importance as a National Value includes its research and scientific-organizational activities, national and international statuses and significance, cultural, educational and outreach activities and importance, rich botanical garden, unique architectural ensemble, and its importance as a centre for Scientific/Astro Tourism.

BAO as IAU Regional Centre

Figure 4. BAO as IAU Regional Centre

doi: https://doi.org/10.52526/25792776-23.70.1-9

In 2015, the Byurakan Astrophysical Observatory (BAO) was appointed by the International Astronomical Union (IAU) as a host of the South West and Central Asia Regional Office. Being one of the 11 regional offices of Astronomy, it coordinates astronomy for development activities in the nearby countries. The official members are: Armenia, Georgia, Iran, Kazakhstan, Tajikistan and Turkey. The activities are performed within three Task Forces: TF1 Universities and Research (Professional Astronomy), TF2 Children and Schools (Astronomical Education) and TF3 Public Outreach.

BAO UNESCO Documentary Heritage item

In 2011, Markarian survey (the First Byurakan Survey, FBS) was included in the UNESCO "Memory of the World" documentary heritage international register. It is one of the 12 UNESCO items in Armenia and one of the rare scientific heritage items of UNESCO in the whole world. FBS contains the records of a unique astronomical survey carried out in BAO by the great Armenian astronomer Beniamin Markarian and his colleagues in 1965-1988. The survey involved the largest ever astronomical spectroscopic study of the nearby universe and is considered as one of the most important achievements of the 20th century astrophysics. It provides data on 40,000,000 low dispersion spectra for 20,000,000 objects. The records were carried out on BAO 1m Schmidt telescope. They cover the whole Northern Sky and part of the Southern Sky at high galactic latitudes and some part in the Milky Way areas. The FBS was conducted originally for search of galaxies with UV-excess (UVX). The discovery of 1515 UVX galaxies by Markarian and colleagues (later called Markarian galaxies) was the first and the most important work based on the FBS plates. It was digitized in 2002-2007 by Areg Mickaelian and his team and the Digitized First Byurakan Survey (DFBS) was created, the largest low-dispersion spectroscopic database in the world, and the first digitization project in Armenia in all spheres (https://www.aras.am//Dfbs/dfbs.html).

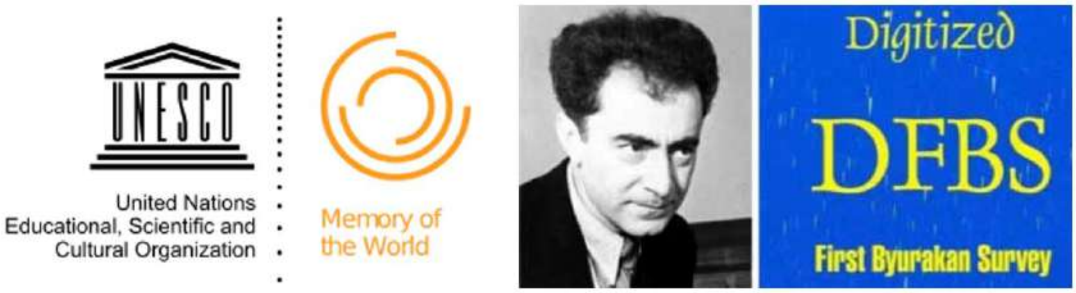

Figure 5. BAO UNESCO Documentary Heritage item

BAO as IAU Outstanding Astronomical Heritage

In 2021, BAO was included in the IAU Outstanding Astronomical Heritage (OAH) list as one of the most important world observatories. This list serves as UNESCO Heritage candidate list. BAO was among the first items that made up this list and started this initiative.

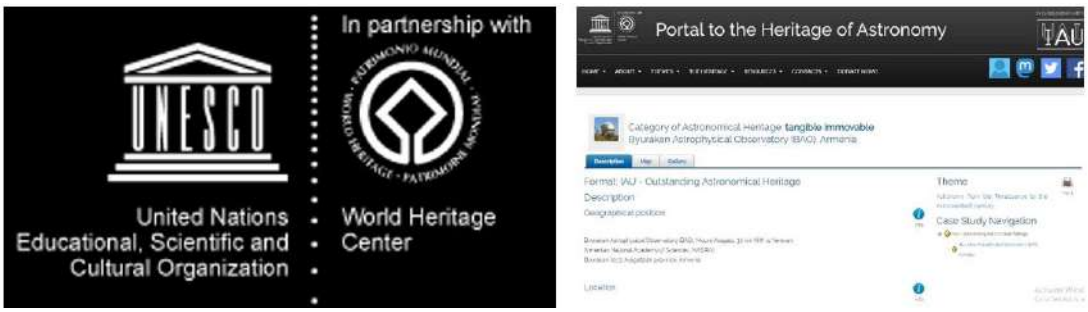

Figure 6. BAO as IAU Outstanding Astronomical Heritage

Armenian Astronomical Society (ArAS)

doi: https://doi.org/10.52526/25792776-23.70.1-9

The Armenian Astronomical Society (ArAS) was founded in 2001 and brings together 100 astronomers from 20 countries. Operating at BAO and being a non-governmental organization (NGO), ArAS aims to develop Astronomy in Armenia, foster the collaboration between the Armenian and foreign astronomical institutions, strengthen the connection between the Armenian and foreign astronomers, contribute to the astronomy education and science popularization in Armenia. ArAS is also an affiliate member of the European Astronomical Society (EAS). ArAS has a very rich webpage, circulates electronic newsletters (ArASNews), organizes Annual Meetings and awards ArAS Annual Prizes for young astronomers (Yervant Terzian Prize).

Byurakan Astrophysical Observatory as a Unique Architectural Ensemble

BAO's architectural ensemble is listed in Armenia as a unique architectural construction. It is also is submitted to the IAU Outstanding Astronomical Heritage (OAH) list as a unique architectural building. The construction of the observatory's architectural complex began in 1946 under the supervision of famous architect Samvel Safarian and the latest buildings were designed and built under the supervision of another famous architect Sargis Gurzadyan. The first buildings were Viktor Ambartsumian's house (now house-museum) and the two telescope towers in front of the administrative building. The architectural ensemble of the observatory comprises of the administrative buildings and telescope towers. Buildings constructed during 1940-1950's were designed by the famous Armenian architect Samvel Safarian, while the ones constructed during 1960-1980's by Sargis Gurzadian.

Figure 7. Byurakan Astrophysical Observatory as a Unique Architectural Ensemble

Armenian National Hero Viktor Ambartsumian House-Museum

Armenian National Hero Viktor Ambartsumian house-museum is situated at the Byurakan Astrophysical Observatory. Viktor Ambartsumian's house was built in 1950. It was turned into a house-museum in 1998 on the occasion of the great scientist's 90th anniversary. The house-museum presents Viktor Ambartsumian's life and activity, family photos, career path including various scientific works, diplomas, certificates and awards. In the same year (1998), BAO was named after Viktor Ambartsumian.

Figure 8. Armenian National Hero Viktor Ambartsumian House-Museum

BAO Pantheon as a Monument of Local Significance

In 2021, by the decree of the Expert committee of the RA Ministry of Education, Science, Culture and Sport, Pantheon of Viktor Ambartsumian and his family members, as well as other Armenian astronomers (established in 1965) situated near the Byurakan Astrophysical Observatory (BAO), was granted the status

doi: https://doi.org/10.52526/25792776-23.70.1-9

of a newfound monument of local significance. According to the BAO directorate decision 2021, the cemetery was renamed “Byurakan Astrophysical Observatory Pantheon”.

BAO Park as an Arboretum

According to the agreement signed between the RA Ministry of Ecology and the Byurakan Astrophysical Observatory in 2017, the Observatory’s green area was recognized as an arboretum (“dendropark”). It has some 140 types of trees and plants, as well as a variety of birds, insects and small animals.

BAO as Scientific (Astro) Tourism Center

In 2016, International Astronomical Union recognized the Byurakan Astrophysical Observatory as the initiator of astronomical tourism (Astro Tourism) in the world, while in 2015 according to the agreement signed the same year, it was recognized as Scientific tourism center of Armenia by the Armenian Institute of Tourism. BAO was recognized as an initiator of astronomical tourism in the world by IAU in 2016 and according to the 2015 agreement with the Armenian Institute of Tourism, as the center of scientific tourism of Armenia.

At the end, we give a summary table with all BAO statuses and initiatives.

BAO official statuses and initiatives.

Table 1.

Year	Statuses / Initiatives	Short	Awarded or recognized by
1946	Was founded as an Armenian Academy Research Institute	Research Institute	RA Government
1946	“Communications of BAO” journal was founded	ComBAO	BAO
1956	BAO Unique Architectural Ensemble was built	Architectural Ensemble	RA Government
1960	BAO 1m Schmidt telescope – among the world Top-10 wide-angle telescopes	BAO 1m Schmidt	
1965	“Astrofizika” (Astrophysics) journal was founded (then as an All-Union journal)	“Astrophysics”	NAS RA
1966	BAO was awarded Lenin Order	Lenin Order	USSR Government
1975	BAO 2.6m telescope – among the Top-10 telescopes in Europe, Asia, Africa and Australia	BAO 2.6m	
1977	BAO Special Council was established	BAO Special Council	NAS RA
1995	BAO Educational and Outreach programs	BAO Edu/Outreach	BAO
1998	Viktor Ambartsumian House-Museum	VA House-Museum	RA Government
2001	Armenian Astronomical Society	ArAS	EAS
2005	Armenian Virtual Observatory	ArVO	IVOA
2006	Byurakan International Summer Schools	BISS	IAU Division C
2009	BAO as initiator of the Scientific Journalism in Armenia	Scientific Journalism	
2009	BAO as initiator of the Scientific Tourism in Armenia, BAO as Astro Tourism Center	Astro Tourism Center	IAU / Armenian Inst. of Tourism
2011	UNESCO “Memory of the World” Documentary Heritage International Register	UNESCO MOW	UNESCO
2013	RA National Value	RA National Value	RA Government
2015	IAU South West and Central Asia Regional Office of Astronomy for Development	IAU SWCA ROAD	IAU
2017	BAO Protected Area – Arboretum	Arboretum	RA Government
2021	BAO Pantheon as a Monument of Local Significance	BAO Pantheon	RA Government
2021	IAU Outstanding Astronomical Heritage	IAU OAH	IAU

doi: https://doi.org/10.52526/25792776-23.70.1-9

Communications of BAO, Vol. 70, Issue 1, 2023, pp.18-22

Prof. Lyudwik Mirzoyan's life and activity

V.V. Hambaryan *[1,2] and A.A. Akopian†[2]

[1]Astrophysical Institute of Friedrich-Schiller-University Jena, Germany
[2]Byurakan Astrophysical Observatory after V.A. Ambartsumian, Armenia

Abstract

Prof. Lyudwik Mirzoyan is one of the best representatives of the first generation of Armenian astronomers who had founded Byurakan Observatory and the Byurakan direction in science. For thirty years he had been the assistant of Victor Hambartsumian at Byurakan Observatory and has a huge input in formulation of the modern understanding of star formation, thus becoming the pioneer in Armenian observational astronomy.

1. Introduction

A XV joint Armenian – Georgian astronomical colloquium dedicated to the 100th anniversary of Academician Lyudwik Mirzoyan, took place in Byurakan Astrophysical Observatory of the National Academy of Sciences of Armenia. The tradition of Armenian – Georgian joint scientific meetings had been established back in the 1970s, and by the initiative of Academician Victor Hambartsumian. Both Victor Hambartsumian and Lyudwik Mirzoyan have played a great role in the development of astronomy in Georgia and, due to their efforts, several joint Armenian – Georgian scientific programs had been implemented. They have educated several generations of Georgian astronomers, guiding their scientific research works. To note, this year in May—and on the occasion of the 90th anniversary of prominent astrophysicist, Academician of the National Academy of Sciences of Armenia, First Armenian Member of the French International Academy of Astronautics, Professor, Honored Scientist of the Armenian Soviet Republic Lyudwik Mirzoyan—the presentation of the book entitled Life Devoted to Byurakan, written by his daughter Nune Mirzoyan, took place at the hall of the Presidium of the National Academy of Sciences of Armenia.

Lyudwik Mirzoyan is one of the best representatives of the first generation of Armenian astronomers who had founded Byurakan Observatory and the Byurakan direction in science. For thirty years he had been the assistant of Victor Hambartsumian at Byurakan Observatory and has a huge input in formulation of the modern understanding of star formation, thus becoming the pioneer in Armenian observational astronomy.

2. Biography

Lyudwik Vasili Mirzoyan (1923-1999) was born on May 1, 1923, in Yerevan. His parents were from the city of Maku in the Atrpatakan region of Iran and had strong ties with prominent Armenian cultural figures. Specifically, L.V. Mirzoyan's father, Margar Mirzoyan, was the brother of Yeghishe Charents' mother, Tekghi Mirzoyan (Telli Mirzayan). His mother, Anush Avdalbegian, was the sister of the renowned Armenian scholar Tadevos Avdalbegian.

Despite losing his father at a young age and facing various economic and psychological challenges, L.V. Mirzoyan managed to get admitted and graduate from the Faculty of Physics and Mathematics of Yerevan State University, obtaining a degree in mathematics. In 1947, he received a recommendation from the academician Victor Ambartsumian to work at the newly established Byurakan Observatory. His pedagogical activities also commenced during this time.

In 1951, under the joint supervision of Ambartsumian and Oleg Melnikov, Mirzoyan successfully defended his dissertation, which focused on the spectrophotometric study of stars belonging to early spectral classes.

*Valeri.Hambaryan@uni-jena.de, Corresponding author
†aakopian57@gmail.com

doi: https://doi.org/10.52526/25792776-23.70.1-18

This achievement earned him the degree of Candidate of Physico-Mathematical Sciences. In 1953, Mirzoyan assumed the role of scientific secretary at the Byurakan Observatory, and in 1959, he became the deputy director–a position he held for approximately three decades.

During this time, the Byurakan Observatory has received international recognition and has become one of the leading observatories in the world, having received the honorary Order of Lenin, the highest state award of the USSR. Since 1965, Mirzoyan headed the Department of Physics of Stars and Nebulae at the Byurakan Observatory.

Since this same year, Mirzoyan was actively involved in the works of the newly founded Soviet Union's journal "Astrophysics". Initially, he served as deputy of editor-in-chief and later as editor-in-chief. Despite the challenging circumstances faced by the country in the 1990s, Mirzoyan's dedicated efforts ensured the continued publication of the journal. In addition to his editorial responsibilities, Mirzoyan served as a member of the scientific publishing board of the Armenian Soviet Encyclopedia, and he authored a majority of the astronomical articles within its pages. His editorial and scientific publishing activities extended beyond these roles, as he authored or edited numerous monographs, international conference materials, symposiums, popular science books, textbooks, and more than 200 articles. Notably, his monographs highlighted the achievements of the Byurakan school of astronomy and underscored the contributions and impact of its founder - V.A. Ambartsumian, in modern astrophysics.

In 1968, Mirzoyan successfully defended his doctoral dissertation in Leningrad, focusing on the physics and kinematics of young stars. This accomplishment led to his recognition as a Doctor of Sciences. Mirzoyan's significant contributions and stature in the field of astronomy were acknowledged through his election as a corresponding member of the International Academy of Astronomy in 1970, a corresponding member of the Academy of Sciences of the Armenian SSR in 1986, and an academician of the National Academy of Sciences in 1996. Furthermore, in 1974, he was bestowed with the honorary title of Honored Scientist of the Armenian SSR. Mirzoyan's scientific, scientific-organizational, pedagogical, and editorial endeavors consistently garnered high praise from Soviet-Union, domestic, and international institutions.

3. Scientific activity

The beginning of L.V. Mirzoyan's scientific activity coincided with two significant, fortunate events for the development of modern astrophysics. The first was the foundation of the Byurakan observatory, and the second was the discovery of stellar associations by V.A.Ambartsumian. The discovery of stellar associations provided a unique opportunity to establish and study early stages of star evolution, making the Byurakan observatory a leading center for such research.

Figure 1. V.Amabartsumian and L.Mirzoyan

L.V. Mirzoyan's early (1950-1970) scientific works focused primarily on the study of stellar associations and their stellar populations, particularly in relation to hot OB stars of the early class. Some of the key

doi: https://doi.org/10.52526/25792776-23.70.1-18

contributions and findings from Mirzoyan's research include:

1) Determination of Interstellar Selective Absorption: Mirzoyan proposed a novel method for determining interstellar selective absorption based on the relationship he established between spectrophotometric gradients and color excesses of OB stars. He demonstrated that the average cosmic absorption law remains consistent in layers parallel to the galactic plane at varying distances.

2) Study of OB-Stellar associations: Mirzoyan introduced the concept of a "synthetic" stellar association stellar association, which involves combining all known stellar association stellar associations and subgroups of OB stars brought to a common center. He analyzed the spatial distribution law and partial density of O-B1 stars around the core of the stellar association stellar association, using data from 27 stellar association stellar associations and 744 O-B1 stars.

3) Determination of Solar Velocity and Oort's Constant: Mirzoyan utilized available data on the linear velocities of 330 OB stars to determine the velocity speed of the Sun and Oort's constant A, which characterizes the rotation of the Galaxy. His calculated value for constant A was significantly smaller than the previously accepted value and was subsequently adopted by the International Astronomical Union.

4) Investigation of the K Effect: Mirzoyan extensively studied the K effect in subsystems of O-B0.5 stars. He demonstrated that the K term, initially positive for nearby stars, gradually decreases and becomes negative with increasing distance from the Sun. Mirzoyan attributed this behavior to the dynamic origin of the effect.

5) Expansion of OB Stellar associations: Mirzoyan confirmed the expansion of OB stellar associations using radial velocities, building upon the predictions made by V.A. Ambartsumian and the works of Blaau et al., which were based on proper motion studies. Mirzoyan's "synthetic" stellar association method enabled him to establish the expansion using radial velocities alone. He also observed that the mean and variation of radial velocities increase with distance from the interstellar core, suggesting that OB stars in the galactic field were ejected from parent associations.

6) Study of Formation and Development of OB Stars: Mirzoyan employed the "synthetic" stellar association method to investigate the rates of formation and development of OB stars. By analyzing available data, he deduced that the continuous decrease in star density from the center of the stellar association results from ongoing star formation. Mirzoyan estimated the average lifetimes of OB stars by interpreting the deviation from the inverse square law as an indication of the statistical aging process.

7) Analysis of Continuous Emission in Unstable Stars: Mirzoyan conducted studies on the continuous emission observed in the spectra of certain unstable stars. He concluded that known mechanisms of continuous emission were insufficient to explain the observed spectral features. Mirzoyan proposed that the observed continuous emission is non-thermal in nature, resulting from the direct quenching of intrastellar energy in the outer layers of stellar atmospheres.

Beginning in the 1970s, Mirzoyan's scientific work focused mainly on the study of red dwarfs, especially flare stars. The method proposed by V.A. Ambartzumian in 1968 to estimate the total number of flare stars inspired to more intense study of flare stars. L.V. Mirzoyan emerged as the in-fact leader of these studies conducted within the framework of an international program. Under his direct guidance and participation, astronomers from Armenia, Georgia, Uzbekistan, Kazakhstan, Bulgaria, and Hungary successfully conducted a comprehensive investigation of flaring star systems such as Orion, Pleiades, Hyades, Praesepe, and others, as well as flare stars in vicinity to the Sun. The main results of these studies were:

1) First and foremost, several hundred new flaring stars in neighboring stellar associations and star clusters were revealed. The studies of the physical characteristics of these stars (spectra, brightnesses, colors, etc.) were performed in both quiescent and flaring states.

2) The study of flare stars of the Sun's vicinity showed that these stars do not form a physical system, but are flare stars that appeared in the galactic field because of the disintegration of stellar associations and star clusters. The research also revealed a lack of relatively high-luminosity flare stars in the galactic field. Moreover, the flare stars majority discovered at the direction of a given stellar association or star

cluster (90%) are members of the association/cluster, confirming that the flaring activity of a dwarf star can be considered a reliable indicator of its association with a specific star cluster or association.

3) Stars in the galactic field do not qualitatively differ from stars in stellar associations and star clusters. Simultaneous observations of star flares provided evidence that the colours of flare radiation are broadly consistent between relatively high-luminosity flare stars of associations and clusters, as well as low-luminosity flare stars of the Sun's vicinity.

4) Some of the observed quantitative differences have been successfully explained by age differences in flare star systems. Evidence for this is the relationship between the age of the flaring star system and the average luminosity of the flaring stars established by Mirzoyan and his colleagues. The study of flare stars confirms Ambartsumian's hypothesis that the stage of flare activity is a regular stage in the evolution of red dwarfs.

5) In the 1970s -90s, in his articles and monographs Mirzoyan presented and supported the sequence of evolution of red dwarfs, suggested by Ambartsumian and Haro: from a protostar to a T Tau type star, a flare star, and, ultimately, to a normal star. During the 1970s, the spectrophotometric examination of unique objects exhibiting extraordinary spectral and photometric behaviors (V1057 Cyg, FG Sge, RW Aur, SS Cyg) continued under the guidance of renowned French astronomers Chalonge and Divan. This research also included a study of the ultraviolet spectrum of the P Cyg star, using by data of the "Copernicus" astronomical satellite (co-authors: Ambartsumian, Snow).

In addition to his work on stellar associations and young unstable stars, Mirzoyan's scientific research extended to various other subjects, including comets, quasars, and galaxy clusters. Notably, his studies on compact groups of galaxies conducted by Shahbazyan in collaboration with renowned astronomers such as Ambartsumian, Arp, and Osterbrock, deserve mention. Mirzoyan's scientific contributions in all above mentionrd areas, along with his numerous articles of a general nature, played a significant role in shaping the scientific outlook of the new generation of astronomers.

The 1980s and 1990s were the peak of Mirzoyan's scientific effectiveness. In this period, research continued in all the above areas, along with the generalization and interpretation of a huge amount of observational data. The use of data from modern (at that time) astronomical satellites such as *ROSAT* and *HIPPARCOS* played a significant role in these achievements.

Mirzoyan's scientific style is characterized by clarity, rigor, lack of exaggerated claims and the desire to impress. His approach is distinguished by clarity and a commitment to accurate and reasonable presentation of scientific results. The influence of Mirzoyan's works on the formation of the scientific worldview of a new generation of astronomers cannot be overestimated.

Ludvik Vasili Mirzoyan stands as one of the most notable representatives of the first brilliant generation of Armenian astronomers, who laid the foundation for the Byurakan observatory. His contributions to both national and world astronomy are enduring and indelible.

doi: https://doi.org/10.52526/25792776-23.70.1-18

4. Instead of an Epilogoue

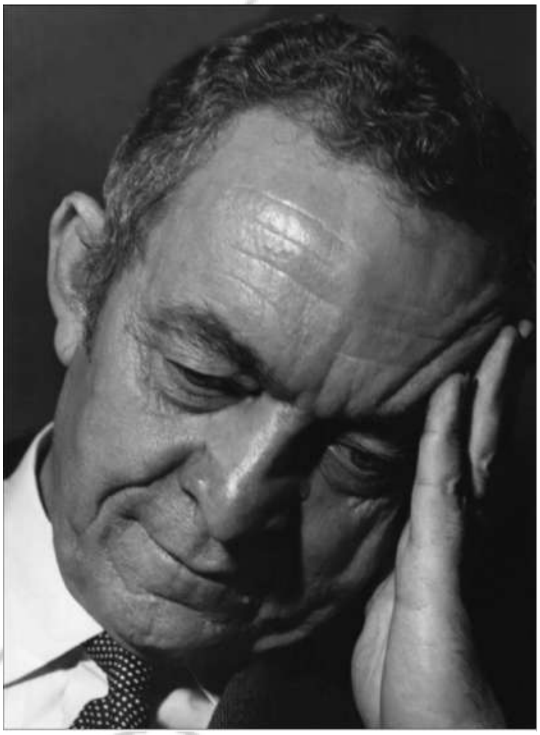

- Strict and Hardworking
- Upright and Impeccable
- Rigorous, Attentive and Instructive supervisor
- Unreserved devotee

doi: https://doi.org/10.52526/25792776-23.70.1-18

Communications of BAO, Vol. 70, Issue 1, 2023, pp. 23-26

Long period fluctuations of solar active regions

G. Dumbadze*[1,2]

[1]Evgeni Kharadze Georgian National Astrophysical Observatory, M. Kostava street 47/57, 0179 Tbilisi, Georgia
[2]Centre for Computational Helio Studies, Ilia State University, G. Tsereteli str 3, 0162 Tbilisi, Georgia

Abstract

The fluctuation spectra of solar active regions (ARs) contain information about the geometrical features and ground physical processes responsible for the appearance of such a background vibration noise. The investigation is based on an analysis of a time series built photospheric magnetograms and comprises case studies of several types of AR structures. We detect characteristic properties of Fourier and wavelet spectra evaluated for the solar active region area and radial magnetic flux time series. There are long-period oscillations, similarly to the characteristic lifetimes of super-granulation, determined from the datasets of the AR total area and radial magnetic flux, respectively. According to our results the fluctuation spectra of the AR areas and radial magnetic fluxes somewhat differ from each other both in terms of values of the spectral power-law exponents, as well as their variability ranges in different consider cases. The characteristic properties of the area and radial magnetic flux fluctuation spectra for the ARs show noticeable discrepancies between each other. It can also be concluded that behind the formation of AR area and radial flux vibration spectra might be different physical mechanisms in action.

Keywords: *solar active regions; oscillations; data analysis.*

1. Introduction

The active regions (ARs) are the complex magnetic structures that emerging on the solar surface. ARs have many sunspots which number, location, and size vary in time. So, the sunspots can be considered as the indicator of the solar magnetic activity. The ARs show complex morphology and dynamics that determine the different types of waves and oscillatory motions. The study of these oscillations can be divided into some branches: umbral chromospheric oscillations with a typical period of three minutes (Centeno et al., 2006, Chorley et al., 2010); umbral photospheric oscillations with a typical period of five minutes (Shergelashvili & Poedts, 2005, Thomas et al., 1984); long-period oscillations with a typical period of several hours (Dumbadze et al., 2017, Efremov et al., 2007); and ultra-long-period oscillations of sunspot umbrae, with typical periods of several days (Gopasyuk, 2004, Khutsishvili et al., 1998).

The target of the present paper is to find the long-period oscillations in different types of ARs and to more systematically examine the existence of them. For this purpose, we selected the ARs according to their morphological structure and study them along their transit across the solar disk. This paper is organized as follows: the data of the observations of the ARs and the data processing methods are described in Sect. 2. The The analysis and discussion of the discovered significant periods are given in Sect. 3. The conclusions are presented in Sect. 4.

2. Methods

For our investigation, the five ARs are selected according to their morphology types so that the observational time span include from roughly $-70°$ to $+70°$ longitude. The data is taken from the Solar Dynamics Observatory (SDO)/Helioseismic and Magnetic Imager (HMI) (Scherrer et al., 2012). Namely, the line-of-sight magnetogram (B_{LOS}) dataset of 45 s cadence is used for the investigation, where the projection effects are corrected using the azimuthal equidistant (Postel) projection. In addition, there are used three components of the magnetic field (*i.e.*, radial B_r, meridional B_θ, and azimuthal B_φ) dataset of 720 s cadence,

*gdumbadze@abao.ge

doi: https://doi.org/10.52526/25792776-23.70.1-23

which are obtained from Space-weather HMI Active Region Patches (SHARP, Bobra et al. (2014)), where the projection effects are corrected using cylindrical equal-area mapping.

We calculate the active pixels of the original B_{LOS} magnetograms (or B_r, B_θ and B_φ) using the thresholds from the $\pm$ 300 $-$ 400 G range. The value of the threshold is chosen individually for each different ARs, so that the spurious small magnetic features around the AR are filtered out, while the main components of the AR remain visible. Using the sequence of snapshots within the observational time span, we produce the time series of the total unsigned radial magnetic flux, determined as

$$|\Phi| = \sum_{\text{active pixels}} |B_r(x, y)| S(x, y), \tag{1}$$

where $B_r(x, y)$ is the radial magnetic field component in each active pixel, and $S(x, y) = 1.33 \times 10^5$ km^2 is the area covered by these pixels on the solar surface corresponding to the cylindrical equal area remapping (Bobra et al., 2014). In addition, we produce the time series for the total areas of the studied ARs for all components of the magnetic field as the total number of the active pixels.

In order to find the characteristic periods, we use three different methods for the period detection: (i) The first method that we use is suggested by Vaughan, that implies to find significant peaks on top of the power-law noise. Using this method, the periodograms of the detrended and apodised datasets are computed and plotted on log-space. To find the peaks above the confidence level, a linear model fit of the obtained power spectrum are plotted. We assume that computed power has the second order two-dimensional chi-square (χ^2_2) distribution as a null hypothesis. The goodness of the model is checked by Kolmogorov-Smirnov (KS) test (Press et al., 2007). If the KS test does not satisfy the null hypothesis, we adjust the slope and the offset until the test is fulfilled. We estimate the 95% probability limit by assuming that the noise is two-dimensional chi-square distributed using the computed slopes and offset coefficients. All peaks above this line can be assumed as outlying periods and those below this line belong to noise. (ii) The second method we use is a method of the spectral re-binning (Appourchaux, 2003) to increase the significant peaks in the power spectrum. It increases outlying peaks and reduce the noise. As an above, the detrendization and apodization also are applied to the dataset. Then, there are computed periodograms and sum the power of every two consecutive bins and divided sum by two. Everything is repeated as in first method, but in this case, instead of a two-dimensional χ^2_2 distribution function, we use a four-dimensional distribution function χ^2_4. (iii) To reduce the noise, we use the method based on the division of the original dataset. The original dataset is divided into four equivalent non-overlapping intervals of time. Each of these intervals are derived the power spectra and summed. In this case, everything is repeated as in the first method. The peaks found by M1 and M2 can be recognized as 'real', if they still remain in the summed spectrum. The multi-method analysis allows us to confirm the significant periods by different methods.

3. Discussion

The long-period oscillations in ARs are studying using the Fourier spectra of the time series, which have certain observational time spans and sampling rates. The period resolution and accuracy of the obtained power spectra are determined by the characteristic parameters of the datasets. As a result, some significant periods in the spectra are included in a strong background noise that have a power-law nature.

The most populated sets of the periods are revealed for the total area of the ARs, while the radial unsigned magnetic flux data has some significant periods. The most frequently detected periods are about 6- and 4.7-hour. These periods are found in the radial unsigned magnetic flux and the total area oscillations in almost all ARs. The frequent presence of these periods might be linked to the periodic flux emergence or cancellation processes. In all analyzed datasets the long-period peaks that are longer than 10 hours can be detected less frequently than those of shorter periods. The evident reason for this is the gradual growth of spectral uncertainty of the periods. This also is accompanied with the presence of two artificial instrumental peaks at 12- and 24-hour (Liu et al., 2012). These two instrumental peaks can mix the 'real' peaks with artificial spectral ones. Probably, these artificial signals does not have enough impact on the spectrum below 10-hour. In general, we show that in all datasets there are long-period oscillations with characteristic periods in the range from 2 to 20 hours. These periods are similar to the characteristic lifetimes of the super-granulation. So, the observed oscillation periods can be intuitively connected with the characteristic turnover times of the super-granulation cells.

We group together the obtained significant periods as the following ranges: (i) 'harmonic' $P_1 - 17.1 \pm 0.71 - 17.4 \pm 0.74$ hours (marked in cyan); (ii) 'harmonic' $P_2 - 7.66 \pm 0.14 - 9.54 \pm 0.90$ hours (marked

doi: https://doi.org/10.52526/25792776-23.70.1-23

in magenta); (iii) 'harmonic' P_3 – $5.69 \pm 0.08 - 6.37 \pm 0.10$ hours (marked in red); (iv) 'harmonic' P_4 – $4.45 \pm 0.19 - 4.88 \pm 0.23$ hours (marked in green); and (v) 'harmonic' P_5 – $3.66 \pm 0.03 - 3.88 \pm 0.05$ hours (marked in blue). All these periods are plotted in Fig. 1. The ratios of the average periods from each group of the same sequence as in Fig. 1 are shown in Fig. 2. For the calculation of the uncertainties found in the period ratios, we use the following relation:

$$\triangle \frac{P_i}{P_{i+1}} = \left| \frac{1}{P_{i+1}} \triangle P_i - \frac{P_i}{P_{i+1}^2} \triangle P_{i+1} \right| \leq \left| \frac{\triangle P_i}{P_{i+1}} \right| + \left| -\frac{P_i}{P_{i+1}^2} \triangle P_{i+1} \right|, \qquad (2)$$

where $P_i > P_{i+1}$ ($i = 1, 2, \ldots$ is the number of 'harmonics' are the global and the total mean periods evaluated for each AR. They sequentially follow each other in descending order. The ratios of the averaged periods look like the sequence of oscillation harmonics typical for a standing oscillations. In Fig. 2 the reference values of the ratios are shown with black solid horizontal lines. We would like to point out that the observed ratios do not exactly coincide with the sequence of ratios of periods corresponding to the pure standing oscillations ($2/1, 3/2, 4/3, \ldots$). However, we can say that these ratios with the entire uncertainty interval are well separated and approximately follow the reference spectrum ratios. Therefore, with the present level of accuracy the observed discrete spectrum follows the sequence of the quasi-standing oscillations with some shift of the periods and corresponding ratios from the reference values. The cause of this shift of the periods might be the incomplete line-tying of the magnetic loop system, or the Doppler shifts due to the internal flows in the ARs, and/or the inhomogeneity of the magnetic loop system constituting the AR below and above the solar surface.

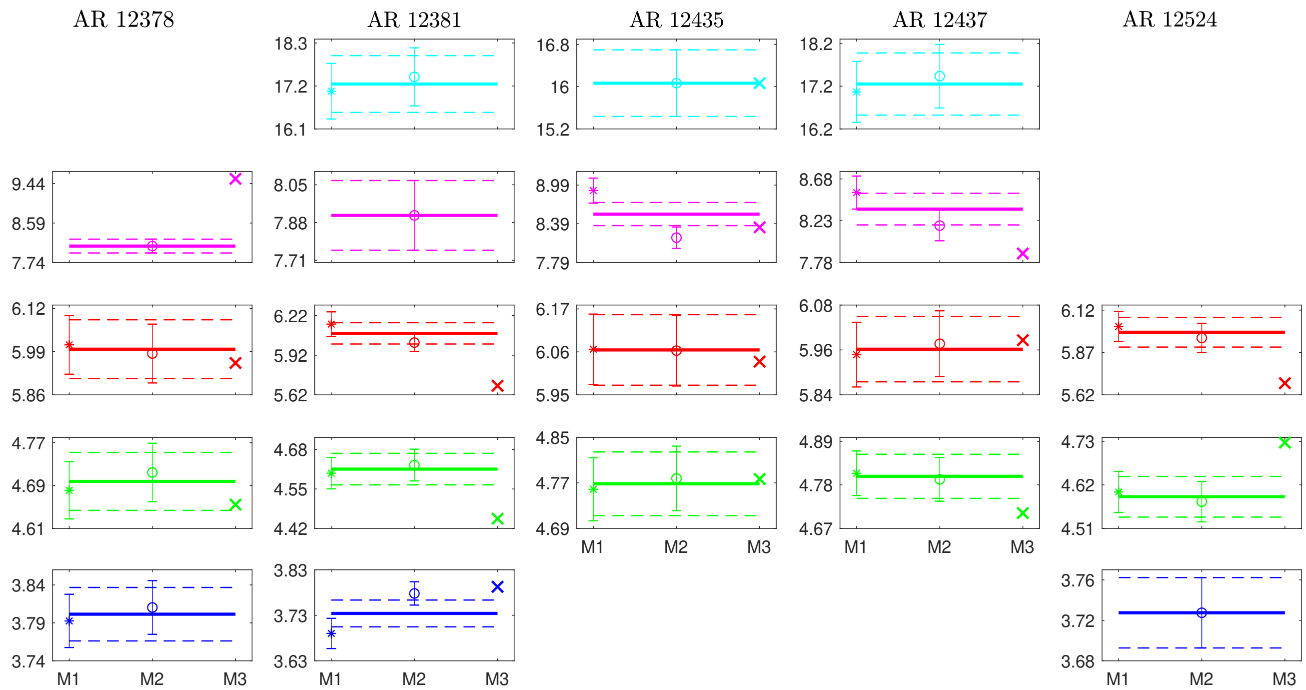

Figure 1. Characteristic mean oscillation periods (measured in hours) calculated as a global average of those found in different time series of the total area of the ARs and the total radial magnetic flux. On the horizontal axes, the M1, M2 and M3 labels, respectively, denote the global mean of the periods obtained by M1 (coloured '$*$' with error bars), M2 (coloured '$\circ$' with error bars), and M3 (coloured '$\times$' with error bars). Moreover, we also indicate the total mean periods by taking the average of the mentioned global means of M1 and M2 (*i.e.*, the mean periods obtained by M3 are excluded from the total mean calculation) via the solid-coloured horizontal lines (with the uncertainties indicated by the dashed coloured lines).

4. Conclusions

The next conclusions might be revealed:

- The most populated sets of the periods are obtained for the total area of the ARs;

doi: https://doi.org/10.52526/25792776-23.70.1-23

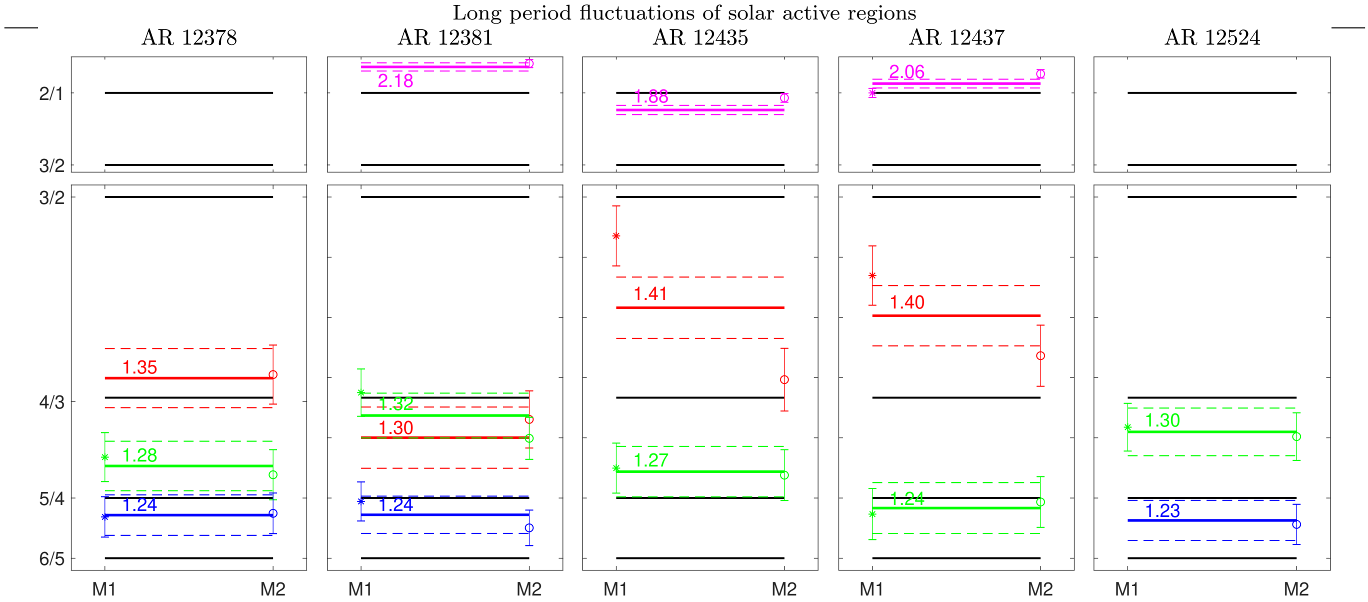

Figure 2. Ratios of global mean periods (P_i/P_{i+1}, $i = 1, 2, \ldots$) of M1, M2 and the total mean periods shown in the panels of Fig. 1. The formatting of the data points and horizontal lines is the same as in Fig. 1. The colouring in each panel coincides with the period standing in the denominator in each ratio. On the vertical axes, the levels of the period ratios in the reference spectrum are labelled and the corresponding horizontal solid black lines are plotted in all panels.

- In all analyzed datasets the long-period peaks that are > 10 hours can be detected less frequently than those of shorter periods < 10 hours;
- The radial unsigned magnetic flux data has some significant periods;
- In all datasets there are long-period oscillations with characteristic periods in the range from 2 to 20 hours;
- With the present level of accuracy the observed discrete spectrum follows the sequence of the quasi-standing oscillations with some shift of the periods and corresponding ratios from the reference values.

All of these long-period oscillation spectra need rigorous analytical or numerical modeling to understand their origin. The physical interpretation of the found oscillations requires the construction of rigorous mathematical models and this is beyond the scope of current purely observational study.

References

Appourchaux T., 2003, Astron. Astrophys. , 412, 903

Bobra M. G., Sun X., Hoeksema J. T., et al. 2014, Solar Physics, 289, 3549

Centeno R., Collados M., Trujillo Bueno J., 2006, Astrophys. J. , 640, 1153

Chorley N., Hnat B., Nakariakov V. M., et al. 2010, Astron. Astrophys. , 513, A27

Dumbadze G., Shergelashvili B. M., Kukhianidze V., et al. 2017, Astron. Astrophys. , 597, A93

Efremov V. I., Parfinenko L. D., Solov'ev A. A., 2007, Astronomy Reports, 51, 401

Gopasyuk O. S., 2004, in Multi-Wavelength Investigations of Solar Activity. pp 249–250

Khutsishvili E., Kvernadze T., Sikharulidze M., 1998, Solar Physics, 178, 271

Liu Y., Hoeksema J. T., Scherrer P. H., et al. 2012, Solar Physics, 279, 295

Press W. H., Teukolsky S. A., Vetterling W. T., et al. 2007, Numerical Recipes 3rd Edition: The Art of Scientific Computing. Cambridge University Press

Scherrer P. H., Schou J., Bush R. I., et al. 2012, Solar Physics, 275, 207

Shergelashvili B. M., Poedts S., 2005, Astron. Astrophys. , 438, 1083

Thomas J. H., Cram L. E., Nye A. H., 1984, Astrophys. J. , 285, 368

doi: https://doi.org/10.52526/25792776-23.70.1-23

Long-term variation of coronal holes latitudinal distribution

D. A. Maghradze *[1,2], B. B. Chargeishvili†[1], D. R. Japaridze‡[1,2], N. B. Oghrapishvili§[1], and K. B. Chargeishvili¶[1]

[1]Evgeni Kharadze Georgian National Astrophysical Observatory, Mt. Kanobili, Abastumani 0301, Georgia
[2]Centre for Computational Helio Studies, Ilia State University, Cholokashvili Ave. 3/5, Tbilisi 0162, Georgia

Abstract

We study the evolution of the latitudinal distribution of coronal holes using the Solar and Heliospheric Observatory (SOHO)/Extreme ultraviolet Imaging Telescope (EIT) 195 Ådata from 1996 May to 2020 April. To measure the presence of coronal holes at a given latitude, we use the presence factor, which estimates the length of an object along a given parallel, expressed as a percentage of half of the equator length. By semi-automatic processing of the data series, we obtained the 361 ×7346 latitude–time matrix. The corresponding diagram shows the significant difference in evolutionary shapes of a latitudinal distribution of non-polar and polar coronal holes. However, the morphology of the evolutionary picture and the migration route of the geometric centre of activity of the coronal hole in the diagram indicate that non-polar and polar coronal holes have the same driving mechanism. It is believed that the migration of the centre of activity of the coronal hole in the latitude–time diagram is a combination of two opposite migration paths. They intersect at the equator and diverge to opposite poles, where they form the so-called polar coronal holes, then again mo v e to lower latitudes, and this happens cyclically. Determining the opposite migration paths by antiphase sinusoids, their deviation from antiphase determines the detected north–south asymmetry in the activity of the coronal hole.

Keywords: *Solar activity, Solar corona, Solar oscillations.*

1. Introduction

We study the evolution of the latitudinal distribution of coronal holes (CH) activity. Section 2 describes observational data and the methodology we used for our study. Section 3 is dedicated to the results of a study of CH activity over the period from 1996 May to 2020 April and their comparison with activities of sunspots and magnetic field variations. Section 4 discusses the results of the paper.

2. Observational data and methodology of their processing

To reveal the cyclic characteristics of the latitudinal distribution of CHs, it is important to use the data of long-term observations, consisting of at least two cycles of activity. Therefore, instead of higher quality Solar Dynamics Observatory (SDO) data, we use observational data obtained by the Solar and Heliospheric Observatory (SOHO)/Extreme ultraviolet Imaging Telescope (EIT) in a 195 Åfilter. We downloaded a series of daily FITS files from the data base for the period 1995–2020. The main constituent step towards solving scientific problems associated with CHs is their identification and segmentation. Our semi-automated GUI code uses a combination of visual inspection with segmentation by global and local thresholding. The code is modification of the automated processing code described in (Maghradze et al., 2020) (hereafter Paper I). The preprocessing of the data was also carried out using the same procedures as described in Paper I , and we summarize them here. Each file in the series went through the IDL 'EIT PREP.PRO' 'SOLARSOFT' routine, which implies a background-subtracted, degridded, flat-fielded, and degradation-corrected output.

*davit.maghradze.2@iliauni.edu.ge, Corresponding author
†bidzina@aidio.net
‡darejan.japaridze@iliauni.edu.ge
§natela.oghrapishvili@iliauni.edu.ge
¶ketevan.chargeishvili@aidio.net

doi: https://doi.org/10.52526/25792776-23.70.1-27

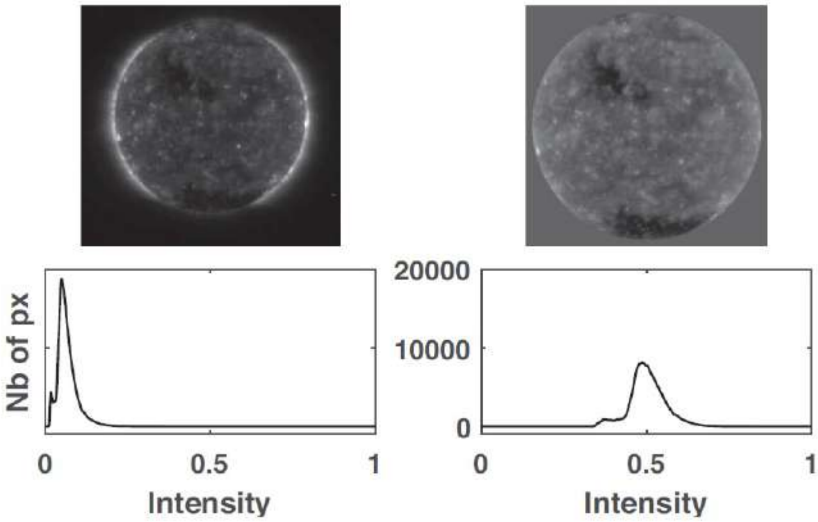

Figure 1. The top left- and right-hand panels display the original image and the image after processing by the modified Bartlett's method. The lower panels are the histograms of the upper images (only the solar disc), respectively.

The intensity threshold required for the segmentation of CHs is not universal and varies not only for different images but also within a single image itself. After converting the image to greyscale with an interval from 0 to 1, to automate the determination of the segmentation intensity threshold, it is necessary to use the features of the image histogram. To do this, we transform the image using a modified Bartlett's (Paper I) method that extracts the root of the power (instead of the Bartlett's square root) so that the average image intensity is 0.5 (see Fig. 1). Because in the identification and segmentation of CHs, the leading role is played by the difference in the intensity of the latter from the environment, it is very important to preliminary remove the artefacts of the change in intensity. The well-known artefact, the limb-brightening effect, caused by the positive altitude gradient of the corona temperature, precludes the application of a single intensity threshold for segmenting an extended object on a disc. Fitting the curves to the centred moving annual average of the empirical intensity distribution profiles from the centre to the limb of the solar disc, they obtained the following radial intensity function:

$$I(i) = a(i)\left[a^{b(i)\rho} - 1\right], \tag{1}$$

where $\rho = \dfrac{r}{R_\odot}$ is the dimensionless distance from the solar disc centre normalized on the solar radius $R_\odot$, $a(i)$ and $b(i)$ are parameters calculated by fitting the function (1) to empirical intensity profile of i image.

The right-hand panel of Fig. 2 shows time evolution of $I(i)$ function and one can see a cyclic variation. It is possible to use the pre-calculated coefficients $a(i)$ and $b(i)$ for each image and construct correction image for the limb-brightening removal, but we decided to apply mean curve of I for all images.

The study showed that within the longitudinal limits ± 70 $\circ$there is no significant deviation between empirical curves of intensity distribution and calculated mean function we use. So the code, using the mean function, creates a correction image (see Fig. 3) to remove the limb-brightening effect. The code then subtracts the corresponding correction image (Fig. 3 (panel c)) from the original, and we get the image without limb brightening. The interactive code interface has the ability to manually adjust the correction image (Fig. 3 (panel b)) for the best result, since the coefficients $a(i)$ and $b(i)$ are obtained by centred moving annual averaging of the intensity profiles, and in some cases the results differ significantly from the real profile of the given image. Another important feature obtained by (Chargeishvili et al., 2019) is that intensity distribution from centre to limb is not polar symmetrical and its isophotes have elliptical shapes with polar elongation. As they show the ratio of major and minor radii is also variable bat mainly it is close to 1.3. The interactive interface of our code has also ability to tune this ratio for better result. After the effect of limb brightening is removed the next step is segmentation of CHs on the disc. To find the

doi: https://doi.org/10.52526/25792776-23.70.1-27

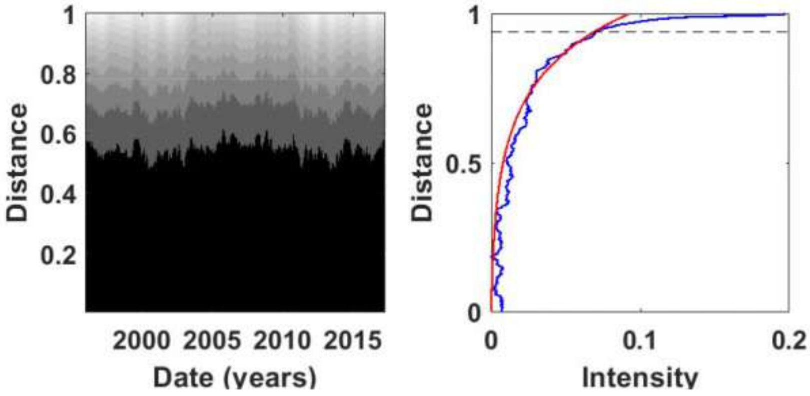

Figure 2. Left-hand panel: evolution of fitted intensity distribution profiles. The right-hand panel is the average of all fitted intensity distribution profiles (red line) and the real intensity distribution profile for a given date (blue line), 70° longitudinal limit (dashed line).

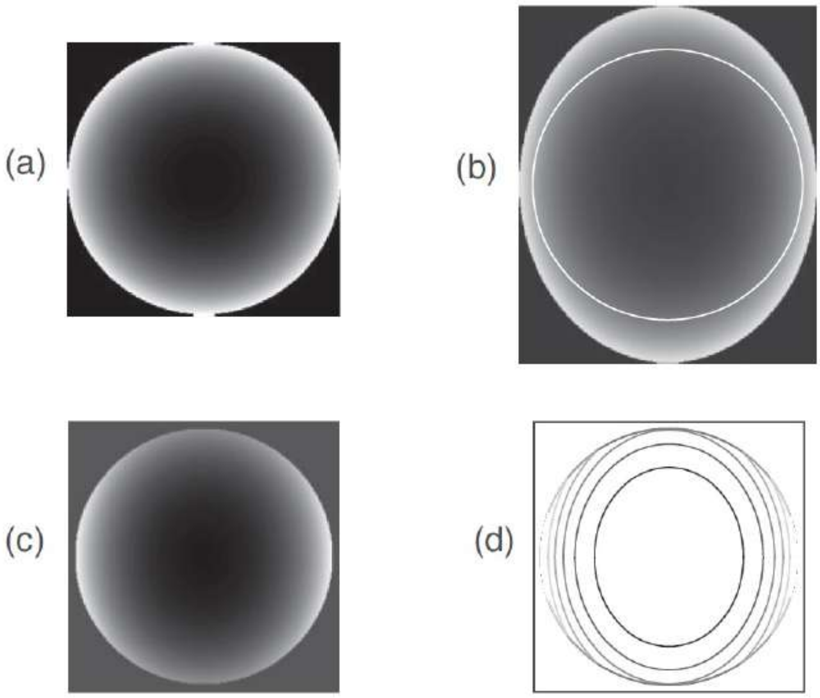

Figure 3. (a) Polar-symmetric correction image obtained by rotating the average of all fitted intensity profiles. (b) Fitting the corrective image to the specified date by elliptical distortion. The white circle is the clipping area for the new correction image. (c) Final correction image. (d) Isophotes of the final correction image.

hump corresponding to the population of dark formations in the resulting histogram, the code smooths the low-intensity wing of the histogram and subtracts the result from the original. On the remaining curve, one gets a concave region, which is easily marked by the code as the intensity threshold (see the top left-hand panel in Fig. 4 and the bottom right-hand panel in Fig. 5) required for segmentation of the CH. Then the code outlines the proposed object. In most cases, this object is indeed a CH, but often the code can outline filaments or coronal dimmings, transition CHs, or even miss any real CHs. In this case, the code has an interactive mode to indicate the region of interest for changing the local intensity threshold, so that the code automatically selects the desired object again. If an object is missegmented, you can undo it separately

doi: https://doi.org/10.52526/25792776-23.70.1-27

from other segmented objects on the disc. In cases where the researcher could not distinguish the probable CH from filaments, the researcher checked in Helioviewer the unipolarity of the suspicious object on the corresponding magnetogram. Also, the code rewind function allows one to check the object in the dynamics of the rotation of the Sun and eliminate confusion with dimmings or transitional CHs.

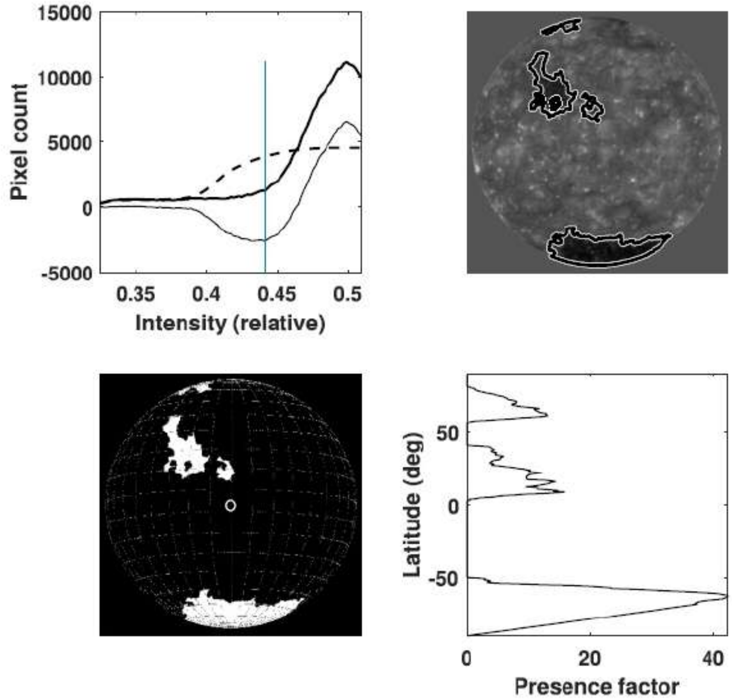

Figure 4. Top left-hand panel: the lower wing of the intensity of the image histogram (bold line), the smoothed histogram (dashed line), the result of their subtraction (normal line), and the threshold (vertical line). Top right-hand panel: segmented CHs on the solar disc. Lower left-hand panel: a binary image of the solar disc and the network of heliospheric coordinates above it. Bottom left-hand panel: distribution of the presence factor (PF) of coronal holes (CHs) at a given date.

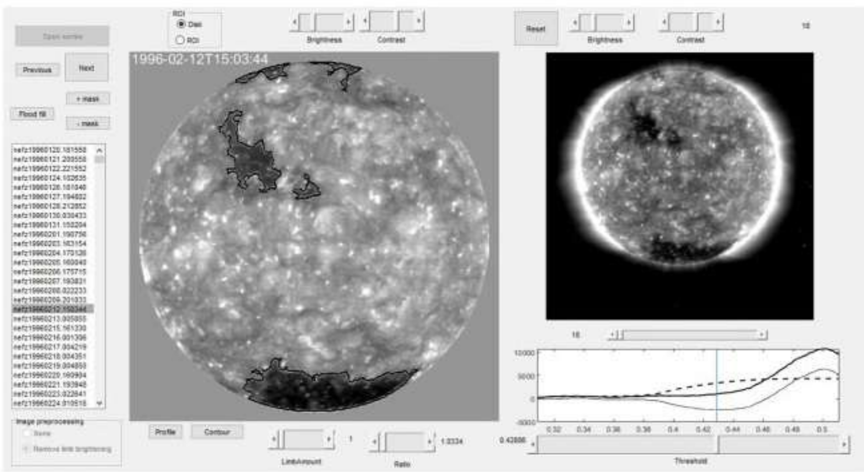

Figure 5. The graphical user interface of the interactive code for CH segmentation and PF latitudinal profile output.

The code, taking the date of observation, Solar-B , solar disc pixel coordinates, and solar disc pixel radius from the FITS file header, operates in heliographic coordinates. The code scans the segmented binary image

doi: https://doi.org/10.52526/25792776-23.70.1-27

of the solar disc within the ranges ±90 latitudes and ±80 longitudes both with spans of 0°.5 and gets data from 361321 points of a disc. Finally, profiles of PFs of each image from the data series are compiled in a latitudinal data matrix.

Since SOHO /EIT observational data have gaps in everyday observations, and also not all images obtained are suitable for processing, the final data are not sampled uniformly. To correctly go through the necessary procedures (say, annual moving averaging) or to compare the CH activity with the activity of the polar magnetic field or the number of spots, we interpolated all variables in the same time domain with uniform sampling.

3. CH activity and relation with sunspots and magnetic fields

We begin the description of our results with the most obvious diagram showing the time evolution of the CH activity latitudinal distribution during more than two solar activity cycles (Fig. 6).

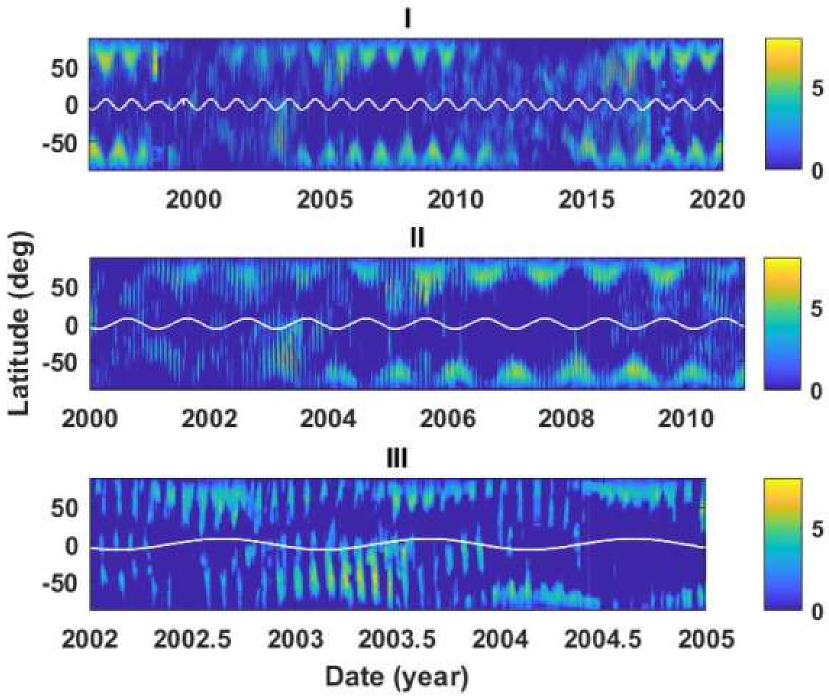

Figure 6. Latitude–time distribution of CHs (from 1996 May to 2020 April). The horizontal axes show time in years, and the vertical axes show latitude. The solid white lines show the change in the heliographic latitude of the central point of the solar disc. The first panel shows the latitudinal distribution of the PF for the entire study period. The second and third panels show the same as the first, but for shorter periods. For better visualization, the square root of the PF values is used.

In general, an approximately 11-yr recurrence of features is typical for all latitudinal zones, but the difference in activity at polar and middle latitudes is obvious. In the polar regions mostly and with a lesser intensity in the mid-zone, along with the 11-yr cycle of solar activity, an annual periodic variation is evident. We also disco v er a shorter, quasi-monthly period in the middle part of the diagram along with north–south asymmetry seen in polar regions. The annual oscillatory structure of the evolution of CH activity closely correlates with the annual variation of the solar B_0 angle, heliographic latitude of the central point of the solar disc. The simplest explanation that comes to mind is that the fluctuation should be observational only and should be caused by the geometric effects of the B_0 variation. CH is not a plain dark place on the surface of the corona. It is the place where the radial open magnetic field arising from the Sun to our sight is confined. The CH is surrounded by closed magnetic structures holding denser and brighter plasma.

We divide the Sun's surface into three zones: north polar, south polar, and mid-latitudes. We consider it useless to divide middle latitudes into northern and southern zones due to the large size of some CHs (they often cover both sides of the equator). We use the following notation: NPZ and SPZ for the north and south polar zones, respectively; MZ for the middle zone; and TZ for the total disc. For ease of comparison

doi: https://doi.org/10.52526/25792776-23.70.1-27

of results in different hemispheres and comparison with the results of the magnetic field and the number of sunspots, we evaluate the CH activity by the value of PF on a 10-point system. We presume that the maximum value of the averaged PF for the entire Sun is equal to 10 conventional magnitudes.

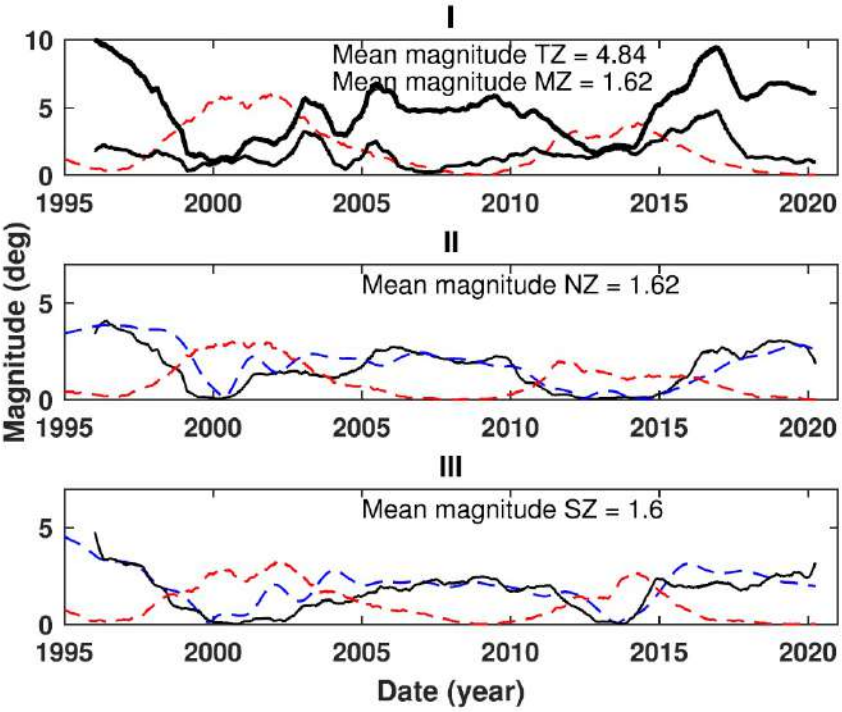

Figure 7. Activity curves. (I) Centred annual moving average of CH activity for the entire disc (black bold solid line), centred annual moving average of CH activity in the middle zone (black solid line), and centred annual moving average of sunspot numbers (red dashed line). (II) Centred annual moving average of CH activity in the north polar zone (black solid line) and averaged north polar magnetic field (blue dashed line). (III) Centred annual moving average of CH activity in the south polar zone (black solid line) and averaged south polar magnetic field (blue dashed line). The red dashed lines represent the sunspot numbers in both hemispheres (panel I) in the Northern and Southern hemispheres (panels II and III, respectively.

Fig. 7 shows different patterns of CH activity in three zones. In general, the CH activity with an average magnitude of about 5 is in antiphase with the sunspot number activity (Fig. 7 (panel I)). Whereas, the middle zone having the average magnitude of activity of about 1.62 is almost in phase with the activity of sunspots with some noticeable delay. In both polar zones (Fig. 7 (panels II and III)), CH activities are in antiphase with sunspot activity and show good coincidence with polar magnetic field cyclic variations. The evolution patterns of CH activities in different polar zones are similar to each other and have similar mean values of activity magnitudes (1.62 and 1.60 for northern and southern polar zones, respectively). Fig. 7 (panel II) and (panel III) show a close correlation between the activity patterns of polar magnetic fields and polar CHs, with correlation coefficients of 0.82 and 0.79 for the Northern and Southern hemispheres, respectively. We found it more convenient to compare the data of polar CHs and polar magnetic fields with the sunspot data flipped up-down (Fig. 8). The correlation between polar magnetic fields and the flipped number of sunspots has very high significance ($p = 0$) with coefficients of 0.39 and 0.46 for the Northern and Southern hemispheres, respectively. We can only compare the activity of CHs and the number of sunspots in the last two cycles. Since variations in the activity patterns of polar CHs and magnetic fields are in such close correlation (which is quite natural), we can compare the activities of magnetic fields and sunspots. The results can be generalized to CHs. So, for example, we see that the durations of minima of CH activities are different in different hemispheres. It fits well with the durations of maxima of the numbers of sunspots in these hemispheres. Comparing the curves of the magnetic field and sunspots, we can say that, in general, the duration of the minima of polar CHs and magnetic fields in each hemisphere correlates well with that of the maximums of sunspots in these hemispheres. We know that sunspots perform their activity in regions of low latitudes, completely different from the region of polar magnetic fields and polar CHs. Such a close correlation between them leads us to the idea that the polar magnetic field (and hence the polar CHs) and

doi: https://doi.org/10.52526/25792776-23.70.1-27

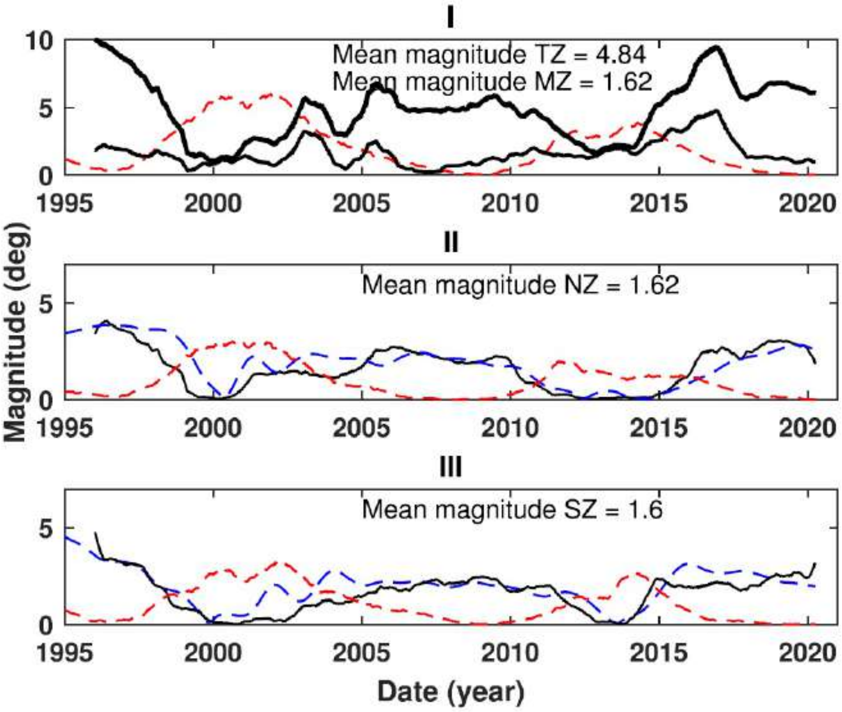

Figure 8. Correlation of the activity of polar CHs (black line) with the activity of the polar magnetic flux (red line) and a hemispheric sunspot numbers (blue line) for the Northern (panel I) and Southern (panel II) hemispheres.

sunspots have a common driving mechanism. Along with sunspots, non-polar CHs should play an important role in the transfer of the magnetic field. But, as can be seen from Fig. 7, the shape of the activity curve of non-polar CHs does not correlate as well with the shapes of the polar curves as the shapes of the activity curves of sunspot numbers in the hemispheres. This may be due to the fact that we cannot assign non-polar CHs to different hemispheres. Looking at Fig. 7 the non-polar zone leaves an impression that it is the exchange area of large-scale open magnetic fluxes (CHs) between polar zones.

To better understand details of latitudinal migration of CH activity, we calculated geometrical centres of PF for all CHs and separate zones. Separate zonal migrations of activity centroids did not reveal any interesting features. The reason we discuss below. As for the migration of PF centroids for the whole disc CHs, we present it over the time latitude diagram of PFs in Fig. 9.

Fig. 9 shows that, despite some deviations during the active phase of cycle 23, the centre of activity is in the Northern hemisphere, and in the phase of minimum sunspot activity moves to the Southern hemisphere and remains there during cycle 24.

4. Conclusions

This study deals with the variation of the latitudinal distribution of CHs. We used SOHO /EIT 195Å daily data from 1996 May to 2020 April. To correctly measure the levels of CH activity at any latitude, we use the so-called CH PF, which estimates the length of an object along a given parallel, expressed as a percentage of half the equator length. After semi-automatic processing of 7346 FITS files, we obtained a 3617346 data matrix for the CH PF values. The resulting diagram (Fig. 6) demonstrates a clear structuring of the time–latitude distribution of PF. The character of structuring differs in the polar and middle zones. According to the local entropy distribution of PF, we divided the Sun into three zones of activity. Zone delimiters come at $\pm 53^\circ$ of latitude. All three zones show oscillatory-type evolution of the CH activity and oscillation with annual periods is dominant. The annual oscillations are in antiphase with the variations of Solar-B. Their amplitudes are comparable at the equator, and the amplitude of the oscillatory pattern grows to wards the higher latitudes.

Annual periodicity is dominant in all zones. Another prominent period is about the synodic period of

doi: https://doi.org/10.52526/25792776-23.70.1-27

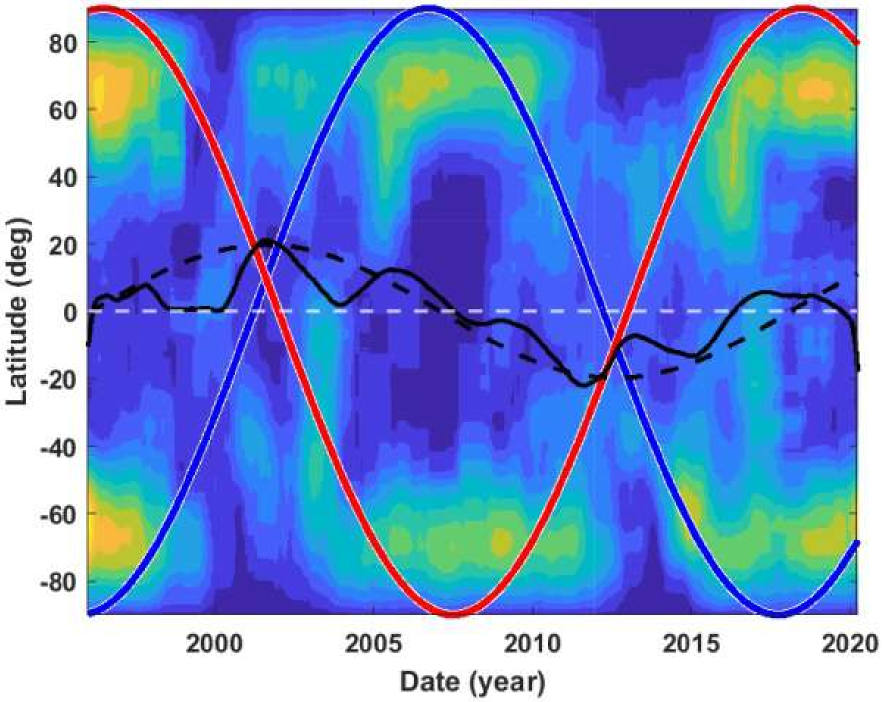

Figure 9. Latitudinal migration of CH activity centroids plotted on the time–latitude diagram of PFs. The black curve is the empirical path of the PF centroids. Red and blue lines indicate simulated migration paths of CHs with oppositely directed magnetic fluxes. The black dashed curve is a superposition of the red and blue curves.

solar rotation. It is reflected in the diagram (Fig. 6) in the form of thin vertical fibres and should be caused by a long lifetime of CHs (several months) along with the hiding of open-structured magnetic features by closed ones.

It should be mentioned that the fact that the SOHO data are obtained from the ecliptic plane gives a significant uncertainty in obtaining the PFs near the pole regions due to the spherical geometry and the projection effect. Moreover, when determining the geometric centre of the PFs near the poles, we cannot take into account the possible existence of CHs on the other side of the disc, and in this case, we obtain centres shifted to lower latitudes.

A key result of this work is that large-scale fluxes of a unipolar magnetic field, the visual manifestation of which are CHs, do not belong to separate zones or even separate hemispheres on their cyclic evolutionary path. On the contrary, we found that the migration of the CH activity centre must be a superposition of two opposite migration paths, as shown in Fig. 9. These migration routes intersect at the equator and diverge to opposite poles, where they form the so-called polar CHs, then again move to non-polar zones, and this repeats cyclically. We considered the opposite migration paths to be governed by antiphase sinusoids. A small deviation from antiphase (0.07π) determines the detected north–south asymmetry in the activity of the CH. The close correlation between sunspot activity and CHs indicates that the generation of large-scale and compact magnetic fluxes is driven by a common mechanism. The results are important for elucidating the details of the mechanism of the magnetic dynamo. In the future, we intend to detail the picture of the evolutionary CH migration by identifying the polarity of the already identified CHs and thereby determining the polarity of the migration paths.

References

Chargeishvili B. B., Maghradze D. A., Japaridze D. R., et al. 2019, Adv. Space Res., 64, 491–503

Maghradze D. A., Chargeishvili B. B., Japaridze D. R., et al. 2020, Adv. Space Res., 65, 1321 (Paper I)

doi: https://doi.org/10.52526/25792776-23.70.1-27

Observations of Gaia Microlensing Events in Abastumani

T. Kvernadze [*], O. Kvaratskhelia, and V. Kozlov

Georgian National Astrophysical Observatory, Abastumani, Georgia

Abstract

Gaia is now one of the most successful and leading transient space mission. It discovers nearly 2000 objects annually from all over the sky, down to about 20 mag, covering all possible classes of transients from supernovae and cataclismic variables to rare phenomena like microlensing events or pair-instability supernovae. The long time baseline of Gaia data allows for more robust detections of photometric anomalies. The gravitational microlensing method is especially sensitive to compact-object lenses in the Milky Way, including white dwarfs, neutron stars or black holes. The team, involved in the photometric follow-up observations of Gaia microlensing events, is collaborating with the International Working Group of Gaia Science Alerts through the BHTOM platform since 2020. Currently, we mainly use the 36-cm SCT-14 telescope of the Georgian National Astrophysical Observatory (Abastumani, Georgia) which is equipped with large format CCD and UBVRI filter set. At present we have processed and submitted for combined light curves observational data of 16 moderately bright Gaia alerts. Some of them clearly show the microlensing event type of light curves, though they need more detailed investigation. Here we present preliminary results of data connected with two such events: Gaia19dke and Gaia21dnc.

Keywords: *Gaia events, gravitational microlensing*

1. Introduction

Gravitational Microlensing is the amplification of the light of a background star due to the transit on the line of sight between this star and an observer of a massive compact object, which acts as a gravitational lens. The lens can be a neutron star, a white or brown dwarf or a black hole, sometimes called MACHOs (MAssive Compact Halo Objects). This phenomenon depends on an effect first discussed by Albert Einstein in his early papers on general relativity (Einstein, 1911, 1915), where he showed how light that passed a massive object would be deflected by the object's gravity. This effect was demonstrated by Eddington's observations during the total Solar eclipse of 29 May 1919 (Dyson et al., 1920).

Gravitational lensing differs from conventional optical lensing as there is not a single point of focus in a focal plane and multiple distorted images of the source appear around the lens. In case of a point-like compact lens it will always produce two images, while a binary lens will generate three or five images. In the special case when lens and source are in perfect alignment towards an observer, the multiple images all merge to form a bright ring around the lens or the so-called 'Einstein ring'.

In the 1964 independent theoretical studies by Liebes and Refsdal (Liebes, 1964, Refsdal, 1964) showed the usefulness of lensing for astronomy. In particular Sjur Refsdal derived the basic equations of gravitational lens theory and subsequently showed how the gravitational lens effect can be used to determine Hubble's constant by measuring the time delay between two lensed images.

In 1979 the gravitational lensing method gained a real boost when the first double quasar Q0957+561 was discovered and confirmed to be a real gravitational lens by Walsh, Carswell and Weymann (Walsh et al., 1979).

In 1986 Paczyński (Paczyński, 1986) suggested a method which greatly increased probability to observe microlensing events. If one could continuously observe the brightness of stars of our neighbouring galaxy Large Magellanic Cloud (LMC) one should see typical fluctuations in some of these stars due to the fact that every now and then one of these compact halo objects passes in front of the star and magnifies its brightness. Due to the relative motion of observer, lensing Macho and source star the projected impact parameter between lens and source changes with time and produces a time dependent magnification.

[*] info@astronomia.ge, Corresponding author

doi:https://doi.org/10.52526/25792776-23.70.1-35

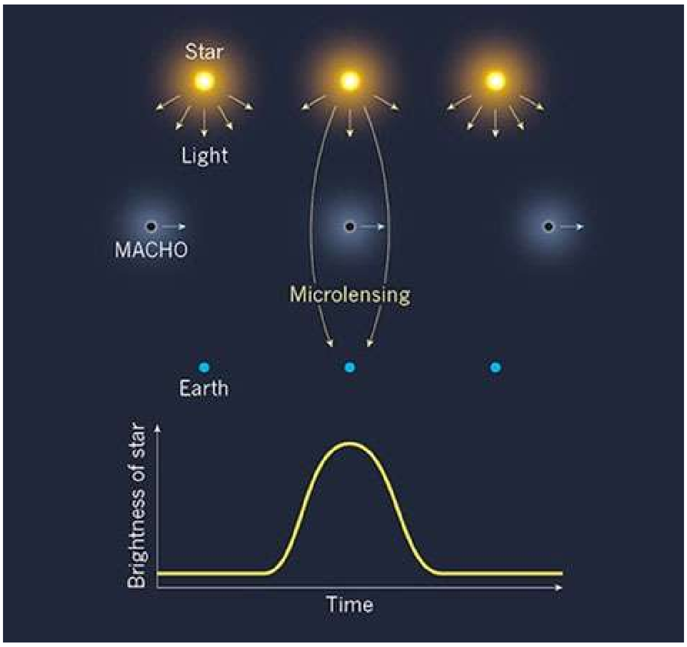

Figure 1. General drawing of a microlensing transit event.

2. Basics of Microlensing Phenomena

Main parameters of a microlensing event are the following (see Figure 2):

- D_L - distance of the lens from the observer;
- D_S - distance of the source from the observer;
- D_{LS} - distance of the lens from the source;
- M_L - mass of the lens;
- α - angular separation of the lens from the observer-source line of sight;
- $\theta_{1,2}$ - angular separation of images of the source from the center of the lens;
- $\epsilon_{1,2}$ - deflection of a light ray passing at radius r from the lens.

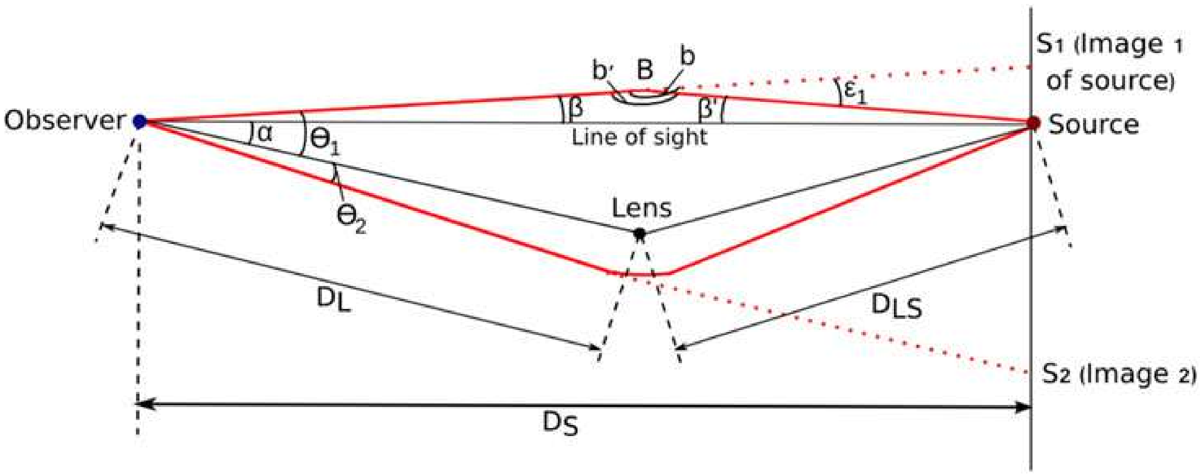

Figure 2. The geometry of a single lens microlensing event.

The closer the light rays get to the lens, the more they are deflected and according to Einstein's equation:

doi:https://doi.org/10.52526/25792776-23.70.1-35

$$\epsilon = \frac{4GM_L}{rc^2}. \tag{1}$$

Making relevant transformation we can get a lens equation:

$$\theta_1^2 - \alpha\theta_1 - \frac{4GM_L D_{LS}}{c^2 D_L D_S} = 0, \tag{2}$$

and finally brightness change or magnification of an image relative to the unlensed source, an Einstein radius and crossing timescale - the time taken for the source to pass behind the Einstein ring of the lens:

$$A(u) = \frac{u^2+2}{u\sqrt{u^2+4}}, \tag{3}$$

$$\theta_E = \sqrt{\frac{4GM_L D_{LS}}{c^2 D_L D_S}}, \tag{4}$$

$$\theta_E = \sqrt{\frac{4GM_L D_{LS}}{c^2 D_L D_S}}, \tag{5}$$

$$t_E = \frac{\theta_E}{\mu_{rel}}. \tag{6}$$

Here u is called an *impact parameter* and μ_{rel} is the (relative) transverse velocity of the lens. Typically $t_E \sim 45$ days, so to detect microlensing events we need to observe about once per day.

For a galactic microlensing events, when the stars in the disk of the Milky Way act as lenses for bulge stars close to the center of the Galaxy, the scale defined by the Einstein radius in milliarseconds is:

$$\theta_E \approx 0.5\sqrt{\frac{M_L}{M_\odot}}. \tag{7}$$

In order to derive an average estimate for the size of θ_E, we can consider an M-dwarf lens star ($M_L = 0.3M_\odot$) at a distance of $D_L = 6.5$ kpc from the Earth, and a source star at a distance $D_S = 8.5$kpc. The corresponding size of the angular Einstein ring radius is then approximately

$$\theta_E \sim 300 \ \ \mu as. \tag{8}$$

if we use equation (6) and assume a typical value for the transverse velocity of $\mu_{LS} \sim 15\mu$as/d, then for lenses of about one Earth-mass t_E is of the order of hours, while in the case of Solar-mass objects the lensing effect may last for a few months (Tsapras et al., 2016, Wood & Mao, 2005, Łukasz Wyrzykowski et al., 2015).

Note that from equation (6) it is obvious that it is not possible to determine the mass of the lens from one individual microlensing event. The duration of an event is determined by three unknown parameters: the mass of the lens, the transverse velocity and the distances of lens and source. It is impossible to disentangle these for individual events. Only with a model for the spatial and velocity distribution of the lensing objects and comparison with “simulated microlensing events” it is possible to obtain information about the masses of the lensing objects and their density (Wambsganss, 1998).

3. Microlensing Event Scenarios

3.1. Single-to-Single Lensing

The basic concepts of microlensing are easier to introduce by considering a simple scenario: a point lens in the foreground bending the light of a point background source. This is commonly referred to as “point source-point lens” (PSPL) lensing model. Modeling single-lens event light curves is quite straightforward as they are simple, smooth and symmetric and usually involves three parameters that describe the shape of the curve, such as u_0, t_0 and t_E (see Figure 1).

doi:https://doi.org/10.52526/25792776-23.70.1-35

3.2. Binary Source Lensing

The case of a binary source is simple, as it generates a linear sum of two single-lens light curves. Naturally, since the two stellar components may have different luminosities and colors, the resulting light curve may be chromatic. If the distance between the two source stars is large and the lens trajectory is along the line joining the two, we may have the perception of two independent microlensing events separated by a few months or years, which are both produced by the same lens. Of course, if the binary source is a gravitationally bound system, it is possible that orbital motion effects may also be detectable.

Binary source events are not as commonly detected as originally predicted (Griest & Hu (1992) estimated that $\sim 10\%$ of all events should show binary source features).

3.3. Binary or Exoplanet Lens

If the lens is multiple, as is the case when the lens is a binary star or a star with planets, the magnification pattern experienced by a background source is no longer circularly symmetric on the sky. In this case, the shape and maximum amplitude of the lightcurve depends on relative path the background source takes through the lens magnification pattern. The resulting lightcurve can exhibit large changes in shape over rather short periods of time if the background star passes near what is known as a caustic in the lensing pattern (Mao & Paczyński, 1991).

The Figure 3 shows variations of brightness of the star Gaia16aye caused by a microlensing event, as a massive object passed across its line of sight. After the initial discovery of this 14.5 magnitude star with Gaia (dark circles on Figure 3), follow-up observation were continued with different terrestrial telescopes (coloured circles), revealing a rather peculiar pattern of brightness variations.

Instead of a single rise and fall, the star has undergone two consecutive brightness peaks of roughly two magnitudes, then became fainter for a few weeks. It later exhibited a sharp increase to magnitude 12 and rapidly declined again.

The intricate pattern of variations suggests that the star is not being lensed by a single object but rather by a binary system. The black line shows the expected brightness variation from a microlensing model with a binary lens, which most likely consists of two stars, but might also involve a planet or even a black hole.

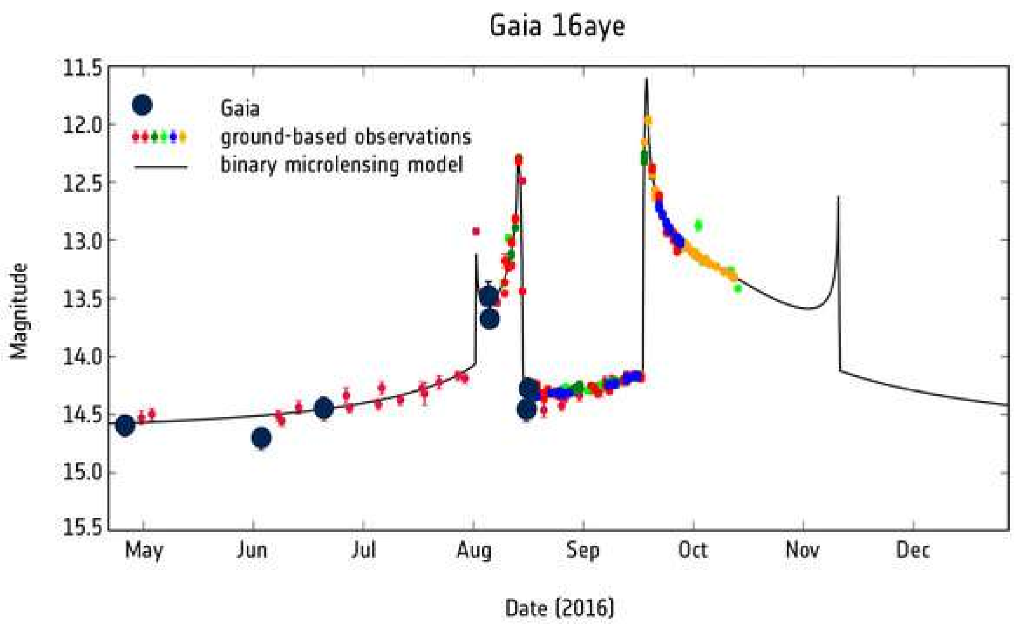

Figure 3. Light curve of binary microlensing event detected by Gaia. Copyright: ESA/Gaia/DPAC, P. Mroz, L. Wyrzykowski, K.A. Rybicki (Warsaw)

The Figure 4 depicts the microlensing event MOA-2011-BLG-028 / OGLE-2011-BLG-0203 follow-up photometric observations. The light curve clearly shows the discovery of a Neptune-mass planet orbiting

doi:https://doi.org/10.52526/25792776-23.70.1-35

a $0.8 \pm 0.3 M_{\odot}$ star in the Galactic bulge. The planet manifested itself during the microlensing event as a low-mass companion to the lens star. The analysis of the light curve provides the measurement of the mass ratio: $(1.2 \pm 0.2) \cdot 10^{-4}$, which indicates the mass of the planet to be 12–60 Earth masses. The lensing system is located at 7.3 ± 0.7 kpc away from the Earth near the direction to Baade's Window. The projected separation of the planet, at the time of the microlensing event, was 3.1–5.2 AU. Although the "microlens parallax" effect is not detected in the light curve of this event, preventing the actual mass measurement, the uncertainties of mass and distance estimation are narrowed by the measurement of the source star proper motion on the OGLE-III images spanning eight years, and by the low amount of blended light seen, proving that the host star cannot be too bright and massive (Skowron et al. (2016)).

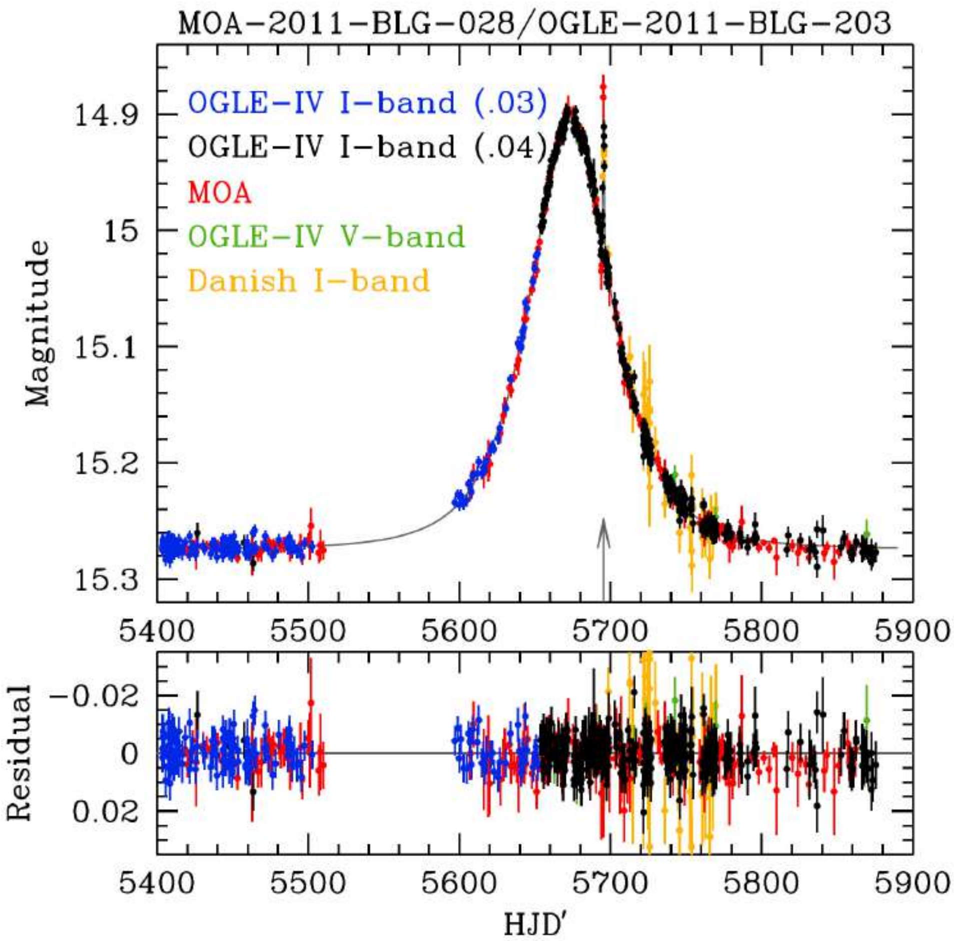

Figure 4. The Light Curve of the Microlensing Event MOA-2011-BLG-028 / OGLE-2011-BLG-0203. The whole OGLE light curve for this object spans 15 years. The black line marks the best-fit microlensing model where the light of a Galactic bulge giant is magnified for ∼200 days (around 2011 April 22nd) by a stellar object near the light's path and is additionally disturbed for ∼2 days (around 2011 May 13th) by a low-mass companion of that object. Copyright: Skowron et al. (2016).

4. Microlensing Event Observations in Abastumani

To obtain adequate photometric data coverage for detailed study of microlensing events, international follow-up photometric network is needed. Currently the network is consisting of several tenths of observatories throughout the world having special web service called the Black Hole Target Observation Management (BHTOM). The BHTOM is an interface for viewing and sharing observational photometric and spectroscopic data of time-domain targets, and for requesting and managing follow-up observations obtained with a network of telescopes. The BHTOM was built within the Time-Domain Work Package of the OPTICON EC Horizon 2020 grant no. 730890.

The Georgian National Astrophysical Observatory (Abastumani, Georgia) has actively joined the network in 2020. We use the 36mm Schmidt-Cassegrain telescope SCT-14 (see Figure 5) for these follow-up photometric observations, which is equipped with the Starlight Express SX-36 CCD camera and standard

doi:https://doi.org/10.52526/25792776-23.70.1-35

Johnson-Cousins UBVRI filter set. The field of view equals 28 x 19 arcmin and pixel size is 0.35 arcsec. The limiting magnitude of this photometric setup reaches 17 magnitude in V. The lowest observable declination equals −35 deg.

The CCD observational images usually are calibrated with bias, dark and flat field frames using MaximDL software tools and several short exposures are stacked to get final images with high S/N. The resulting CCD images are uploaded to the BHTOM service for final photometric calibration and inclusion into collective follow-up photometric data set.

Figure 5. The SCT-14 equipped with the Starlight Express SX-36 CCD, UBVRI filter set and guiding system.

During the last 2 years we have observed 16 Gaia events following the BHTOM system alerts and observing priorities. The data of objects are listed in the Table 1. Nine of these 16 are confirmed microlensing events.

Table 1. List of Gaia alerts observed in Abastumani

Gaia event Name	**RA DEC (J2000)**	**Mag.**	**Event Type**
Gaia19dke	19:25:58 +28:24:24	15.49	Long-term microlensing with parallax
Gaia21efs	20:29:41 +31:17:42	15.78	Bright microlensing
Gaia22awa	19:04:51 -08:34:00	15.11	Microlensing candidate
Gaia22duy	18:41:09 -10:23:47	17.03	Long bright microlensing near the Bulge
Gaia21dnc	21:38:10 +26:27:59	15.48	Microlensing event with a planetary anomaly
Gaia20fnr	06:01:04 -18:58:03	13.16	Bright microlensing
Gaia21bfr	18:46:08 -10:12:26	17.02	Bright microlensing
Gaia20dwf	18:26:29 -20:04:52	16.73	Microlensing candidate
Gaia23bay	19:49:42 +10:43:41	11.99	Bright microlensing candidate
Gaia21arx	05:36:24 -06:17:30	12.24	! Young stellar object
Gaia21ecy	19:01:22 +11:52:03	14.28	! Possibly a Be-type star outburst
Gaia18arn	21:35:15 +50:28:50	17.23	! Microlensing not confirmed
Gaia21cgt	19:52:39 +26:11:34	15.15	! Most likely a Be-type outburst
Gaia21asp	19:28:32 +19:50:11	14.59	! Microlensing not confirmed
8C0716_714	07:21:53 +71:20:36	14.00	! Highly variable BL Lac S5 0716+714
TCrB	15:59:30 +25:55:12	10.00	! Very bright symbiotic star to explode soon

doi:https://doi.org/10.52526/25792776-23.70.1-35

5. Preliminary Results of Some Microlensing Events

5.1. Gaia19dke

Gaia19dke event was reported by the Gaia Science Alert system (Hodgkin et al., 2021) on the 8th of August 2019 as a small rise of brightness in the Gaia G-band in a previously non-varying star. While Gaia scans the sky, it returns to the same location on average within 30 days. Each visit typically provides two independent measurements separated by 106 minutes coming from the two fields of view of the spacecraft. As of October 2022, Gaia collected 145 measurements for Gaia19dke. The light curve from Gaia is collected in the Gaia broad-band filter G-band and exhibited multiple peaks, with the main peak reaching about 14.8 mag in G-band. As the event at its baseline was relatively bright with G $\sim$15.5 mag, it was possible to collect a vast number of follow-up observations using small-sized telescopes including the SCT-14 of the Abastumani Observatory. The earliest follow-up started 21 days after the announcement on the event on the Gaia Science Alerts web page. The modeling of the event with single point source single lens microlensing model with annual parallax gives the following preliminary parameters (see Table 2):

Table 2. Some preliminary microlensing parameters of Gaia19dke for lens mass distribution of $\propto M^{-1.75}$

Parameter	**Value**
Source star	G5m III
Source distance D_S	4.9±1.2 kpc
Lens mass M_L	0.81 $M_\odot$
Lens distance D_L	2.21 kpc
Lens type probability - White Dwarf	66%
Lens type probability - Neutron Star	18%
Lens Type probability - Black Hole	9%

5.2. Gaia21dnc

First alert of Gaia21dnc event as AT2021uey was announced by the ZTF survey (Bellm et al., 2019, Masci et al., 2019) on 11 June 2021. The alert was named ZTF18abktckv, and the confirmation of the microlensing nature of the alert was made three months later by Möller & et al. (2021) due to the peculiar shape of the signal. The ASAS-SN survey alerted it on 7 July 2021. The Gaia Science Alert system (Hodgkin et al., 2021) alerted the same event on 27 July 2021 as Gaia21dnc. The alert was recognized to be candidate microlensing event, which triggered follow-up observations by smaller telescopes. The light curve of Gaia21dnc well covered by different datasets and is 1.5 mag brighter than the baseline. There is a 3-day long anomaly at HJD = 2459400. During the anomaly, photometry was obtained only by the ASAS-SN and ZTF surveys. The data modeling indicates that the lens of this microlensing event is an M-dwarf star with a Jupiter-like planet. The preliminary parameters are listed in the Table 3.

Table 3. Some preliminary microlensing parameters of Gaia21dnc

Parameter	**Value**
Source star	Metal-poor F giant
Source distance D_S	6.9±2.4 kpc
Lens mass M_L	0.59±0.24 $M_\odot$
Lens distance D_L	0.9 kpc
Lens type	M-dwarf
Jupiter-like planet mass	1.61±0.66 M_{jup}
a (AU)	3.8:
lg(P), day	3.6:

doi:https://doi.org/10.52526/25792776-23.70.1-35

References

Bellm E. C., et al., 2019, Publ. Astron. Soc. Pac. , 131, 018002

Dyson F., Eddington A., Davidson C., 1920, Philos. Trans. R. Soc. Lond. Ser. A, 220, 291

Einstein A., 1911, Ann. Phys., 340, 898

Einstein A., 1915, Sitzungsber. Preuss. Akad. Wiss., 1, 831–839

Griest K., Hu W., 1992, The Astrophysical Journal, 397, 362

Hodgkin S. T., et al., 2021, Astron. Astrophys. , 652, A76

Liebes S., 1964, Phys. Rev., 133, 835

Mao S., Paczyński B., 1991, The Astrophysical Journal, 374

Masci F. J., et al., 2019, Publ. Astron. Soc. Pac. , 131, 018003

Möller A., et al. 2021, Mon. Not. R. Astron. Soc. , 501, 3272

Paczyński B., 1986, Astrophys. J., 304, 1

Refsdal S., 1964, MNRAS, 128, 295

Skowron J., et al., 2016, The Astrophysical Journal, 820, 4

Tsapras Y., et al., 2016, Monthly Notices of the Royal Astronomical Society, 457, 1320

Walsh D., Carswell R., Weymann R., 1979, Nature, 279, 381

Wambsganss J., 1998, Living Reviews in Relativity, 1

Wood A., Mao S., 2005, MNRAS, 362, 945

Łukasz Wyrzykowski et al., 2015, The Astrophysical Journal Supplement Series, 216, 12

doi:https://doi.org/10.52526/25792776-23.70.1-35

Communications of BAO, Vol. 70, Issue 1, 2023, pp. 43-48

Search and identification of high-velocity stars by dynamical ejection and supernovae from multiple stars

V. Hambaryan *[1,2] and R. Neuhaeuser†[1]

[1]Astrophysical Institute of Friedrich-Schiller-University Jena, Germany
[2]Byurakan Astrophysical Observatory after V.A. Ambartsumian, Armenia

Abstract

The project, funded by Science Committee of RA (ARPI program), intended to search, detection, kinematic study and identification of the birth places of the high-velocity and isolated neutron stars that encountered in the past with a stellar groups (multiple stars, stellar clusters, associations, etc.) closer than 10 pc, i.e. to test the concept: a high-velocity star and a stellar group or some of its members in the past were "in the same place at the same time".

We plan to use stars with the high-quality astrometry and radial velocities from the very recently released *Gaia* DR3 catalogue and empirically select high-velocity candidates. Next, by using full gravitational potential of the Galaxy to calculate the motion of a stellar groups and a candidate of high-velocity star from their current positions to the proximity epoch. For numerical integration we will utilize the fast and accurate numerical integration.

1. Introduction

In this project, we plan to search, detection, kinematic study and identification of the birth places (star clusters, associations and multiple stars, Ambartsumian, 1947, 1955) of the high-velocity stars in the Galaxy.

High-velocity stars, such as all high-mass OB-stars, are thought to have formed in the stellar groups and a certain part of them (see, e.g., Renzo et al., 2019) were ejected into the general Galactic field either Dynamical Ejection (in a Trapezium type young multiple systems, Ambartsumian, 1954, Poveda et al., 1967) or Binary Ejection Mechanisms (the secondary star of a close binary receives its ejection velocity and becomes unbound when the primary explodes as a supernova, Blaauw, 1961). The proper motion of a high-velocity star often points exactly away from a stellar group, of which the star was formerly a member. The majority of these stars in the literature are high-mass O and B type stars (see, e.g., Hoogerwerf et al., 2000, 2001, Tetzlaff et al., 2010) with ejection velocities less than 200 $\mathrm{km s^{-1}}$ (Perets & Šubr, 2012). Recent results show it is possible for low-mass G/K type stars with ejection velocities up to ~ 1300 $\mathrm{km s^{-1}}$(Tauris, 2015).

Obviously, the definition of a high-velocity star (a star moving faster than 60-100 km/s relative to the average motion of the stars in its neighbourhood) is somewhat arbitrary and it depends on the many factors (for example, star mass, age, origin, galactic potential, velocity distribution model, etc.). Therefore, empirical (i.e. outliers from multivariate distribution of kinematic parameters of stars depending on the distance from the center of the Galaxy, see, e.g., Hambaryan (2018)) determination of them might be more robust given the huge number of stars with reliable astrometric parameters and radial velocities provided by *Gaia* mission (Gaia Collaboration et al., 2018).

Hyper-velocity stars (HVSs): are another subclass of high velocity stars, the fastest stars in our Galaxy, which have extreme velocities above the escape speed of the Milky Way. HVSs can obtain their large velocity from a number of different processes. Hills (1988) first theoretically predicted the formation of HVSs via three-body interactions between a binary star system and the massive nucleous in the Galactic Center (GC). Hyper-velocity stars are stars with velocities that are substantially different from that expected for a star belonging to the normal distribution of stars in a galaxy. Such stars may have velocities on the order of 1000 km/s.

*Valeri.Hambaryan@uni-jena.de, Corresponding author
†Ralph.Neuhaeuser@uni-jena.de

doi: https://doi.org/10.52526/25792776-23.70.1-43

Pulsars: Some neutron stars are inferred to be traveling with similar speeds as HVSs. This could be related to runaway-stars and their ejection mechanism. Neutron stars are the remnants of supernova explosions, and their extreme speeds are very likely the result of an asymmetric supernova explosion or the loss of their near partner during the supernova explosions that forms them.

1.1. Origin mechanisms

High space *peculiar* velocities of stars are explained mainly by two different mechanisms: dynamical ejection due to gravitational interaction in multiple stellar systems or clusters (Poveda et al., 1967) and disruption of a multiple stellar system as result of a SN explosion of a massive star (Blaauw, 1961); a binary companion would get unbound, if at least half of the mass of the binary system is lost in the SN. In both such cases, the ejected star(s) are then called *runaway stars*, e.g. the former companion of the SN progenitor travels roughly with its former orbital velocity – a neutron star formed in the SN obtains a high kick velocity from the SN. See Boubert et al. (2017) and Renzo et al. (2019) for more details about runaway stars from SNe.

While runaway stars are often thought to have higher than normal space velocities, it is also possible to get unbound by leaving the system with normal to small velocity, sometimes then called *walkaway stars*; furthermore, runaway stars are not always single stars, as close binaries can also get unbound.

Depending on the separation of a multiple stars and component masses prior to the explosion (i.e. phase of mass transfer before the supernova, and the subsequent inversion of the mass ratio) and the amount of asymmetry involved (i.e. the magnitude of the kick velocity imparted to the neutron star during the explosion), the progenitor binary will either get unbound (ejecting a single high-velocity star and neutron star) or it will remain bound (see, e.g., Tauris & Takens, 1998). In case of the latter, its center of gravity will be accelerated and one could expect to observe a binary system, either as a member of a stellar association or runaway close binary nearby to a parental stellar group, comprised by a neutron star and a normal star as High- or Low-Mass X-ray Binary (HMXB or LMXB, respectively), if the separation is sufficiently small for accretion to occur (Ankay et al., 2001, Hambaryan et al., 2022).

In addition we will investigate a neutron star/high-velocity star pairs very likely both ejected from multiple stellar system during supernova event.

In order to disentangle between different scenarios of the origin of high-velocity stars or high-velocity binaries we plan to model ejection mechanism in multiple stellar systems, i.e. simulation of the dynamics of a *nbody* system as well as supernova explosion of progenitors, providing kick velocities of them. Moreover, these models we plan to apply for fitting individual cases, to asses progenitor mass and evolution. Finally, these parameters will provide an important input to estimate robust initial mass functions of a stellar group and to obtain more realistic star formation picture of individual stellar groups as well as in the Galaxy in general.

2. Project Aims and Objectives

The **three main goals** of this project are:

1) Compilation of a catalog of runaway stars from Gaia data and an investigation of the frequency of runaway stars around young stellar groups:
   - Which percentage of runaway stars (or mass) gets ejected ?
   - What are the mass and velocity distributions of ejected stars ?

2) Search for runaway star-neutron star pairs indicating binary SN ejection (e.g.: what is the kick velocity distribution of neutron stars ?)

3) Search for pairs (or higher order multiples) of runaway stars which got dynamically ejected. A comparison of (2) with (3) will then also show how effective these two mechanisms are to produce runaway stars (Hoogerwerf et al., 2000, 2001, had only one case each, at least one of them is dubious).

4) Search and identification of the places of origin of *hyper-velocity stars* (such stars may have velocities on the order of 1000 km/s, first theoretically predicted the formation of them via three-body interactions between a binary star system and the massive nucleous in the Galactic Center) yet another subtask of our project which may shed

doi: https://doi.org/10.52526/25792776-23.70.1-43

It is also well possible that for some SNe, we can find more than just one runaway star, because many pre-SN systems are expected to be higher order multiples than binary stars (we search for both early- and late-type runaways).

Furthermore, whenever a pair of runaway star and neutron star is found, we can estimate the following parameters:

- Lifetime of SN progenitor from the difference between cluster age and flight time since the SN.
- The current peculiar space velocity of the runaway star is roughly equal to its orbital velocity at the time of the SN; hence, from the masses of the runaway and the SN progenitor we can estimate the orbital separation and period (e.g. assuming a circular orbit).
- The orbital separation (or perihelion separation) can then be compared to the Roche lobe of the SN progenitor shortly before the SN, to investigate possible binary evolution and interaction.
- For neutron stars, in the same way, we can estimate the kick velocity due to the SN (taking into account a possible gravitational pull from a massive runaway for a short period after the SN).
- We can then search for SN debris (α elements etc) on the runaway star atmosphere.
- For each 3D location of a SN, we will check for cavities in the ISM, ^{26}Al sources, and soft X-ray emission.

3. Selection of new runaway stars from Gaia

Identifying true high-velocity outliers in the Gaia archive is challenging.

First of all, we will select among ~ 33 million stars *Gaia DR3* (Gaia Collaboration, 2022, Gaia Collaboration et al., 2022) sources for which astrometric parameters (positions, parallax and proper motions) and RV have relative measurement uncertainties not exceeding 10%. Further, these sources will be converted into galacto-centric cartesian coordinates (X,Y,Z,U,V,W). Then their space velocity will be analyzed for each component, the empirical distribution in a spherical/cylindrical ring of 5-10 pc width around center of the Galaxy. The estimates of distribution parameters (median, most probable value, the highest posterior density (HPD) intervals[1] of the total velocity in a spherical ring, having at least 100 sources, will be performed with kernel-density estimates. From this distribution, high-velocity candidates will be selected as outliers which have a value $V_{space} > V_{HPD_{hi}}(99\%)$. Note, that this is a conservative criterion with higher confidence for a high-velocity candidate star. In addition, we will also use Mahalanobis distance (Leys et al., 2018) and Sigma-clipping algorithms to identify outliers.

Next, we will use *Gaia DR3* astrometric data and will utilise a number of methods (e.g., the UPMASK (Unsupervised Photometric Membership Assignment in Stellar Clusters; Krone-Martins & Moitinho, 2014), non-parametric (e.g., Clusterix 2.0; Balaguer-Núñez et al., 2020) and parametric (e.g., BANYAN-Sigma Gagné et al., 2018)) to calculate membership probabilities of the selected stars for any stellar group (cluster, association, multiple stars) by using bonafide members of them.

The application of these methods and using major astronomical databases (e.g. SIMBAD) and imaging surveys (from infrared to X-rays) will allow us roughly classify types of selected stars and their environment.

For very promising candidates of *high-velocity stars* we are planning to perform additional photometric and spectroscopic follow up observations for detection of possible bow-shocks and peculiar chemical composition suggesting interaction of a SN shell and runaway star.

4. Methods

To study the Galactocentric motion of a single point mass (a star, binary or cluster) we use a numerical integration of its equations of motion in the gravitational field of the Galaxy expressed in a rectangular Galactocentric frame. Namely, for the Galactocentric motion of *high-velocity* candidate star and the possible parental stellar group we will use of the code described in Neuhäuser et al. (2020), which computes the orbits by a numerical integration of their equations of motion as defined by the Galactic gravitational potential.

[1]The highest posterior density interval is determined as a probabilistic region around a posterior mode, and is similar to a confidence interval in a classical statistics (Gregory, 2005, Gregory & Loredo, 1992).

doi: https://doi.org/10.52526/25792776-23.70.1-43

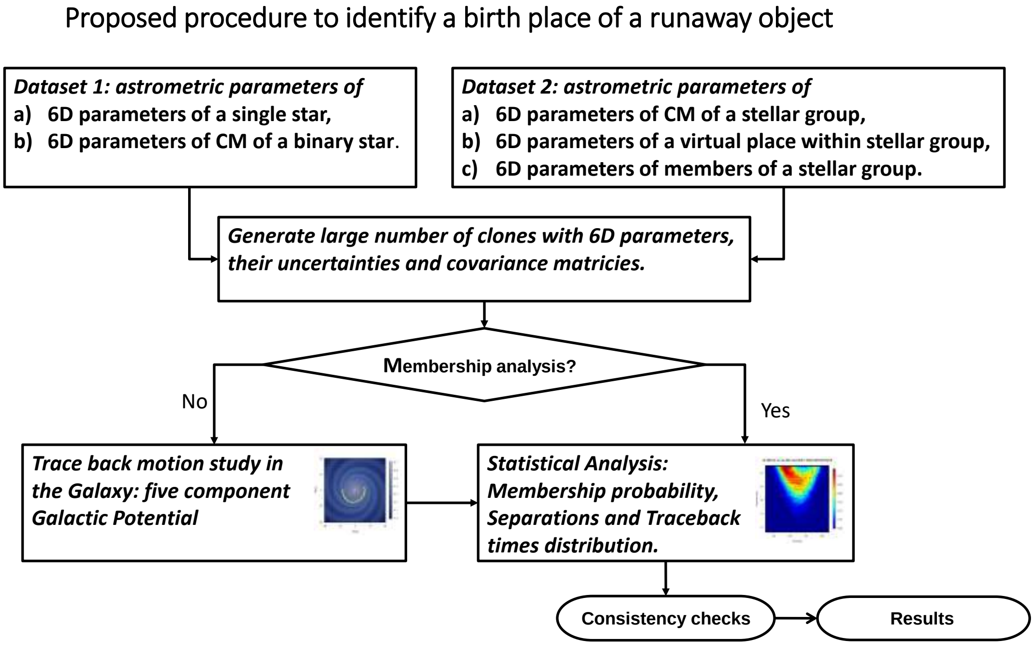

Figure 1. The flowchart of the proposed processing for identification of the birth place of runaway object (the concept "in the same place at the same time").

Further, to identify a probable parental stellar group as a correct counterpart of a *high-velocity* candidate star we will follow to the algorithm depicted in Fig. 1. Moreover, it is obvious, that using as an input astrometric and kinematic parameters and their uncertainties of both one can get, in principle, only certain number of trajectories satisfying some of the criteria (e.g., minimum separation) of the close stellar passage. In each case, one clearly gets a probabilistic output (see, e.g., Hoogerwerf et al., 2000, 2001, Neuhäuser et al., 2020, Tetzlaff et al., 2010). Whether this number is expected from a real pair or by chance, i.e. occured in the same volume of the space during some time interval in the past, needs further statistical analysis, given the above mentioned uncertainties of parameters. Finally, further consistency checks must be performed as listed in Neuhäuser et al. (2020), e.g. that there should not be any more massive (O-type) star in the host group left that is not yet exploded or that the flight time should not be larger than the age of a hosting group or neutron star (if known).

In preparation of this new project and to be ready for the new Gaia data, a new software was written from scratch to trace back the orbits of stars through the Galaxy.

A sample application of it is to find possible common origins of runaway stars and neutron stars at their birth place – from dynamical ejection or in a supernova, e.g. those which contributed to the ^{60}Fe on Earth (Neuhäuser et al., 2020).

To trace back of a star's orbit the well-known equation of motion is numerically integrated backwards in time for the Galactic potential. The number of simulated orbits per star (here: 3 million) as well as the number of steps and step width (here: 1000 years) for the integration are configurable. After each step the mutual separations between the objects are calculated and the minimum separations are determined.

The 'success' of a simulation run can be rated according to certain criteria such as the number of close encounters within, e.g., 10 pc (Hoogerwerf et al., 2000, 2001) or 15 pc (Tetzlaff et al., 2010). We also compute the likelihood for each run: in order to determine most likely past flight path of runaway stars, neutron stars, and associations among the many simulations, we used as measure the multivariate Gaussian likelihood. This likelihood is the sum of likelihoods of the input parameters and their uncertainties (with covariance matrices), as well as output parameters, i.e. positions and the time of a close approach within a stellar association or subgroup.

The Galactic potential used is a three-component model consisting of potentials for disk, spheroid bulge, and halo from Johnston et al. (1996), quite similar (if not the same) as used by Hoogerwerf et al. (2000, 2001):with an axisymmetric disk as first term (Miyamoto & Nagai, 1975), a spherically symmetric bulge as second term (Hernquist, 1990),and a massive spherical Galactic halo as third term (Johnston et al., 1996).

Alternatively, we also used model number III from Bajkova & Bobylev (2017) as Galactic potential, also

doi: https://doi.org/10.52526/25792776-23.70.1-43

in Galactocentric Cartesian coordinates. with an axisymmetric disk as first term (Miyamoto & Nagai, 1975), a spherically symmetric bulge as second term (Hernquist, 1990), and a massive spherical Galactic halo as third term (Navarro et al., 1996) derived by fitting of modern data on circular velocities of Galactic objects located at distances up to 200 kpc from the Galactic center (Bajkova & Bobylev, 2017). With any of the two potentials, this leads to a first-order system of six ordinary differential equations, the integration of which is done by means of the Runge-Kutta-Fehlberg (order 4,5) method. Alternatively, we also used the Gauss-Everhardt orbit integrator (Avdyushev, 2010). Further, we plan to supplement the Galactic gravitational potential with the more realistic, non-axisymmetric and time dependent terms, which take into account the influence of the central bar of the Galaxy and the spiral density wave (Bajkova & Bobylev, 2019, Fernández et al., 2008, Palous et al., 1993). Alternatively, we will use empirically determined Galactic gravitational potential based on the *Gaia* data.

Positions, distances (and/or parallaxes), and proper motions for neutron stars are listed in the Australian Telescope National Facility (ATNF) Pulsar Catalogue (Manchester et al., 2005, Taylor et al., 1993); proper motions in Galactic longitude and latitude have been transformed to equatorial proper motions with the usual Galactic parameters as above; there are currently 395 neutron stars with both a distance estimate and a transverse velocity – having excluded those which are either too young to be connected to the ^{60}Fe deposition (those related to SN remnants) or too old to be related to young OB associations (milli-second pulsars); more are expected to be found during the project duration, maybe already by SKA; pulsar distances are either independent estimates (like a parallax) with measurement uncertainties or, otherwise, from the dispersion measure (Yao et al., 2017).Among the above mentioned 395 neutron stars, there are 68 pulsars for which there is a Gaia DR2 star at the same position (as listed in the *Gaia DR3* catalog and Simbad), i.e. pulsars in binaries with Gaia stars; for those pulsars, we use the parallaxe and proper motion of the Gaia star also for the pulsar (and in three cases, also the Gaia RV can be used for the pulsar).

Positions, distances, proper motions, and RVs for stellar groups are compiled by (Cantat-Gaudin et al., 2020, Hunt & Reffert, 2023, Mel'nik & Dambis, 2017, Melnik & Dambis, 2020, Soubiran et al., 2018).

Given the measurement uncertainties of input parameters (i.e., astrometric and kinematic) and their covariance matrices (correlations between them), and given that the number of simulations in any Monte Carlo simulation is finite, one can expect some number of trajectories where the separations between two objects are less than a few pc (indicating a close encounter,i.e. a common origin in a binary SN or dynamical ejection, see, e.g., Hambaryan et al., 2022, Hoogerwerf et al., 2000, 2001, Neuhäuser et al., 2020, Tetzlaff et al., 2010). Note, that this number must be compared with the expected number of trajectories which is expected by chance (see, e.g., Neuhäuser et al., 2020).

Acknowledgments

This work was supported by the Science Committee of RA (Adjunct Research Professorship Program (Remote Laboratory) project No 22RL-039).

References

Ambartsumian V. A., 1947, The evolution of stars and astrophysics

Ambartsumian V. A., 1954, Communications of the Byurakan Astrophysical Observatory, 15, 3

Ambartsumian V. A., 1955, The Observatory, 75, 72

Ankay A., Kaper L., de Bruijne J. H. J., Dewi J., Hoogerwerf R., Savonije G. J., 2001, Astron. Astrophys. , 370, 170

Avdyushev V., 2010, Vychisl. Tekhnol., 15, 31

Bajkova A., Bobylev V., 2017, Open Astronomy, 26, 72

Bajkova A. T., Bobylev V. V., 2019, Mon. Not. R. Astron. Soc. , 488, 3474

Balaguer-Núñez L., et al., 2020, Mon. Not. R. Astron. Soc. , 492, 5811

Blaauw A., 1961, Bull. Astron. Inst. Neth. , 15, 265

Boubert D., Erkal D., Evans N. W., Izzard R. G., 2017, Mon. Not. R. Astron. Soc. , 469, 2151

Cantat-Gaudin T., et al., 2020, Astron. Astrophys. , 640, A1

Fernández D., Figueras F., Torra J., 2008, Astron. Astrophys. , 480, 735

Gagné J., Roy-Loubier O., Faherty J. K., Doyon R., Malo L., 2018, Astrophys. J. , 860, 43

doi: https://doi.org/10.52526/25792776-23.70.1-43

Gaia Collaboration 2020, VizieR Online Data Catalog, p. I/350

Gaia Collaboration 2022, VizieR Online Data Catalog, p. I/355

Gaia Collaboration et al., 2018, Astron. Astrophys. , 616, A1

Gaia Collaboration et al., 2022, arXiv e-prints, p. arXiv:2208.00211

Gregory P. C., 2005, Bayesian Logical Data Analysis for the Physical Sciences: A Comparative Approach with 'Mathematica' Support

Gregory P. C., Loredo T. J., 1992, Astrophys. J. , 398, 146

Hambaryan V., 2018, Communications of the Byurakan Astrophysical Observatory, 65, 211

Hambaryan V., et al., 2022, Mon. Not. R. Astron. Soc. , 511, 4123

Hernquist L., 1990, Astrophys. J. , 356, 359

Hills J. G., 1988, Nature. , 331, 687

Hobbs G., Lorimer D. R., Lyne A. G., Kramer M., 2005, Mon. Not. R. Astron. Soc. , 360, 974

Hoogerwerf R., de Bruijne J. H. J., de Zeeuw P. T., 2000, Astrophys. J. Lett. , 544, L133

Hoogerwerf R., de Bruijne J. H. J., de Zeeuw P. T., 2001, Astron. Astrophys. , 365, 49

Hunt E. L., Reffert S., 2023, Astron. Astrophys. , 673, A114

Johnston K. V., Hernquist L., Bolte M., 1996, Astrophys. J. , 465, 278

Krone-Martins A., Moitinho A., 2014, Astron. Astrophys. , 561, A57

Leys C., Klein O., Dominicy Y., Ley C., 2018, Journal of Experimental Social Psychology, 74, 150

Manchester R. N., Hobbs G. B., Teoh A., Hobbs M., 2005, Astron. J. , 129, 1993

Mel'nik A. M., Dambis A. K., 2017, Mon. Not. R. Astron. Soc. , 472, 3887

Melnik A. M., Dambis A. K., 2020, Mon. Not. R. Astron. Soc. , 493, 2339

Miyamoto M., Nagai R., 1975, Publ. Astron. Soc. Jpn. , 27, 533

Navarro J. F., Frenk C. S., White S. D. M., 1996, Astrophys. J. , 462, 563

Neuhäuser R., Gießler F., Hambaryan V. V., 2020, Mon. Not. R. Astron. Soc. , 498, 899

Palous J., Jungwiert B., Kopecky J., 1993, Astron. Astrophys. , 274, 189

Perets H. B., Šubr L., 2012, Astrophys. J. , 751, 133

Poveda A., Ruiz J., Allen C., 1967, Boletin de los Observatorios Tonantzintla y Tacubaya, 4, 86

Renzo M., et al., 2019, Astron. Astrophys. , 624, A66

Soubiran C., et al., 2018, Astron. Astrophys. , 619, A155

Tauris T. M., 2015, Mon. Not. R. Astron. Soc. , 448, L6

Tauris T. M., Takens R. J., 1998, Astron. Astrophys. , 330, 1047

Taylor J. H., Manchester R. N., Lyne A. G., 1993, Astrophys. J. Suppl. Ser. , 88, 529

Tetzlaff N., Neuhäuser R., Hohle M. M., Maciejewski G., 2010, Mon. Not. R. Astron. Soc. , 402, 2369

Yao J. M., Manchester R. N., Wang N., 2017, Astrophys. J. , 835, 29

doi: https://doi.org/10.52526/25792776-23.70.1-43

Communications of BAO, Vol. 70, Issue 1, 2023, pp. 49-53

Spectroscopy of new Herbig-Haro objects discovered in frames of BNBIS

T.A. Movsessian *[1] and T.Yu. Magakyan †[1]

[1]Byurakan Astrophysical Observatory, Aragatsotn reg., Byurakan, 0213 Armenia

Abstract

We present long-slit spectroscopy of some new Herbig-Haro objects and outflow systems discovered in the frames of Byurakan Narrow Band Imaging Survey (BNBIS) performed on 1 m Schmidt telescope of Byurakan Observatory. Spectroscopic observations were carried out with 6 m telescope (Russia) using SCORPIO2 spectral camera. All selected objects are associated with deeply embedded infrared sources in the molecular clouds. Long-slit spectroscopy allows to obtain position velocity diagrams of the emission structures like Herbig-Haro objects. Velocity fields of the outflows from IRAS 06277+1016 infrared source in Mon R1, from V963 Mon and 2MASS 06084223-0657385 in Mon R2 as well as from IRAS 06212-1049 are presented. Our spectroscopic data revealed bipolar outflow nature of the outflows associated with 2MASS 06084223-0657385 and IRAS 06212-1049.

Keywords: *Star formation, Herbig-Haro objects, jets and outflows*

1. Introduction

Herbig-Haro objects for a long time have been recognised as a sign of high activity of star formation in molecular clouds. In fact they represent shocked excitation zones where supersonic flows from young stellar objects (YSO) collide with interstellar medium and form small cloudlets with pure emission spectrum including permitted and low excitation forbidden emission lines ([O I], [S II] etc). Thus, the discovering of new HH objects is important as for the further studies of the phenomenon of directed outflows from young stars, as well as for the searches for new star forming regions and groups.

On the other hand, it is well known that the sources of directed outflows of low and intermediate mass usually are associated with compact reflection nebulae of characteristic conical shape. Moreover, deep images in the optical and infrared ranges reveal their bipolar nature. Such shape is a consequence of the presence of circumstellar disks and conical cavities near the YSOs illuminating these nebulae, created by matter outflow. In the overwhelming majority of cases HH objects and HH flows are located along the axes of these cometary nebulae, which proves a direct relationship between all these phenomena.

In this work we present some newly discovered Herbig-Haro objects and groups as well as their spectral investigations. Searches of HH objects in dark clouds were performed in the frames of Byurakan Narrow Band Imaging Survey (BNBIS), which is carried out using the 1m Schmidt telescope of Byurakan Observatory (Movsessian et al., 2021). Long-slit spectra allow to create PV diagrams of outflow systems, which provide information about velocity along the slit as well as reveal bipolar nature of some outflows.

2. Observations

Direct images were obtained with 1m Schmidt telescope of Byurakan observatory equipped with 4K×4K Apogee (USA) liquid-cooled CCD detector, which provides about 1 square degree field of view with image scale of 0.868″per pixel (Dodonov et al., 2017). During observations the narrow-band filters centered on 6560 Å and 6760 Å, both with a FWHM of 100 Å, were used to obtain Hα and [S II] images, respectively. A midband filter, centered on 7500 Å with a FWHM of 250 Å, was used for the continuum imaging.

*tigmov@bao.sci.am, Corresponding author
†tigmag@sci.am

doi: https://doi.org/10.52526/25792776-23.70.1-49

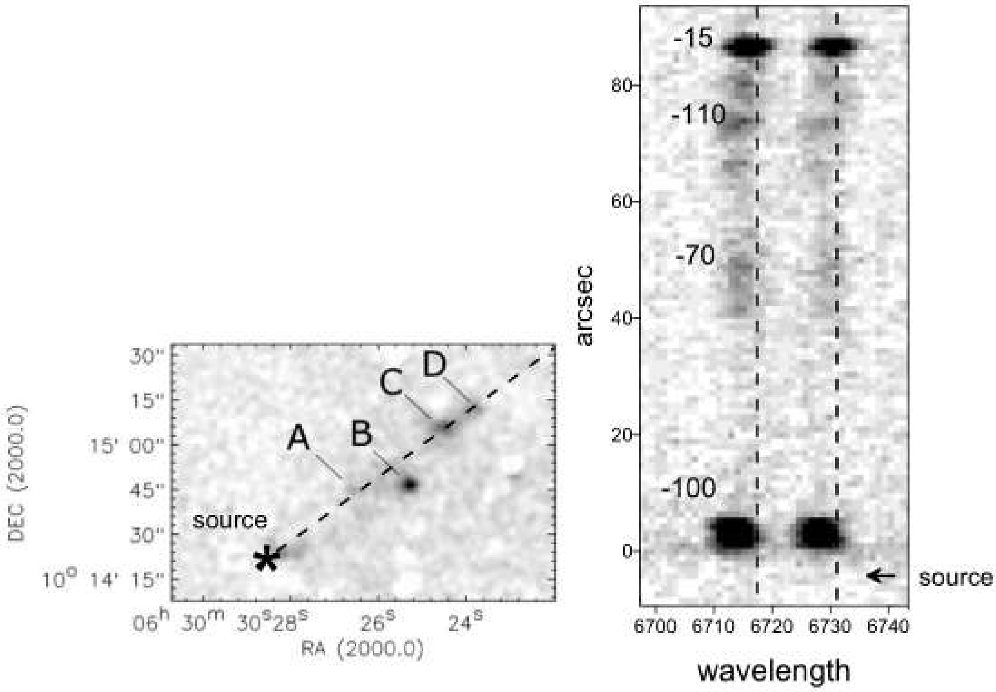

Figure 1. Direct image of IRAS 06212-1049 associated with a chain of HH objects in Hα+[S II] emission (left). HH objects are marked by letters and dotted line show the position of the slit. On the right panel the PV diagram in [S II] emission with the values of radial velocities is presented. Vertical dotted lines indicate the zero velocity of each line of the doublet.

Images were reduced in the standard manner using IDL package, which includes bias subtraction, cosmic ray removal, and flat fielding using "super flat-field", constructed by several images (Dodonov et al., 2017).

Spectral observations were performed on 6 m telescope of Special Astrophysical Observatory (SAO) of the Russian Academy of Sciences using SCORPIO-2 (Spectral Camera with Optical Reducer for Photometrical and Interferometrical Observations (Afanasiev et al., 2017) multi-mode focal reducer mounted in the primary focus of the telescope in the spectroscopic mode. As a detector CCD 261-84 of 2048$\times$4104 pixels, with the 15$\times$15-μm pixel size was used. To increase the S/N ratio of the observed data the 1$\times$2 pixel binning was applied providing 0.2$\times$0.4 image scale. The field of view was $6.1'$ with a scale of $0.2''$ per pixel. During the observations the VPHG 1200 grism in the wavelength range of 3650-7300Å was used. The spectral resolution was about 5.2Å across the full range of wavelengths (a mean reciprocal dispersion was 0.89Å/px) and a spatial scale along the slit was $0.4''$/pixel.

3. Results

3.1. The outflow system associated with IRAS 06277+1016

IRAS 06277+1016 is located in the Mon R1 association to the north-west from the famous Mon OB1 association on the distance of 800pc. This object was discovered during the BNBIS when several new HH objects as well as collimated outflow systems were found, and was designated as HH 1203. This outflow system represents the chain of Herbig-Haro objects traced by the axis of cone shape reflection nebula associated with IRAS 06277+1016. Detailed description of the newly discovered HH objects and outflow systems in Mon R1 can be found in Movsessian et al. (2021).

On the Fig.1 the narrow band image of the outflow (left panel) with superposed position of the slit of the spectrograph, as well as the position velocity (PV) diagram in [S II] doublet (right panel) are presented. The pure emission nature of the knots in this system is obvious. As can be seen from the PV diagram, radial velocities in the knots of the outflow system are negative with values of about -100 km s^{-1}. Moreover, in a distance of $7''$ from the infrared source the bright knot in [S II] emission is found, which can be an evidence of a short jet lying in the direction of the axis of HH 1203 flow. Its existence confirms the assumption that

doi: https://doi.org/10.52526/25792776-23.70.1-49

the infrared object, apparently embedded in the nebula, is the source of HH 1203.

3.2. IRAS 06068-0643 (V963 Mon)

This variable star is located in about one degree south from Mon R2 association. Mon R2 association is a well studied region of star formation which contains early-type stars (Racine, 1968), molecular outflows (Meyers-Rice & Lada, 1991), an embedded HII region (Downes et al., 1975) and clusters of infrared sources (Thronson et al., 1980). However, HH objects were searched there only episodically; some of them were found in the eastern side of Mon R2 (Carballo & Eiroa, 1993). Our attention was drawn to the area south of the central part of Mon R2, where several nebulous objects and an eruptive star V899 Mon are located.

V963 Mon is located in the southern part of the Mon R2 association about 2.5′ SW from V899 Mon. This source is associated with compact reflection nebula and shows spectral features, as well as photometric variability typical for EXOrs (Wils et al., 2009).

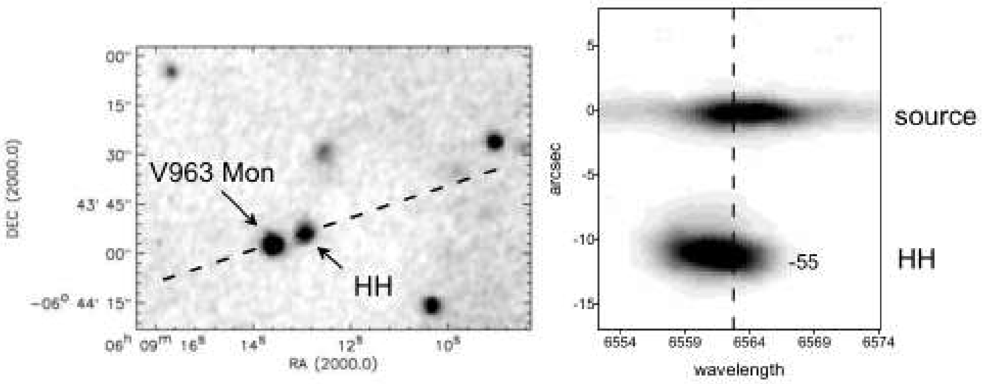

Figure 2. Direct image of V963 Mon associated with a helical chain of HH objects in Hα+[S II] emission (left). Bright HH objects are marked and dotted line shows the position of the slit. On the right panel the PV diagram in Hα emission with value of radial velocity is presented. Vertical dotted line indicate the zero velocity of the emission.

During the survey a chain of new HH objects was discovered near this object. This chain of HH objects has an unusual helical form with very bright spot near the V963 Mon. In the Hα image (Fig.2 (left panel)) the chain of HH knots is visible near the source. In the same image the position of the slit of spectrograph is shown also. PV diagram in Hα emission is presented on the right panel. Radial velocity of HH objects is about 55 km s^{-1}.

3.3. 2MASS 06084223-0657385

About 20 arcmin south-west from V899 Mon near the 2MASS 06084223-0657385 infrared source, associated with bipolar reflection nebula, several HH knots were revealed. HH objects lie along a parabolic curve, at the apex of which the infrared source is located (Fig.3, left panel). Therefore, it can be argued that we are dealing with a bipolar outflow with an unusual arc-shaped structure. Such a morphology is typical either for so-called irradiated jets or outflows from the sources with high proper motion. We incline to the second scenario, because irradiated outflows are usually represented by a very narrow emission filaments without prominent knotty structures (Bally & Reipurth, 2001). Taking this scenario into account we estimated the probable proper motion value of the source to be about 50 km s^{-1}, which is quite acceptable. The estimated total length of this bipolar outflow will be about 1.5 pc for the distance of 900 pc. This outflow system represents giant or so-called parsec-scale HH flow.

On the PV diagram in [S II] emission (Fig.3, right panel) in the both sides of the stellar continuum, beside of the 2MASS 06084223-0657385 stellar spectrum the several emission knots are distinctly visible. One of these emission knots is not discernible on the direct image on the bright reflection nebular background. The radial velocities of emission knots indicate the bipolar nature of this outflow with positive velocities in eastern and negative ones in western branch. Vertical dotted lines indicate the zero velocity for each line of the doublet.

doi: https://doi.org/10.52526/25792776-23.70.1-49

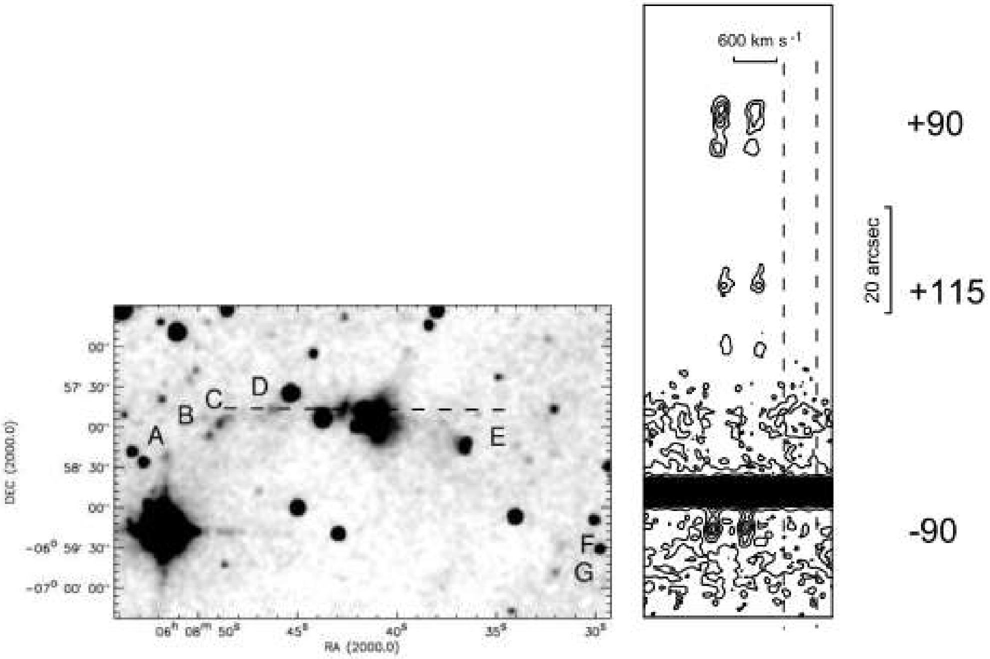

Figure 3. Direct image of 2MASS 06084223-0657385 associated with the parabolic chain of HH objects in Hα+[S II] emission (left). HH objects are marked by letters and dotted line shows the position of the slit. On the right panel the PV diagram in [S II] emission with values of radial velocities is presented. Vertical dotted lines indicate the zero velocity of each line of the doublet.

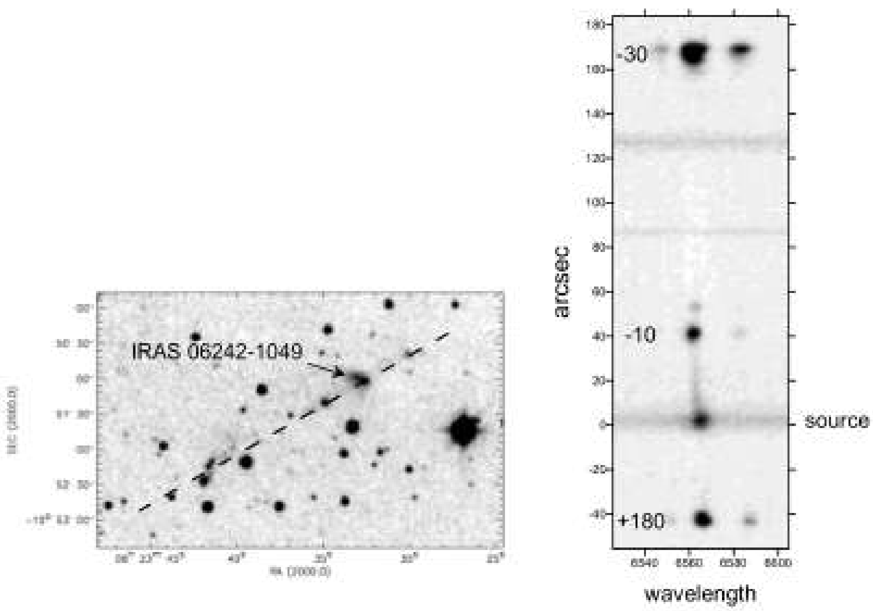

Figure 4. Direct image of IRAS 06242-1049 associated with cone shape reflection nebula and the chain of HH objects in Hα+[S II] emission (left). Dotted line shows the position of the slit. On the right panel the PV diagram in Hα emission with value of radial velocities is presented.

doi: https://doi.org/10.52526/25792776-23.70.1-49

3.4. IRAS 06212-1049

The infrared source IRAS 06212-1049 is associated with a cone-shaped reflection nebula, the axis of which is oriented to the southeast. The deep images of the PanSTARRS survey show also a faint nebula in the opposite direction from the source, which indicates the bipolar morphology. The object is located near the dark cloud LDN 1652, which has a distance of 830 pc, so its distance can be considered the same. On the images obtained in the Hα and [S II] emission lines, several HH knots, located along the axis of the reflection nebula, were detected (Fig.4, left panel). Obviously, they represent a collimated optical flow. In the distance of about 830 pc the total length of the outflow will be about 0.9 pc.

As in the all previous cases we present PV diagram of this outflow system (Fig.4, right panel), which indicates the bipolar nature of this outflow with very high positive velocity in the western knot and low negative velocities in knots of the eastern branch. This again confirms the bipolar nature of the collimated outflow from IRAS 06212-1049.

4. Conclusion

Since the beginning of 2019, when the BNBIS survey was started, more than 100 new HH objects and outflow systems have been found. Among them the several giant outflow systems, narrow jets as well as the curved HH flow should be mentioned. The sources of outflows are associated with cone shape reflection nebulae, often of bipolar structure. Moreover, all collimated outflows are directed along the axes of these reflection nebulae.

This article presents long-slit observations of some selected objects and HH groups from the survey, performed with the 6-meter telescope. In the several cases outflows are bipolar with two branches with positive and negative radial velocities. e.g. of 2MASS 06084223-0657385 and IRAS 06212-1049.

In addition to the all results presented above, this work demonstrates that the 1-m Schmidt telescope of Byurakan Observatory, which was used several decades ago for well-known surveys of active galaxies such as the First Byurakan Survey and Second Byurakan Survey, can still lead to important discoveries.

Acknowledgements

This work was partly supported by the grant 21T-1C031 of the RA State Committee of Science.

References

Afanasiev V. L., Amirkhanyan V. R., Moiseev A. V., Uklein R. I., Perepelitsyn A. E., 2017, Astrophysical Bulletin, 72, 458

Andre P., Montmerle T., 1994, Astrophys. J. , 420, 837

Bally J., Reipurth B., 2001, Astrophys. J. , 546, 299

Carballo R., Eiroa C., 1993, in Errico L., Vittone A. A., eds, Astrophysics and Space Science Library Vol. 186, Stellar Jets and Bipolar Outflows. p. 213, doi:10.1007/978-94-011-1924-5˙37

Dodonov S. N., Kotov S. S., Movsesyan T. A., Gevorkyan M., 2017, Astrophysical Bulletin, 72, 473

Downes D., Winnberg A., Goss W. M., Johansson L. E. B., 1975, Astron. Astrophys. , 44, 243

Meyers-Rice B. A., Lada C. J., 1991, Astrophys. J. , 368, 445

Movsessian T. A., Magakian T. Y., Dodonov S. N., 2021, Mon. Not. R. Astron. Soc. , 500, 2440

Racine R., 1968, Astron. J. , 73, 588

Reipurth B., Bally J., 2001, Ann. Rev. Astron. Astrophys. , 39, 403

Thronson H. A. J., Gatley I., Harvey P. M., Sellgren K., Werner M. W., 1980, Astrophys. J. , 237, 66

Wils P., Greaves J., Drake A. J., Catelan M., 2009, Central Bureau Electronic Telegrams, 2033, 1

doi: https://doi.org/10.52526/25792776-23.70.1-49

Communications of BAO, Vol. 70, Issue 1, 2023, pp. 54-59

Investigations of late-type giant stars from the First Byurakan Spectral Sky Survey

G.R. Kostandyan [*], K. S. Gigoyan [†] and K. K. Gigoyan [‡]

INAS RA V. Ambartsumian Byurakan Astrophysical Observatory (BAO), Byurakan 0213, Aragatzotn Province, Armenia

Abstract

We study late-type giants found in the First Byurakan Survey (FBS) data base. The third Gaia data release (Gaia EDR3) photometric and astrometric data have been used to characterize our sample of 1 100 M-type giants and 130 C-type stars found at high latitudes. Phase dependent light-curves from large sky area variability data bases such as Catalina Sky Survey (CSS) and The light curves from the Catalina Sky Survey (CSS), All-Sky Automated Survey for Supernovae (ASAS-SN) and Transiting Exoplanet Survey Satellite (TESS) databases were exploited to study their variability nature. Using TESS light curves, the variability types of some objects have been established for the first time.

Keywords: *late-type -stars: AGB – stars: variables: TESS and Gaia data*

1. Introduction

The First Byurakan Survey (FBS), also known as the Markarian survey, was the first systematic objective-prism survey of the extragalactic sky. This survey was conducted by B. E. Markarian and collaborators from 1965 to 1980 (Markarian, 1967). The spectral plates were obtained at the Byurakan Astrophysical Observatory (BAO) using the 1-m Schmidt telescope. Various Kodak emulsions were used during the observations, providing a spectral range of 3400–6900 Å.

The selection and study of faint late-type stars (LTSs, M-type and carbon (C) stars) at high Galactic latitudes were one of the main priorities of the second part of the FBS. C stars can be identified through the presence of Swan bands of C_2 molecule at 4737, 5165, and 5636 $\AA$ (N – type C stars). Several objects showing the C_2 band-head at 4382 Å are early – type C stars (R or CH type stars). M – type stars can easily be distinguished because of the titanium oxide (TiO) molecule absorption bands at 4584, 4762, 4954, 5167, 5500 and 6200 $\AA$.

All FBS plates have been digitized, resulting in the creation of the Digitized First Byurakan Survey (DFBS) data base (Mickaelian et al., 2007). Its images and spectra are available on the DFBS web[1] portal in Trieste. All DFBS plates were analyzed for LTSs. The second version of the "Revised And Updated Catalogue of the First Byurakan Survey of Late-Type Stars", containing data for 1471 M- and C-stars (130 C-type stars, 241 M dwarfs, and 1100 M-type giants), was generated (Gigoyan et al., 2019).

The main goal of the present paper is the characterization of FBS late-type giants selected on First Byurakan Survey (FBS) plates, using modern astronomical databases, mainly Gaia EDR3 (EDR3; Gaia Collaboration et al., 2021), Catalina Sky Survey (CSS), All-Sky Automated Survey for Supernovae (ASAS-SN)(Jayasinghe et al., 2018, Kochanek et al., 2017, Shappee et al., 2014) and Transiting Exoplanet Survey Satellite (TESS)(Stassun et al., 2019).

Our small paper is structured as follows. Section 2 considers photometric and astrometric data, cross-correlations with *Gaia* EDR3, 2MASS and WISE.

In Section 3 we present the results of light curve analysis and classification of FBS late-type giants. Section 4 summarizes our results.

[*]kostandyan@bao.sci.am, Corresponding author

[†]kgigoyan@bao.sci.am

[‡]karengigoyan@bao.sci.am

[1]http://www.ia2-byurakan.oats.inaf.it for more details, see also the web site at ArAS http://www.aras.am/Dfbs/dfbs.html/

doi: https://doi.org/10.52526/25792776-23.70.1-54

2. Gaia EDR3, 2MASS and WISE photometric data

Gaia EDR3 (Gaia Collaboration; Gaia Collaboration et al., 2021) provides high-precision astrometry, three-band photometry, effective temperatures, and information on astrophysical parameters for about 1.8 billion sources over the full sky brighter than G = 21.0 magnitude. All FBS red giants were cross-matched with the *Gaia* EDR3 catalogue sources. These objects are relatively bright, so that G - band brightnesses were in the range $9.4 < G < 18.2$ mag.

To discriminate dwarf/giant luminosity class, we used the traditional color-color plots (J-H vs. H-Ks). Giant stars are notable for having infrared colors different from the M dwarfs. This has been known since Bessell & Brett (1988) and Bessell (1991). M dwarfs are very well separated on *JHK* Near-IR colour-colour diagram. Figure 1 presents the 2MASS *J-H* versus H-K_s colour-colour diagrams for all 1471 FBS LTS. Among the FBS M-type stars with the largest 2MASS colours (J-$H = 2.23$, H-$K_s = 1.71$) is the object FBS 2216+434, which subtype is estimated M6-M7, and is associated with the unknown source IRAS 22165+4326.

The WISE four band photometry provide useful color indices for giant carbon stars: we show in figure 3 W1-W2 versus W1-W4. Dusty C stars are well separated in a rising branch, while non-dusty C stars are mixed with the other ones. Mira variables are a bit above the main locus of the late type stars. Semiregular variables are spread all along the main locus, while nonvariable stars are grouped in the blue corner.

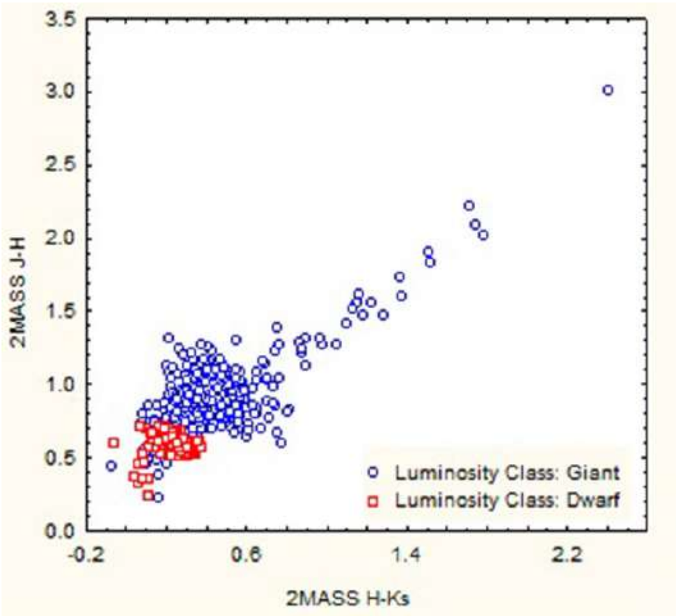

Figure 1. The 2MASS *J-H* versus H-K_s colour-colour diagram for 1471 FBS LTSs stars.

3. Optical variability

To study optical variability for FBS late-type giant stars, the basic data coming from the three most prominent and wide-area sky surveys were used and considered: the Catalina Sky Survey (CSS, second public data release CSDR2, accessed via `http://nesssi.cacr.caltech.edu/DataRelease/`, the All-Sky Automated Survey for Supernovae (ASAS-SN, accessed via `https://asas-sn.osu.edu/variables/` (Jayasinghe et al., 2018, Kochanek et al., 2017, Shappee et al., 2014)) and Transiting Exoplanet Survey Satellite (TESS).

3.1. Catalina Sky Survey

The CSS comprises two main parts surveying the Northern (Drake et al., 2014) and the Southern (Drake et al., 2017) sky, respectively. Both surveys were analyzed by the Catalina Real-Time Transient Survey (CRTS) in search for optical transient (V < 21.5 mag) phenomena. CSS was used as the primary source for attributing variability types, periods, and amplitudes to the FBS giant carbon stars. The light curve analysis confirms nine stars as Mira-type variables, 43 as Semi-Regulars (SR) with very well expressed periodicity,

doi: https://doi.org/10.52526/25792776-23.70.1-54

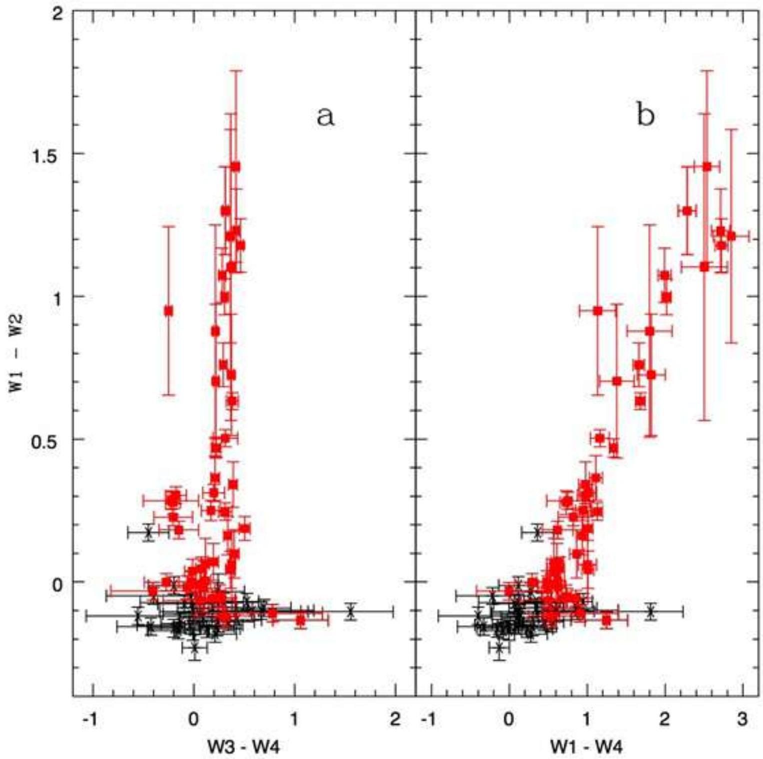

Figure 2. WISE W1-W2 vs. W3-W4 and WISE W1-W2 vs. W1-W4 color-color plots (with error bars) for all C stars. Crosses are early type stars, filled squares are late N-type AGB stars.

and two objects as Irregular (Irr)-type variables. The variability types of 27 stars are presented for the first time.

3.2. ASAS-SN

The ASAS-SN project is an all-sky optical monitoring to a photometric depth V $\leq$ 17 mag providing also variability classification. As a consequence, ASAS-SN was used as the primary source for attributing variability types, periods, and amplitudes to the FBS M giants. For the few objects missing in the ASAS-SN data base, variability parameters were determined from CSDR2 light curves using the VStar-data visualization and analysis tool (Benn, 2012). Our final sample consists of 690 Semi-Regular (SR)-type, 299 L-type and 111 Mira-type variables. The period of a Mira increases with increasing luminosity, and hence depends on its mass and its evolutionary status along the AGB. Thus, longer period Miras tend to correspond to higher masses (see Figure 6 in Hughes & Wood (1990)). Periods for the 111 FBS M-type Miras have been taken from the ASAS-SN data base. All these periods were checked by visual inspection of the light curves and corrected in some cases. The periods are between 250 and 300 days with hardly any Miras showing periods above 400 days. This suggests that the FBS Mira sample mainly consists of low mass AGB stars with a typical mass around 1 M_{Sun}.

3.3. TESS

NASA's Transiting Exoplanet Survey Satellite (TESS) is an all-sky space-based mission designed to search for planets transiting around nearby M dwarfs (Ricker et al., 2014). Its observed ∼73% of the sky across 26 sectors, each lasting 27.4 days and covering a $24° \times 96°$ field of view. TESS observed a number of stars at 2-mn cadence and collected full frame images (FFIs) every 30 minutes, covering the entire mission phase. By the end of 2 two-year primary mission, TESS identified 2241 exoplanet candidates (Guerrero et al., 2021), known as TESS Objects of Interest (TOIs).

For the M-type giants that do not have light curves in ASAS-SN, TESS light curves are analyzed. 32 red giants have light curves. Three stars have no data in the catalogs of variable stars. There is a light curve only for FBS 1752+666 of these three stars in CSS. Figure 4 and figure 5 present light curves of CSS and

doi: https://doi.org/10.52526/25792776-23.70.1-54

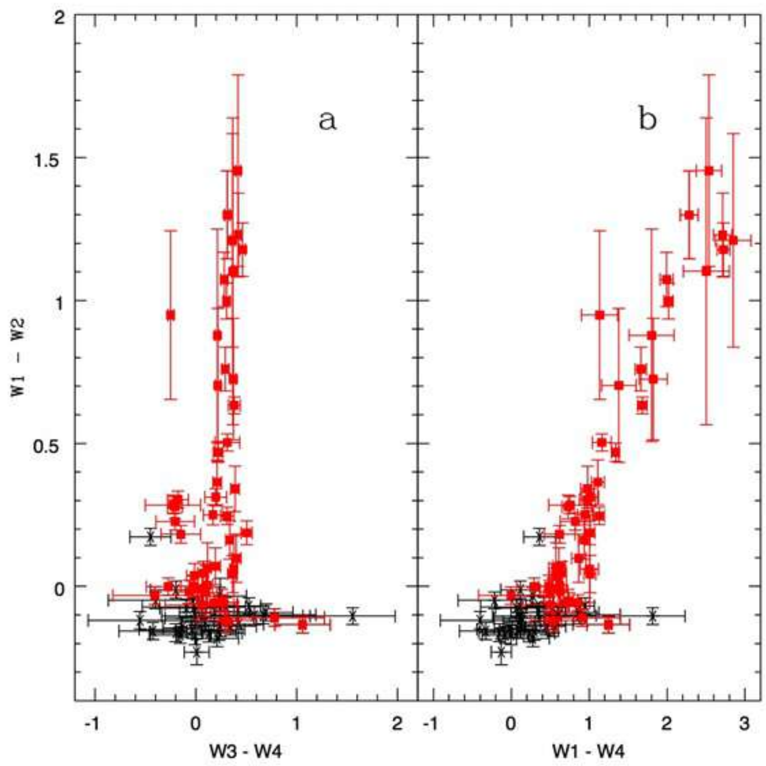

Figure 3. WISE W1-W2 vs. W3-W4 and WISE W1-W2 vs. W1-W4 color-color plots (with error bars) for all C stars. Crosses are early type stars, filled squares are late N-type AGB stars.

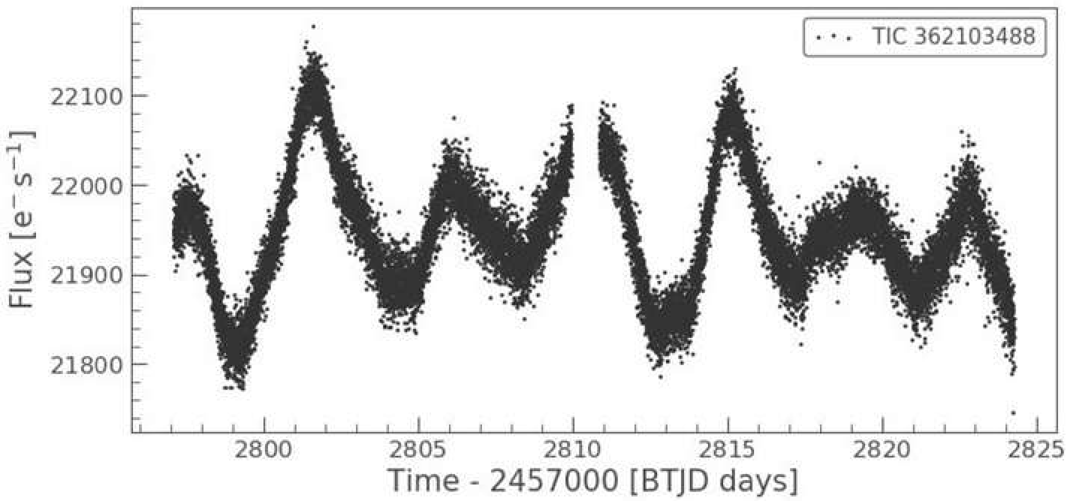

Figure 4. Light curve of CSS for FBS 1752+666.

doi: https://doi.org/10.52526/25792776-23.70.1-54

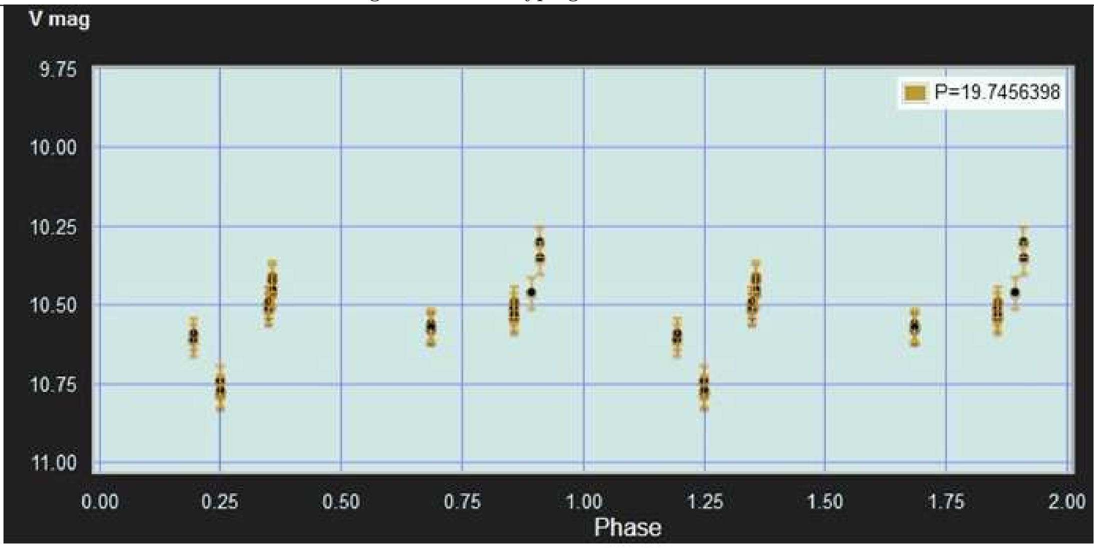

Figure 5. Light curve of TESS for FBS 1752+666 .

TESS of FBS 1752+666. The light curve analysis confirms that this object is Semi-Regular (SR) variable with very well expressed periodicity. The variability type FBS 1752+666 is presented for the first time. The amplitude of variability is 0.4^m, the period is 19.74 days. The lightkurve package based on Python was used to analyze the TESS light curve (Barentsen et al., 2019).

4. Discussion and conclusion

For study the red giants identified in the First Byurakan Survey (FBS) low-resolution spectroscopic database, Gaia EDR3 high-accuracy astrometric and photometric data were used. These objects are relatively bright, so that G - band brightnesses were in the range $9.4 < G < 18.2$ mag.

Variability study is one aspect of our programs aimed to investigate FBS red giants. We have examined optical variability using the three most prominent wide-area sky surveys, the CSS, ASAS-SN and TESS, to clarify their variability nature.120 objects are Mira-type variables, 734 are SR, and 301 are Irr-type variables. The light curve analysis confirms FBS 1752+666 as Semi-Regular (SR) with very well expressed periodicity. The variability type FBS 1752+666 is presented for the first time. The amplitude of variability is 0.4^m, the period is 19.74 days.

References

Bailer-Jones C. A. L., Rybizki J., Fouesneau M., Demleitner M., Andrae R., 2021, Astron. J. , 161, 147

Barentsen G., et al., 2019, KeplerGO/lightkurve: Lightkurve v1.6.0, Zenodo, doi:10.5281/zenodo.3579358

Benn D., 2012, Journal of the American Association of Variable Star Observers (JAAVSO), 40, 852

Bessell M. S., 1991, Astron. J. , 101, 662

Bessell M. S., Brett J. M., 1988, Publ. Astron. Soc. Pac. , 100, 1134

Drake A. J., et al., 2014, Astrophys. J. Suppl. Ser. , 213, 9

Drake A. J., et al., 2017, Mon. Not. R. Astron. Soc. , 469, 3688

Gaia Collaboration et al., 2021, Astron. Astrophys. , 650, C3

Gigoyan K. S., Mickaelian A. M., Kostandyan G. R., 2019, Mon. Not. R. Astron. Soc. , 489, 2030

Guerrero N. M., et al., 2021, Astrophys. J. Suppl. Ser. , 254, 39

Hughes S. M. G., Wood P. R., 1990, Astron. J. , 99, 784

Jayasinghe T., et al., 2018, Mon. Not. R. Astron. Soc. , 477, 3145

Kochanek C. S., et al., 2017, Publ. Astron. Soc. Pac. , 129, 104502

Markarian B. E., 1967, Astrofizika, 3, 55

doi: https://doi.org/10.52526/25792776-23.70.1-54

Mickaelian A. M., 2008, Astron. J. , 136, 946

Mickaelian A. M., et al., 2007, Astron. Astrophys. , 464, 1177

Ricker G. R., et al., 2014, in Oschmann Jacobus M. J., Clampin M., Fazio G. G., MacEwen H. A., eds, Society of Photo-Optical Instrumentation Engineers (SPIE) Conference Series Vol. 9143, Space Telescopes and Instrumentation 2014: Optical, Infrared, and Millimeter Wave. p. 914320 (arXiv:1406.0151), doi:10.1117/12.2063489

Shappee B. J., Prieto J. L., Grupe D., Kochanek C. S., Stanek K. Z.and Walker Z., Yoon Y., 2014, Astrophys. J. , 788, 48

Stassun K. G., et al., 2019, Astron. J. , 158, 138

doi: https://doi.org/10.52526/25792776-23.70.1-54

Communications of BAO, Vol. 70, Issue 1, 2023, pp. 60-67

TYC 1417-891-1 and TYC 1478-742-1: Eclipsing variable stars. The Gaia EDR3 and TESS photometric data.

K. K. Gigoyan [*], K. S. Gigoyan [†] and G.R. Kostandyan [‡]

INAS RA V. Ambartsumian Byurakan Astrophysical Observatory (BAO), Byurakan 0213, Aragatzotn Province, Armenia

Abstract

Based on the TESS (Transiting Exoplanet Survey Satellite) phase dependent light curves, we confirm the eclipsing type variability nature for two G – type dwarfs: TYC 1417-891-1 and TYC 1478-742-1. Both objects show EA (Algol – type) light curves morphology. Orbital period for TYC 1417-891-1 is P $\approx$ 8.0 day and for TYC 1478-742-1, P $\approx$ 13.6 day. We present Gaia EDR3 and TESS catalogue important physical parameters as well as LAMOST spectra. Both objects are relatively bright and are located at a distance of 260.59 ($\pm$3.21) pc (TYC 1417-891-1) and 117.42 ($\pm$0.74) pc (TYC 1478-742-1). The TESS light curve of TYC 1478-742-1 show also flares as well. We discuss possible nature of the secondary and faint objects around these stars.

Keywords: *variables, eclipsing variables: TESS and Gaia data.*

1. Introduction

Variable stars are an important and dynamic area of modern astronomical research. Brightness variability is seen for most stars. Variability provides extra observational information (periods, amplitudes, etc.) which can be used to determine physical parameters such as a mass, radius, luminosity, and rotation rates. These parameters can be used to deduce some characteristics of the stars. The study of variability allows us to directly observe changes in the stars: both the rapid and sometimes violent changes associated especially with stellar birth and death, and also changes associated with most stellar evolution. Variable stars are classified as several broad classes: pulsating, eclipsing, rotating, eruptive, cataclysmic, and many other. Each class of variable stars is divided into several subclasses. More detail, the improved system of variability classification is presented by authors of the "General Catalogue of Variable Stars"(GCVS) (accessed via https://www.sai.msu.su/gcvs/gcvs/vartype.htm for details; Samus' et al., 2017). Historically, there are three basic classes of eclipsing variables, based solely on the overall light curve shape, EA (Algol), EB (Beta Lyrae), and EW (W Ursae Majoris) - types. An overview of variable stars, in general, the techniques for discovering and studying variable stars, and description of the main types of variable stars are presented also in the book of Percy (2007) and in papers by Drake et al. (2014, 2017). Correct class determination of the variables can be very important for studies of stellar populations. Some types of variable stars, such as RR Lyrae stars and Cepheids, are excellent tools to study our Galaxy. Long period variables (LPV, $\triangle$V $\geq$ 2.5 mag., or Miras), which are Asymptotic Giant Branch (AGB) stars, are also very important distance indicators (Whitelock et al., 2008).

The number of discovered variable stars increases dramatically, particularly in the last two decades. Catalogs of about 47 055 periodic variables in Northern and 37 745 in Southern hemisphere were published by Drake et al. (2014, 2017), based on the Catalina Sky Survey (CSS). Data for near 116000 variables were presented by Christy et al. (2023), based on All – Sky Automated Survey for Supernovae (ASAS – SN) observations. A new catalogue of 6330 eclipsing variables was presented by Malkov et al. (2006). A new version of the catalogue of eclipsing variables is presented by Avvakumova et al. (2013). This catalogue contains parameters and morphological types of light curves for some 7200 stars. Eclipsing binaries, from the surveys ASAS, NSVS, and LINEAR are analyzed by Lee (2015). An updated catalog of 4680 northern

[*] karengigoyan@bao.sci.am, Corresponding author
[†] kgigoyan@bao.sci.am
[‡] kostandyan@bao.sci.am

doi: https://doi.org/10.52526/25792776-23.70.1-60

Table 1. TESS observations of two stars from she MAST

Star	TESS Target Name	Data of Observations	Exposure length (sec)
TYC 1417-891-1	88063457	2021-11-07	120
TYC 1417-891-1	88063457	2022-01-24	120
TYC 1478-742-1	462578519	2022-04-23	120

eclipsing binaries with Algol – type light curve morphology was presented by Papageorgiou et al. (2018). Data for near 220000 variables have been identified in the ASAS-SN survey (Jayasinghe et al., 2020). Recently, more than 40000 eclipsing binary candidates identified by the ASAS – SN, were also presented by Rowan et al. (2022). These new results, undoubtedly, are very important for the further versions of the GCVS (Samus' et al., 2017).

TESS (Transiting Exoplanet Survey Satellite, Ricker et al., 2014) is an all – sky space based mission designed to search for planets transiting around nearby dwarfs. Phase dependent light curves for all FBS M dwarfs (Gigoyan et al., 2023) were analyzed using the Presearch of Data Conditioning Simple Aperture Photometry (PDCSAP) at the Mikulski Archive for Space Telescopes (MAST, access via https://mast.stsci.edu/portal/Mashup/Clients/Mast/Portal.html/). During the analysis of the TESS data, our attention was drawn there on phased light curves of Target Numbers 88063457 and 462578519. These two objects were associated in SIMBAD (http://simbad.u-strasbg.fr) astronomical data base with the proper motion stars TYC 1417-891-1 ((RA = $09^h51^m39.93^s$, DEC = $20°12'23.8''$) and TYC 1478-742-1 (RA = $14^h48^m28.91^s$, DEC = $+15°05'12.3''$), coordinates are for Equinox J2000.0) without information on spectral types and variability. We classified these two objects as EA (Algol – type) eclipsing binaries and analyzed their TESS phase dependent light curves. The purpose of this paper is to present most important physical parameters from the Gaia EDR3 and TESS catalogues. We also discuss possible nature of the secondary and faint objects around these eclipsing variables. This paper is structured as follows. In Section 2 of this paper, we present the TESS light curves for TYC 1417-891-1 and TYC 1478-742-1. Section 3 presents LAMOST moderate-resolution spectra for these two objects. Photometric data, cross-correlations with Gaia EDR3 and TESS catalogues and important physical parameters are considered in Section 4. Finally, in Section 5, we discuss the results obtained for these two stars, and we provide the concluding remarks.

2. TESS light curves

The Transiting Exoplanet Survey Satellite (TESS, Ricker et al., 2014) is an ongoing NASAs Astrophysics Explorer Mission designed to detect exoplanets around the nearest M dwarfs, ideal to follow – up observations for further characterization. TESS was launched on 2018 April 18, and the TESS Prime Mission (PM) ran from 2018 July 25 to 2020 July 4. During its 2 years PM, TESS observed $\sim 73\%$ of the sky across 26 observing "Sectors", resulting in observing times ranging from ~ 1 month near the ecliptic to ~ 1 year near the poles. It monitored bright stars with a 2 minutes short cadence and provided full-frame images every 30 minutes. The wide red bandpass of the TESS cameras (600-1000 nm) makes TESS capable of detecting Earth and super – Earth – sized exoplanets ($R \leq 1.75 R_{\odot}$) transiting M dwarfs. TESS observed TYC 1417-891-1 twice: during its second year of operation in its high – cadence, two minutes cadence mode in Sector 45 (2021 June, and December), and also in Sector 46 (2021 March, and 2022 January). TESS observed TYC 1478-742-1 in 23 April 2022, in Sector 51, as well in two – minute cadence mode. Table 1 presents TESS observational data for TYC 1417-891-1 and TYC 1478-742-1 from the MAST.

We downloaded the PDCSAP light curves for these stars from the MAST using the lightkurve package (Barentsen et al., 2019).

Figure 1 and 2 shows TESS SAP (Simple Aperture Photometry) original light curves of TYC 1417-891-1 and of TYC 1478-742-1 from Sectors 46 and 51.

Both objects (Fig. 1 and 2) show TESS light curves with almost flat maxima. We classify both objects as EA (Algol – type) eclipsing variables. For TYC 1417-891-1 both minimum (primary and secondary) are very well expressed on TESS phase dependent light curves. For TYC 1478-742-1 there is a gap in the TESS data when the primary eclipse would be appeared. The TESS light curve of this object also shows flares. We used Box Least Squares (BLS; Kovács et al., 2002) periodogram analysis method to estimate the orbital periods. We determined the orbital period P ≈ 8 day for TYC 1417-891-1 and near P ≈ 13.6

doi: https://doi.org/10.52526/25792776-23.70.1-60

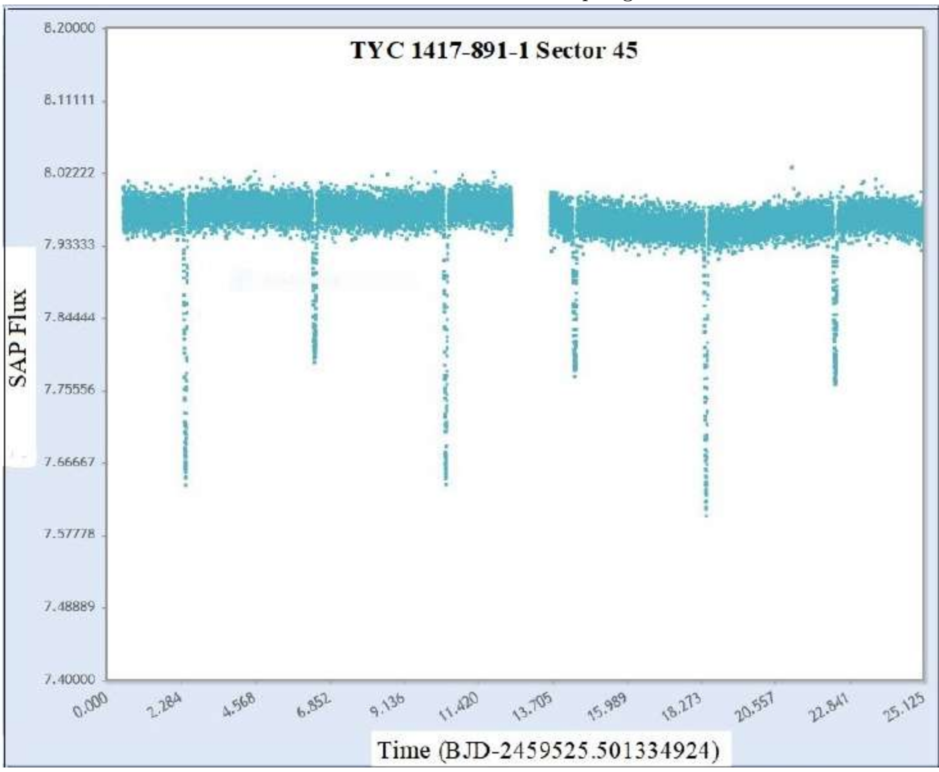

Figure 1. The TESS SAP original flux time series photometry of TYC 1417-891-1 from Sector 46. The X-axis show the time in Barycentric Julian Days (BJD) and Y-axis shows the normalized TESS SAP flux.

Table 2. LAMOST Data for Two Stars

Star	LAMOST Designation	Obs. Identifier	Data of Obs	Subclass
TYC 1417-891-1	J095139.94+201223.3	286412016	2014-12-26	G5V
TYC 1478-742-1	J144828.92+150512.2	350111159	2015-05-26	G8V

days for TYC 1478-742-1. Important note, both objects have monitored photometric data in Catalina Sky Survey (Drake et al. (2014, 2017) data base, see also http://nesssi.cacr.caltech.edu/DataRelease/). Their CSS identifiers are consequently CSS J095139.9+201222 and CSS J144828.9+150511. The CSS light curves do not present the primary and secondary eclipses for both objects as well, such as TESS light curves. Only the CSS phase dependent light curve for TYC 1478-742-1 shows flare with amplitude $\Delta m_v \approx 0.75$mag. We want to note also, that photometric data for TYC 1417-891-1 is available in AAVSO VSX database (https://www.aavso.org/vsx/), with name VSSP J095139.94+ 201223.2, Period = 8.00405 days, Mag. range = 11.325($\pm$0.08) in V-band, spectral type G6, and variability type EA+UV (UV – eruptive variables of the UV Ceti types). There are no data for the second object TYC 1478-742-1 in AAVSO VSX data base.

3. LAMOST spectra

Moderate – resolution CCD spectra for TYC 1417-891-1 and TYC 1478-742-1 were secured by LAMOST (Large Sky Area Multi-Object Fiber Spectroscopic Telescope) observations (Cui et al. (2012), spectrum is available online at http://dr7.lamost.org./search/). In Table 2, we provide information on LAMOST spectral observations.

Figure 3 present the LAMOST moderate-resolution spectra for TYC 1417-891-1 and TYC 1478-742-1.

4. Photometric Data. Physical Parameters.

4.1. Gaia EDR3 Data

Gaia EDR3 (Gaia Collaboration et al., 2021) provides high-precision astrometry, three-band photometry, radial velocities, effective temperatures, and information on numerous astrophysical parameters for

doi: https://doi.org/10.52526/25792776-23.70.1-60

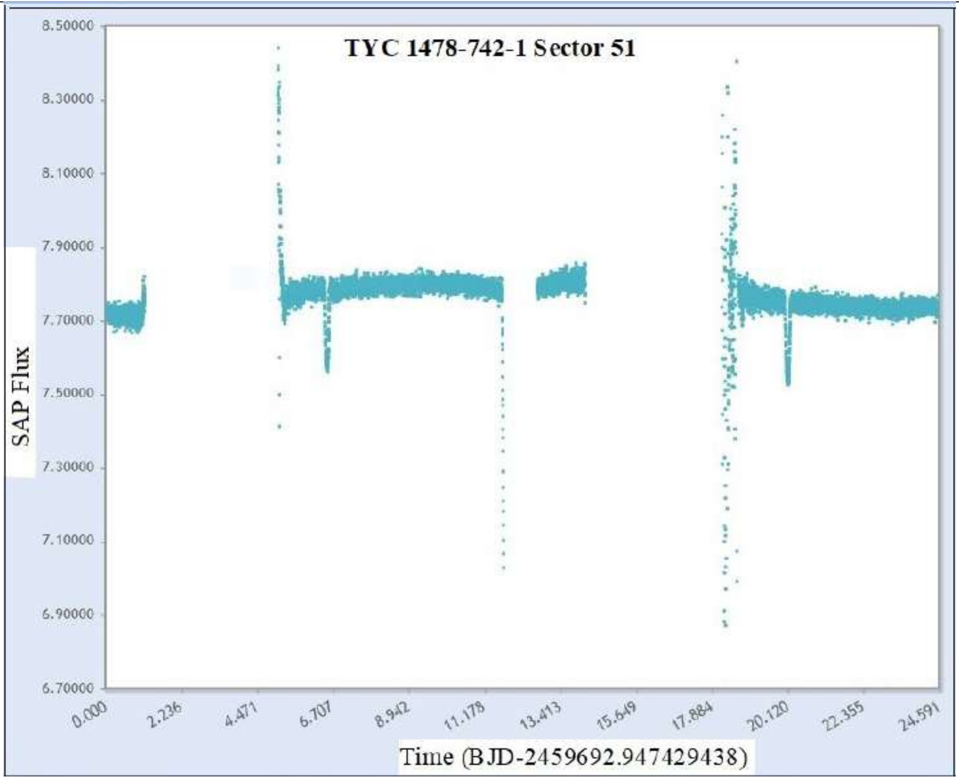

Figure 2. The TESS SAP original flux time series photometry of TYC 1478-742-1 from Sector 51. The X and Y axis description is the same, as in Figure 1.

Table 3. LAMOST Data for Two Stars

Star	Gaia EDR3 Name	G-mag	BP mag	BP-RP mag.	R(pc)
TYC 1417-891-1A	627614504288922112	11.089	11.448	0.885	261.97
B	627614504288958464	17.292	18.707	2.658	275.67
TYC 1478-742-1A	1186217744648523008	11.265	11.738	1.117	124.17
B	1186217740354601600	17.648	17.837	0.967	1943.05

approximately 1.8 billion sources brighter than G = 21.0 magnitude. Gaia EDR3 database gives data for two objects in 10 arcsec. search radius around positions of TYC 1417-891-1 and TYC 1478-742-1. We used the distance information for both objects derived from Gaia EDR3 by Bailer-Jones et al. (2021) . In Table 3 we give some important Gaia EDR3 data for TYC 1478-742-1 and for TYC 1417-891-1 in 10 arcsec. search radius (A - for the bright, primary source and B-for the secondary faint source).

4.2. TESS Photometric Data

NASAs TESS is an all–sky space–based mission designed to search for planets transiting around nearby dwarfs (Ricker et al., 2014). TESS completed its PM July 2020 and now it is in its extended mission. We have cross–matched these two dwarfs with the TESS Input Catalog, Version 8.2 (TIC V8.2; Paegert et al., 2021), giving the important physical parameters for stars, parallaxes, proper motions, TESS T- magnitudes, temperatures, masses, and luminosities in solar units Stassun et al. (2018). This catalogue also gives data for two objects in 10 arcsec. search radius around positions of TYC 1417-891-1 and TYC 1478-742-1. Table

Table 4. TIC v8.2 Catalog Data for TYC 1478-742-1 and for TYC 1417-891-1

Star	TIC Number	2MASS J-H color	2MASS H-K color	Rad (R_{Sun})	Mass (M_{Sun})	Lum (L_{Sun})	T_{Eff} (K)	Dist (pc)
TYC 1417-891-1A	88063457	0.351	0.056	1.443(±0.405)	1.010(±0.126)	1.949(±0.018)	5678	261.20(±3.21)
B	88063458	0.644	0.291	0.405(±0.017)	0.397(±0.025)	0.018(±0.005)	3348	271.16(±9.81)
TYC 1478-742-1A	462578519	0.454	0.111	0.727(±0.037)	0.884(±0.107)	0.348(±0.009)	5200	117.42(±0.749)
B	1100510113							1981.76(±446.77)

doi: https://doi.org/10.52526/25792776-23.70.1-60

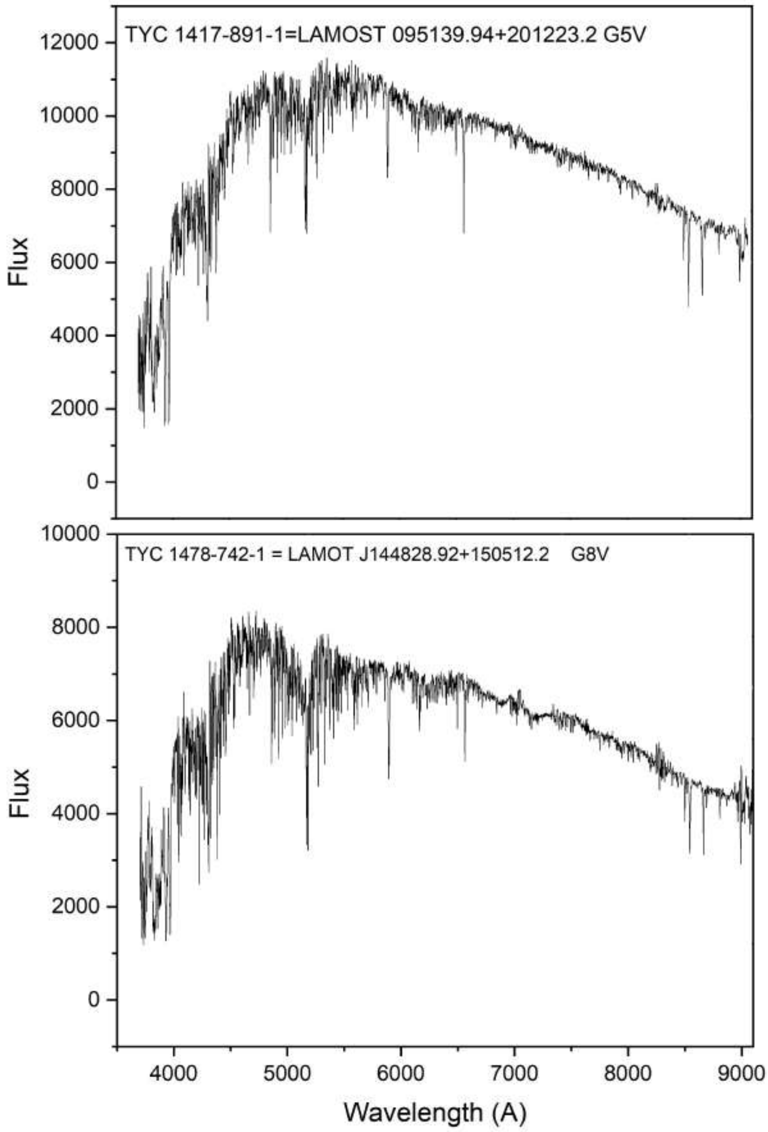

Figure 3. LAMOST moderate-resolution CCD spectra for TYC 1417-891-1 and TYC 1478-742-1 in the range 3900-9100 Å.

4 includes other very important physical parameters from the TIC, V8.2 Paegert et al. (2021). The bright and faint components are noted as A and B, as in Table 1.

5. Discussion and conclusions. Further works.

EA (Algol-type) eclipsing variables are binaries (semi-detached systems) with spherical or slightly ellipsoidal components. Various sub-classes of semi-detached systems can be separated (for example hot and cool Algol-types). For cool semi–detached systems the component is of types G and later (see paper by Malkov et al. (2006) for more detail). With the help of standard image visualization and analysis is software SAOImage ds9, we search STScI Digitized Sky Survey POSS2 and POSS1 images (online at https://archive.stsci.edu/cgi-bin/dss_form/) around position of each object. Obviously, the DSS2 I (infrared) and B (blue) direct images of this two primary and bright objects A are elongated. Figure 4 presents DSS2 I finder chart for TYC 1417-891-1 (the primary bright star is circled as A, and the secondary faint object as B, as it is presented in Table 3 and 4 for this objects). Such images are very characteristic for numerous of nearby dwarf binary systems (particularly such as GJ 2069, which is also eclipsing binary, see more detail López-Morales & Clemens (2004). The Gaia EDR3 catalog gives proper motion (pm) value = 22.920 mas/yr for second faint object B. The TIC V8.2 (Paegert et al., 2021) catalogue distances are consequently r = 261.201 (± 3.218) pc and r = 271.164 (±9.812) pc for TYC 1417-891-1 A and B components (Table 4). If these objects (circled as A and B in Figure 4 are gravitation- ally bound, i. e. they are physical

doi: https://doi.org/10.52526/25792776-23.70.1-60

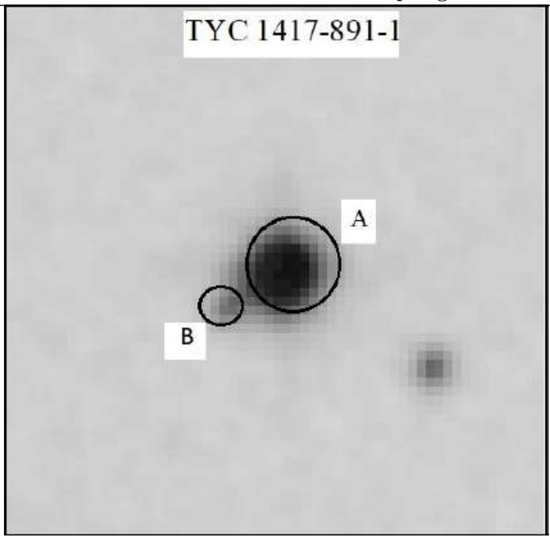

Figure 4. POSS2 I finder chart for TYC 1417-891-1 (A for bright and B for faint and very close object) taken in 1996. Obviously, the bright star A is elongated. Field is $\sim$ 1.5 arcmin. x 1.5 arcmin.

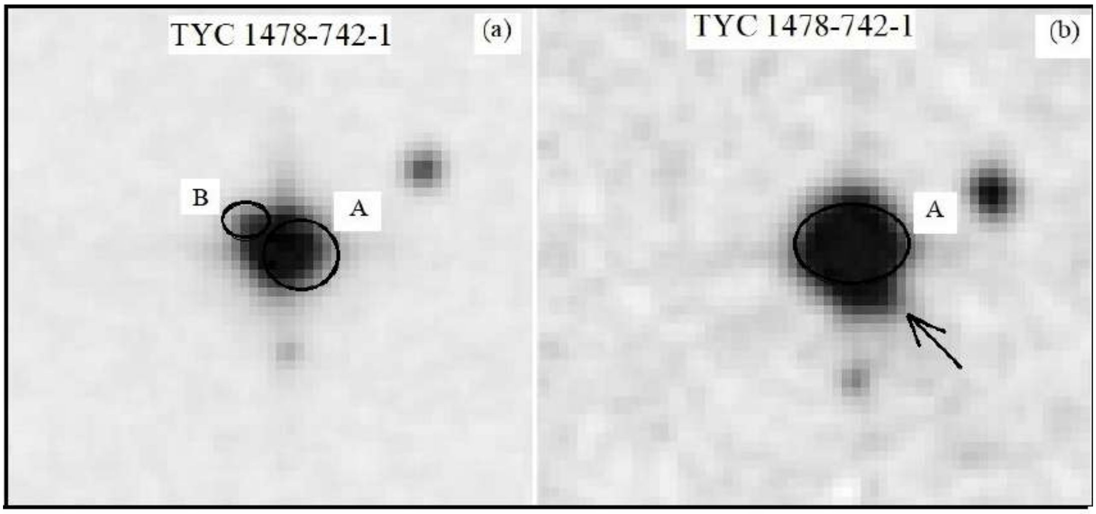

Figure 5. Figure 5(a) POSS2 blue image of TYC 1478-742-1 taken in 1996. Circled (B) is the very close and faint object existing in Gaia EDR3 and TESS catalogues. Figure 5 (b) is the POSS1 B image of the same object. Arrow indicate the very faint object in south-east direction. For this object there are no data in Gaia EDR3 and TESS catalogues. Field is 2 arcmin $\times$ 2 arcmin.

companions at the same distances, therefore their G-band absolute magnitudes can be obtained M(G) = +6.0 for bright A star and M(G) = +10.20 for faint object B. Such parameters for faint object (M(G) = +10.20, BP-RP = 2.658 mag., T_{eff} = 3348 K) placed it in red dwarfs sequence on Hertzsprung-Russeill Diagram (HRD, see Fig. 5 by Babusiaux et al. (2018) and is typical for M4-M5 subtype dwarfs (Cifuentes et al., 2020). As a supplement, 2MASS (Skrutskie et al., 2006) J-H = 0.644 and H-K = 0.291 Near-Infrared (NIR) colors for this object (Table 4) also indicate the belonging to the group of dwarf M stars (see NIR JHK colors of M dwarfs in papers by Bessell (1991), Bessell & Brett (1988)). Most probably, TYC 1417-891-1 is a triple system, with two very close and bright stars, having practically equal magnitudes, and third component as M dwarf.

The primary and bright object A for the second object TYC 1478-742-1 is also elongated on POSS2 I and B finder charts. Gaia EDR3 and TESS data bases gives very different distance values for bright A and for faint B sources ($r \approx$ 1980 pc for faint object B). In figure 5 (a) and (b) we present POSS2 B (a)(for Equinox J2000) and POSS1 B (b)(for Equinox B1950) direct images for object TYC 1478-742-1. Meanwhile, Gaia EDR3and TESS catalogs show proper motion for object B (the Gaia EDR3 catalogue data is 22.92 mas/yr for proper motion). On DSS1 B (equinox B1950) chart we see very faint object, which we indicate by arrow (Figure 5 (b)). This object is not visible on DSS2 B and I chart (Figure 5(a)). We note, that the

doi: https://doi.org/10.52526/25792776-23.70.1-60

scaling factor of DSS2 is 1.6 time better than DSS1. This point needs to study more detail in the future. For this faint object there are no 2MASS JHK photometric data and Gaia EDR3 BP-RP = 0.967 mag. The TESS light curve shows flares.

High-spatial-resolution CCD imaging and speckle interferometry in the future allow us to study the nature of the companions around these objects in more detail. Our conclusions can be summarized as follows:

(a) Based on TESS phase dependence light curves, we confirm EA-type eclipsing variability nature for objects TYC 1417-891-1 and TYC 1478-742-1 consequently with orbital period $P \approx 8.0$ day and $P \approx 13.6$ day. EA-variability type for TYC 1478-742-1 we present for the first time.

(b) Using Gaia EDR3 and TESS data bases, we present some very important physical characteristics for two objects, such as, mass, radius, luminosities, effective temperatures, etc. They are spectral subtypes G5V (TYC 1417-891-1) and G8V (TYC 1478-742-1) and consequently at a distances 261 pc and 124 pc.

(c) Most probably TYC 1417-891-1 present a triple system having two bright and very close companions, and third very faint companion as M dwarf.

Acknowledgements

This work is supported by ERASMUS+2019-1FRO-KA 107-061818. KKG and KSG are grateful to Administration of OVSQ Observatory an LATMOS Laboratory (France) for organizing their visit to LATMOS Laboratory during June and July 2022. This research has made use of the VizieR catalogue access tool, CDS, Strasbourg, France., and Two Micron All-Sky Survey, which is a joint project of the University of Massachusetts and the Infrared Processing and Analysis Center, funded by NASA and NSF. We used LAMOST telescope spectra. The LAMOST is a National Major Scientific project build by the Chinee Academy of Sciences. This work has made use of data from European Space Agency (ESA) mission Gaia(https://cosmos.esa.int/gaia/). This paper includes data collected by the TESS mission, which are publicly available from the Mikulski Archive for Space Telescopes (MAST).

We thank Prof. Michelle Kunimoto and Oleg Malkov for helpful comments and suggestions. Authors thank also our anonymous Referee for valuable suggestions and contributions.

References

Avvakumova E. A., Malkov O. Y., Kniazev A. Y., 2013, Astronomische Nachrichten, 334, 860

Babusiaux C., van Leeuwen F., Barstow M. A., Jordi C., Zucker S., Zurbach C., Zwitter T., 2018, Astron. Astrophys. , 616, A10

Bailer-Jones C. A. L., Rybizki J., Fouesneau M., Demleitner M., Andrae R., 2021, Astron. J. , 161, 147

Barentsen G., et al., 2019, KeplerGO/lightkurve: Lightkurve v1.6.0, Zenodo, doi:10.5281/zenodo.3579358

Bessell M. S., 1991, Astron. J. , 101, 662

Bessell M. S., Brett J. M., 1988, Publ. Astron. Soc. Pac. , 100, 1134

Christy C. T., et al., 2023, Mon. Not. R. Astron. Soc. , 519, 5271

Cifuentes C., et al., 2020, Astron. Astrophys. , 642, A115

Cui X.-Q., et al., 2012, Research in Astronomy and Astrophysics, 12, 1197

Drake A. J., et al., 2014, Astrophys. J. Suppl. Ser. , 213, 9

Drake A. J., et al., 2017, Mon. Not. R. Astron. Soc. , 469, 3688

Gaia Collaboration et al., 2021, Astron. Astrophys. , 650, C3

Gigoyan K. S., Sarkissian A., Kostandyan G. R., Gigoyan K. K., Meftah M., Bekki S., Azatyan N., Zamkotsian F., 2023, pasa, 40, e023

Jayasinghe T., et al., 2020, Mon. Not. R. Astron. Soc. , 491, 13

Kovács G., Zucker S., Mazeh T., 2002, Astron. Astrophys. , 391, 369

Lee C.-H., 2015, Mon. Not. R. Astron. Soc. , 453, 3474

López-Morales M., Clemens J. C., 2004, Publ. Astron. Soc. Pac. , 116, 22

Malkov O. Y., Oblak E., Snegireva E. A., Torra J., 2006, Astron. Astrophys. , 446, 785

Paegert M., Stassun K. G., Collins K. A., Pepper J., Torres G., Jenkins J., Twicken J. D., Latham D. W., 2021, arXiv e-prints, p. arXiv:2108.04778

Papageorgiou A., Catelan M., Christopoulou P.-E., Drake A. J., Djorgovski S. G., 2018, Astrophys. J. Suppl. Ser. , 238, 4

Percy J. R., 2007, Understanding Variable Stars

doi: https://doi.org/10.52526/25792776-23.70.1-60

Ricker G. R., et al., 2014, in Oschmann Jacobus M. J., Clampin M., Fazio G. G., MacEwen H. A., eds, Society of Photo-Optical Instrumentation Engineers (SPIE) Conference Series Vol. 9143, Space Telescopes and Instrumentation 2014: Optical, Infrared, and Millimeter Wave. p. 914320 (arXiv:1406.0151), doi:10.1117/12.2063489

Rowan D. M., et al., 2022, Mon. Not. R. Astron. Soc. , 517, 2190

Samus' N. N., Kazarovets E. V., Durlevich O. V., Kireeva N. N., Pastukhova E. N., 2017, Astronomy Reports, 61, 80

Skrutskie M. F., et al., 2006, Astron. J. , 131, 1163

Stassun K. G., et al., 2018, Astron. J. , 156, 102

Whitelock P. A., Feast M. W., Van Leeuwen F., 2008, Mon. Not. R. Astron. Soc. , 386, 313

doi: https://doi.org/10.52526/25792776-23.70.1-60

Communications of BAO, Vol. 70, Issue 1, 2023, pp. 68-76

Multiwavelength search and studies of active galaxies

A.M. Mickaelian[*], H.V. Abrahamyan[†], G.M. Paronyan[‡], G.A. Mikayelyan[§], R.R. Andreasyan[¶], A.G. Sukiasyan[‖], L.A. Hambardzumyan[**], and V.K. Mkrtchyan[††]

NAS RA V. Ambartsumian Byurakan Astrophysical Observatory (BAO)

Abstract

We review the field of active galaxies (both AGN and Starbursts) focusing on their multiwavelength search and studies at the Byurakan Astrophysical Observatory (BAO). Many famous historical surveys carried out in Byurakan are known and many more are active and ongoing. We give examples of studies in optical wavelengths, IR, radio and X-ray, as well as multiwavelength studies. The studies are characterized by multiwavelength approach to statistical analysis of large amount of data obtained in different wavelengths. Results on HRC/BHRC sample objects (optical identifications of ROSAT X-ray sources), studies of Markarian galaxies in UV and multiwavelength SEDs, abundance and star formation determinations in Mrk galaxies from SDSS spectra, revised optical classification of "LINERs", study and classification of SDSS spectra for Byurakan-IRAS Galaxies, summary of observations and study of Byurakan-IRAS Galaxies (BIG objects), discovery of new bright ULIRGs from the IRAS PSC/FSC Combined Catalogue and their spectral classification, radio variable sources at 1400 MHz and their optical variability, classification of BZCAT objects having uncertain types (BZU objects), and optical variability of blazars are presented. At the end, we briefly present our new fine classification of active galaxies based on all our previous studies.

Keywords: *Active Galaxies – Active Galactic Nuclei – QSO – Blazar – Seyfert galaxy – LINER – Starburst galaxy – Markarian galaxies*

Introduction

The Byurakan Astrophysical Observatory (BAO) was always active in surveys, especially extragalactic ones. Here is the list of the most important surveys carried out by BAO astronomers (Table 1).

Table 1. Most important extragalactic surveys by BAO astronomers.

Years	Authors	Survey	Short	Type of objects	Number of objects
1965-1980	B. Markarian, V. Lipovetsky, J. Stepanian	First Byurakan Survey (Markarian Survey)	FBS	UV-excess galaxies	1544
1973-1979	R. Shahbazian	Shahbazian Survey	Shkh	Compact groups of compact galaxies	377
1976	M. Arakelian	Arakelian Survey	Akn	High surface brightness galaxies	621
1978-1991	B. Markarian, J. Stepanian, L. Erastova, V. Chavushyan	Second Byurakan Survey	SBS	UVX and Emission-line galaxies, QSOs	3600
1979-2005	M. Kazarian et al.	Kazarian Survey	Kaz	UV-excess galaxies	706
1987-1996	H. Abrahamian, A. Mickaelian	First Byurakan Survey, 2nd Part	FBS BSOs	QSOs and Seyferts	1103
1995-2004	A. Mickaelian et al.	Byurakan-IRAS Galaxies	BIG	IRAS galaxies	1278
2002-2006	A. Mickaelian et al.	Byurakan-Hamburg-ROSAT Catalogue	BHRC	ROSAT sources	4253
2018	H. Abrahamyan, A. Mickaelian et al.	Variable radio sources at 1400 MHz	NVSS/FIRST	Variable radio sources	6301

The importance of active galaxies is rather high as they play crucial role in many aspects, such as:

- Formation and evolution of galaxies
- Morphology

[*]aregmick@yahoo.com, Corresponding author
[†]abrahamyanhayk@gmail.com
[‡]paronyan_gurgen@yahoo.com
[§]gormick@mail.ru
[¶]randreasyan@gmail.com
[‖]andranik.suqiasyan.1995@mail.ru
[**]hambardzumyanlian@gmail.com
[††]varduhi.mkrtchyan.99@bk.ru

doi: https://doi.org/10.52526/25792776-23.70.1-68

- Interacting and merging galaxies
- Star formation in galaxies
- The luminosity function of galaxies
- Radiation mechanisms
- Multiwavelength activity
- The presence of relativistic jets
- The theory of supermassive black holes
- Energy sources
- Cosmological role of Active Galaxies

The recent results on active galaxies are related to their multiwavelength studies using large amount of data from X-ray, UV, optical, IR and radio ranges, namely large-area or all-sky surveys, with heavy use of cross-correlations, classifications on activity types using our observations and SDSS spectra, building diagnostic diagrams, Spectral Energy Distributions (SEDs), etc. For classification of SDSS spectra, we have used our new approach that is focused on detailed analysis of the most important emission lines and introducing fine details, like subtypes for the main broad-line Seyfert galaxies and narrow-line Seyfert ones. Results on HRC/BHRC sample objects (optical identifications of ROSAT X-ray sources), studies of Markarian galaxies in UV and multiwavelength SEDs, abundance and star formation determinations in Mrk galaxies from SDSS spectra (for spectra having higher signal-to noise ratio), revised optical classification of LINERs, study and classification of SDSS spectra for Byurakan-IRAS Galaxies (BIG objects), summary of observations and study of BIG objects, discovery of new bright ULIRGs from the IRAS PSC/FSC Combined Catalogue (complied earlier by our group) and their spectral classification using SDSS spectra, 6301 radio variable sources at 1400 MHz and their optical variability, classification of BZCAT objects having uncertain types (BZU objects), and optical variability of blazars are given in individual sections.

Optical studies of active galaxies

Among the optical studies, most important are studies of Markarian (Mrk) galaxies and FBS Blue Stellar Objects (BSOs). We have carried out a homogeneous classification for activity types for Markarian galaxies by means of the SDSS spectra. 779 Mrk galaxies appeared to have SDSS spectroscopy (due to smaller sky area covered by SDSS compared to Markarian Survey). We give in Table 2 the distribution by activity types for these 779 Mrk objects.

Table 2. The distribution by activity types for these 779 Mrk objects based on SDSS spectroscopy.

Type	**Number**	%	**Type**	**Number**	%
HII	533	68.42	QSO	2	0.26
Composite	31	3.98	NLS1.5	5	0.64
LINER	12	1.54	NLS1.2	8	1.03
Sy 2.0	4	0.51	NLS1	4	0.51
Sy 1.9	5	0.64	AGN	11	1.41
Sy 1.8	8	1.03	Em	52	6.68
Sy 1.5	11	1.41	Abs	65	8.34
Sy 1.2	21	2.70	Star	3	0.39
Sy 1.0	4	0.51	**TOTAL**	779	100.00

Infrared Studies of Active Galaxies

IRAS Point Source Catalog (PSC) served as the main source for identification and study of IR galaxies, among which there are many Active Galaxies, as well as high-luminosity IR galaxies (ULIRGs, HLIRGs).

doi: https://doi.org/10.52526/25792776-23.70.1-68

In Figure 1 we give infrared and far-infrared luminosities of IRAS galaxies vs. redshift. The outliers are objects with especially high IR/FIR luminosity, so called IR-excess galaxies. This way we have introduced a new class of objects.

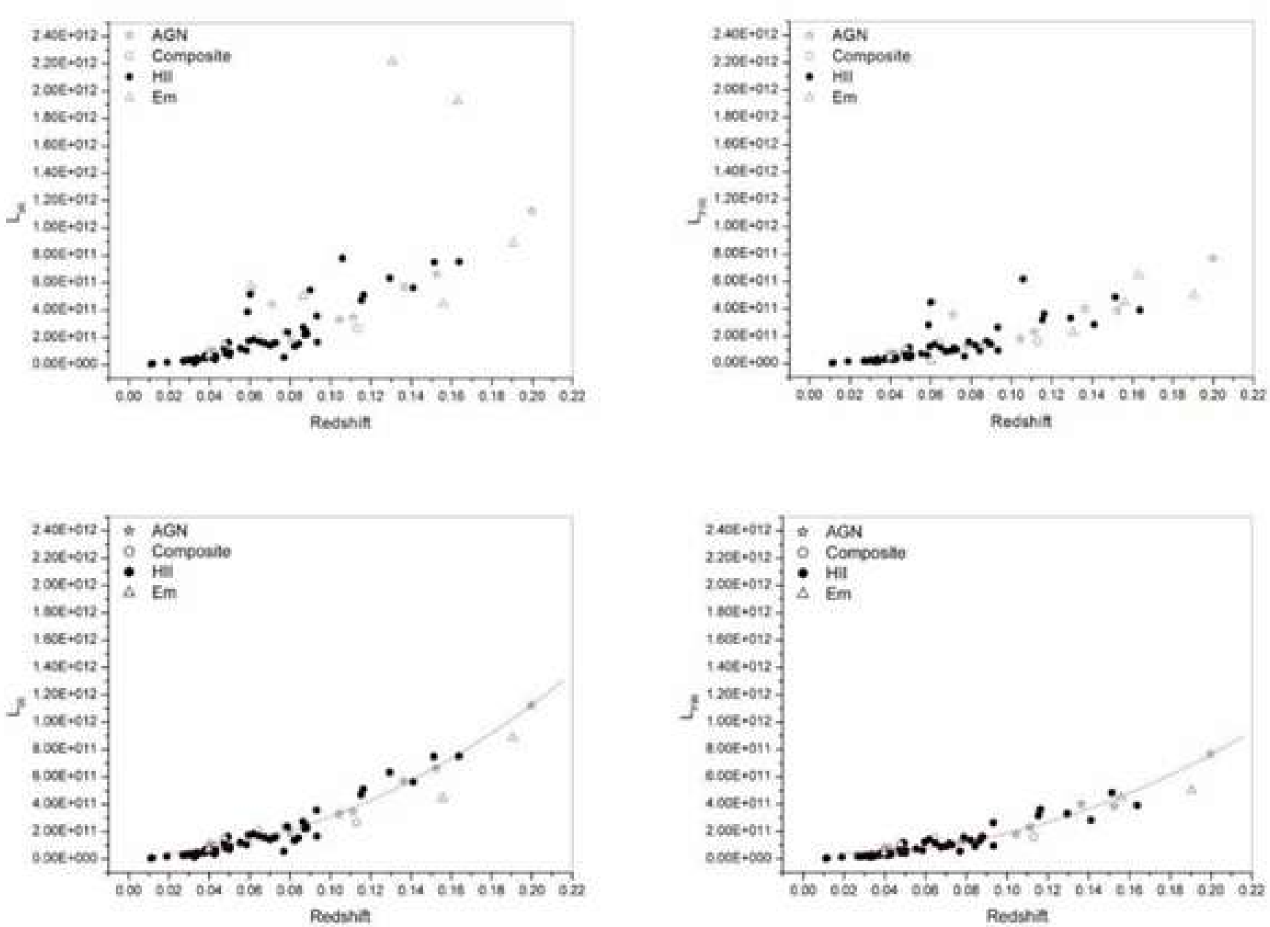

Figure 1. Infrared and Far-Infrared luminosities of IRAS galaxies vs. redshift. The outliers are objects with especially high IR/FIR luminosity, so called IR-excess galaxies.

High-luminosity IR galaxies

High-luminosity IR galaxies (LIRGs, ULIRGs, and HLIRGs) are important for studies related to star-formation processes in the early Universe, as their luminosity allows to detect them at large distances. High IR indicates active star-formation and often starburst processes, which is typical to HII (starburst, SB) and/or existence of Active Galactic Nuclei (AGN). An interesting question is whether the starburst triggers AGN or vice versa or there is no direct impact. Considering that very often such objects manifest double and multiple structure, it is also interesting to investigate the interrelationship between the SB, nuclear activity and interactions or merging. We have analyzed the IRAS PSC/FSC Combined Catalogue for search for new bright ULIRGs. By means of the SDSS DR14 data, namely redshifts for those objects having spectroscopy, we have calculated the IR luminosities and have found 114 very high-luminosity IR galaxies; 107 ULIRGs and 7 HLIRGs. Among them, 48 new ULIRGs and 7 new HLIRGs have been discovered. These objects have been studied by SDSS color-color, luminosity-redshift and other diagrams. Further studies included the content of the sample for activity types and other available data. The classification for their activity types resulted in: 1 BLL, 2 Quasars, 29 Seyfert types 1.0-1.8, 5 Seyfert type 2, 14 LINERS, 36 HII regions, and 14 objects with Composite spectra (Composites). Among the type 1 Seyfert galaxies there are many objects with Narrow Lines (NLS1s).

doi: https://doi.org/10.52526/25792776-23.70.1-68

Radio Studies of Active Galaxies

We have carried out several projects on studies of radio galaxies and radio properties of active and normal galaxies.

Radio variable sources at 1400 MHz and their optical variability

We have cross-correlated NVSS and FIRST radio catalogues having radio flux measurements at the same 1.4 GHz frequency. This way we benefit from repeated observations from both catalogues, as they give more accurate positions and fluxes and more important, reveal large differences between the two measured fluxes, thus allowing to establish radio variability. As a result, 79,382 radio variables have been revealed, including 6301 with flux differences at 1.4 GHz larger than 15 mJy, 1917 with flux differences $>$ 45 mJy and 260 with flux differences $>$ 200 mJy. By using a special technique, 2425 optically variable objects out of 6301 radio sources have been revealed. 2425 radio sources with both high radio and optical variability into four categories have been divided. 1206 (19%) out of 6301 radio sources have activity types from available catalogues and 619 (25.5%) out of 2425 radio sources with at the same time radio and optical variability have activity types from available catalogues. In addition, 279 radio sources out of 2425 have high variability in optical range. We have established their activity types when available. The IR fluxes and colors for the 6301 variable radio sources have been studied. Color-color diagrams show that most of the "unknown" sources are galaxies. The activity types for 110 (42%) out of 260 extremely high variable radio sources also have been retrieved.

Blazars

The definition of Blazars has several criteria, both historical and introduced by ourselves. We list here all related physical parameter that may define a Blazar:

- Selected radio sources
- X-ray and gamma-ray emission
- Radio spectral index is α = -0.154±0.01 (based on 1435 objects)
- Average flux ratio radio/opt = 17.996 (based on 1810 objects)
- Average flux ratio X/opt = 0.052 (based on 1101 objects)
- Average flux ratio radio/X = 86.197 (based on 1860 objects)
- Average optical variability: ΔR = 1.20±0.13, ΔB = 0.98±0.11
- Average radio variability: |FIRST-NVSS|-3σ = 38.01 mJy (based on 805 sources)
- Absolute magnitudes (SDSS$_r$ band): M_{BZB}= -22.19, M_{BZG}= -22.44, M_{BZQ}= -22.97, M_{BZU}= -22.42, M_{All}= -22.78.

Classification of BZCAT objects for activity types

Having 3561 objects in the BZCAT catalogue v.5, it is important to clarify what physical type of objects are included. They are divided into 4 groups: BZB (BL Lac objects), BZQ (Flat Spectrum Radio Quasars, FSRQs), BZG (Blazar-like extended objects; galaxies) and BZU (Uncertain type). Another paper of this volume is dedicated to these studies (Abrahamyan et al.), so we will not focus on this topic in details.

X-ray Studies of Active Galaxies

Optical identifications of ROSAT Faint Source Catalogue (FSC) led to revelation of many new interesting optical objects, including a big number of extragalactic ones. The Joint HRC/BHRC Catalogue is based on the combination of two major studies; optical identification projects of ROSAT BSC and ROSAT FSC, both based on Hamburg Quasar Survey (HQS) low-dispersion spectra. The 1st one was published by Zickgraf et al. (2003; A&A 406, 535) and resulted in 5341 identified BSC sources and the 2nd one was published by

doi: https://doi.org/10.52526/25792776-23.70.1-68

Mickaelian et al. (2006; A&A 449, 425) and resulted in 2791 identified FSC sources. While the 1st project used only HQS, in the 2nd one we used HQS, DSS1 and DSS2 to find faint objects and to achieve almost 100% result for studies X-ray sources.

A work was carried out to reveal all X-ray galaxies in HRC/BHRC Combined Catalogue (Paronyan et al. 2018) by cross-correlations with known catalogs of AGN and galaxies, their optical images (including DSS1/DSS2 and SDSS) and other parameters (radio, IR, X-ray properties, etc.). We have carried out classification of X-ray galaxies for their activity types using SDSS spectroscopic database and have revealed active galaxies (AGN and Starbursts). The classification has been carried out according to our new scheme and many narrow-line objects (Seyferts and Quasars) have been revealed.

Activity types of HRC/BHRC objects

In this study we carried out detailed spectral classification of 371 (173+198) AGN candidates from the Joint HRC/BHRC sample, which is a combination of HRC (Hamburg-ROSAT Catalogue) and BHRC (Byurakan-Hamburg-ROSAT Catalogue). These objects were revealed as optical counterparts for ROSAT X-ray sources; however, spectra for 371 of them were given in SDSS without definite spectral classification. We studied these 371 objects using the SDSS spectra and revealed the detailed activity types for them. Three diagnostic diagrams and direct examination of the spectra were used to obtain more confident classification. We also identified these sources in other wavelength ranges and calculated some of their parameters.

The Database of Markarian galaxies

We have created a Database of Markarian galaxies with multiwavelength data (MW) including all possible information from gamma-ray, X-ray, UV, optical, IR, sub-mm/mm and radio domains (https://www.bao.am/activities/projects/21AG-1C053/mg/). In Figure 2 we give an example of such page for the famous Blazar Mrk 421 with its various images and numerical data.

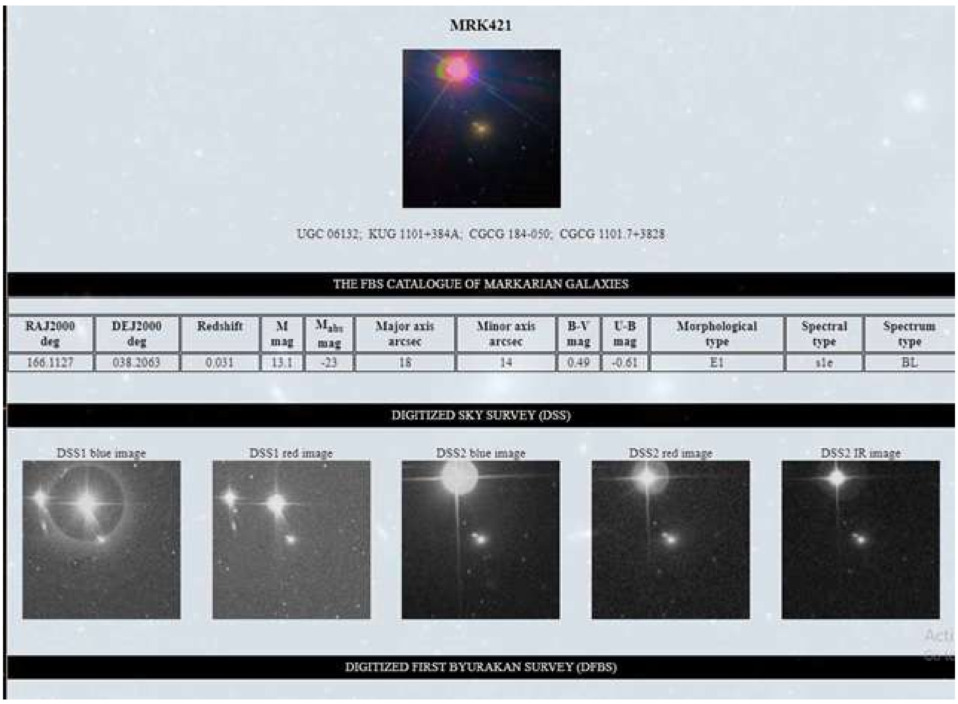

Figure 2. An example of the individual page for the famous Blazar Mrk 421 with its various images and numerical data.

Fine Classification of Active Galaxies

We have carried out a detailed Fine classification of the emission-line spectrum of active galaxies (https://www.bao.am/activities/projects/21AG-1C053/mickaelian/). One of the most important results is

doi: https://doi.org/10.52526/25792776-23.70.1-68

the introduction of subtypes for Narrow-Line Quasars (NLQ) similar to Narrow-Line Seyfert 1 galaxies (NLS1: NLS1.0, NLS1.2, NLS1.5, NLS1.8, NLS1.9, introduced by Osterbrock & Pogge 1985). These galaxies have soft X-ray detected by ROSAT surveys and have the same physical nature as X-ray QSOs, hence this classification scheme will extend their luminosity range to higher ones. We have introduced NLQ1.0, NLQ1.2, NLQ1.5, NLQ1.8 and NLQ1.9, though the last 2 subtypes are extremely rare and are rather difficult to reveal.

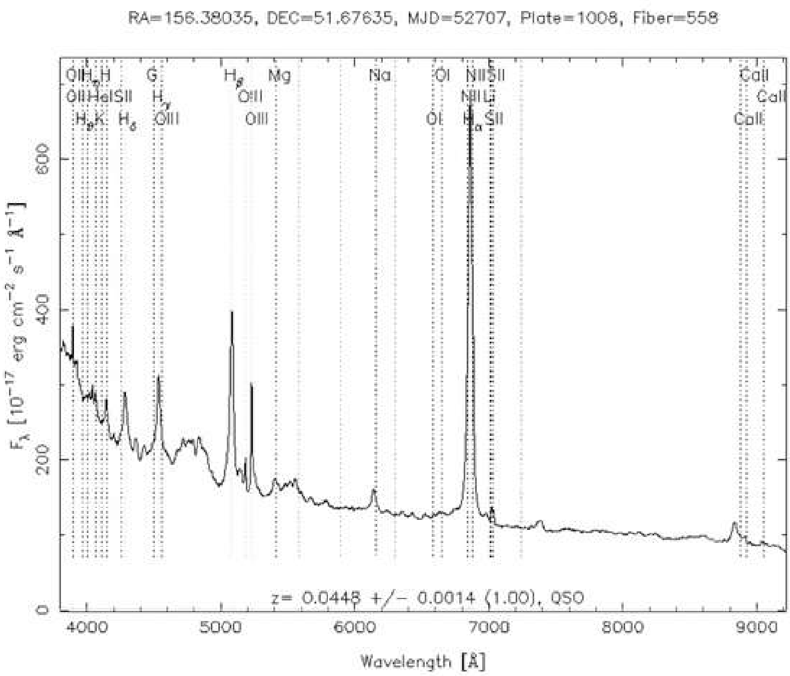

Figure 3. An example of Narrow Line Seyfert Galaxy having comparatively narrow broad lines (H-alpha, H-beta, etc.) and two bumps on both sides of H-beta, consisting of many FeII and some other lines. Such objects also have strong soft X-ray radiation.

Our classification scheme may be given as the following:

- Broad Line QSOs – BLQ (BLQSO) – Q1.0, Q1.2, Q1.5, Q1.8, Q1.9
- Narrow Line QSOs – NLQ (NLQSO) – NLQ1.0, NLQ1.2, NLQ1.5, NLQ1.8, NLQ1.9
- Broad Line Seyferts – BLS (S, Sy, Sey) – S1.0, S1.2, S1.5, S1.8, S1.9 (Osterbrock 1981)
- Narrow Line Seyferts – NLS (NLS1, Osterbrock & Pogge 1985) – NLS1.0, NLS1.2, NLS1.5, NLS1.8, NLS1.9
- Narrow Line AGN – NLA (NLAGN) – S2.0, LINER (Heckman 1980), HII (Sargent & Searle 1970)
- Composite Spectrum objects – Comp (Veron et al. 1997) – HII/LINER, HII/Sy, LINER/Sy, HII/LINER/Sy.

In addition, we will introduce two more novelties:

- Diagnostic Diagrams for BLS (based on decomposition of line profiles into broad and narrow lines for S1.2, S1.5, S1.8, S1.9 types and further classification of objects by diagnostic diagrams),
- Classifications based on the shorter wavelength range of QSOs; classification by L-alpha, CIV, CIII and MgII lines.

Summary of the Results

In Table 3 we list all our accomplished or ongoing projects on multiwavelength search and studies of active galaxies. We give the years, authors, name of the survey, short designation, objective or types of objects discovered and studied, and the number of objects.

doi: https://doi.org/10.52526/25792776-23.70.1-68

Table 3. Summary of the accomplished and ongoing projects on multiwavelength search and studies of active galaxies.

Years	Authors	Survey	Short	Objectives	Number of objects
1986-2001	H. Abrahamian, A. Mickaelian	First Byurakan Survey, 2nd Part	FBS BSOs	QSOs and Seyferts	1103
1994-2010	A. Mickaelian et al.	Byurakan-IRAS Galaxies	BIG	IRAS galaxies	1278
2001-pres.	A. Mickaelian	Bright AGN	AGN	Statistical studies of bright AGN	~10 000
2002-2006	A. Mickaelian et al.	Byurakan-Hamburg-ROSAT Catalogue	BHRC	ROSAT sources	2791
2003-2010	L. Sargsyan, A. Mickaelian et al.	Spitzer ULIRGs	Spitzer	ULIRGs	32
2010-pres.	A. Mickaelian et al.	Markarian galaxies	Mrk	Markarian galaxies	1544
2010-pres.	G. Paronyan, A. Mickaelian, et al.	HRC/BHRC AGN content	X-ray AGN	X-ray AGN	4253
2015-pres.	H. Abrahamyan, A. Mickaelian et al.	IRAS PSC/FSC Combined Catalogue extragalactic sources	IRAS	IRAS galaxies	145 902
2013-2018	H. Abrahamyan, A. Mickaelian et al.	Variable radio sources at 1400 MHz	NVSS/FIRST	Variable radio sources	6301
2013-pres.	A. Mickaelian, G. Paronyan, H. Abrahamyan et al.	Search for X-ray/radio AGN	ROSAT/NVSS	X-ray/radio AGN	9193
2014-pres.	H. Abrahamyan, A. Mickaelian et al.	MW study of Blazars	BZCAT	Blazars	3561
2018-pres.	G. Mikayelyan, A. Mickaelian et al.	IRAS PSC/FSC Combined Catalogue ULIRGs/HLIRGs	ULIRG/HLIRG	High luminosity IR galaxies	114
2001-2007	A. Mickaelian, et al.	Fine analysis of AGN spectra	Bright AGN	Physical properties of AGN	90
2002-pres.	A. Mickaelian, et al.	Search for new AGN in DFBS	DFBS AGN	New bright active galaxies	~10 000
2006-pres.	A. Mickaelian, et al.	Fine classification of active galaxies	Mickaelian classification	Accurate types and subtypes of active galaxies	~10 000

Acknowledgements

This work was partially supported by the Republic of Armenia Ministry of Education and Science (RA MES) Science Committee, in the frames of the Advanced Research Project 21AG-1C053 (2021-2026). This work was made possible in part by research grant PS-astroex-2597 from the Armenian National Science and Education Fund (ANSEF) based in New York, USA (2022-2023).

References

Abrahamian H. V., Gigoyan K. S., 1989, Astrofizika, 31, 601

Abrahamian H. V., Mickaelian A. M., 1995, Astrofizika, 38, 201

Abrahamian H. V., Lipovetski V. A., Mickaelian A. M., Stepanian J. A., 1990, Astrofizika, 33, 213

Abrahamian H. V., Lipovetsky V. A., Mickaelian A. M., Stepanian J. A., 1991, Astrofizika, 33, 213

Abrahamyan H. V., Mickaelian A. M., Paronyan G. M., Mikayelyan G. A., Gyulzadyan M. V., 2018, Astronomy and Computing, 25, 176

Abrahamyan H. V., Mickaelian A. M., Paronyan G. M., Mikayelyan G. A., Gyulzadyan M. V., 2019a, Communications of the Byurakan Astrophysical Observatory, 66, 1

Abrahamyan H. V., Mickaelian A. M., Paronyan G. M., Mikayelyan G. A., 2019b, Astronomische Nachrichten, 340, 437

Abrahamyan H. V., Mickaelian A. M., Paronyan G. M., Mikayelyan G. A., Sukiasyan A. G., 2023, Astrophysics, 66, 11

Arakelyan M. A., Dibai É. A., Esipov V. F., 1975a, Astrophysics, 11, 8

Arakelyan M. A., Dibai É. A., Esipov V. F., 1975b, Astrophysics, 11, 254

Arakelyan M. A., Dibai É. A., Esipov V. F., 1976a, Astrophysics, 12, 122

Arakelyan M. A., Dibai É. A., Esipov V. F., 1976b, Astrophysics, 12, 456

Arakelyan M. A., Dibaj E. A., Esipov V. F., 1976c, Astronomicheskij Tsirkulyar, 914, 7

Heckman T. M., 1980, Astron. Astrophys. , 88, 365

Kazarian M. A., 1979a, Astrofizika, 15, 1

Kazarian M. A., 1979b, Astrofizika, 15, 193

Kazarian M. A., 1984, Astrofizika, 20, 35

Kazarian M. A., 1987, Astrofizika, 27, 399

Kazarian M. A., Kazarian E. S., 1980, Astrofizika, 16, 17

Kazarian M. A., Kazarian E. S., 1982, Astrofizika, 18, 512

Kazarian M. A., Kazarian E. S., 1987, Astrofizika, 26, 5

Kazarian M. A., Kazarian E. S., 1988, Astrofizika, 28, 487

Markarian B. E., Lipovetskii V. A., Stepanian D. A., 1979a, Astrofizika, 15, 201

doi: https://doi.org/10.52526/25792776-23.70.1-68

Markarian B. E., Lipovetskii V. A., Stepanian D. A., 1979b, Astrofizika, 15, 363

Markarian B. E., Lipovetskii V. A., Stepanian D. A., 1979c, Astrofizika, 15, 549

Markarian B. E., Lipovetskii V. A., Stepanian D. A., 1980a, Astrofizika, 16, 5

Markarian B. E., Lipovetskii V. A., Stepanian D. A., 1980b, Astrofizika, 16, 609

Markarian B. E., Stepanian J. A., Lipovetskij V. A., 1980c, Astronomicheskij Tsirkulyar, 1141, 1

Markarian B. E., Stepanian J. A., Lipovetskij V. A., 1980d, Astronomicheskij Tsirkulyar, 1141, 1

Markarian B. E., Stepanian J. A., Lipovetsky V. A., 1980e, Astronomicheskij Tsirkulyar, 1142, 1

Markarian B. E., Stepanian J. A., Lipovetsky V. A., 1980f, Astronomicheskij Tsirkulyar, 1142, 1

Markarian B. E., Lipovetskii V. A., Stepanian D. A., 1981, Astrofizika, 17, 619

Markarian B. E., Stepanyan D. A., Lipovetskij V. A., 1982a, Astronomicheskij Tsirkulyar, 1233, 2

Markarian B. E., Stepanian J. A., Lipovetskij V. A., 1982b, Astronomicheskij Tsirkulyar, 1237, 1

Markarian B. E., Lipovetskii V. A., Stepanian D. A., 1983a, Astrofizika, 19, 221

Markarian B. E., Stepanian J. A., Lipovetsky V. A., 1983b, Astronomicheskij Tsirkulyar, 1265, 1

Markarian B. E., Stepanian J. A., Lipovetsky V. A., 1983c, Astronomicheskij Tsirkulyar, 1265, 1

Markarian B. E., Lipovetskii V. A., Stepanian D. A., 1984a, Astrofizika, 20, 419

Markarian B. E., Lipovetskii V. A., Stepanian D. A., 1984b, Astrofizika, 21, 35

Markarian E., Lipovetsky V. A., Stepanian J. A., 1984c, Astrofizika, 21, 419

Markarian B. E., Erastova L. K., Lipovetskii V. A., Stepanian D. A., Shapovalova A. I., 1985a, Astrofizika, 22, 215

Markarian B. E., Erastova L. K., Stepanian J. A., Lipovetsky V. A., Shapovalova A. I., 1985b, Astronomicheskij Tsirkulyar, 1381, 5

Markarian B. E., Erastova L. K., Stepanian J. A., Lipovetsky V. A., Shapovalova A. I., 1985c, Astronomicheskij Tsirkulyar, 1381, 5

Markarian B. E., Stepanian D. A., Erastova L. K., 1986, Astrofizika, 25, 345

Markarian B. E., Erastova L. K., Lipovetsky V. A., Stepanian J. A., Shapovalova A. I., 1988a, Astrofizika, 28, 27

Markarian B. E., Erastova L. K., Lipovetsky V. A., Stepanian J. A., Shapovalova A. I., 1988b, Astrofizika, 28, 476

Markarian B. E., Lipovetsky V. A., Stepanian J. A., Erastova L. K., Shapovalova A. I., 1989, Soobshcheniya Spetsial'noj Astrofizicheskoj Observatorii, 62, 5

Markaryan B. E., Erastova L. K., Stepanyan D. A., Lipovetskii V. A., Shapovalova A. I., 1987, Soviet Astronomy Letters, 13, 1

Mickaelian A. M., 1997, in Philip A. G. D., Liebert J., Saffer R., Hayes D. S., eds, The Third Conference on Faint Blue Stars. p. 501

Mickaelian A. M., 2000, Astronomical and Astrophysical Transactions, 18, 557

Mickaelian A. M., 2001, in Clowes R., Adamson A., Bromage G., eds, Astronomical Society of the Pacific Conference Series Vol. 232, The New Era of Wide Field Astronomy. p. 278

Mickaelian A. M., 2003, in IAU General Assembly. p. E1

Mickaelian A. M., Gigoyan K. S., 1998a, Astrophysics, 41, 161

Mickaelian A. M., Gigoyan K. S., 1998b, Astrophysics, 41, 232

Mickaelian A. M., Gigoyan K. S., 2000, Astrophysics

Mickaelian A. M., Gigoyan K. S., Russeil D., 1997, Astrophysics, 40, 379

Mickaelian A. M., Akopian S. A., Balaian S. K., Burenkov A. N., 1998, Astronomy Letters, 24, 635

Mickaelian A. M., Gonçalves A. C., Veron-Cetty M. P., Veron P., 1999, Astrofizika, 42, 1

Mickaelian A. M., Gonçalves A. C., Véron-Cetty M. P., Véron P., 2001, Astrophysics, 44, 14

Mickaelian A. M., Balayan S. K., Hakopian S. A., 2002, in Green R. F., Khachikian E. Y., Sanders D. B., eds, Astronomical Society of the Pacific Conference Series Vol. 284, IAU Colloq. 184: AGN Surveys. p. 217

Mickaelian A. M., Abrahamyan H. V., Paronyan G. M., Mikayelyan G. A., 2021, Frontiers in Astronomy and Space Sciences, 7, 82

Mickaelian A. M., Abrahamyan H. V., Mikayelyan G. A., Paronyan G. M., 2022, Communications of the Byurakan Astrophysical Observatory, 69, 10

doi: https://doi.org/10.52526/25792776-23.70.1-68

Mikayelyan G. A., Mickaelian A. M., Abrahamyan H. V., Paronyan G. M., 2018, Communications of the Byurakan Astrophysical Observatory, 65, 13

Osterbrock D. E., Pogge R. W., 1985, Astrophys. J. , 297, 166

Paronyan G. M., Mickaelian A. M., Harutyunyan G. S., Abrahamyan H. V., Mikayelyan G. A., 2019, Astrophysics, 62, 147

Paronyan G. M., Mickaelian A. M., Abrahamyan H. V., Mikayelyan G. A., 2020, Astrophysics, 63, 166

Sargent W. L. W., Searle L., 1970, Astrophys. J. Lett. , 162, L155

Veron P., Goncalves A. C., Veron-Cetty M. P., 1997, Astron. Astrophys. , 319, 52

doi: https://doi.org/10.52526/25792776-23.70.1-68

A study of active galaxies in groups of galaxies and in the field.

R.R.Andreasyan [*], S.A.Hakopian[†], A.P.Mahtessian[‡], H.V.Abrahamyan[§], G.M.Paronyan,[¶] and A.G.Sukiasyan[‖]

NAS RA V.Ambartsumian Byurakan Astrophysical Observatory, Byurakan 0213, Aragatsotn Province, Armenia

Abstract

We study regions with radius of 500 pc around of the central radio galaxies from our sample. For this study were chosen about 30 nearby 3C radio galaxies of different FR types. We bring the maps of optical galaxies that are overlaid on the radio map of 3C radio source. It was used also the maps of these regions in all available wavelength. Here we present more detail analyses and new results for the radio galaxy of FRI type 3C31.

The dependencies of the morphological types of the first and second ranked group galaxies on the magnitude gap were studied. It is shown that there is no increase in the relative number of elliptical galaxies among the first and second ranked group galaxies with large magnitude gaps. Some results are presented on studies of a sample of about hundred galaxies ("100SBS") from two adjacent fields of SBS, which have spectral data in SDSS. Comparative analysis was done between two classifications that the 100SBS objects got - from one side Starburst or Starforming in SDSS, from the other - SfGcont and SfGneb, with a possibility of further detailing in accordance to our scheme for star-forming galaxies.

Keywords: *Radio galaxies, groups of galaxies, FR type, SBS fields, galaxie formation*

1. Introduction

The study of active galaxies is one of traditional direction of Byurakan observatory. In this paper we present some of recent works carried out in the department of active galaxies of BAO. These are: The investigation of properties of the neighborhood of giant extragalactic radio sources. The study of galactic groups and clusters. The spectrophotometric observations of SBS galaxies. The study of formation and morphology of magnetic fields of galaxies and particularly in our Galaxy etc.

Extragalactic radio sources mainly are divided on two groups: compact and extended radio sources. One of the well-known classifications of extended radio galaxies is the (FR) classification of Fanaroff and Riley (Fanaroff & Riley, 1974), which is based on the radio brightness distribution over the radio image. Radio galaxies with relatively lower radio luminosity, in which the radio brightness decreases from the center to the edges, are classified as I class radio galaxies (FRI), and radio galaxies with higher radio luminosity, in which the radio brightness increases from the center to the edges of the II class (FRII). Figure 1 shows examples of extragalactic radio sources of FRI and FRII types.

At present, the Fanaroff-Riley dichotomy has been studied quite well and many other differences in physical and morphological features have been found for different classes of radio galaxies. Partly in our early studies a correlation was found between the optical and radio axes of nearby radio galaxies (Andreasyan & Sol, 1999), a correlation of the ellipticity of parent optical galaxies associated with radio galaxies of different classes (Andreasyan & Sol, 2000), a correlation of the average radio polarization angles with the radio axes (Andreasyan et al., 2002), etc.

[*]randrasy@bao.sci.am, Corresponding author
[†]susanaha@bao.sci.am
[‡]amahtes@bao.sci.am
[§]abrahamyanhayk@gmail.com
[¶]paronyan$_g$*urgen@yahoo.com*
[‖]andranik.suqiasyan.1995@mail.ru

doi: https://doi.org/10.52526/25792776-23.70.1-77

These large differences in morphology and physical properties of different classes of extragalactic radio sources can be due to differences in parent optical galaxies or in differences of the extragalactic medium around the radio source in which the radio source is expanding. In order to reveal the influence of the environment on extragalactic radio source, we study the close proximity (regions with radius of 500 pc around of the central radio galaxies) of the well-known Giant radio sources 3C 31, 3C 449, NGC 315, NGC 6251 from our sample of about 30 nearby 3C radio galaxies of different FR types chosen from Andreasyan & Abrahamyan (2021).

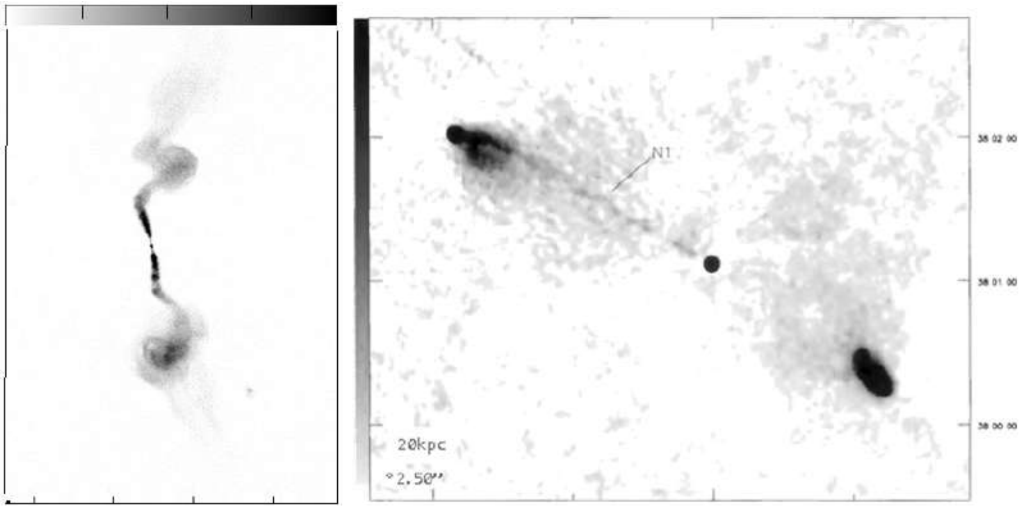

Figure 1. Extragalactic radio sources of FRI (left) and FRII (right).

.

2. The study of the neighborhood of radio galaxies.

For the study we construct the maps of optical galaxies that are overlaid on the radio map of 3C radio source. We use also the maps of these regions in all available wavelength. Here we present more detail analyses and new results for the radio galaxy of FRI type 3C 31.

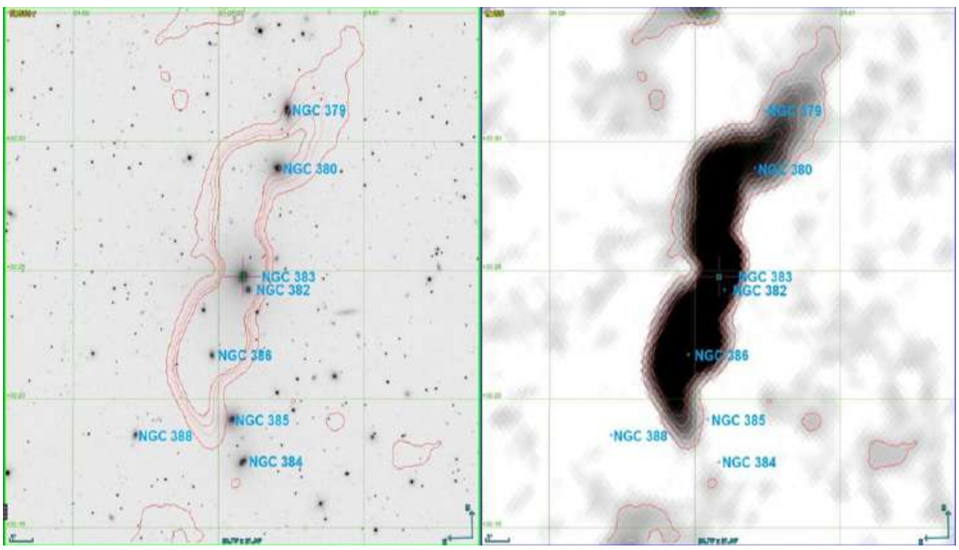

Figure 2. The region of a group of galaxies with the central object NGC 383 and radio source 3C 31 of the FRI class at a frequency of 1400 MHz.

The 3C 31 class FRI radio source has been identified with the NGC 383 parent galaxy, which is the central object of the group of galaxies, which in turn is a member of the Perseus-Pisces supercluster (Sakai et al., 1994) and has been studied quite well. Numerous results and useful data have now been obtained for these objects (Croston & Hardcastle, 2014, Hardcastle et al., 2002, Laing & Bridle, 2002, Martel et al., 1999, Parma et al., 1999, Strom et al., 1983). Of these, here we highlight some of the data of interest to

doi: https://doi.org/10.52526/25792776-23.70.1-77

us, which can be used in the present work. On figure 2 we bring the radio map of 3C31 at frequency of 1400 MHz (corresponding to FIRST observations) with the overlaid optical region with the central galaxy NGC383. As it is seen a group of galaxies in the form of a chain has the direction of the radio image. It is more obvious on the Figure 2 of same region from the paper Heesen et al. (2018) at different frequencies, 145, 360, and 615 MHz corresponding to LOFAR, VLA, and GMRT observations, respectively.

From figures we see that the elliptical galaxies NGC 380 and NGC 386 are located respectively in the northern and southern parts of the 3C 31 radio image. These galaxies, together with the central SA0 type galaxy of the group NGC 383 are on the same line, the direction of which coincides with the direction of central part of radio image with great accuracy (Heesen et al., 2018). Radio jet simulations (Laing & Bridle, 2002) have shown that the direction of the central jet is approximately 520 with the line of sight. Moreover, the northern part of the jet approaches the observer, while the southern part moves away. On the other hand, the analysis of the redshifts of the mentioned optical galaxies shows that the relative line of sight velocity of the northern galaxy NGC 380 compared to the central galaxy NGC 383 is directed towards the observer, and the relative velocity of the southern galaxy NGC 386 is directed away from the observer. This probably suggests that the direction of the spatial velocities of these galaxies also coincides with the direction of the velocities of the radio jets and, therefore, galaxies NGC 380 and NGC 386 move away from the central galaxy NGC 383 in opposite directions coincide with the direction of the radio jets. We calculated the time of removal of galaxies from the central galaxy. The calculation results are shown in Table 1. Δz is difference of redshifts from the central galaxy NGC 383, ΔV and ΔV_0 – the relative line of sight and spatial velocities respectively, d and d_o -the projected on the sky and spatial distances, T- the time of removal of galaxies.

Table 1. Results of Calculations.

Galaxies	Δz	ΔV km/s	ΔV_0 km/s	**d** kpc	d_0 kpc	**T** My
NGC380	-0.00224	-672	1092	97.07	123.2	110
NGC386	+0.00153	+459	745.5	70.64	89.64	118

The table shows that the galaxies NGC 380 and NGC 386 were near the galaxy NGC 383 about 110 million years ago. A very close passage of these three galaxies then probably occurred, after which the recession of the galaxies NGC 380 and NGC 386 from the more massive central galaxy NGC 383 began. A natural question arises whether such a close passage can be the cause (trigger) of the beginning of radioactivity of the central galaxy. A reliable argument for such assumption can be considered that the modeling of the spectral characteristics of the radio emission of the central part of the radio galaxy 3C31 gives an estimate of the age of the central jet of about 100 million years (Heesen et al., 2018).

3. The spectrophotometric observations of SBS galaxies.

An important direction in the work of our department is the spectrophotometric observations of galaxies of the Second Byurakan Survey (SBS) (Hakopian, 2021). The observations were carried out with the 2.6m telescope of the Byurakan observatory and the 6m telescope of the SAO of the Russian Federation. Here are some works that are part of a large program launched in 2013 (Hakopian, 2014). Out of 7 preselected areas, nearby ($0.01 < z < 0.029$) galaxies were studied in two areas 4 and 5 (Fig. 3). Approximately 80% of galaxies turned out to be galaxies with active star formation (SfG - star-forming galaxy). Spectral data from SDSS (Sloan Digital Sky Survey-www.sdss.org) were also known for them.

The studied SfG star-forming galaxies, by some analogy with (Terlevich, 1997), were classified into two classes SfGcont, i.e. star-forming in continual phase and SfGneb, i.e. star-forming in nebular phase. Each class was divided into 5 subclasses according to spectral data. Such data are the intensities and equivalent widths of the Balmer $H\alpha$ line. For SfGcont 1, the equivalent widths start from EW($H\alpha$) = $5\mathring{A}$, and for SfGneb 1 from EW($H\alpha$) = $100\mathring{A}$. Below are examples of such galaxies and their spectra (fig.4).

4. The study of galactic groups and clusters.

Another direction of work of our department is the finding and studying the physical properties of galactic groups (Mahtessian et al., 2018). The accepted mechanism for the evolution of galaxies in groups is based on the process of merging of galaxies. However, there is another, opposite mechanism of group

doi: https://doi.org/10.52526/25792776-23.70.1-77

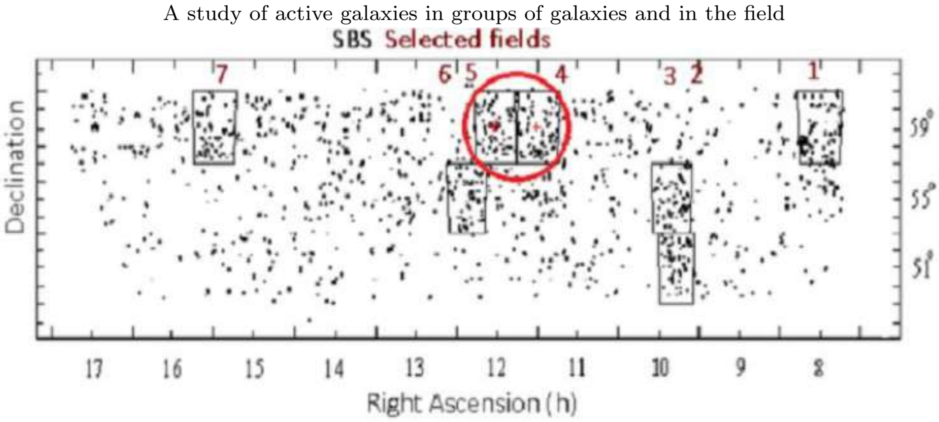

Figure 3. The areas of the study

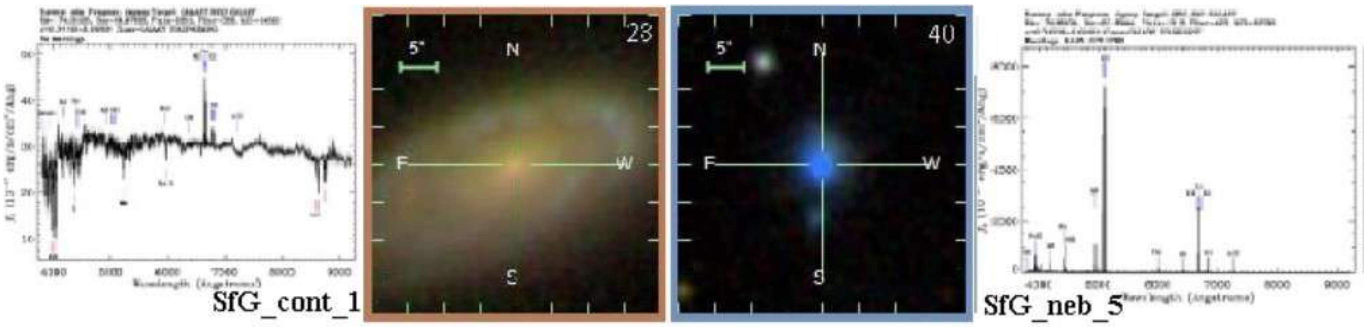

Figure 4. Examples of galaxies classified as SfGcont 1 and SfGneb 5.

evolution corresponding to the concept of V. Ambartsumyan. Many observational data can be successfully explained by both mechanisms, but some data are better suited to the second mechanism.

According to the galaxy merger mechanism, the mass and luminosity of the central galaxy should increase with time, and the difference between the luminosities of the first and second most luminous galaxies should also increase. Moreover, the main galaxy of the group becomes elliptical. According to the second scenario, such an effect should not be observed. The above mentioned has been verified by statistical analysis of data from a large list of galaxy groups that is complete up to a magnitude of 15.5 m (Mahtessian, 2011, Mahtessian & Movsessian, 2010). As a result of the analysis, the expectations corresponding to the merger mechanism were not confirmed, which shows in favor of the mechanism of the Byurakan concept.

5. The study of formation and morphology of magnetic fields of galaxies

There are regular magnetic fields with inductions of several micro gauss observed in numerous galaxies. The generation of these fields is explained by the dynamo associated with motions of the interstellar medium in appropriate objects. The growth of magnetic fields is exponential and these become stabilized when the equipartition of energy between magnetic fields and turbulent motions is reached. For starting this generation mechanism, some initial "seed" magnetic fields are necessary, and these fields are not explained within the dynamo theory. Among approaches explaining the magnetic fields in galaxies, there is the so-called Biermann battery mechanism (Mikhailov & Andreasyan, 2021). This mechanism relates to fluxes of protons and electrons flowing from the central portion of the object, with these fluxes being dragged by rotational motions of the medium. This results in circular currents, which are different for various particles due to their different masses. The total current becomes nonzero and generates the magnetic field. We have constructed a self-consistent model and derived an integral equation, which permits both to determine the order of magnitude of the initial magnetic field and to study in detail its spatial structure.

Another direction of the study of magnetic field structure of our Galaxy and Metagalactic Space based on the use of Faraday rotation data of extragalactic radio sources and pulsars. The plane of polarization of radiation is rotating when this radiation pass thru the magnetoionic medium. The rotation depends from the wavelength of radiation, and this gives the possibility to find so cold rotation measure (RM) by formulae:

doi: https://doi.org/10.52526/25792776-23.70.1-77

$$RM = d\Psi/d(\lambda^2) = \alpha \int n_e B_L dL, (\alpha = 8.1 * 10^5), \quad (1)$$

For pulsars from the observations it is possible to obtain also dispersion measure (DM). It depends on the effect that the same signal in different frequencies reaches the observer at different times.

$$t_2 - t_1 = (2\pi e^2)(1/\omega_2^2 - 1/\omega_1^2)DM, \quad (2)$$

$$DM = \int n_e dL, \quad (3)$$

Here $d\psi$ – is the difference of plane of polarization in different wavelength λ, t –is the time of receiving the radio signal from pulsar, ω – is the frequency of radio wave. In these formulas, integration is carried out over the entire traversed path of radiation (L in parsecs) from the object to the observer. Formula 3 makes it possible to determine the distance of a pulsar with the known electron density distribution in the Galaxy, and Formula 1 together with formula 3 makes possible to determine the average component of the tension of interstellar magnetic field $[B_L]$ on the line of sight in micro gauss (μG).

$$< B_L >= (1/\alpha)(RM)/(DM) = 1.23 * (RM)/(DM), \quad (4)$$

This gives a possibility to study the magnetic field in different directions (e.g. Andreasyan et al., 2020). On the figure 5 we bring some results for Galactic magnetic field from above mentioned paper where was shown that in the galactocentric ring with the radius $5kpc < R < 7kpc$ the magnetic field has an anti-clockwise direction.

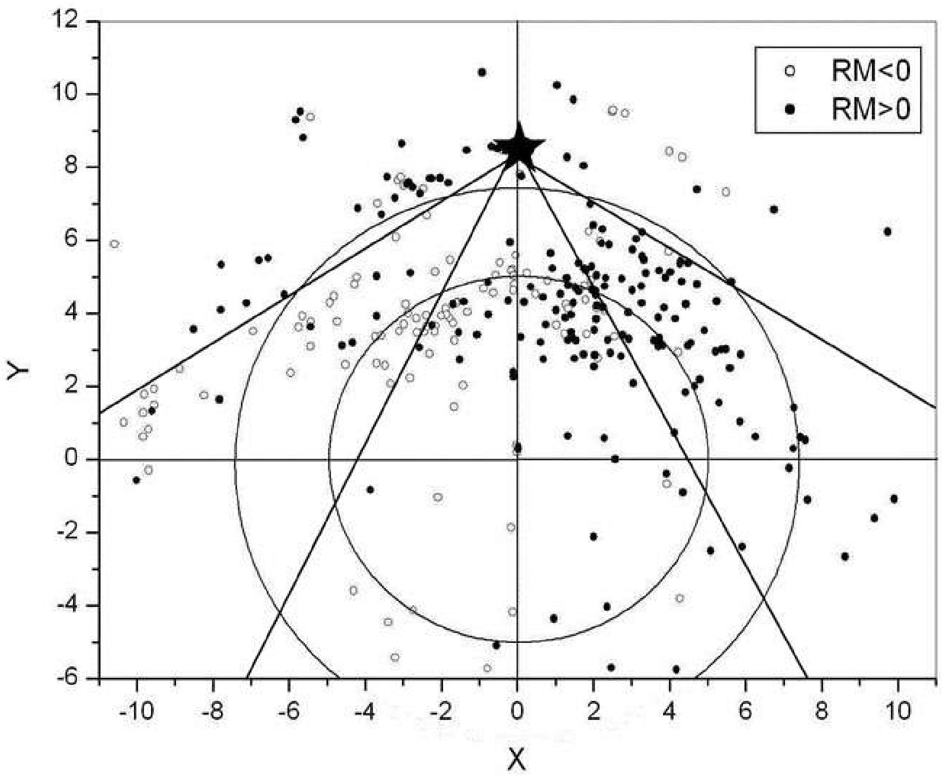

Figure 5. The Galactic distribution of RM signs of pulsars with $|RM| > 200rad/m^2$.

References

Andreasyan R. R., Abrahamyan H. V., 2021, Communications of the Byurakan Astrophysical Observatory, 68, 75

Andreasyan R. R., Sol H., 1999, Astrophysics, 42, 275

Andreasyan R. R., Sol H., 2000, Astrophysics, 43, 413

Andreasyan R. R., Appl S., Sol H., 2002, Astrophysics, 45, 198

doi: https://doi.org/10.52526/25792776-23.70.1-77

Andreasyan R. R., Mikhailov E. A., Andreasyan H. R., 2020, Astronomy Reports, 64, 189

Croston J. H., Hardcastle M. J., 2014, Mon. Not. R. Astron. Soc. , 438, 3310

Fanaroff B. L., Riley J. M., 1974, Mon. Not. R. Astron. Soc. , 167, 31P

Hakopian S., 2014, in Mickaelian A. M., Sanders D. B., eds, Vol. 304, Multiwavelength AGN Surveys and Studies. pp 36–36 (arXiv:1403.0127), doi:10.1017/S1743921314003238

Hakopian S. A., 2021, Communications of the Byurakan Astrophysical Observatory, 68, 522

Hardcastle M. J., Worrall D. M., Birkinshaw M., Laing R. A., Bridle A. H., 2002, Mon. Not. R. Astron. Soc. , 334, 182

Heesen V., et al., 2018, Mon. Not. R. Astron. Soc. , 474, 5049

Laing R. A., Bridle A. H., 2002, Mon. Not. R. Astron. Soc. , 336, 328

Mahtessian A. P., 2011, Astrophysics, 54, 162

Mahtessian A. P., Movsessian V. G., 2010, Astrophysics, 53, 70

Mahtessian A. P., Movsisyan V. H., Mahtessian L. A., Karapetian G. S., 2018, Communications of the Byurakan Astrophysical Observatory, 65, 401

Martel A. R., et al., 1999, Astrophys. J. Suppl. Ser. , 122, 81

Mikhailov E. A., Andreasyan R. R., 2021, Astronomy Reports, 65, 715

Parma P., Murgia M., Morganti R., Capetti A., de Ruiter H. R., Fanti R., 1999, Astron. Astrophys. , 344, 7

Sakai S., Giovanelli R., Wegner G., 1994, Astron. J. , 108, 33

Strom R. G., Fanti R., Parma P., Ekers R. D., 1983, Astron. Astrophys. , 122, 305

Terlevich R., 1997, in Franco J., Terlevich R., Serrano A., eds, Revista Mexicana de Astronomia y Astrofisica Conference Series Vol. 6, Revista Mexicana de Astronomia y Astrofisica Conference Series. p. 1

doi: https://doi.org/10.52526/25792776-23.70.1-77

Communications of BAO, Vol. 70, Issue 1, 2023, pp. 83-87

Classification of Blazars by Activity Types

H.V. Abrahamyan [*], A.M. Mickaelian[†], G.A. Mikayelyan[‡], G.M. Paronyan[§], A.G. Sukiasyan[¶], V.K. Mkrtchyan[‖] and L.A. Hambardzumyan[**]

NAS RA V. Ambartsumian Byurakan Astrophysical Observatory (BAO)

Abstract

Blazars are the most energetic sources in the Universe. They unify two major types of objects: BL Lac objects and Flat Spectrum Radio Quasars (FSRQ). So far, 3561 blazars are known from BZCAT v.5 catalogue. However, in BZCAT v.5 all blazars are grouped into four main classes, where extended radio sources and some unknown objects are added: BZB (BL Lac objects), BZQ (FSR Quasars), BZG (Blazar-like (BZQ-like) Galaxies) and BZU (Blazars of Unknown subtypes). There is no information about optical classification of these sources. We have accomplished optical classification for BZU and BZG sources, which have optical spectra from SDSS catalogue. Most of these sources had no optical class before or have changed their optical classification after our work. For some blazars, we obtained optical classes for the first time. In the current work we have done an overall optical investigation for all classes of blazars (BZB, BZQ, BZG and BZU). After the optical classification, some BZU sources, which have SDSS spectra, have changed to QSO (BZQ) or Galaxies (BZG). This way we give a better understanding of objects included in BZCAT v.5.

Keywords: *Blazar, Quasar, Active Galactic Nuclei, optical classification.*

Introduction

Blazars are considered to be the most energetic sources in the Universe. BLL Lac was discovered by Hoffmeister (Hoffmeister, 1929). The originally discovered source was considered to be a variable star. Later, a thorough study of this source showed that it was extragalactic radio source. Discovered source was a radio source which had optical variability. At present 3,561 blazars are known. The disclosed sources have been published by Massaro et al. (2015) as a general list. In this catalog, Massaro grouped all blazars in four main classes: BZB, BZQ, BZG and BZU. According to the definition, blazars should be radio sources and have optical variability. But information about variability is not complete in this catalogue. Information for optical variability of blazars is given by Abrahamyan et al. (2019b).

The blazar category includes BL Lac objects and Optically Violently Variable (OVV) quasars. The generally accepted theory is that BL Lac objects are intrinsically low-power radio galaxies while OVV quasars are intrinsically powerful radio-loud quasars. The name "blazar" was coined in 1978 by Edward Spiegel to denote the combination of these two classes.

So, summarize different physical properties of blazars we must understand which properties show different types of blazars (table 1).

Classification method

We have used several methods for classification of the SDSS spectra (Mickaelian et al., 2022);

[*]abrahamyanhayk@gmail.com, Corresponding author
[†]aregmick@yahoo.com
[‡]gormick@mail.ru
[§]paronyan_gurgen@yahoo.com
[¶]andranik.suqiasyan.1995@mail.ru
[‖]varduhi.mkrtchyan.99@bk.ru
[**]hambardzumyanlian@gmail.com

doi: https://doi.org/10.52526/25792776-23.70.1-83

Table 1. Distribution of types of objects in BZCAT.

N	Type	Numbers
1	BZB	1151
2	BZG	274
3	BZQ	1909
4	BZU	227
All		**3561**

- By eye (taking into account all features and effects)
- By diagnostic diagram using [OIII]/H_β and [NII]/H_α ratios (Reines et al., 2013),
- By diagnostic diagram using [OIII]/H_β and [SII]/H_α ratios (Reines et al., 2013),
- By diagnostic diagram using [OIII]/H_β and [OI]/H_α ratios (Reines et al., 2013).

Classification of BZCAT objects having uncertain types

For optical classification of BZCAT objects having uncertain types (Abrahamyan et al., 2019a), in the first step we cross-corelated these objects with SDSS (Abdurro'uf et al., 2022). As results we have 81 identification from which 43 have spectra. Our work is dedicated to these 43 objects. For a better understanding of the properties of BZU objects we cross-correlated with VCV-13 (Véron-Cetty & Véron, 2010), SDSS and NED.

Using information from VCV-13, SDSS and NED we can conclude the following:

- In SDSS: 13 objects are “galaxies” (extended objects) and 30 are “stars” (point-like objects),
- In VCV-13: 6 objects are BL or BL?, 2 objects are HP (HPQ), 6 objects are Sy1, 1 object is Sy1.2, 3 objects are Sy1.5, 1 object is Sy1n (Narrow Line Seyfert 1), 5 objects are Sy2, and for 19 objects we do not have any information,
- In NED: 13 objects are galaxies, 26 objects are quasars and 4 objects are RadioS (radio sources). Among these objects we have 4 BL Lac, 18 FSS (Flat-Spectrum Radio Source), 1 CSS (Compact Steep Spectrum), 1 Sy1, 1 Sy1.2, and 1 Sy 1.5,
- In NED we have radio morphology: 4 objects have radio jets, 1 object is FRII and 1 object is core-dominated radio object.

So, having optical spectra of 43 BZU, we reclassified these objects. As the main results we have:

1) 37 (86%) objects from 43 changed classification (table 3).

Table 2. New classification of BZU.

N	Old	New	Numbers
1	BZU	BZB	1 (2%)
2	BZU	BZG	14 (33%)
3	BZU	BZQ	22 (51%)
4	BZU	BZU	6 (14%)
All			**43 (100%)**

2) Using the information on redshift from BZCAT, SDSS and NED, for 5 objects these numbers are different (5BZUJ0933+0003, 5BZUJ1051+4644, 5BZUJ1058+0133, 5BZUJ1302+5748, 5BZUJ2156-0037). We checked and corrected redshift and for 4 (5BZUJ0933+0003, 5BZUJ1051+4644, 5BZUJ1302+5748, 5BZUJ2156-0037) sources is given by SDSS and for 1 (5BZUJ1058+0133) sources is given by BZCAT.

doi: https://doi.org/10.52526/25792776-23.70.1-83

Table 3. Spectral classification using SDSS spectra

Activity Type	**Numbers**
Abs	1
BLL	1
Em	4
LINER	2
NLQSO	1
QSO	17
QSO 1.2	3
QSO 1.5	1
Sy 1.2	1
Sy 1.5	2
Sy 1.8	1
Sy 2.0	3
Unknown	6
Total	43

3) Using SDSS spectra we have carried out classification in optical range. In table 3 we give information for this classification.

   In VCV–13 catalogue, if the absolute magnitude is more than -22.25 then the sources are classified as quasars in Véron-Cetty & Véron (2010). So, using that, among our sources we had classification QSO 1.2 and QSO 1.5. If these sources have absolute magnitude less than -22.25, we classify them as Sy1.2 and Sy1.5.
   QSO 1.2 and QSO 1.5 have the same properties which have Sy 1.2 and Sy1.5, and according to VCV catalogue there is only absolute magnitude limit -22.25.

Classification of BZCAT objects having BZG types

BZG objects from the BZCAT catalog were selected for study (Abrahamyan et al. (2023)). It is clear from Table 1 that we have 274 galaxies. 150 of the 274 BZG objects have optical spectra in the SDSS spectroscopic catalog. For these objects we have carried out a detailed classification using the SDSS spectra (table 1).

Using the data from various catalogs and the data bases VCV-13, NASA/IPAC Extragalactic Database (NED) and SDSS, we have clarified the optical classification of these sources prior to our classification. Table 2 lists these data. As it can be seen from Table 4, these objects do not have a detailed optical classification. They were classified as galaxies because in the optical range (in optical images) they have an extended shape.

Table 4. Classification of BZG Objects from VCV-13, NED, and SDSS

Classification	**SDSS spectra**	**VCV-13**	**NASA/IPAC**
S1	-	8	5
S2	-	4	1
S3 (LINER)	-	2	-
S?	-	1	-
BL	-	54	49
BL?	-	33	6
QSO	7	2	-
AGN	-	2	-
Galaxy	143	-	-
FSS source	-	-	21
Total	**150**	**106**	**82**

Figure 1 shows optical images of two of these extended blazars. The measurements of the SDSS spectra

doi: https://doi.org/10.52526/25792776-23.70.1-83

are very often based on lines at the noise level and of low quality.

As a result, automatic measurements lead to some unreal results. Thus, it is necessary to carefully check the spectra at all wavelengths and to decide which measurements should be used for further study.

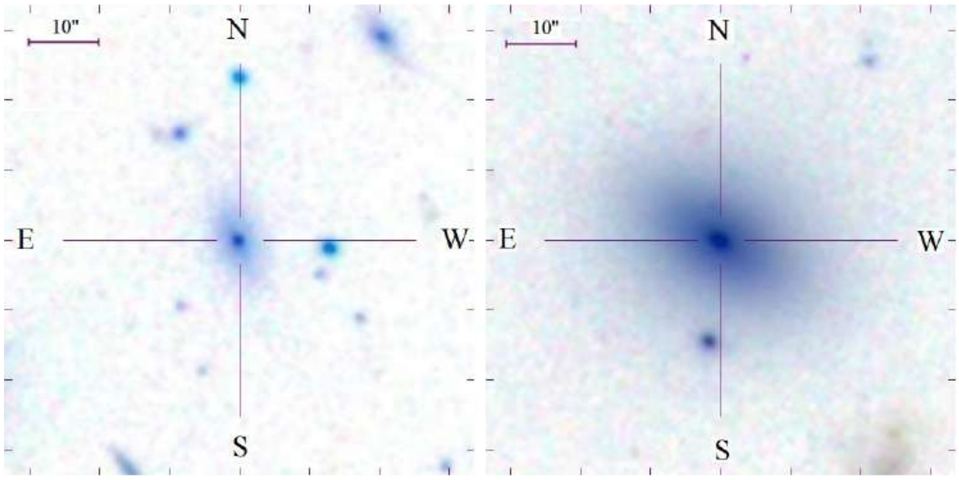

Figure 1. Optical images of the extended blazars 5BZG J0850+4036 and 5BZG 5BZG J0906+4124 from SDSS.

In Table 5 and in Fig. 2 we show our spectral classification for 150 BZG objects using the SDSS spectra. It is clear from Table 3 and Fig. 2 that these objects are mostly Em and Abs (about 80%) galaxies and had not been classified prior to us. 30 (20%) of the objects (S, LINER, and Composite) had no optical classification or changed class; only the blazar 5BZG J1532+3020 was classified as a LINER and remained as a LINER. Thus, it may be concluded that we are providing a detailed optical classification for essentially all the 150 objects.

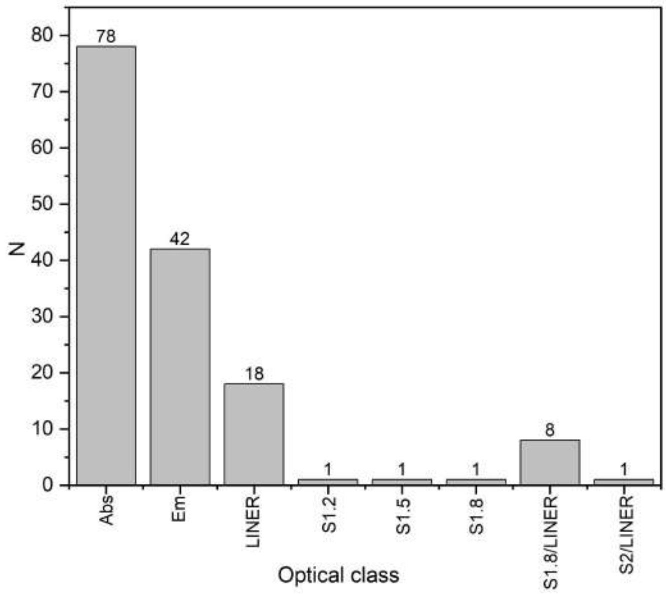

Figure 2. The new classification of the BZG objects using the SDSS spectra.

In order to clarify the optical nature of the extended blazars we have chosen BZG objects from the BZCAT catalog. Optical spectra from the SDSS catalog for 150 of the 274 BZG objects were used for a detailed spectral classification. Table 5 and Fig. 2 show that out of 150 objects, 30 (20%) have high quality optical spectra. We provided a new detailed spectral classification for 149 of the objects and only one object remained with its previous classification as a LINER.

doi: https://doi.org/10.52526/25792776-23.70.1-83

Table 5. Classification of BZG Objects Ising the SDSS Spectra

S1.2	1 (0.7%)
S1.5	1 (0.7%)
S1.8	1 (0.7%)
LINER	18 (12%)
S1.8/LINER	8 (5.2%)
S2.0/LINER	1 (0.7%)
Em	42 (28%)
Abs	78 (52%)
All	**150 (100%)**

Summary and Results

So, having optical spectra of 43 BZU, we reclassified these objects. As the main results we have: 1) 37 (86%) objects from 43 changed classification, 2) For 5 objects that numbers are different (5BZUJ0933+0003, 5BZUJ1051+4644, 5BZUJ1058+0133, 5BZUJ1302+5748, 5BZUJ2156-0037). We checked and corrected redshift and for 4 (5BZUJ0933+0003, 5BZUJ1051+4644, 5BZUJ1302+5748, 5BZUJ2156-0037) sources is given by SDSS and for 1 (5BZUJ1058+0133) source is given by BZCAT.

In order to clarify the optical nature of the extended blazars we have chosen BZG objects from the BZCAT catalog. Optical spectra from the SDSS catalog for 150 of the 274 BZG objects were used for a detailed spectral classification. In Table 5 and in Fig. 2 we show that of the 150 objects, 30 (20%) have high quality optical spectra. We provided a new detailed spectral classification for 149 of the objects and only one object remained with its previous classification as a LINER. A radio study showed that of the 150 objects, 104 have radio spectra. It is clear from Table 5 that these objects mostly have a flat radio spectrum (69%). For these objects, in the radio spectra the value of the radio-spectral index is less than ± 0.5 . Quasars predominate with these kinds of radio spectra, i.e., the objects being studied should be related, most likely, to Seyfert galaxies (objects classified as Em) and hidden AGN (objects classified as Abs). Table 3 shows that of the 150 objects, 78 have Abs spectra, although they are presented as BZG objects in the BZCAT catalog. Our detailed radio and optical study of these objects showed that in them the radio fluxes (1400 MHz, FIRST) form a fraction of 0.16 of the optical flux (SDSS_r). And also, of the 78 objects, 66 are X-ray sources. This again confirms our assumption that these objects may be hidden AGN.

In the future, we plan to carry out optical classification of BZCAT objects having BZQ and BZB types.

Acknowledgements

This work was partially supported by the Republic of Armenia Ministry of Education and Science (RA MES) State Committee of Science, in the frames of the research projects No. 15T-1C257 and 21AG-1C053 (2021-2026). This work was made possible in part by research grants from the Armenian National Science and Education Fund (ANSEF) based in New York, USA (PS-astroex-2597, 2022-2023).

References

Abdurro'uf et al., 2022, Astrophys. J. Suppl. Ser. , 259, 35

Abrahamyan H. V., Mickaelian A. M., Paronyan G. M., Mikayelyan G. A., Gyulzadyan M. V., 2019a, Communications of the Byurakan Astrophysical Observatory, 66, 1

Abrahamyan H. V., Mickaelian A. M., Paronyan G. M., Mikayelyan G. A., 2019b, Astronomische Nachrichten, 340, 437

Abrahamyan H. V., Mickaelian A. M., Paronyan G. M., Mikayelyan G. A., Sukiasyan A. G., 2023, Astrophysics, 66, 11

Hoffmeister C., 1929, Astronomische Nachrichten, 236, 233

Massaro E., Maselli A., Leto C., Marchegiani P., Perri M., Giommi P., Piranomonte S., 2015, Astrophys. Space. Sci. , 357, 75

Mickaelian A. M., Abrahamyan H. V., Mikayelyan G. A., Paronyan G. M., 2022, Communications of the Byurakan Astrophysical Observatory, 69, 10

Reines A. E., Greene J. E., Geha M., 2013, Astrophys. J. , 775, 116

Véron-Cetty M. P., Véron P., 2010, Astron. Astrophys. , 518, A10

doi: https://doi.org/10.52526/25792776-23.70.1-83

Study of the X-ray properties of radio sources, based on NVSS catalogue

G. M. Paronyan[*], A. M. Mickaelian[†], H. V. Abrahamyan[‡], G. A. Mikayelyan[§], A. G. Sukiasyan[¶], L. A. Hambardzumyan[‖] and V. K. Mkrtchyan[**]

NAS RA V. Ambartsumian Byurakan Astrophysical Observatory (BAO), Armenia

Abstract

An identification of radio sources from the NVSS list with ROSAT X-ray sources was made as well as also with optical objects from SDSS DR 16. We have tried to find the connection between the fluxes of different wave ranges, for different types of objects. We also have tried to find the relationship between the sizes and polarization angles of sources with the types of objects and recurrence. The fluxes detected from X-ray, optical, and radio bands for them are compiled. This database allows an investigation on broad band energy distribution and other possible correlations among spectral indices and luminosities for various types of extragalactic objects.

Keywords: *active galactic nuclei - radio source - NVSS - quasar - X-ray*

1. Introduction

In this work an attempt was made to create an X-ray selected radio source catalogue and make its multiwavelength (MW) studies, in order to find connections between the fluxes in different ranges of electromagnetic waves.

To ensure the homogeneity and completeness of the sample, only data from ROSAT catalogues have been taken for X-ray sources. The ROSAT satellite was endowed with an X-ray detector having sensitivity between 0.1–2.4 keV and with a mirror of 84 cm diameter. With this satellite a whole sky survey was accomplished in X-ray.

ROSAT data are mainly listed in three catalogs: ROSAT Bright Source Catalogue (BSC) (Voges et al., 1999a), ROSAT Faint Source Catalogue (FSC) (Voges et al., 2000b) and Second ROSAT all-sky survey (2RXS) source catalog (Boller et al., 2016a). They are clearly distinguished from each other by X-ray flux expressed in count-rate (CR) (the number of particles registered by the receiver per unit time). ROSAT-BSC contains 18,811 sources with CR $>$ 0.05 ct/s, while ROSAT-FSC, 105,924 sources with CR $<$ 0.05ct/s with a sensitivity limit CR $<$ 0.0005 ct/s. Thus ROSAT all-sky survey (2RXS) source catalog contain 135,118 X-ray sources (Boller et al., 2016a). There are thousands of interesting objects among them, and even though a number of recent X-ray missions have been conducted, ROSAT so far remains the only all-sky enough deep survey, particularly containing some 60,000–70,000 X-ray AGN.

In both catalogues, the selection of radio sources was made due to the following advantages of NVSS (Condon et al., 1998).

The NRAO VLA Sky Survey (NVSS) covers the sky north of -40 deg (82% of the celestial sphere) at 1.4 GHz. The principal data products are: (1) a set of 2326 4deg x 4deg continuum "cubes" with three planes containing Stokes I, Q, and U images plus,

(2) a catalog of almost 2x10^6 discrete sources stronger than S $\sim$ 2.5 mJy. The images all have theta = 45 arcsec FWHM resolution and nearly uniform sensitivity.

[*]paronyan_gurgen@yahoo.com, Corresponding author
[†]aregmick@yahoo.com
[‡]abrahamyanhayk@gmail.com
[§]gormick@mail.ru
[¶]andranik.suqiasyan.1995@mail.ru
[‖]hambardzumyanlian@gmail.com
[**]varduhi.mkrtchyan.99@bk.ru

doi: https://doi.org/10.52526/25792776-23.70.1-88

We combined these two Catalogues and created a new homogeneous and complete catalogue of X-ray selected radio source, which covers all sky limited by north of -40 deg.

Thus we have obtained the X-ray large-area homogeneous complete radio sources sample and made possible detailed studies of their MW properties.

2. Combination of ROSAT and NVSS and collection of accurate photometric data

In order to avoid further mistakes and errors, before starting the main work, we studied in details the catalogue.

For detection of AGN‘s these two catalogues were cross-matched with the Catalogue of QSOs and Active Nuclei, Version 13 (Véron-Cetty & Véron, 2010, , hereafter VCV-13). VCV-13 includes only those objects, which have optical spectra and their spectroscopic studies confirmed their AGN nature. It contains 168,940 AGN. To complement VCV-13, we also used BZCAT (Massaro et al., 2015) due to its better completeness for blazars (high probability X-ray sources).

We have carried out homogeneous search for all available data in various databases, including non-optical ranges. In order to make final identifications we used all the listed catalogues, which more or less guarantee the completeness condition (we have used all-sky or large-area surveys) and provide many flux measurements at different bands:

- γ-ray: FERMI (Nolan et al., 2012), INTEGRAL (Bird et al., 2010);
- X-ray: ROSAT (Boller et al., 2016a), XMM-Newton DR12 (Webb et al., 2023); Chandra Source Catalog V2.0 (Evans et al., 2019);
- UV: GALEX (**?**);
- Optical: APM (McMahon et al., 2000), USNO-B1.0 (Monet et al., 2003), GSC 2.3.2 (Lasker et al., 2021), SDSS DR16 (Ahumada et al., 2020);
- IR: 2MASS Point Source Catalogue (PSC, Cutri et al., 2003), 2MASS Extended Source Catalogue (ESC, Skrutskie et al., 2006), WISE (Cutri & IPAC/WISE Science Data Center Team, 2012), IRAS Point Source Catalogue (PSC, Beichman et al., 1988), IRAS Faint Source Catalogue (FSC, Moshir et al., 1992), IRAS PSC/FSC Combined Catalogue (Abrahamyan et al., 2015); IRAS Combined Catalogue contains all sources from PSC and FSC;
- Radio: NVSS (Condon et al., 1998), FIRST (White et al., 1997).

Out of the 9193 objects (from cross-correlation between ROSAT and NVSS), 3259 sources were confirmed as AGN by means of optical spectral classifications, the main criteria in VCV-13 and BZCAT.

Graphs and histograms of the distribution of sources at different ranges, stellar magnitudes and the data dependence on each other were built in order

We have carried out cross-correlations of our sample with the recent all-sky and large-area catalogues from γ-ray to radio. To determine the correct search radius for all cross-correlations and avoid misidentifications, a preliminary identification was made with a large radius, and then the distribution of distances of identifications was constructed for all sources. This allowed determine the correct search radius. Figure 1 gives an example of such computation for NVSS catalogue.

We conclude that objects with distances from the input positions up to 20 arcsec should be considered as genuine associations, though the real search radius were taken larger not to miss some genuine associations having larger positional errors.

Table 1 provides the numbers of 8037 identified ROSAT sources in various catalogues.

For 2372 objects in our sample there are spectra from SDSS DR16, we are do a detailed spectral classification thus.

In order to distinguish AGN among all X-ray sources, we need to identify which are the flux ratio limits that give us opportunity to do this. Graphs and histograms based on the collected data were constructed for this purpose. This will allow finding all observed QSOs and other AGN in the nearby Universe having detected X-ray radiation and the exact number of existing X-ray AGN as a fraction of all AGN.

doi: https://doi.org/10.52526/25792776-23.70.1-88

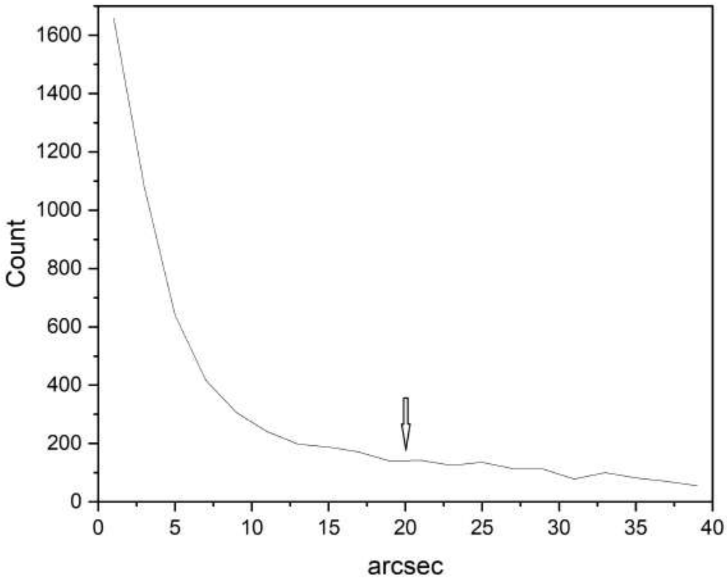

Figure 1. Example of computation of the correct radius of identifications for NVSS catalogue.

Table 1. Results of cross-correlations of ROSA/NVSS sources with MW catalogues.

Catalogs	Search (arcsec)	N	Catalogs	Search (arcsec)	N
FERMI	250	1129	INTEGRAL	250	104
XMM-Newton DR12	20	815	Chandra V2.0	20	611
ROSAT	–	9193	GALEX	40	6056
APM	10	4222	USNO-B1.0	10	7721
GSC 2.4.2	10	6067	SDSS DR16	40	2372
2MASS	5	3825	WISE	10	7870
IRAS	60	409	NVSS	30	9193
FIRST	20	3512	VCV-13	30	3094
BZCAT	15	1318			

3. Physical and statistical properties of identified X-ray sources

The Catalogue consists of 9193 X-ray selected sources, including 3993 confirmed AGN, QSO or BL Lac and 5200 their candidates. In order to check these objects as AGN, QSO or BL Lac and to find new ones, we have built diagrams of the dependence between various data for these sources, as well as normal galaxies and stars have been used for comparisons.

In Figure 2 the hardness ratio HR2 is plotted *vs*. Count for different classes of objects. There is a slight difference in the distribution of HR2 showing a separation between QSO, AGN and BL Lac. To remind, hardness ratios are defined as:

$$HR2 = \frac{[D]-[C]}{[D]+[C]}, \tag{1}$$

where [D] and [C] are the count rates in the corresponding energy bands: C = 0.52–0.90 keV, and D = 0.91–2.01 keV.

An interesting feature is seen in AGN. Their distribution has a double peak, this may be due to the fact that two types of objects are possibly hidden under this definition. This issue will be carefully studied by us in the future.

Having X-ray and Radio fluxes, we have built the dependence of luminosity on redshift graph (see Figure 3).

Active galaxies and Blazars are very interesting objects in the Universe. In order to understand some physical properties, we must identify which properties our objects have in X-ray and radio range. We have 3993 active galaxies with X-ray/radio fluxes at different wavelengths. A very important X-ray/radio

doi: https://doi.org/10.52526/25792776-23.70.1-88

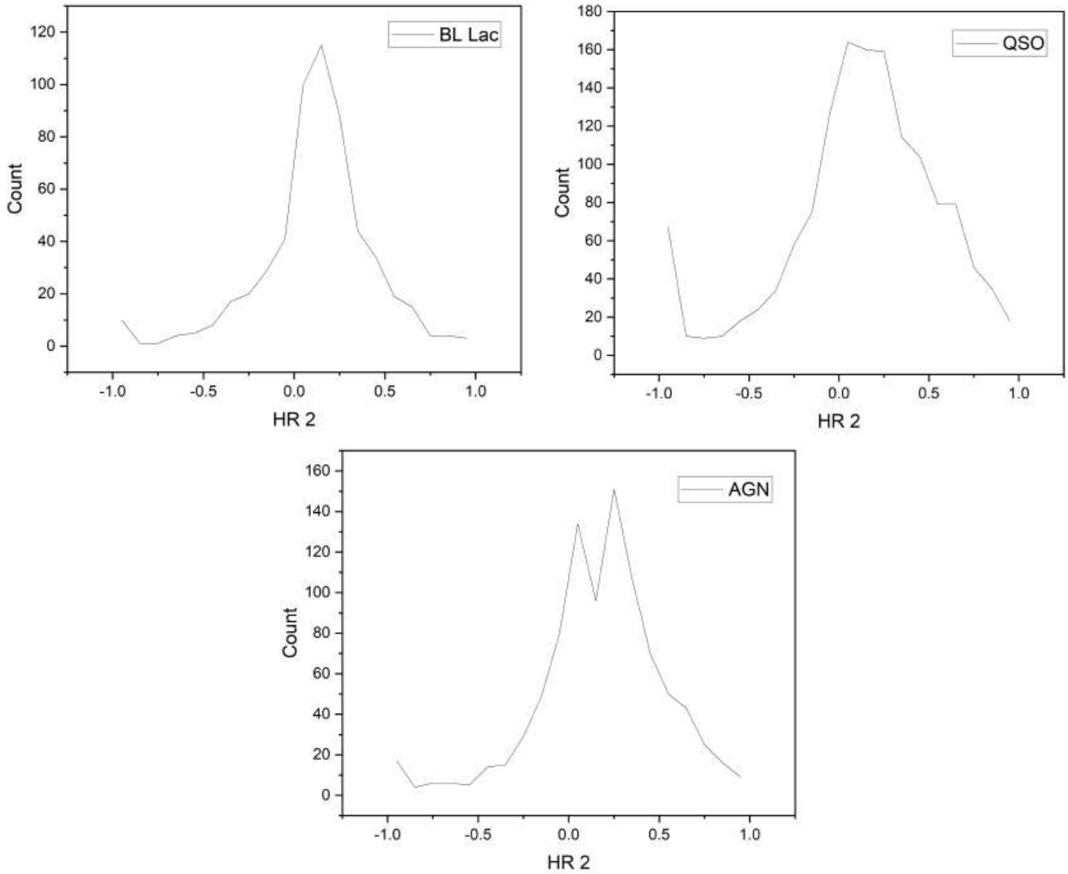

Figure 2. The distribution of HR2 for various types of object: BL Lac, QSO and AGN.

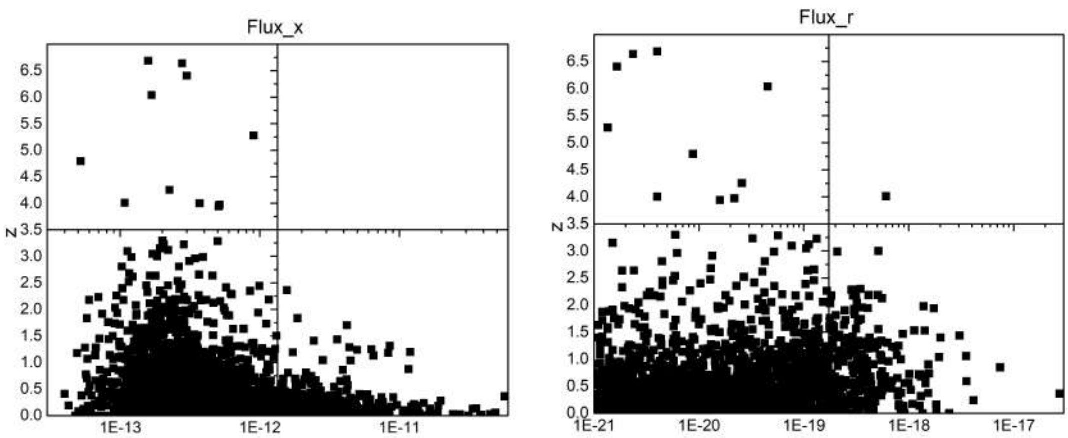

Figure 3. Distribution of redshift to X-ray and Radio flux.

property for objects is the spectral index. Using more bands, we have developed a graph for all sources (lg[flux] vs. lg[frequencies]). Using an lg[flux] versus lg[frequencies] graph for each source, we have made linear fitting. The software "Origin" gives the formula for each linear fit, and using that, we have measured the X-ray/radio spectral index for each source.

The table shows that in the X-ray range, the energy flux decreases from BL Lac to QSO, but but in the radio range, on the conversely, the flux increases from BL Lac to QSO. This is a very interesting effect and will be throughly studied by us in the future.

4. Summary and Conclusion

We have cross-correlated ROSAT PSC and FSC X-ray catalogues with NVSS radio catalogue to reveal objects with both X-ray and radio, very high probability active galaxies (mostly AGN but also Starbursts).

doi: https://doi.org/10.52526/25792776-23.70.1-88

Table 2. Distribution of X-ray and Radio band fluxes for Blazars, AGN's and QSO's

N	Catalog	BL Lac	AGN	QSO
1	$NVSS_F$	6.24x10^{-20}	1.33x10^{-19}	2.64x10^{-19}
2	$FIRST_F$	3.09x10^{-20}	3.41x10^{-20}	1.17x10^{-19}
3	$ROSAT_F$	3.49x10^{-12}	2.41x10^{-12}	8.44x10^{-13}
4	XMM_{F8}	2.45x10^{-11}	1.64x10^{-11}	6.83x10^{-12}
5	$Chandra_{Fb}$	3.18x10^{-12}	2.41x10^{-12}	1.64x10^{-12}

Moreover, objects having both X-ray and radio must be among the strongest AGN, namely Blazars and powerful QSOs. Therefore, SDSS spectra will be later used for classification for activity types.

Further work will be related to multiwavelength studies of these sources, as well as detailed classification for the activity types (based on our Fine Classification; Mickaelian et al., 2021, https://www.bao.am/activities/projects/21AG-1C053/mickaelian/).

Acknowledgements

This work was partially supported by the Republic of Armenia Ministry of Education and Science (RA MES) State Committee of Science, in the frames of the research projects No. 15T-1C257 and 21AG-1C053 (2021-2026). This work was made possible in part byresearch grants from the Armenian National Science and Education Fund (ANSEF) based in New York, USA (PS-astroex-2597, 2022-2023)

References

Abrahamyan H. V., Mickaelian A. M., Knyazyan A. V., 2015, Astronomy and Computing, 10, 99

Ahn C. P., et al., 2014, Astrophys. J. Suppl. Ser. , 211, 17

Ahumada R., et al., 2020, Astrophys. J. Suppl. Ser. , 249, 3

Beichman C., G. N., Habing H., P.E. C., T.J. C., 1988, Infrared astronomical satellite (IRAS) catalogs and atlases. Volume 1: Explanatory supplemen, 1

Bird A. J., et al., 2010, Astrophys. J. Suppl. Ser. , 186, 1

Boller T., Freyberg M. J., Trümper J., Haberl F., Voges W., Nandra K., 2016a, Astron. Astrophys. , 588, A103

Boller T., Freyberg M. J., Trümper J., Haberl F., Voges W., Nandra K., 2016b, Astron. Astrophys. , 588, A103

Cohen M., Wheaton W. A., Megeath S. T., 2003, Astron. J. , 126, 1090

Condon J. J., Cotton W. D., Greisen E. W., Yin Q. F., Perley R. A., Taylor G. B., Broderick J. J., 1998, Astron. J. , 115, 1693

Cox A. N., 2000, Allen's astrophysical quantities

Cutri R. M., IPAC/WISE Science Data Center Team 2012, in American Astronomical Society Meeting Abstracts #219. p. 401.06

Cutri R. M., et al., 2003, 2MASS All Sky Catalog of point sources.

Evans I. N., et al., 2019, VizieR Online Data Catalog, p. IX/57

Fukugita M., Ichikawa T., Gunn J. E., Doi M., Shimasaku K., Schneider D. P., 1996, Astron. J. , 111, 1748

Hagen H. J., Groote D., Engels D., Reimers D., 1995, Astron. and Astrophys. Suppl. Ser. , 111, 195

La Franca F., Gregorini L., Cristiani S., de Ruiter H., Owen F., 1994, Astron. J. , 108, 1548

Landt H., Padovani P., Perlman E. S., Giommi P., Bignall H., Tzioumis A., 2001, Mon. Not. R. Astron. Soc. , 323, 757

Lasker B. M., et al., 2008, Astron. J. , 136, 735

Lasker B., et al., 2021, VizieR Online Data Catalog, p. I/353

Laurent-Muehleisen S. A., Kollgaard R. I., Ciardullo R., Feigelson E. D., Brinkmann W., Siebert J., 1998, Astrophys. J. Suppl. Ser. , 118, 127

Massaro E., Maselli A., Leto C., Marchegiani P., Perri M., Giommi P., Piranomonte S., 2015, Astrophys. Space. Sci. , 357, 75

McMahon R. G., Irwin M. J., Maddox S. J., 2000, VizieR Online Data Catalog, p. I/267

Mickaelian A. M., Hovhannisyan L. R., Engels D., Hagen H. J., Voges W., 2006, Astron. Astrophys. , 449, 425

Mickaelian A. M., Abrahamyan H. V., Paronyan G. M., Mikayelyan G. A., 2021, Frontiers in Astronomy and Space Sciences, 7, 82

doi: https://doi.org/10.52526/25792776-23.70.1-88

Monet D. G., et al., 2003, Astron. J. , 125, 984

Morrissey P., et al., 2007, Astrophys. J. Suppl. Ser. , 173, 682

Moshir M., Kopman G., Conrow T. A. O., 1992, IRAS Faint Source Survey, Explanatory supplement version 2

Natali F., Giallongo E., Cristiani S., La Franca F., 1998, Astron. J. , 115, 397

Nolan P. L., et al., 2012, Astrophys. J. Suppl. Ser. , 199, 31

Oke J. B., 1974, Astrophys. J. Suppl. Ser. , 27, 21

Padovani P., 1993, Mon. Not. R. Astron. Soc. , 263, 461

Paronyan G. M., Mickaelian A. M., Harutyunyan G. S., Abrahamyan H. V., Mikayelyan G. A., 2019, Astrophysics, 62, 147

Perlman E. S., Padovani P., Giommi P., Sambruna R., Jones L. R., Tzioumis A., Reynolds J., 1998, Astron. J. , 115, 1253

Perlmutter S., et al., 1999, Astrophys. J. , 517, 565

Riess A. G., et al., 2004, Astrophys. J. , 607, 665

Schmitt J. H. M. M., Fleming T. A., Giampapa M. S., 1995, Astrophys. J. , 450, 392

Schwope A., et al., 2000, Astronomische Nachrichten, 321, 1

Skrutskie M. F., et al., 2006, Astron. J. , 131, 1163

Urry C. M., Padovani P., 1995, Publ. Astron. Soc. Pac. , 107, 803

Véron-Cetty M. P., Véron P., 2010, Astron. Astrophys. , 518, A10

Voges W., et al., 1999a, Astron. Astrophys. , 349, 389

Voges W., et al., 1999b, Astron. Astrophys. , 349, 389

Voges W., et al., 2000a, IAU Circ., 7432, 1

Voges W., et al., 2000b, IAU Circ., 7432, 3

Webb N. A., et al., 2020, Astron. Astrophys. , 641, A136

Webb N. A., et al., 2023, VizieR Online Data Catalog, p. IX/68

White R. L., Becker R. H., Helfand D. J., Gregg M. D., 1997, Astrophys. J. , 475, 479

Wisotzki L., 2000, Astron. Astrophys. , 353, 861

Wright E. L., et al., 2010, Astron. J. , 140, 1868

Zickgraf F. J., Engels D., Hagen H. J., Reimers D., Voges W., 2003, Astron. Astrophys. , 406, 535

de Vaucouleurs G., de Vaucouleurs A., Corwin H. G. J., Buta R. J., Paturel G., Fouque P., 1991, Sky Telesc. , 82, 621

della Ceca R., Maccacaro T., Gioia I. M., Wolter A., Stocke J. T., 1992, Astrophys. J. , 389, 491

doi: https://doi.org/10.52526/25792776-23.70.1-88

BL Lacertae: a study of quasi-stationary feature trajectories in the inner part of a relativistic jet

L.A. Hambardzumyan *[1,2], T.G. Arshakian †[1], and A.B. Pushkarev ‡[3]

[1]Byurakan Astrophysical Observatory after V.A. Ambartsumian, Armenia
[2]Astrophysical Research Laboratory, YSU, Armenia
[3]Crimean Astrophysical Observatory, Nauchny, Crimea

Abstract

Radio interferometric VLBA observations allow the mapping of relativistic jets with sub-milliarcsecond resolution, which enables the studying of the fine structure and dynamics of the jets in active galactic nuclei. A quasi-stationary component (QSC) near the radio core is observed in a number of blazars. VLBA monitoring of the BL Lacertae object at 15 GHz has shown that the QSC located at about 0.26 mas from the radio core is followed by superluminal components, whose dynamics forms the structure of the jet on parsec scales. We study the trajectory of the QSC using the 164 epochs taken from the MOJAVE (Monitoring Of Jets in Active galactic nuclei with VLBA Experiments) database. The trajectory of the QSC is complex, and we use a moving average smoothing filter to track the intrinsic motion of the QSC. At small time scales of few months, we find that the QSC makes a swinging motion with about 23 reversals over 20 years with an average period of about 0.5 years. The trajectories between the reversals have varying lengths with a mean value of about 30 μas ($\sim$ 0.04 pc) and curvatures of varying degrees. Number of clockwise reversals are about twice less than that of anticlockwise reversals.

Keywords: *BL Lacertae objects: individual: BL Lacertae, galaxies: active, radio continuum: galaxies, galaxies: jets.*

1. Introduction

About 10% of active galactic nuclei (AGN) are radio-loud. The central engine transforms the accretion power of a disk orbiting around a supermassive black hole into the kinetic energy of relativistic plasma in bipolar outflows. Synchrotron radio emission is generated towards the observer by the jet plasma moving along the helical magnetic fields. Observations with interferometric radio telescopes make it possible to map the radio jets with the highest resolution. This opens a possibility to study the structure of the jet and its dynamics on sub-milliarcsecond scales.

As a class of radio-loud AGNs, blazars are characterised by jets oriented at small angles to the line of sight. In this article we study the archetypical source of this class, BL Lacertae, located at redshift $z = 0.0686$ (Vermeulen et al., 1995) (scale factor is 1.3 pc mas^{-1}). Monitoring of BL Lacertae with Very Long Baseline Array (VLBA) at 15 GHz has revealed that the jet consists of a bright radio core followed by a quasi-stationary component (QSC) at a distance of 0.26 mas. The latter is labeled as C7 (Arshakian et al., 2020, Cohen et al., 2014, 2015). Moving superluminal components appear to emerge beyond C7 component. Cohen et al. (2015) suggested that the dynamics of the quasi-stationary component C7 shapes the behavior of the jet downstream up to distances of hundreds parsecs. Arshakian et al. (2020) used larger data sample collected from 116 epochs (1999–2016) and confirmed the link between the large amplitudes of C7 shaking and excitation of superluminal transverse waves propagating downstream during both the active and stable states of the jet. They showed that C7 moves mostly with superluminal speeds ($\sim 2c$) and its on-sky brightness distribution is asymmetric along and across the jet axis.

Here, we use the VLBA monitoring data at 15 GHz accumulated during almost over 20 years time period (164 epochs), which is a part of the MOJAVE (Monitoring Of Jets in Active galactic nuclei with VLBA

*hambardzumyanlian@gmail.com, Corresponding author
†t.arshakian@gmail.com
‡pushkarev.alexander@gmail.com

doi: https://doi.org/10.52526/25792776-23.70.1-94

Experiments) program (Kellermann et al., 1998, Lister et al., 2018), to perform a detailed analysis of the C7 trajectory on sub-parsec scales.

2. Scatter of C7 positions

Data reduction, modeling and error estimation are described in Lister et al. (2009), Cohen et al. (2014, 2015) and Arshakian et al. (2020). The distribution of scattered positions of C7 for a time period of 1999.37–2019.97 is shown in Figure 1. The median center is at position $\mathrm{RA}_{\mathrm{med}} = -0.051$ mas and $\mathrm{Dec}_{\mathrm{med}} = -0.255$ mas. The line connecting the radio core and the median center of C7 is considered to be the central axis of the jet, which has a positional angle PA $= -169°$. The scatter of C7 positions has a quasi-circular distribution (~ 0.1 mas) with a slight elongation along the jet axis. To study the C7 motion, Arshakian et al. (2020) introduced a displacement vector **r**, which describes the direction of motion of C7 between two consecutive epochs. The time intervals Δt between observations vary from a few days to several months with a median value of about 34 days. The median positional uncertainties of C7 along and across the jet are 5 μas and 2 μas, respectively. Arshakian et al. (2020) treated them as lower limits, while the real errors can be larger by a factor from 1.5 to 2.

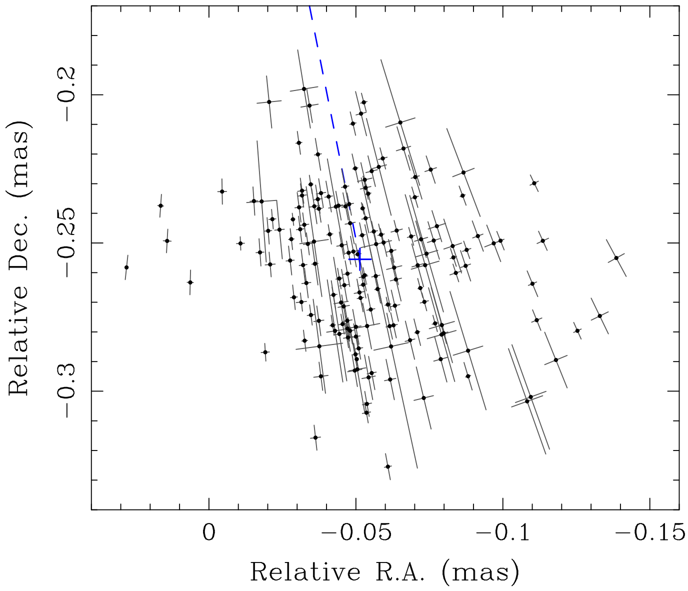

Figure 1. On-sky distribution of 164 positions of C7 in the RA–Dec plane. The positional errors of C7 are asymmetric along and across the jet. The jet central axis (dashed line) connects the radio core put at the phase center (0,0) with the median position of C7 (plus sign).

3. Detailed analysis of trajectory of quasi-stationary component

We study the trajectory of C7 and its morphology for 164 epochs of observations, which is larger than that of Arshakian et al. (2020) by 48 epochs covering additional four years. The observed motion of C7 component is a combination of its intrinsic and asymmetric motion of the radio core, which occurs along the jet axis (Arshakian et al., 2020). It was estimated that the anisotropic core shift has a standard deviation 0.025 mas, while the C7 intrinsic motion has a mean displacement 0.02 mas and standard deviation 0.012 mas, implying that their contribution to the apparent motion of C7 are of comparable importance. To reduce the impact of the core shift we apply the moving average smoothing filter to apparent trajectory of C7 and thus recover the C7 intrinsic trajectory. In Figure 2, we present the C7 trajectory smoothed with sliding window of size $m = 4$ (where m is the number of consecutive positions), which seems to be optimal for our study. In this case, the smoothing scale is about 0.055 mas, which translates to about 0.07 pc.

doi: https://doi.org/10.52526/25792776-23.70.1-94

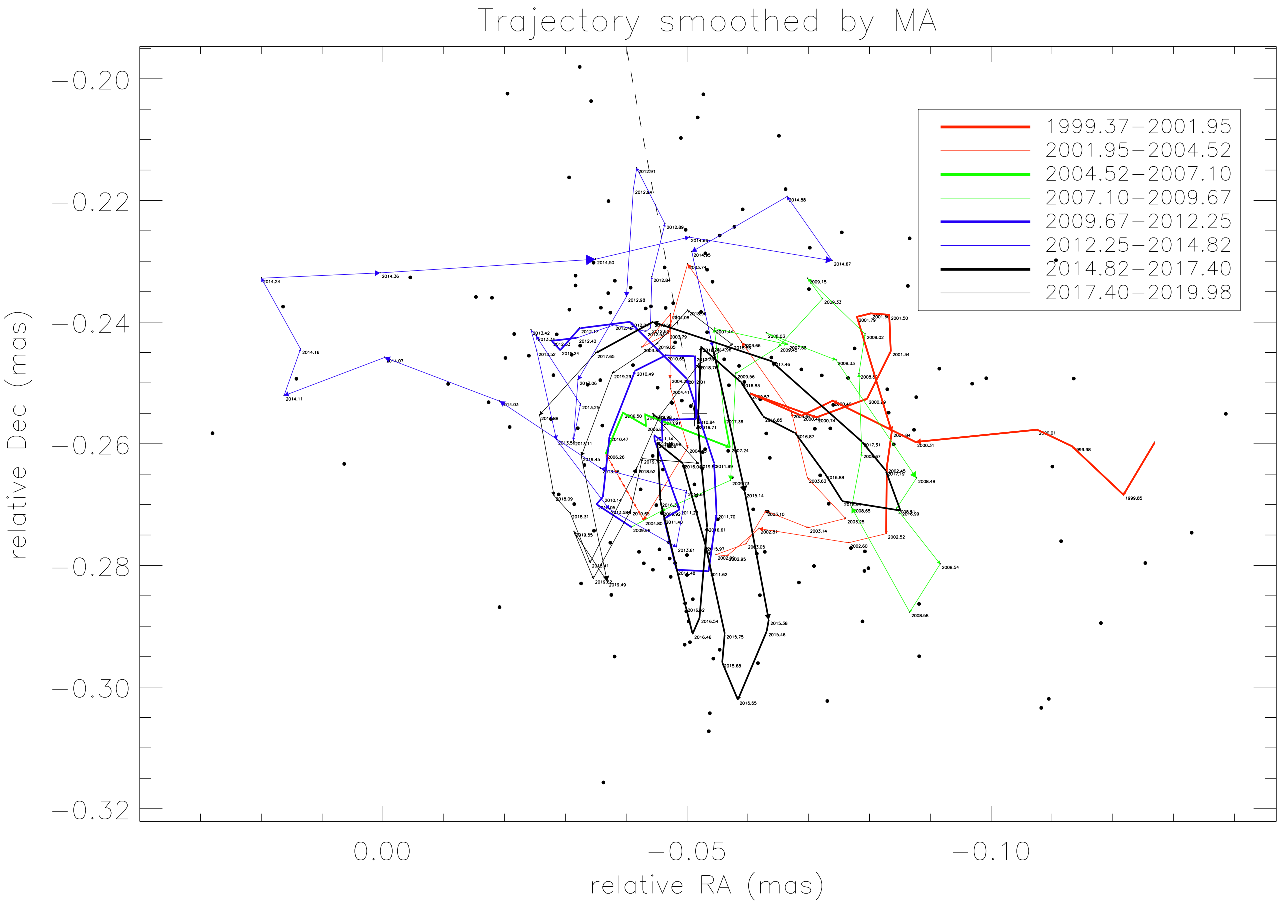

Figure 2. The apparent trajectory of C7 smoothed by moving average method with sliding window of length $m = 4$. The numbers along the smoothed trajectory are the observation epochs in years. The observed positions of C7 component are marked by dots. The radio core is at $(0, 0)$ position, which is connected with the median position of C7 (plus sign) by the jet central axis (dashed line). Thick and thin colored lines represent the time intervals of 2.95 years. Arrows indicate the direction of movement.

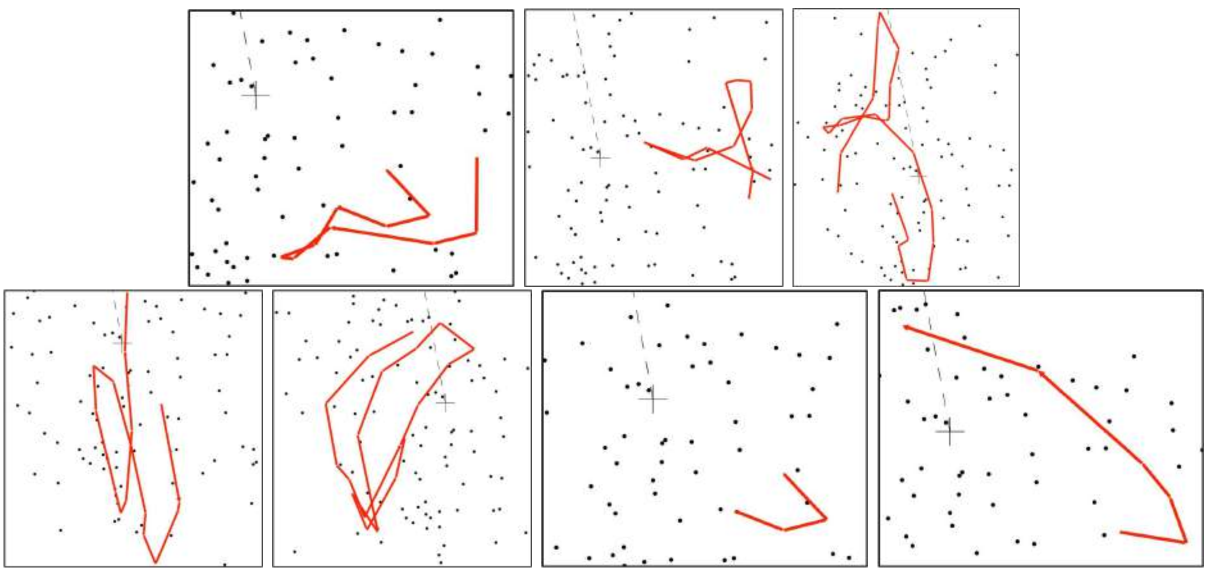

Figure 3. Examples of types of reversals: U-type irregular reversals (upper three panels), U-type quasi-regular reversals (lower first two panels), V-type reversal (third panel), and arch-like motion. The reversals shown occur during the following time intervals: 1 - 2001.79–2003.14, 2 - 2000.01–2001.84, 3 - 2011.00–2012.98, 4 - 2017.30–2019.63, 5 - 2014.95–2016.61, 6 - 2ßß2.96–2003.25, 7 - 2016.87–2017.31. The median position of the scatter is marked by a plus sign and dashed line connects the median position of C7 and radio core.

doi: https://doi.org/10.52526/25792776-23.70.1-94

Visual inspection of the trajectory reveals repetitive patterns, which may appear from a few to many times. Patterns like a reversing motion appear very frequently, there are also arch- and loop-like motion but they are less frequent. Between these patterns, the motion of C7 is represented by curving trajectories of varying degrees as well as quasi-oscillatory movements (see Figure 3).

Reversal motions on large spatial scales are conspicuous, e.g. component C7 moving westward and then reversing eastward during 2014–2014.5 (thin blue line in Figure 2) or component moving southward and reversing northward in 2015.55 during 2014.96-2016.04 (thick black line). Both reversals occur at spatial scales around 0.05 mas (0.07 pc) and have clockwise motion. It should be noted that most reversals occur on time scales of a few months.

3.1. Reversals and their characteristics

To define and characterise a reversal motion of C7 we introduce some criteria. We consider that a reversal is real if it consists of at least three successive segments of trajectory (or four epochs), which includes the reversal point and the angle at the reversal point is $< 90°$. We identify 23 reversals and among these we distinguish the U-turns ($< 45°$), V-turns ($> 45°$ and $< 90°$) and loop-like reversals (see Figure 3).

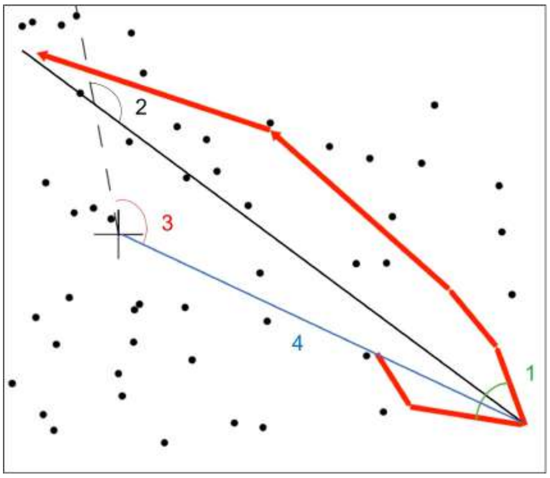

Figure 4. Characteristics of reversals: 1 - reversal angle, 2 - angle between jet and reversal direction, 3 - azimuthal angle, 4 - radial distance. Demonstrated is a typical U-reversal during 2016.85–2017.31. The median position of the scattered positions is marked by a plus sign and dashed line connects the median position of C7 and radio core.

To characterise the reversals, we performed the following measurements (see Figure 4):

- Reversal angle is the angle between two segments at the turning point. It is noticeable that 20 reversals have U-turns, 3 V-turns and among these 3 reversals have a loop-like structure.
- Time intervals between two successive reversals. Typical reversal period is about 0.5 yr and it is mostly ranged from 0.2 to 1.5 yr, with two outliers of about 3–3.5 yr (see Figure 5).
- Clockwise and counterclockwise direction of motion is defined at the turning point of a reversal. There are 15 counterclockwise and 8 clockwise reversals.
- Amplitude of reversals is the half of the length of segments making up the turn. The distribution of amplitudes has a mean value 0.032 mas and standard deviation 0.013 mas (Figure 6, top left panel). Amplitudes with the clockwise and counterclockwise reversals have similar distributions.
- Azimuthal angle is the angle between the median center and the turning point. Azimuthal angles of the clockwise and counterclockwise reversals have a uniform distribution. This tendency is true for the V-type reversals (Figure 6, bottom left panel).
- Radial distance is defined as the distance between the median center of scattered positions and the turning point. In Figure 6 (top right panel) it is clearly seen that the distribution of reversals are not random, there is a clustering of reversals at 0.029 mas with standard deviation 0.015 mas. Radial

doi: https://doi.org/10.52526/25792776-23.70.1-94

distances of the clockwise reversals (except one outlier) are smaller and lie within ~ 0.03 mas from the median center.

- Angle between the jet and the reversal direction. Angles for counterclockwise reversals have peak between 0° and 20° (Figure 6, bottom right panel), which indicates that majority of directions of counterclockwise reversals coincide with direction of the jet within 20°. Contrary, the angles of clockwise reversals have a uniform distribution.

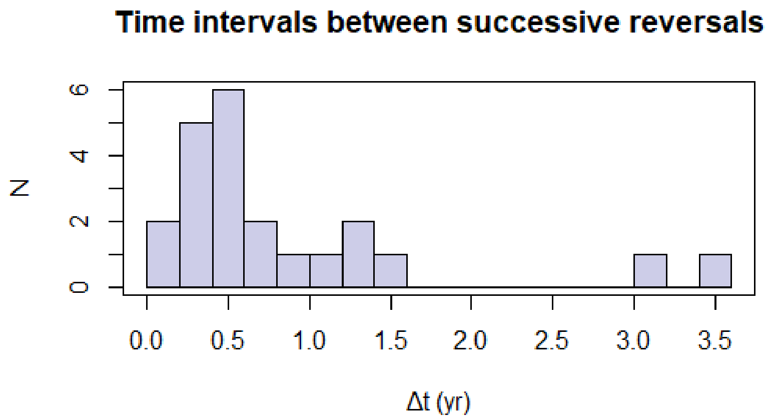

Figure 5. Distribution of time intervals between successive reversals.

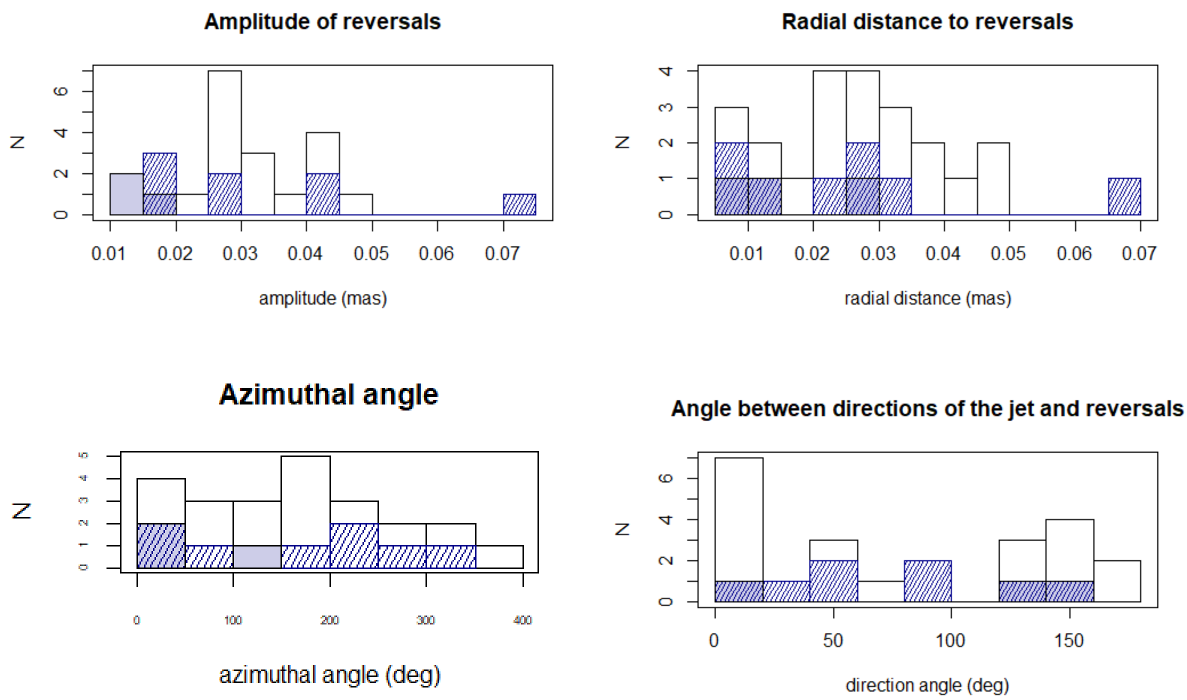

Figure 6. Distributions of amplitudes of reversals, radial distance to reversing point, azimuthal angle and angle between the jet and the direction of reversal. The white colour represents all types of reversals, the blue colour indicates the V-turns and the sloping blue lines indicate the clockwise reversals.

.

4. Discussion and Summary

A detailed analysis of the smoothed trajectory of the quasi-stationary C7 component shows that it performs swinging motion at various scales within 0.1 mas over a time period of 20 years. We identify

doi: https://doi.org/10.52526/25792776-23.70.1-94

recurrent motion patterns such as 20 U-type and 3 V-type reversals. The reversals occur with a typical period of 0.5 yr and the mean amplitude of about 0.03 mas. The fact that the component moves in most cases along a U-turn trajectory indicates the physical nature of this movement. Such motions can occur, for example, when a transverse wave passes along the jet, while the stationary component behaves like a seagull on a wave, i.e. moving across the stream. For BL Lac, the jet viewing angle is about 8° (Cohen et al., 2015), so the component will make reversal movements from the observer's point of view. In this case, changing the angle between the jet and reversal direction (Figure 4) means generating a new transverse wave in the jet. It is known that transverse waves move with relativistic velocities of the order of 0.95–0.98 of the speed of light (Cohen et al., 2015), which can form an illusion of superluminal velocities of the quasi-stationary component in the observer's rest of frame. The measurement of superluminal velocities of C7 component exceeding the speed of light by two times was found by Arshakian et al. (2020). A detailed study of such a scenario will be carried out in subsequent papers.

The number of the counterclockwise turns is more than twice the number of clockwise turns. To understand such a significant difference, it is necessary to investigate at what time and spatial scales the reversals occur. The same applies to the angle between the jet and reverse directions.

Acknowledgements

The VLBA is a facility of the National Radio Astronomy Observatory, a facility of the National Science Foundation that is operated under cooperative agreement with Associated Universities, Inc. This research has made use of data from the MOJAVE database that is maintained by the MOJAVE team (Lister et al., 2018).

References

Arshakian T. G., Pushkarev A. B., Lister M. L., Savolainen T., 2020, Astron. Astrophys. , 640, A62

Cohen M. H., et al., 2014, Astrophys. J. , 787, 151

Cohen M. H., et al., 2015, Astrophys. J. , 803, 3

Kellermann K. I., Vermeulen R. C., Zensus J. A., Cohen M. H., 1998, AJ, 115, 1295

Lister M. L., et al., 2009, Astron. J. , 138, 1874

Lister M. L., Aller M. F., Aller H. D., Hodge M. A., Homan D. C., Kovalev Y. Y., Pushkarev A. B., Savolainen T., 2018, Astrophys. J. Suppl. Ser. , 234, 12

Vermeulen R. C., Ogle P. M., Tran H. D., Browne I. W. A., Cohen M. H., Readhead A. C. S., Taylor G. B., Goodrich R. W., 1995, Astrophys. J. Lett. , 452, L5

doi: https://doi.org/10.52526/25792776-23.70.1-94

The discrepancy between the values of the Hubble constant and the effect of dark energy on baryonic matter

H.A.Harutyunian *

Byurakan Astrophysical Observatory, Armenia

Abstract

It seems clear that researchers have not yet fully appreciated the true implications of the discovery of dark energy for understanding evolutionary processes in the baryonic universe. Based on general physical considerations, we consider here the influence of dark energy on baryon objects at the level of atomic nuclei and elementary particles. For such an analysis, the concept is adopted, according to which the entire baryonic Universe interacts with dark energy on all cosmic scales. The consequences seem quite dramatic, since the accumulation of energy in the baryon world changes the energy balance and reduces the binding energy of all objects, including atomic nuclei. Consequently, the nuclear mass defect decreases, their mass increases, and both effects make the nuclei more and more unstable. This leads to the destabilization of all nuclei and their gradual transfer to the stage of radioactive decay, which increases over time the relative amount of light elements, including hydrogen. Evolution under the influence of dark energy, on the other hand, increases the masses of atomic nuclei. We have used this hypothetical effect to interpret the so-called "Hubble tension" paradox. This also makes it possible to estimate the growth of the proton mass due to dark energy.

Keywords: *Dark energy, baryon matter, interaction, energy exchange, Hubble constant: Hubble tension, evolution, mass growth, blueshift, metallicity*

1. Introduction.

The main paradigm, on the basis of which the model of the physical world is built in any field of science, is always consistent with the set of empirical data existing at a given stage in the development of science. When the accuracy of the data is not high enough, a more primitive or at least not perfect model of the physical processes under consideration can be used as the basis for the theoretical interpretation of these data. Therefore, any refinement of empirical data in a given field of science can often lead to paradoxical results if the main paradigm of this field is completely or partially erroneous.

Undoubtedly such was the world of Ptolemy - the geocentric system of the Universe. It was based on observational data on the movement of planets and stars, and at one time described the details of these movements quite well. But since the model was wrong, the accuracy was ensured by a set of free parameters, so the required accuracy could be provided only in a limited period of time. This is similar to polynomial approximation of an unknown function. In interpolation mode, the method works quite well, but it is worth going beyond the fixed values of the argument, and violent oscillations begin.

Modern cosmology is one of the most intensively researched and theoretically developed branches of science. It was built on the basis of observational data and some fundamental hypotheses, among which the central ones are the big bang hypothesis, as well as the Kant-Laplace hypothesis about the formation of cosmic objects (and their systems) from more rarefied matter. Any new phenomenon, observational fact, must be consistent with a number of such "absolute truths".

Today I wanted to dwell on one problem, refusing at the same time from the dictates of petrified ideas about the evolution of cosmic objects. Rather, taking into account new observational data, namely, the existence of dark energy, based on the analysis of physical processes, the idea is put forward that atomic nuclei and elementary particles also undergo secular evolutionary changes. Such a conclusion follows from the results of the self-consistent application of physical laws. And this result allows us to naturally interpret some paradoxes that do not have an unambiguous explanation to this day.

*hhayk@bao.sci.am

doi: https://doi.org/10.52526/25792776-23.70.1-100

We will focus here only on one of the mentioned dilemmas, which is associated with the existence of two different values of the Hubble constant and is known as the Hubble tension. This phenomenon is explained here by the fact that the determination of the ”early” value of the Hubble constant does not deal with real space objects and the properties of baryonic matter, while the ”later” value is determined by measurements of the velocities and distances of real galaxies.

We also know from the history of science and should carefully keep in the mind that researchers always try to keep all established ideas intact but not change any principal idea. They usually prefer to add new loose parameters to fit new observable facts or patterns to existing models and ideas. Major changes in comprehensive understanding of the physical world around that are highly valued by different paradigms take place not very frequent but very rarely and only when the inertia of the old type of thinking is reduced to a negligible level. Most probably this form of thinking underlies cognition through the human psyche. Of course, this is an issue, which has more philosophical than physical or astrophysical essence. However, when choosing a methodology for ongoing research, existing implicit trends should be taken into account.

2. Interaction between baryonic matter and the carrier of dark energy.

Obviously, the very fact of the discovery of dark energy (Perlmutter et al., 1999, Riess et al., 1998) through the fact of the acceleration of galaxies directly indicates the interaction of two substances, namely the baryon universe and the carrier of dark energy, whatever the latter may be. It is due to this interaction that energy is transferred to galaxies, which ensures the acceleration of the expansion of the Universe. It is clear that any interaction involves the exchange of energy between the interacting substances. This is what we know and usually interpret based directly on observational data. And all this applies to cosmological scales and cosmological objects as integral formations.

On the other hand, the contemporary science asserts that dark energy fills homogenously all spatial scales. If we also take into account that dark energy is purely positive, while all baryon objects and their systems have negative total energy (according to modern concepts), then it is obvious that the baryon world acquires energy during this kind of interaction and energy exchange at all scales. As one can notice, this conclusion has been arrived at using only the self-consistent physical approach, if the homogeneity of dark energy accepted by scientific community is true.

Let’s take the next step, relying on the general physical laws of interaction and energy transfer known to us. If we accept that dark energy fills all space on all scales, then we inevitably come to the conclusion that interaction with baryonic matter must also occur on all scales. And this, in turn, means that in a detailed study of the issue, we must take into account the exchange of energy and the consequences of this process for all scales, starting with the microcosm. The physical consequences thus obtained can be verified with the help of observational data relating to the corresponding objects.

Above we noted one essential circumstance about the energy state of baryonic objects common to the entire baryonic Universe. This is what any baryonic objects have, or are thought to have, negative energy. Therefore, when interacting with a carrier of dark energy, according to the known laws of physics, they must inevitably acquire additional energy. This applies both to gravitationally interacting or bound objects and systems, and to elementary particles and atomic nuclei. What happens at the level of atomic nuclei ultimately leaves its mark on the entire baryonic universe, and therefore must be accurately accounted for.

3. Atomic nuclei and dependence of baryons’ mass on physical conditions.

It is well known that atomic nuclei, as all baryonic objects, exist as integral entities only due to the binding energy of the nuclei, which is nothing but a lack of mass (mass defect). Each baryon in the nucleus exists, while having a smaller mass compared to the free state. This means that in order to completely divide the nucleus into the composing it baryons, one needs to give the nucleus the energy equivalent of the missing mass. There is another aspect of this situation that is not often noticed. It is that the missing mass for one baryon varies from nucleus to nucleus. A nucleon losses some part of its mass being bound in a nucleus and the same nucleon possesses different masses in different nuclei.

This fact can be interpreted as follows. Under the physical conditions of atomic nuclei, identical baryons, which are considered by modern physics absolutely indistinguishable from each other, can have different masses. It does mean that the same nucleon easily changes its mass being in different physical conditions

doi: https://doi.org/10.52526/25792776-23.70.1-100

and obey the conditions for existence. So, one can arrive at a conclusion that in principle, these baryons can have a different mass, if the physical conditions require it.

There are all prerequisites for such a phenomenon. Let’s discuss this briefly. If the interaction of baryonic objects with the carrier of dark energy really occurs at all scales, then it also takes place on the scales of atomic nuclei and elementary particles. Then the transfer of energy to the atomic nucleus reduces its nuclear binding energy. But this, on the other hand, means that the mass defect also decreases and, consequently, we will observe an increase in the mass of the nucleus and, accordingly, the mass of bound baryons.

Let’s emphasize that for this process doesn’t even matter what the density of dark energy is. However negligible the density would be, any non-zero value would increase the mass of the baryons. The fact is that energy is a cumulative type of substance, it can be accumulated and therefore the amount of energy will be integrated over time. In other words, over time the change in energy will reach the noticeable amount and have essential physical consequences, which we are going to discuss further in this report.

It is very important to find the “fingerprints” of the predictable changes occurred with the atomic nuclei. We can mention here several. First one, which provides an observable feature is the change in wavelengths of spectral lines. Indeed, let’s show it using the example of hydrogen-like atoms, line wavelength for which is given by the following relation:

$$\frac{1}{\lambda_{mn}} = Ry\frac{1}{hc}\frac{M_p}{M_p+m_e}\left(\frac{1}{m^2}-\frac{1}{n^2}\right), \tag{1}$$

where

$$Ry = \frac{m_e e^4}{8\varepsilon_0^2 h^2} \tag{2}$$

is the Rydberg constant. Instead of protons mass M_p one could write $M_n$for denoting hydrogen-like atoms consisted of several baryons. We see that the wavelengths of spectral lines depend inversely on the reduced mass of nucleus and electron

$$m_r = \frac{M_n m_e}{M_n + m_e}. \tag{3}$$

Obviously, when the masses of the nucleus and electron increase, spectral lines get blueshifted. This means that the more the object is affected by this mechanism, the more are its spectral lines blueshifted. On the other hand, one can conclude that the farther the object is, the bigger its spectral lines’ redshift due to the bigger nuclear binding energy. In other words, the objects located far away should possess some additional redshift not conditioned by the Hubble expansion of the Universe. This is due to the evolutionary process of atomic nuclei and elementary particles taking place because of interaction between the baryonic matter and the carrier of dark energy. This process is a universal mechanism converting dark energy into mass and increasing the mass of the baryonic universe simultaneously with its expansion. One of the most challenging problems is to find a method for quantitative separation of these two types of redshifts, if any.

The second feature, showing a kind of ”fingerprint”, is associated with a decrease in the binding energy of the nuclei, which obviously reduces the stability of all nuclei. On the basis of general physical considerations, it can be shown that the constant decrease in the binding energy of nuclei eventually transfers any given nucleus into the category of radioactively decaying. And this, in turn, means that after some time, instead of a given nucleus, there will be two (or more) lighter nuclei. From this we can draw several conclusions that radically change our understanding of the formation of chemical elements and the evolution of their abundance: a) Over time, the metallicity of all space objects and the universe as a whole decreases; b) In earlier epochs of the life of the universe, there were atomic nuclei consisting of a larger number of hadrons (with a large atomic number) with smaller masses and higher binding energy; c) With time, the half-life of radioactive atomic nuclei decreases.

4. The rate of evolution depending on the mass of the object.

None of these features can be observed directly. However, some of them could manifest themselves in an implicit form. In order to find possible ”fingerprints”, consider the following question. If indeed baryonic matter interacts with a carrier of dark energy on all scales, while receiving energy and, as a result, evolving, then it is interesting which objects are more easily subject to the influence of dark energy - massive or low-mass objects.

doi: https://doi.org/10.52526/25792776-23.70.1-100

To study this issue, we proceed from the following considerations. Any object exists due to its binding energy. For the objects bound through gravitation, this is the gravitational energy that can be calculated. The amount of dark energy is proportional to the volume of a given object, since dark energy is uniformly distributed. From a physical point of view, it is natural to assume that an object is the more subject to evolutionary changes, the greater the ratio of dark energy to binding energy, all other conditions being equal.

The gravitational energy of objects, as is known, is generally proportional to the square of the mass and inversely proportional to the size. In general, it depends on the density distribution and on the geometry of the object and each time must be calculated with exact consideration of the specified values. But in simple cases it is calculated analytically and the corresponding formulas are well known. For example, the homogeneous spherical object possesses of gravitational energy given by the following relation:

$$E_{gr} = kG\frac{M^2}{R} \tag{4}$$

where M is the mass of the object and R is its radius. Now one can introduce the amount od dark energy located in the same volume with the spherical object in this way

$$E_{de} = V\rho_{de}, \tag{5}$$

where

$$V = \frac{4\pi}{3}R^3 \tag{6}$$

is the volume of the object and ρ_{de} is the dark energy density. Then the ratio of "destroying" dark energy and "maintaining" gravitational energy for the given object will have the following form

$$\eta = \frac{E_{de}}{E_{gr}} = kG\frac{R}{M}\frac{\rho_{de}}{\rho_{bm}}, \tag{7}$$

where ρ_{bm} is the density of the baryonic mater within the object under consideration. As can be seen, in this purely model example, the introduced coefficient decreases with an increase in the mass of the object, provided that the density of objects of this family is unchanged. Naturally, this model does not actually work, and a more realistic case must be considered. However, our conclusion remains valid if the mass M grows faster than the radius R.

What conclusion can be drawn from the result obtained? Since the effect of dark energy is more effective where the introduced ratio is greater, this result can be interpreted as follows. The greater the mass of an object, the more difficult it is for evolutionary changes under the influence of dark energy. That is, all the effects that have been listed above occur more easily for low-mass objects and are more delayed in the case of more massive objects.

Let us now compare this result with well-known observational facts. Since the 1970s, the phenomenon of the dependence of the metallicity of galaxies on their luminosity has been studied in sufficient detail. A very large amount of evidence shows that the metallicity of massive galaxies is much higher than that of dwarf galaxies. Our results, combined with observational data, can be interpreted as follows. The process of evolution under the influence of dark energy goes in the direction of fragmentation of atomic nuclei and an increase in the relative number of light elements and, first of all, hydrogen. Then hydrogen is not the primary element from which the rest are synthesized, but the final product of evolution.

The paradoxical discoveries of recent decades related to the existence of "mature" galaxies on the very outskirts of the universe, heavy elements at the same distances, the amazing fact that it is galaxies and not quasars that have the largest redshifts, all the more strengthen the confidence in the correctness of our paradigm. But we will talk about these facts and their detailed analysis in another article. And here, after trying to substantiate this paradigm, we will focus on another paradox, which is known as the Hubble tension.

5. The new headache called "Hubble tension".

Since the discovery of the expansion of the Universe by Lemaitre and Hubble, much work has been devoted to improving methods for determining the main expansion parameter, which was once called the Hubble constant. Starting from a value of $500 - 600$ km/s per Mpc, the refinement of this parameter over several decades led to a value of about 70 km/s per Mpc. From the very beginning, as one would expect,

doi: https://doi.org/10.52526/25792776-23.70.1-100

the scatter in the measured values of this quantity was large, but the researchers were sure that the scatter tends to zero as the accuracy of the measurements increases. This tendency is true and is observed in all empirical works.

But in the case of measuring the Hubble constant, such expectations were not justified. The refinement of the measurements led to the fact that for this constant two different values have been obtained, which differ from each other at the level of 4-6 sigma. One group of measurements, which uses data from the microwave background of the sky, gives a value of 67.4 ± 0.5 km/s per Mpc, while other methods, which use the measured distances of objects and their velocities, provide a value of 74.0 ± 1.5km/s per Mpc.

This is a very confusing result for astronomers and physicists, since any parameter can have only one value, measured by any methods, provided that all methods are correct and take into account all possible sources of error. This can happen when some effect is not taken into account or when they do not know about this effect.

Here, in our opinion, attention should be paid to the following circumstances. First, those methods that involve the use of background radiation do not deal with the physical properties of the baryonic universe. Second, the Hubble constant is larger precisely when it is measured using baryonic objects. This suggests that the reason may be hidden in the physical properties of baryonic matter. Let's consider the question, which means that the Hubble constant in the case of measurements with baryonic objects turns out to be 6.6 km/sec per Mpc more. This means that for one Mpc, these methods from somewhere gain so much more decrease in speed. Decreasing speed in this language is nothing more than an extra blueshift. Where can it come from. But this is precisely what was discussed in the previous paragraph, namely, that due to interaction with a carrier of dark energy, the spectral lines of all elements move to the blue side of the spectrum. It remains to do some calculations in order to determine the rate of increase in the mass of atomic nuclei and elementary particles, at which we will get these additional 6.6 km/sec per Mpc. To do this, we first note that a distance of 1 Mpc in terms of time equals 3.26 million years. That is, we must proceed from the fact that these additional 6.6 km/sec per Mpc appear due to the increase in mass over 3.26 million years. Thus, we observe change of wavelengths on

$$\Delta z = \frac{\Delta v}{c} = \frac{6.6}{300000} = 2.2 \times 10^{-5} \tag{8}$$

for the time interval 3.26 million years. Using this one can calculate the annual growth of mass of the atomic nuclei and elementary particles. It is easy to find the analogous change for one year or for the distance of one light year. One should divide the spectral change on to the 3.26 million years. It gives for the blueshift per year

$$\Delta z_{year} = 6.7 \times 10^{-12}. \tag{9}$$

On the other hand, if using the expression (1) for expressing the change of blueshift by the mass growth, one finds

$$\Delta z = \frac{\Delta \lambda}{\lambda} = \frac{m_{r2} - m_{r1}}{m_{r2}} = \frac{\Delta m_r}{m_r}, \tag{10}$$

where m_{r1} and m_{r2} are the reduced masses of nucleus and electron, measured in a one-year difference. So, we can obtain from (9) and (10) the following expression

$$\frac{\Delta m_r}{m_r} = 6.67 \times 10^{-12}. \tag{11}$$

From this relation one can calculate the rate of the proton mass change. If the mass change takes place equally for protons and electrons, one can obtain from the relation (11) the following estimate

$$\frac{\Delta m_n}{m_n} \approx 6.6 \times 10^{-12}. \tag{12}$$

The same estimate is valid for any nuclei and, in a particular case, for the proton which possess of mass $M_p = 1.67262192369(51) \times 10^{-24}$ g.

The accuracy of determination of the proton mass, although very high, is about an order less than one needs to find its secular change, if any. Since according this paradigm the masses of elementary particles and atomic nuclei grow up constantly in the course of time, it seems not to be very difficult to check it empirically. However, to this end, new methods of measurement must be invented, since if the paradigm under consideration is correct, then mass standards, most probably, also change with time. One should overcome this difficulty to obtain really acceptable results.

doi: https://doi.org/10.52526/25792776-23.70.1-100

Which methods are applicable for such measurements, we cannot mention here. This problem, certainly, must be considered separately and very scrupulously to find any self-consistent method and corresponding solution.

6. Concluding remarks.

Obviously, we have not yet appreciated the true significance of the discovery of dark energy for understanding the processes of evolution in the baryonic universe. It is still perceived as another ordinary discovery, which slightly corrects our ideas about our world on a large scale. However, this is by no means the case. If we take into account the possibility of interaction between baryonic matter and the carrier of dark energy and all the consequences of this interaction for baryonic matter, then we inevitably come to the conclusion that all evolutionary processes in the baryonic world are controlled precisely by this influence.

If the paradigm we consider here is correct then one can find several ”fingerprints” of the corresponding physical processes. One of those signs is associated with the cosmic objects’ metallicity and its distribution. The point is that interaction between the baryonic matter and the carrier of dark energy leads ultimately to the fragmentation of atomic nuclei. It does mean that the relative number of light elements should increase over time. In other words, the longer evolution of object under the influence of dark energy, the lower the metallicity. This effect is know since 70s of the last century. That is the dependence of the metallicity of galaxies on the mass (luminosity).

We applied the results obtained on the secular growth of mass of atomic nuclei to explain the paradox called ”Hubble tension”. For this we have used the fact that atom’s spectral lines should be shifted to the blur end of spectrum if the mass of nucleus increases. This approach allows one to estimate the annual change of the mass of atomic nuclei including the proton mass (hydrogen atom’s nucleus).

A lot of observational facts fit our ideas following from the paradigm under consideration. It needs to have a comprehensive study of all possible ”fingerprints”, paying a special attention to ones, which, in their turn, predict new phenomena or provide a method to measure predicted changes in the objwcts’ characteristics.

References

Perlmutter S., et al., 1999, Astrophys. J. , 517, 565

Riess A. G., et al., 1998, Astron. J. , 116, 1009

doi: https://doi.org/10.52526/25792776-23.70.1-100

Cosmological Scalar Field ϕCDM Models

Olga Avsajanishvili *

E.Kharadze Georgian National Astrophysical Observatory, 47/57 Kostava St.,Tbilisi 0179, Georgia

Abstract

Cosmological models that go beyond the standard Lambda Cold Dark Matter (ΛCDM) scenario, namely, scalar field ϕCDM models, are considered. The Hubble expansion rate of the universe, the dynamic and the energetic domination of dark energy, the formation of matter density fluctuations and the large-scale structure growth rate in these models compared to the standard spatially-flat ΛCDM model are investigated.

Keywords: *dark energy, scalar field, Hubble expansion rate, large-scale structure growth rate.*

1. Introduction

Our universe is expanding with an acceleration according to reliable observational datasets: measurements of Supernovae type Ia magnitudes (Perlmutter et al., 1999, Riess et al., 1998), measurements of the temperature anisotropy and the polarization in the cosmic microwave background (CMB) radiation (Bennett et al., 1996, Smoot et al., 1992), examining of the large-scale structure of the universe (Dodelson et al., 2001, Percival et al., 2007) measurements of baryon acoustic oscillations peak length scale (Blake et al., 2011, Eisenstein et al., 2005) measurements of the Hubble parameter (Stern et al., 2010).

One of the possible explanations for this empirical fact is that the energy density of the universe is dominated by so-called dark energy, a component with an effective negative pressure (Copeland et al., 2006, Peebles & Ratra, 2003).

The simplest description for dark energy is the concept of vacuum energy or the time-independent cosmological constant Λ, first introduced by Albert Einstein (Einstein, 1915a,b). The cosmological model based on such a description of dark energy in the spatially flat universe is called the standard, concordance or fiducial Lambda Cold Dark Matter (ΛCDM) model. In the ΛCDM model, the general theory of relativity describes the gravity in the universe on large scales. The energy density associated with the cosmological constant is 68.5% of the total energy density of the universe at present (Aghanim et al., 2020).

Being still a fiducial cosmological model at present, the ΛCDM model has several still unsolved problems, the number of which increases as more accurate observational data are obtained (Abdalla et al., 2022, Di Valentino et al., 2019). The main of which are the fine tuning or the cosmological constant problem, the coincidence problem, the Hubble parameter tension problem, the parameter S_8 tension problem, the problem of the shape of the universe, and the preference for observational data of dynamical dark energy (in particular, phantom dark energy) (Abdalla et al., 2022, Aghanim et al., 2020, Di Valentino et al., 2019, 2021).

The presence of all the above discrepancies of the ΛCDM model is interpreted as a crisis of modern cosmology (Di Valentino et al., 2019). Although some of them may be due to systematic errors, their persistence strongly points to the need for new physics and new cosmological models that go beyond the standard ΛCDM scenario, on the one hand, and on tensions and anomalies in the current CMB data, on the other (Di Valentino, 2022).

The main alternative to the ΛCDM model are dynamical scalar field ϕCDM models (Ratra & Peebles, 1988a,b, Wetterich, 1988). In these models, dark energy is represented in the form of a slowly varying uniform cosmological scalar field at present. This family of models avoids the coincidence problem of the ΛCDM model. In these models, the energy density and the pressure are time dependent functions under the assumption that the scalar field is described by the ideal barotropic fluid model.

*olga.avsajanishvili@iliauni.edu.ge

doi: https://doi.org/10.52526/25792776-23.70.1-106

In general, dynamical dark energy models are characterized by the equation of state (EoS) parameter w_ϕ, which is the ratio of the pressure p_ϕ to the energy density p_ϕ: $w_\phi = p_\phi/\rho_\phi$. If for the ΛCDM model, the EoS parameter is a constant and equals minus one, then for ϕCDM models, the EoS parameter is a time-dependent function. Dynamical dark energy can mimic the cosmological constant at present, while becoming almost indistinguishable from it. These models are divided into phantom models (Caldwell, 2002) and quintessence models (Caldwell & Linder, 2005, Peebles & Ratra, 2003). These two classes of models differ from each other: (i) by the range of values of the EoS parameter at present epoch: this is $-1 < w_0 < -1/3$ for the quintessence field, and $w_0 < -1$ for the phantom field; (ii) by the sign of the kinetic term in the Lagrangian: positive for the quintessence field, and negative for the phantom field; (iii) by the form of the Klein-Gordon scalar field equation of motion; (iv) by the dynamics of scalar fields: the quintessence field rolls gradually to the minimum of its potential, while the phantom field rolls to the maximum of its potential; (v) by the temporal evolution of dark energy: for the quintessence field, the dark energy density remains almost unchanging with time, while it increases for the phantom field; (vi) by forecasting the future of the universe: depending on the spatial curvature of the universe, quintessence models predict either an eternal expansion of the universe, or a repeated collapse. On the other hand, phantom models predict the destruction of any gravitationally-related structures in the universe.

This paper is organized as follows: models under study are presented in Section 2, results and discussions are considered in Section 3, conclusions are summarized in Section 4.

We applied the natural system of units, where $c = k_B = 1$.

2. Models

We considered two types of scalar field ϕCDM models in the spatially flat universe: the quintessence and phantom scalar field ϕCDM models. The flat, homogeneous and isotropic universe is described by the Friedmann-Lemaître-Robertson-Walker spacetime metric $ds^2 = -dt^2 + a(t)^2 d\mathbf{x}^2$, where t is the cosmic time and $a(t)$ is the scale factor (normalized to be unity at present epoch $a_0 \equiv a(t_0)$).

The action for quintessence and phantom scalar field ϕCDM models are, respectively

$$S = \frac{M_{pl}^2}{16\pi} \int d^4x \Big[\sqrt{-g}\Big(\pm \frac{1}{2} g^{\mu\nu}\partial_\mu\phi\partial_\nu\phi - V(\phi)\Big)\Big], \tag{1}$$

here M_{pl} is a Planck mass, the "$+/-$" sign before kinetic term corresponds to the quintessence/phantom model, the over-dot denotes a derivative with respect to the cosmic time, $g^{\mu\nu}$ is the metric tensor, $g \equiv \det(g^{\mu\nu})$ is the determinant of the metric tensor $g^{\mu\nu}$, and $V(\phi)$ is the self-interacting potential of the scalar field ϕ.

2.1. Quintessence scalar field Ratra-Peebles ϕCDM model

We studied the quintessence scalar field ϕCDM model with the inverse power law Ratra-Peebles potential (Ratra & Peebles, 1988a), which has a form

$$V(\phi) = \frac{1}{2}\kappa M_{\rm pl}^2 \phi^{-\alpha}, \tag{2}$$

where $\alpha > 0$ and $\kappa > 0$ are model parameters. The model parameter α defines the steepness of this potential, for $\alpha = 0$, the ϕCDM model reduces to the ΛCDM model. We considered values of the parameter α in the range $0 < \alpha \leq 0.7$, according to observations (Samushia, 2009). The form of the quintessence Ratra-Peebles potential in 3D space is presented in the left panel of Fig. 1.

The Klein–Gordon scalar field equation of motion and the normalized Hubble parameter for the quintessence scalar Ratra-Peebles field ϕCDM model read, respectively, as

$$\ddot{\phi} + 3\frac{\dot{a}}{a}\dot{\phi} - \frac{1}{2}\kappa\alpha M_{\rm pl}^2 \phi^{-(\alpha+1)} = 0, \tag{3}$$

$$E(a) = H(a)/H_0 = \Big(\Omega_{\rm r0}a^{-4} + \Omega_{\rm m0}a^{-3} + \frac{1}{12H_0^2}\Big(\dot{\phi}^2 + \kappa M_{\rm pl}^2\phi^{-\alpha}\Big)\Big)^{1/2}, \tag{4}$$

where $H(a) = \frac{\dot{a}}{a}$ is a Hubble expansion rate of the universe; H_0 is a Hubble constant $H_0 = 100h$ km c^{-1} Mpc^{-1}, with h is a dimensionless normalized Hubble constant; $\Omega_{\rm r0}$ is a radiation density parameter at present epoch,

doi: https://doi.org/10.52526/25792776-23.70.1-106

$\Omega_{\rm m0}$ is a matter density parameter at present epoch. We fixed values of parameters $\Omega_{m0} = 0.315$, $h = 0.674$ to the best-fit values obtained by Planck collaboration (Aghanim et al., 2020).

The dark energy density parameter Ω_ϕ and the matter density parameter $\Omega_{\rm m}$ are defined, respectively, as

$$\Omega_\phi = \frac{1}{12H_0^2}\Big(\dot\phi^2 + \kappa M_{\rm pl}^2\phi^{-\alpha}\Big), \qquad \Omega_{\rm m} = \frac{\Omega_{\rm m0}a^{-3}}{\Omega_{\rm r0}a^{-4} + \Omega_{\rm m0}a^{-3} + \frac{1}{12H_0^2}\Big(\dot\phi^2 + \kappa M_{\rm pl}^2\phi^{-\alpha}\Big)}. \tag{5}$$

The energy density ρ_ϕ, the pressure p_ϕ and the EoS parameter w_ϕ for the quintessence scalar field Ratra-Peebles ϕCDM model are of the form, respectively

$$\rho_\phi = \frac{M_{\rm pl}^2}{32\pi}\Big(\dot\phi^2 + \kappa M_{\rm pl}^2\phi^{-\alpha}\Big), \quad p_\phi = \frac{M_{\rm pl}^2}{32\pi}\Big(\dot\phi^2 - \kappa M_{\rm pl}^2\phi^{-\alpha}\Big), \quad w_\phi = \frac{p_\phi}{\rho_\phi} = \frac{\dot\phi^2 - \kappa M_{\rm pl}^2\phi^{-\alpha}}{\dot\phi^2 + \kappa M_{\rm pl}^2\phi^{-\alpha}}. \tag{6}$$

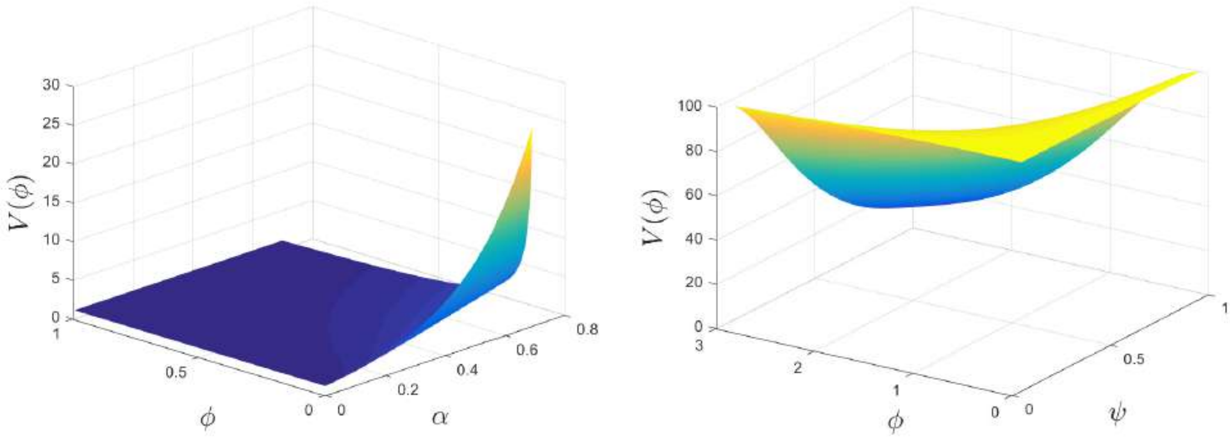

Figure 1. The form of the quintessence Ratra-Peebles potential $V(\phi) \sim \phi^{-\alpha}$ in 3D space, in units $M_{\rm pl} = 1$ (left panel). The form of the phantom inverse hyperbolic cosine potential $V(\phi) \sim \cosh(\psi\phi)^{-1}$ in 3D space (right panel).

2.2. Phantom scalar field inverse hyperbolic cosine ϕCDM model

We also studied the phantom scalar field ϕCDM model with the inverse hyperbolic cosine potential $V(\phi) = V_0\cosh^{-1}(\psi\phi)$ (Rakhi & Indulekha, 2009), where $\psi > 0$ and $V_0 > 0$ are model parameters. In the right panel of Fig. 1 is shown the form of the phantom inverse hyperbolic cosine potential in 3D space.

The Klein–Gordon scalar field equation of motion and the normalized Hubble parameter for the phantom inverse hyperbolic cosine scalar field ϕCDM model are given, respectively, as

$$\ddot\phi + 3\frac{\dot a}{a}\dot\phi - V_0\psi\tanh(\psi\phi)\cosh^{-1}(\psi\phi) = 0, \tag{7}$$

$$E(a) = H(a)/H_0 = \Big(\Omega_{\rm r0}a^{-4} + \Omega_{\rm m0}a^{-3} + \frac{1}{6H_0^2}\Big(-\frac{\dot\phi^2}{2} + V_0\cosh^{-1}(\psi\phi)\Big)\Big)^{1/2}. \tag{8}$$

The dark energy density parameter Ω_ϕ and the matter density parameter $\Omega_{\rm m}$ are defined, respectively, as

$$\Omega_\phi = \frac{1}{6H_0^2}\Big(-\frac{\dot\phi^2}{2} + V_0\cosh^{-1}(\psi\phi)\Big), \qquad \Omega_{\rm m} = \frac{\Omega_{\rm m0}a^{-3}}{\Omega_{\rm r0}a^{-4} + \Omega_{\rm m0}a^{-3} + \frac{1}{12H_0^2}\Big(-\frac{\dot\phi^2}{2} + V_0\cosh^{-1}(\psi\phi)\Big)}. \tag{9}$$

The energy density ρ_ϕ, the pressure p_ϕ and the EoS parameter w_ϕ for the phantom inverse hyperbolic cosine scalar field ϕCDM model have the form, respectively

$$\rho_\phi = \frac{M_{\rm pl}^2}{16\pi}\Big(-\frac{\dot\phi^2}{2}+V_0\cosh^{-1}(\psi\phi)\Big), \quad p_\phi = \frac{M_{\rm pl}^2}{16\pi}\Big(-\frac{\dot\phi^2}{2}-V_0\cosh^{-1}(\psi\phi)\Big), \quad w_\phi = \frac{p_\phi}{\rho_\phi} = \frac{-\dot\phi^2/2 - V_0\cosh^{-1}(\psi\phi)}{-\dot\phi^2/2 + V_0\cosh^{-1}(\psi\phi)}. \tag{10}$$

doi: https://doi.org/10.52526/25792776-23.70.1-106

3. Results and discussion

3.1. Background in the universe for scalar field ϕCDM models

To study the background in the universe for scalar field ϕCDM models, we jointly numerically integrated the first Friedmann's equation and the Klein-Gordon scalar field equation of motion, namely, Eq. (3) and Eq. (4) for the quintessence Ratra-Peebles scalar field ϕCDM model, Eq. (7) and Eq. (8) for the phantom inverse hyperbolic cosine scalar field ϕCDM model.

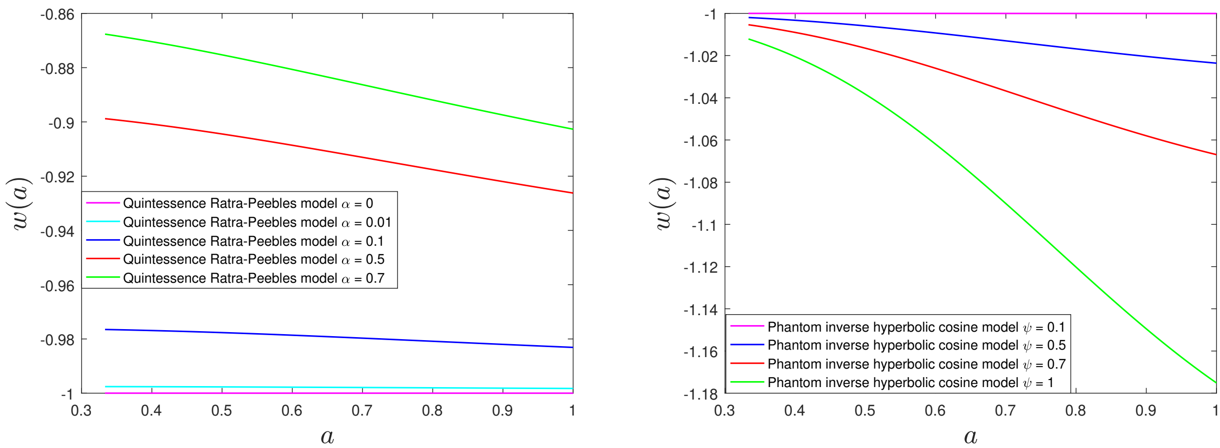

Figure 2. Dependence of the EoS parameter on the model parameter α in the quintessence Ratra-Peebles ϕCDM model (left panel). Dependence of the EoS parameter on the model parameter ψ in the phantom inverse hyperbolic cosine scalar field ϕCDM model (right panel).

The evolution of the EoS parameter for scalar field ϕCDM models depending on model parameters are presented in Fig. 2. A larger value of the parameter α in the quintessence Ratra-Peebles model (left panel of Fig. 2) and the parameter ψ in the phantom inverse hyperbolic cosine model (right panel of Fig. 2) causes an increase in dark energy and, thus, a stronger time dependence of the EoS parameter in these models and vice versa.

In order to study the influence of scalar fields on the Hubble expansion rate of the universe, we numerically calculated the Eq. (4) for the quintessence Ratra-Peebles ϕCDM model and Eq. (8) for the phantom inverse hyperbolic cosine scalar field ϕCDM model. The expansion rate of the universe is faster in quintessence scalar field ϕCDM models and slower in phantom scalar field ϕCDM models compared to the ΛCDM model (the left panel of Fig. 3).

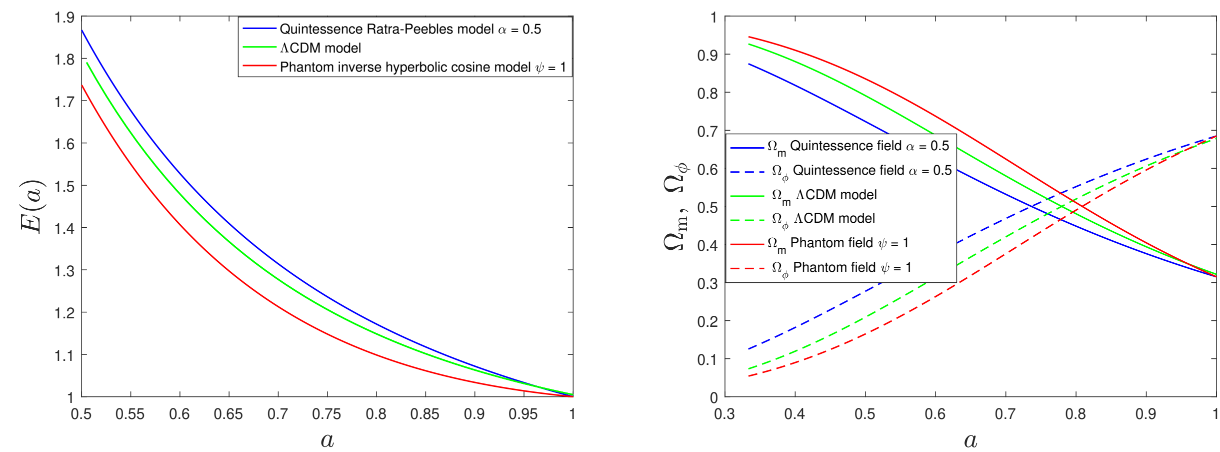

Figure 3. The evolution of the normalized Hubble expansion rate $E(a)$ in ϕCDM models for fixed values of model parameters compared to the ΛCDM model (left panel). The evolution of the matter density parameter Ω_m and the dark energy density parameter Ω_ϕ in ϕCDM models for fixed values of model parameters compared to the ΛCDM model (right panel).

doi: https://doi.org/10.52526/25792776-23.70.1-106

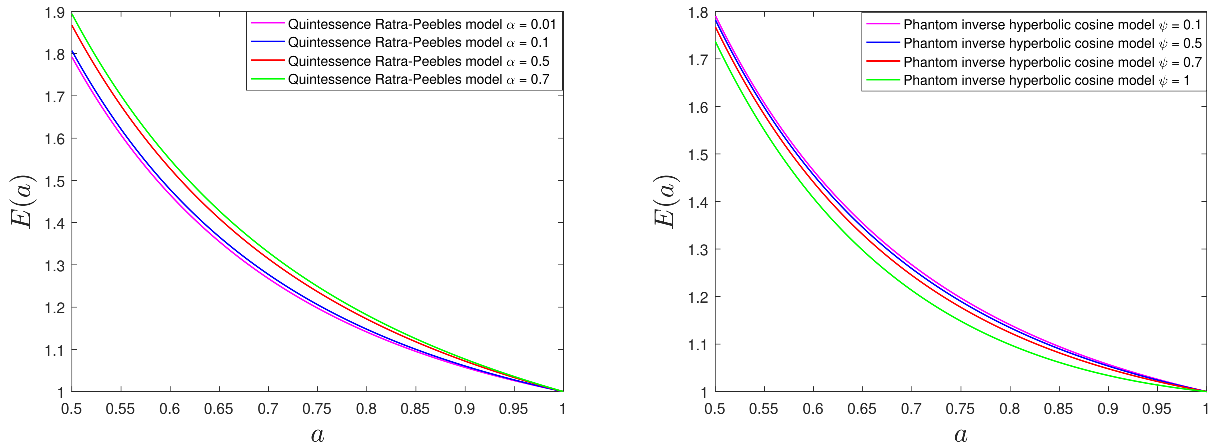

Figure 4. Dependence of the normalized Hubble expansion rate $E(a)$ on the model parameter α in the quintessence Ratra-Peebles ϕCDM model (left panel) and on the model parameter ψ in the phantom inverse hyperbolic cosine scalar field ϕCDM model (right panel).

In quintessence scalar field models, the Hubble expansion of the universe occurs faster with an increase in the value of the model parameter α (the left panel of Fig. 4), and, conversely, in phantom scalar field models, with an increase in the value of the model parameter ψ, the Hubble expansion of the universe occurs more slowly (the right panel of Fig. 4).

By investigating the influence of scalar fields on energy components in the universe, we found that the epoch of dominance of dark energy is established earlier in the quintessence Ratra-Peebles scalar field ϕCDM model and later in the phantom inverse hyperbolic cosine scalar fieldϕCDM model, compared to the ΛCDM model (the right panel of Fig. 3).

In the quintessence Ratra-Peebles scalar field ϕCDM model, the energetic domination of dark energy began earlier with an increase in the value of the model parameter α (the upper left panel of Fig. 5), and, conversely, in phantom scalar field models, with an increase in the value of the model parameter ψ, the energetic domination of dark energy began later (the upper right panel of Fig. 5). While the dynamic dominance of dark energy began earlier in the quintessence Ratra-Peebles scalar field ϕCDM model than in the phantom inverse hyperbolic cosine scalar field ϕCDM model (bottom panels of Fig. 5). Both in the quintessence and in the phantom scalar fields model, the dynamic dominance of dark energy began earlier than the energy dominance at the fixed values of model parameters in these models (Fig. 5).

3.2. The evolution of the large-scale structure in the universe for scalar field ϕCDM models

In order to study the influence of ϕCDM models on the formation of the large-scale structure in the universe, we numerically integrated the linear perturbation equation (Pace et al., 2010) relative to the matter density fluctuation δ

$$\delta'' + \left(\frac{3}{a} + \frac{E'}{E}\right)\delta' - \frac{3\Omega_{m0}}{2a^5E^2}\delta = 0. \tag{11}$$

We also calculated the linear growth factor $D(a) = \delta(a)/\delta(a_0)$ and the large-scale structures growth rate $f(a) = d\ln D(a)/d\ln a$.

The evolution of the linear growth factor $D(a)$ in ϕCDM models for fixed values of model parameters are presented in the left panel of Fig. 6. Larger values of matter density fluctuations are generated in quintessence scalar field ϕCDM models and smaller ones in phantom scalar field ϕCDM models, compared to the ΛCDM model (the left panel of Fig. 6). The large-scale structure growth rate $f(a)$ is slower in quintessence scalar fields, but faster in phantom scalar fields compared the ΛCDM model (the right panel of Fig. 6), because the Hubble expansion is faster in quintessence scalar fields than in phantom scalar fields (the left panel of Fig. 3), which leads to suppression of the large-scale structure growth rate in the universe.

In the quintessence Ratra-Peebles scalar field ϕCDM model, the larger values of matter density fluctuations are generated with an increase in the value of the model parameter α (the upper left panel of Fig. 7), and, conversely, in the phantom inverse hyperbolic cosine scalar field ϕCDM model, the smaller

doi: https://doi.org/10.52526/25792776-23.70.1-106

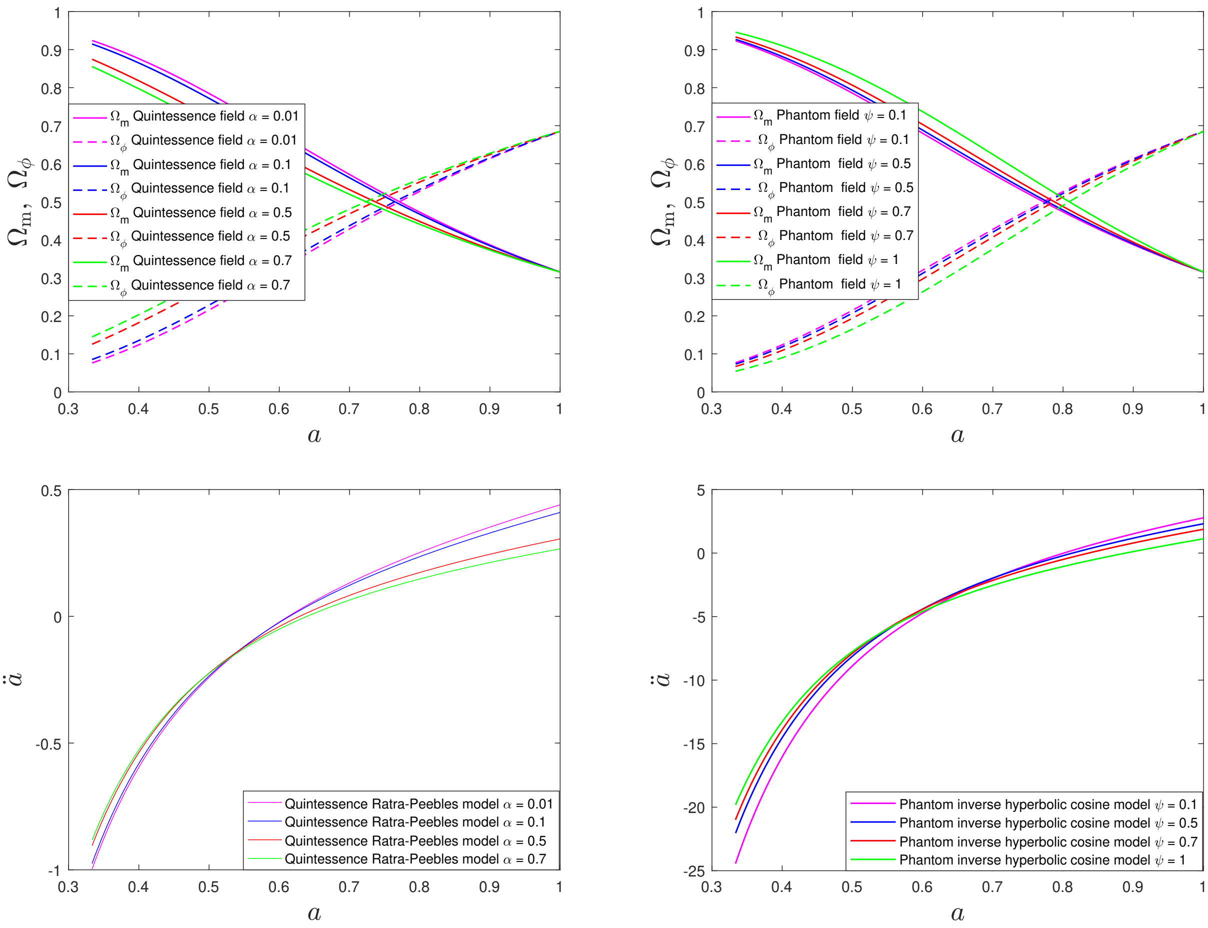

Figure 5. The energetic domination of dark energy in the quintessence Ratra-Peebles scalar field ϕCDM model depending on the model parameter α (upper left panel). The energetic domination of dark energy in the phantom inverse hyperbolic cosine scalar field ϕCDM model depending on the model parameter ψ (upper right panel). The dynamic domination of dark energy in the quintessence Ratra-Peebles scalar field ϕCDM model depending on the model parameter α (bottom left panel). The dynamic domination of dark energy in the phantom inverse hyperbolic cosine scalar field ϕCDM model depending on the model parameter ψ (bottom right panel).

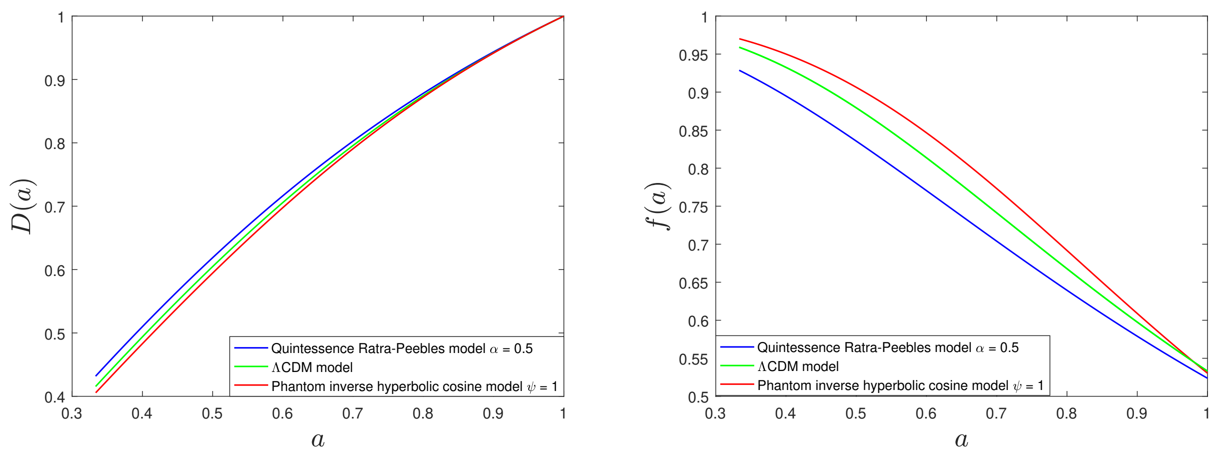

Figure 6. The evolution of the linear growth factor in ϕCDM models for fixed values of model parameters compared to the ΛCDM model (left panel). The evolution of the large-scale structure growth rate in ϕCDM models for fixed values of model parameters compared to the ΛCDM model (right panel).

values of matter density fluctuations are generated with an increase in the value of the parameter ψ (the upper right panel of Fig. 7). In the quintessence Ratra-Peebles scalar field ϕCDM model, the large-scale

doi: https://doi.org/10.52526/25792776-23.70.1-106

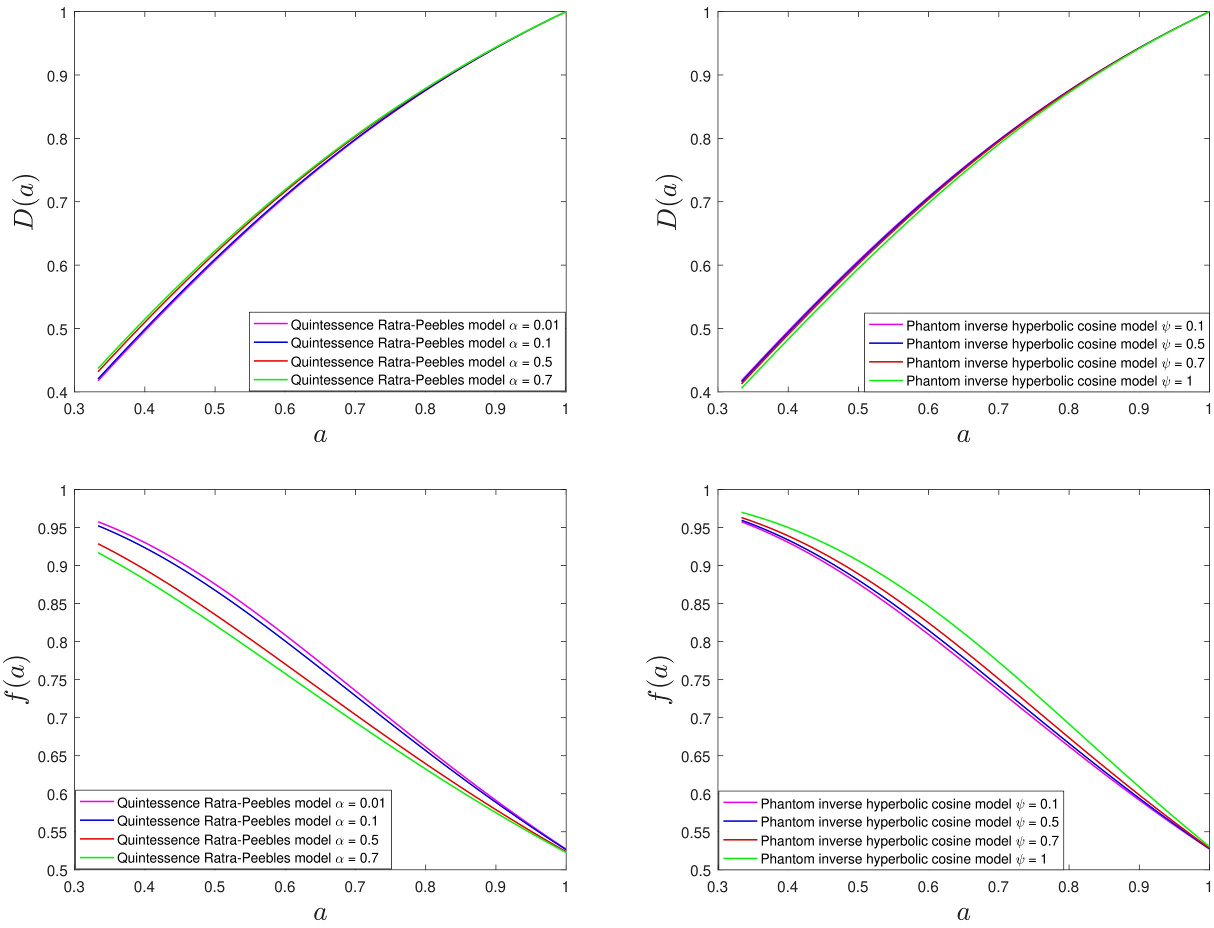

Figure 7. The evolution of the linear growth factor in the quintessence Ratra-Peebles scalar field ϕCDM model depending on the model parameter α (upper left panel). The evolution of the linear growth factor in the phantom inverse hyperbolic cosine scalar field ϕCDM model depending on the model parameter ψ (upper right panel). The evolution of the large-scale structures growth rate in the quintessence Ratra-Peebles scalar field ϕCDM model depending on the model parameter α (bottom left panel). The evolution of the large-scale structures growth rate in the phantom inverse hyperbolic cosine scalar field ϕCDM model depending on the model parameter ψ (bottom right panel).

structure growth rate $f(a)$ slows down with an increase in the value of the model parameter α (the bottom left panel of Fig. 7), and, conversely, in the phantom inverse hyperbolic cosine scalar field ϕCDM model, with an increase in the value of the parameter ψ, the large-scale structure growth rate rapids (the bottom right panel of Fig. 7).

4. Conclusions

Scalar field ϕCDM models differ from the ΛCDM model in a number of characteristics, which are generic for these models. Compared to the ΛCDM model:

- the Hubble expansion rate of the universe is faster in quintessence scalar field models and slower in phantom scalar field models;
- the dynamic and the energetic domination of dark energy began earlier in quintessence scalar field models and later in phantom scalar field models;
- larger values of matter density fluctuations are generated in phantom scalar field models and smaller ones in quintessence scalar field models;
- the large-scale structures growth rate of the universe is faster in phantom scalar field models and slower in quintessence scalar field models.

doi: https://doi.org/10.52526/25792776-23.70.1-106

Acknowledgements

This work was supported by Shota Rustaveli National Science Foundation of Georgia (SRNSFG) [YS-22-998].

References

Abdalla E., Abellán G. F., Aboubrahim A., et al. 2022, JHEAp, 34, 49

Aghanim N., Akrami Y., Ashdown M., et al. 2020, Astron. Astrophys. , 641, A6

Bennett C. L., Banday A., Gorski K. M., et al. 1996, Astrophys. J. Lett. , 464, L1

Blake C., Kazin E., Beutler F., et al. 2011, Mon. Not. R. Astron. Soc. , 418, 1707

Caldwell R. R., 2002, Phys. Lett., B545, 23

Caldwell R. R., Linder E. V., 2005, Phys. Rev. Lett., 95, 141301

Copeland E. J., Sami M., Tsujikawa S., 2006, Int. J. Mod. Phys., D15, 1753

Di Valentino E., 2022, Universe, 8, 399

Di Valentino E., Melchiorri A., Silk J., 2019, Nature Astron., 4, 196

Di Valentino E., Mena O., Pan S., et al. 2021, Class. Quant. Grav., 38, 153001

Dodelson S., Narayanan V. K., Tegmark M., et al. 2001, Astrophys. J. , 572, 140

Einstein A., 1915a, Sitzungsber. Preuss. Akad. Wiss. Berlin (Math. Phys.), 1915, 778

Einstein A., 1915b, Sitzungsber. Preuss. Akad. Wiss. Berlin (Math. Phys.), 1915, 844

Eisenstein D. J., Zehavi I., Hogg D. W., et al. 2005, Astrophys. J. , 633, 560

Pace F., Waizmann J.-C., Bartelmann M., 2010, Mon. Not. R. Astron. Soc. , 406, 1865

Peebles P. J. E., Ratra B., 2003, Rev. Mod. Phys., 75, 559

Percival W. J., Cole S., Eisenstein D. J., et al. 2007, Mon. Not. R. Astron. Soc. , 381, 1053

Perlmutter S., Aldering G., Goldhaber G., et al. 1999, Astrophys. J. , 517, 565

Rakhi R., Indulekha K., 2009, arXiv:0910.5406

Ratra B., Peebles P. J. E., 1988a, Astrophys. J. , 325, L17

Ratra B., Peebles P. J. E., 1988b, Phys. Rev., D37, 3406

Riess A. G., Filippenko A. V., Challis P., et al. 1998, Astron. J. , 116, 1009

Samushia L., 2009, PhD thesis, Kansas State U., arXiv:0908.4597

Smoot G. F., Bennett C. L., Kogut A., et al. 1992, Astrophys. J. Lett. , 396, L1

Stern D., Jimenez R., Verde L., et al. 2010, JCAP, 02, 008

Wetterich C., 1988, Nucl. Phys., B302, 645

Dependence of standardization parameters of type Ia supernova light curves on redshift

A.P. Mahtessian *[1], G.S. Karapetian† , M. A. Hovhannisyan‡[2], and L.A. Mahtessian§[2]

[1]Byurakan Astrophysical Observatory after V. Ambartsumian NAS of the Republic of Armenia, Byurakan, Aragatzotn Province, Republic of Armenia, 0213

[2]Institute of Applied Problems of Physics NAS of the Republic of Armenia 25 Hrachya Nersissian Str., Yerevan, Republic of Armenia, 0014

Abstract

The paper shows that the parameters X_1 and C used to standardize the luminosity of type Ia supernovae in the SALT2 model are highly dependent on redshift. This leads to the fact that during standardization, with increasing z, the average absolute stellar magnitude of type Ia supernovae artificially increases and, therefore, for a given apparent magnitude, we attribute to them, on average, a greater distance than they actually have. And therefore it is believed that they are receding with acceleration. Therefore, such standardization is unsuitable for measuring distances to type Ia supernovae. If the standardization parameter $(-\alpha X_1 + \beta C)$ is replaced by the redshift-dependent parameter (ϵz), then the parameter Ω_Λ turns into 0 in the ΛCDM model.

Keywords: *Supernovae Ia; Luminosity standardization; Cosmological Parameters; Cosmology*

1. Introduction

Type 1a supernovae are considered standard candles. Standard candles are light sources that have the same brightness regardless of place and time. The Hubble diagram is commonly used to estimate the value of cosmological parameters. But on the Hubble diagram, the spread of points is quite large. To reduce the scatter of points and to estimate the cosmological parameters more accurately, it will be necessary to standardize the luminosity's of type Ia supernovae. In modern cosmology, the SALT2 model is most often used to standardize the luminosity of supernovae (Guy & et al. (2007)). This model uses two parameters X_1 and C. Where X_1 characterizes the shape of the light curve (describes the stretching of the light curve in time), and the parameter C describes the color of the supernova at maximum brightness. In particular, the distance estimate assumes that supernovae with the same color, shape, and galactic environment have, on average, the same intrinsic luminosity for all redshifts. Given these parameters, the standardization equation can be written as follows:

$$\mu = B_{obs} - (M_B - \alpha X_1 + \beta C)$$

where $\mu = 5\log D_L(z) + 25$ is the distance modulus, B_{obs} corresponds to the peak apparent magnitude in the B band, and α, β, M_B are the parameters of the standardization equation for distance estimation.

When standardizing the luminosity, it is assumed that the dependence of the decay time of the brightness of supernovae on the maximum brightness, as well as the dependence of the color at the peak on the maximum brightness, do not depend on the age of the predecessor. In Lee & et al. (2022) showed that there is a strong relationship between the parameters α, β and the age of the population of the host galaxy. This dependence lies in the fact that in younger galaxies type 1a supernovae at maximum brightness have a weaker luminosity than supernovae in relatively old galaxies. Since redshift characterizes age on average, the dependence of these parameters on redshift should be observed. Rigault & et al. (2020) studied the star formation rate in

*amahtes@gmail.com, Corresponding author

†garenk53@gmail.com

‡martik.hovhannisyan1956@gmail.com

§am.ml@bk.ru

doi: https://doi.org/10.52526/25792776-23.70.1-114

local environments of type 1a supernovae and found a strong dependence of the standardization parameters on the local star formation rate. In this paper, we study the dependence of standardization parameters on redshift (z) based on some known samples of type Ia supernovae (Kowalski & et al. (2008), Amanullah & et al. (2010), Betoule & et al. (2014)). All data is taken from the authors of these articles, without any changes. It is shown that there is a strong correlation between these parameters and z. We will also discuss what happens if we replace the $(-\alpha X_1 + \beta C)$ term with a redshift dependent term (ϵz).

2. Results

On Fig.1. the dependence of the value $\Delta M = -\alpha X_1 + \beta C$, introduced to standardize the luminosities of type 1a supernovae, on the redshift is shown for the sample of Kowalski & et al. (2008).

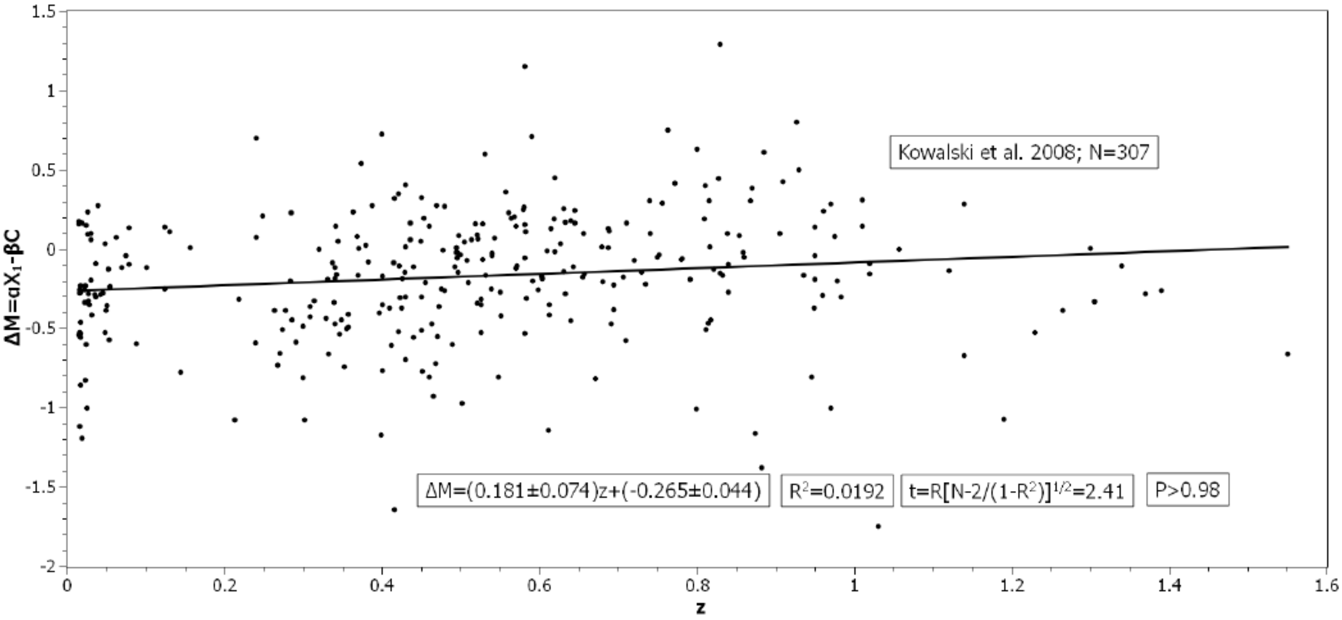

Figure 1. Dependence of the value ΔM introduced for standardization of luminosities of type Ia supernovae on redshift, for the sample of Kowalski & et al. (2008). Correlation significance < 0.02 (2.4σ).

As can be seen from the figure, there is an obvious relationship between the discussed quantities. Let us evaluate the significance of the correlation. For this we will use the value

$$t = \sqrt{(n-2) \div (1-R^2)}$$

which the subject of Student's distribution. Here R the correlation coefficient between the values ΔM and z

We get t=2.41, from which it follows that the significance of the correlation is high $\alpha = 1 - P \approx 0.02$.

On Fig.2. the dependence of the value $\Delta M = -\alpha X_1 + \beta C$ on the redshift is shown, for the sample of Amanullah & et al. (2010). As can be seen, there is a strong correlation at the level of 3.5σ.

On Fig.3. the dependence of the value $\Delta M = -\alpha X_1 + \beta C$ on the redshift is shown, for the sample of Betoule & et al. (2014). There is also a strong correlation at the level of 6.7σ.

For the last sample (Betoule & et al. (2014), we consider the dependence of the parameters αX_1 and βC on the redshift separately.

In Fig.4. The redshift dependence of αX_1, introduced to standardize the luminosity's of type 1a supernovae, is shown for the sample of Betoule & et al. (2014). Significance of correlation > 0.999 (5σ).

In Fig.5. The dependence of the value of βC, introduced to standardize the luminosity's of type 1a supernovae, on redshift is shown for the sample of Betoule & et al. (2014). Significance of correlation > 0.999 (5σ).

Thus, in all studied samples of type 1a supernovae, a strong dependence of the luminosity standardization parameter on the redshift is observed. The correlation is also observed separately for both parameters X_1 and C.

doi: https://doi.org/10.52526/25792776-23.70.1-114

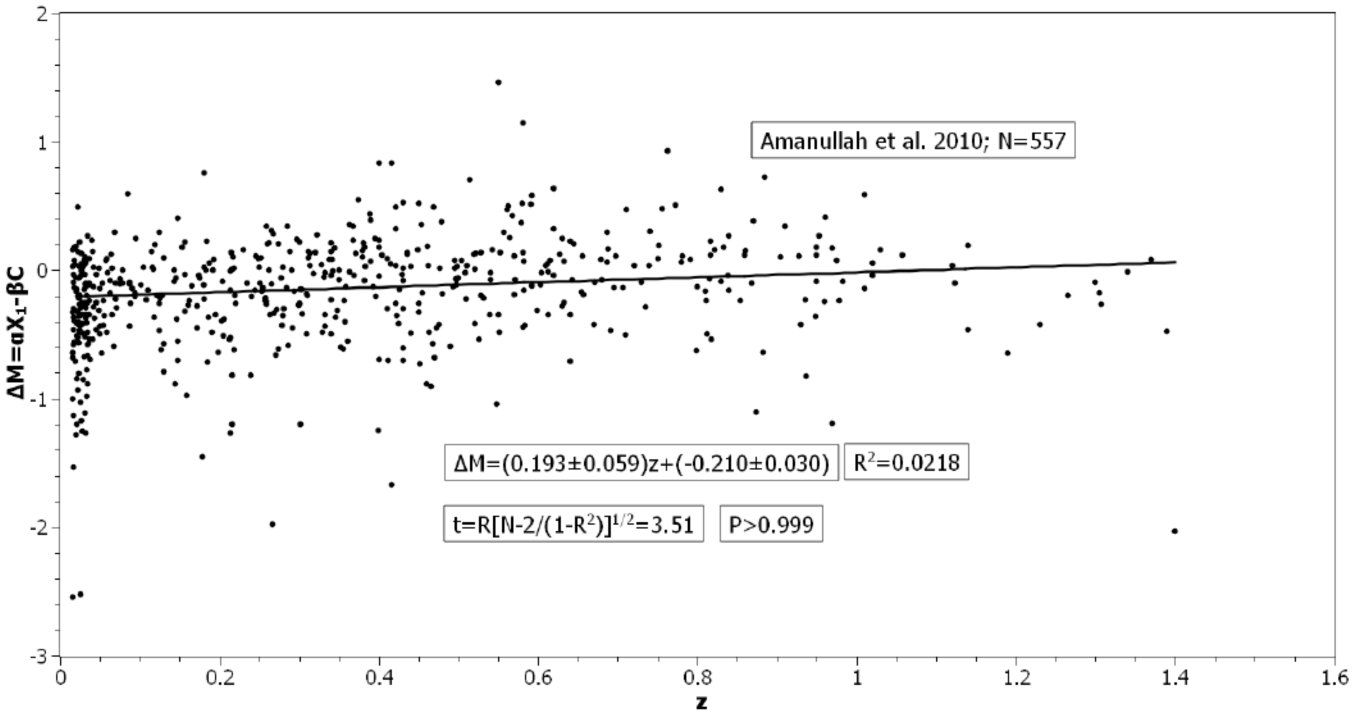

Figure 2. The same as in fig. 2 for a sample of Amanullah & et al. (2010). The correlation is significant at the 3.5σ level.

Such a correlation means that at large z we artificially increase the average absolute magnitude of supernovae during standardization and, therefore, for a given apparent magnitude, on average, we attribute to them a greater distance than they actually have. And so we believe that they are being receding with acceleration.

Thus, we can conclude that such standardization is unsuitable for measuring the distances of type 1a supernovae.

Let's see what happens if we ignore these corrections and estimate the cosmological parameters for the ΛCDM model without standardizing the luminosity's.

We will also try to replace these parameters with a parameter characterizing the evolution of supernovae. We assume that the dependence of the absolute magnitude on the redshift is linear.

For this, we will use observational data from Betoule & et al. (2014), without making any changes to the apparent magnitude B_{obs} of supernovae.

This sample was obtained from a collaboration between SDSS-II (Sloan Digital Sky Survey) and SNLS (SuperNova Legacy Survey) (Betoule & et al. (2014): https://vizier.cds.unistra.fr/viz-bin/VizieR?-source=J/A+A/568/A22).

The collaboration was called JLA - Joint Light curve Analysis. It includes some stars at low redshifts ($z < 0.1$), stars selected from SDSS-II ($0.05 < z < 0.4$) and stars selected from SNLS ($0.2 < z < 1$). A total of 740 spectroscopically confirmed Type Ia supernovae with high-quality light curves.

During the simulation, the authors obtained the following values of the cosmological parameters: $\Omega_M = 0.295; \Omega_\Lambda = 0.705$ (Betoule & et al. (2014)). Let's see what we get.

If we do not take into account evolution, then we will have:

$$M(z) = M_0 = B_{obs} - 5 \log D_L - 25 \tag{1}$$

With the assumption of evolution:

$$M(z) = M_0 + \epsilon z = B_{obs} - 5 \log D_L - 25 \tag{2}$$

where B_{obs} is the apparent magnitude, M_0 is the absolute magnitude at $z = 0$, D_L is the luminosity distance, ϵ is the absolute magnitude evolution coefficient.

Or we can replace the standardization equation with the equation

$$\mu = B_{obs} - (M_0 + \epsilon z) \tag{3}$$

doi: https://doi.org/10.52526/25792776-23.70.1-114

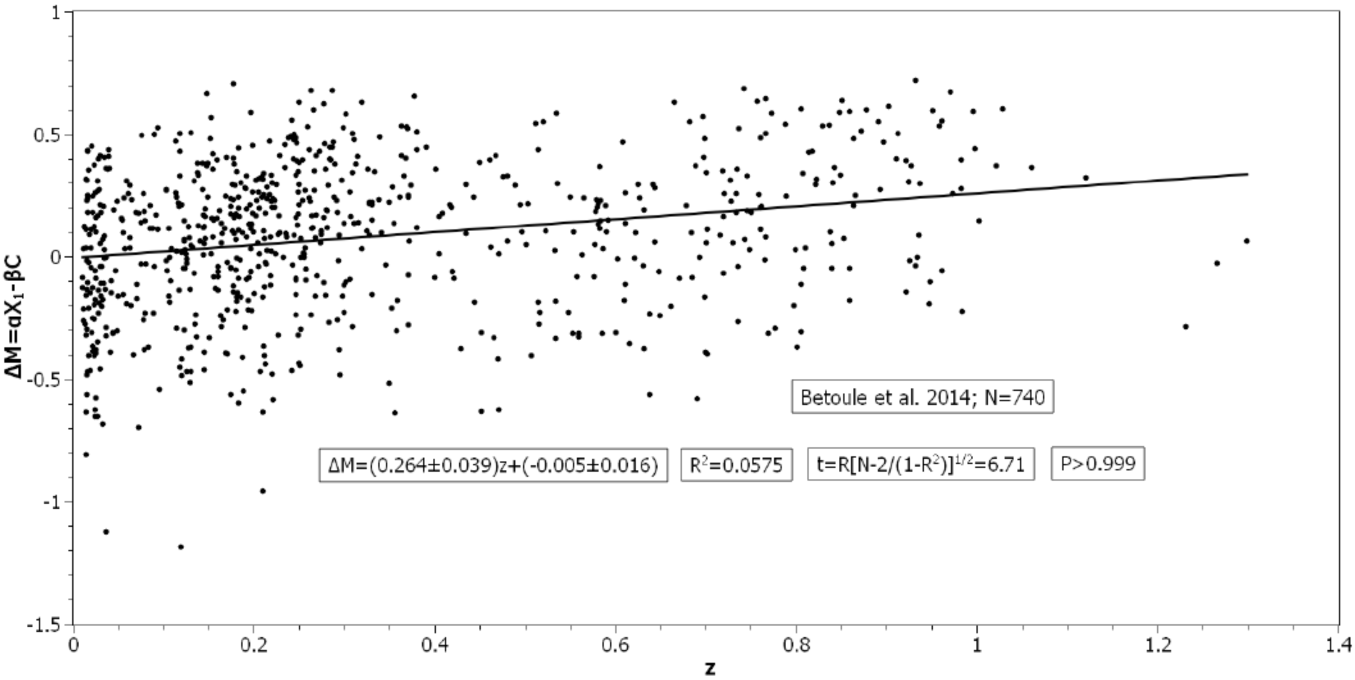

Figure 3. The same as in fig. 2 and 3 for a sample of Betoule & et al. (2014). The correlation is significant at the 6.7σ level.

In the case of the ΛCDM model, the dependence of the luminosity distance on redshift is given by the following formula:

$$D_L(z,\Omega_M,\Omega_\Lambda,\Omega_K) = CH_0^{-1}\,(1+z)\,|\Omega_K|^{-\frac{1}{2}}\,sinn\left\{|\Omega_K|^{\frac{1}{2}}\int_0^z dz\Big[(1+z)^2\,(1+\Omega_M z)-z(2+z)\Omega_\Lambda\Big]^{-\frac{1}{2}}\right\} \tag{4}$$

where z is the redshift of the object. H_0 is the Hubble constant (Accepted $H_0 = 72.305\ km.s^{-1}.Mps^{-1}$). Ω_K is related to the curvature of space and in the case of flat universe it is 0 (Carroll & et al. (1992): $\Omega_K = 1-\Omega_M-\Omega_\Lambda$, $sinn = sinh$, when $\Omega_K \geq 0$ and $sinn = sin$, when $\Omega_K \leq 0$. In the case of $\Omega_K = 0$, we will have:

$$D_L(z,\Omega_M,\Omega_\Lambda) = \frac{C(1+z)}{H_0}\times$$
$$\int_0^z dz\,\left[(1+z)^2(1+\Omega_M z)-z(2+z)\Omega_\Lambda\right]^{-\frac{1}{2}} \tag{5}$$

or

$$D_L = \frac{C(1+z)}{H_0}\int_0^z dz\,\left[(1+z)^3\Omega_M+\Omega_\Lambda\right]^{-\frac{1}{2}}$$

If we assume that $\Omega_\Lambda = 1$, and $\Omega_M = 0$, we will have (Weinberg (2008))

$$D_L(z) = \frac{C}{H_0}\left(z+z^2\right) \tag{6}$$

If $\Omega_\Lambda = 0$, and $\Omega_M = 1$, we have

$$D_L(z) = \frac{2C}{H_0}\left[(1+z)-\sqrt{1+z}\right] \tag{7}$$

It should be noted that in 1998, prior to the work of Riess & et al. (1998) and Perlmutter & et al. (1999) commonly used the equations of general relativity (GR) with zero cosmological constant ($\Lambda = 0$). Using this model, Mattig (1958) integrated these equations exactly and obtained the luminosity distance as a function of redshift.

$$D_L(z,q_0) = \frac{C}{H_0 q_0^2}\left[q_0 z+(q_0-1)\left(\sqrt{1+2q_0 z}-1\right)\right] \tag{8}$$

doi: https://doi.org/10.52526/25792776-23.70.1-114

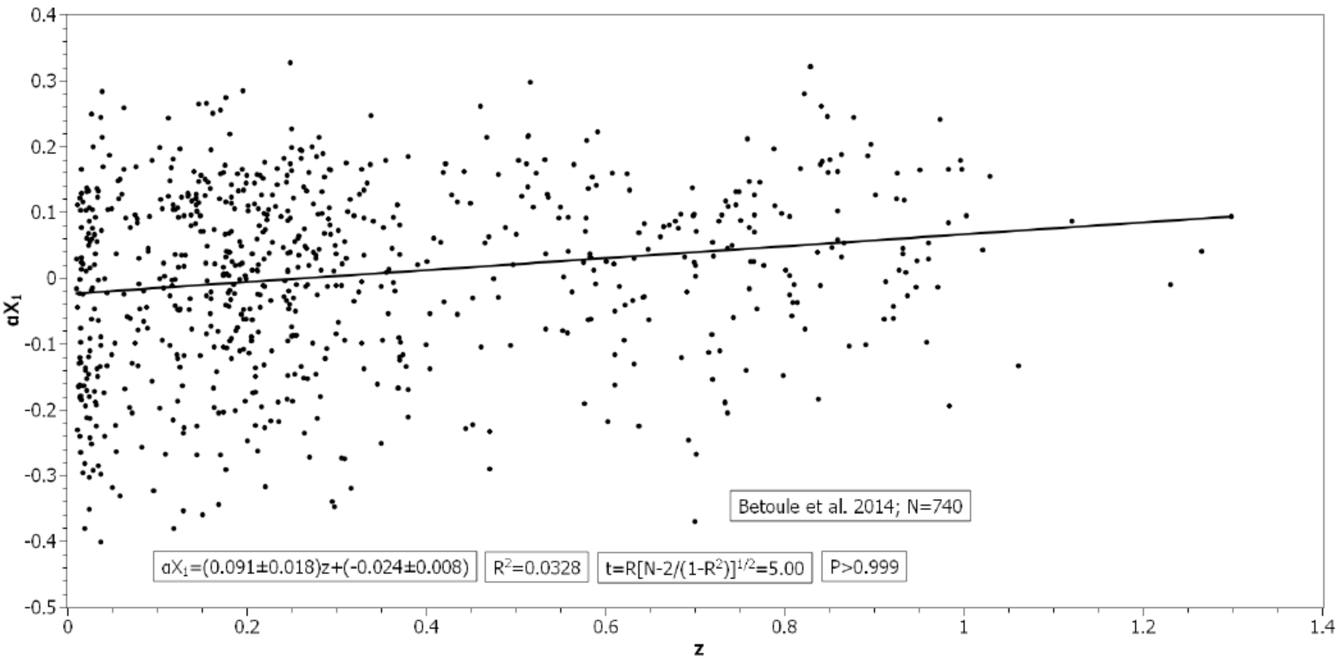

Figure 4. Dependence of the value αX_1 introduced for standardization of luminosity's of type 1a supernovae on redshift, for the sample of Betoule & et al. (2014). Correlation significance < 0.001 (5σ).

Where q_0 is the deceleration parameter, in this case:

$$q_0 = \frac{\Omega_M}{2} \tag{9}$$

(8) with $q_0 = 0.5$ coinciding with (7).

For the luminosity distance in the case of a flat universe we will use formula (5), for the luminosity distance in the model with zero cosmological constant ($\Lambda = 0$) we will use formula (8).

We will also discuss the general case (4) with nonzero space curvature.

On the Hubble diagram, the theoretical curve can be represented by the following relationship:

$$B^{th}_{mag}(z, \Omega_M, \Omega_\Lambda, \Omega_K) = M_0 + \epsilon z + 5 \log D_L(z, \Omega_M, \Omega_\Lambda, \Omega_K) + 25 \tag{10}$$

for the Friedmann-Robertson-Walker model, or

$$B^{th}_{mag}(z, q_0) = M_0 + \epsilon z + 5 log D_L(z, q_0) + 25 \tag{11}$$

for the model with zero cosmological constant.

We need to find those values of the parameters Ω_M, Ω_Λ, Ω_K, M_0, ϵ in the first case and q_0, M_0, ϵ in the second case, so that the sum of squares $(B^{obs} - B^{th}_{mag}(z))$ would be minimal:

$$Chi^2 = \sum \left(B_{obs} - B^{th}_{mag}(z)\right)^2 = min. \tag{12}$$

In Table. 1. The values of the cosmological parameters of the ΛCDM and CDM models are given under various assumptions about the curvature of space and the evolution of type 1a supernovae for the JLA sample (Betoule & et al. (2014)).

It can be seen from the table that under the assumption of a flat Universe without the evolution of supernova luminosity, we obtain $\Omega_\Lambda = 0.505$, $\Omega_M = 0.495$, but the error in this case is the largest. For a flat Universe, the case with the assumption of the evolution of supernova luminosity's is more acceptable. But then the fraction of dark energy in the Universe turns out to be quite small (almost 0).

If we do not make restrictions on the curvature of space, then we will get a better approximation to the Hubble diagram. In this case, both under the assumption of the absence of evolution of supernova luminosity's and under the assumption of the existence of evolution, the fraction of dark energy turns out to be exactly equal to zero, and the curvature of space turns out to be negative. In this case, the required

doi: https://doi.org/10.52526/25792776-23.70.1-114

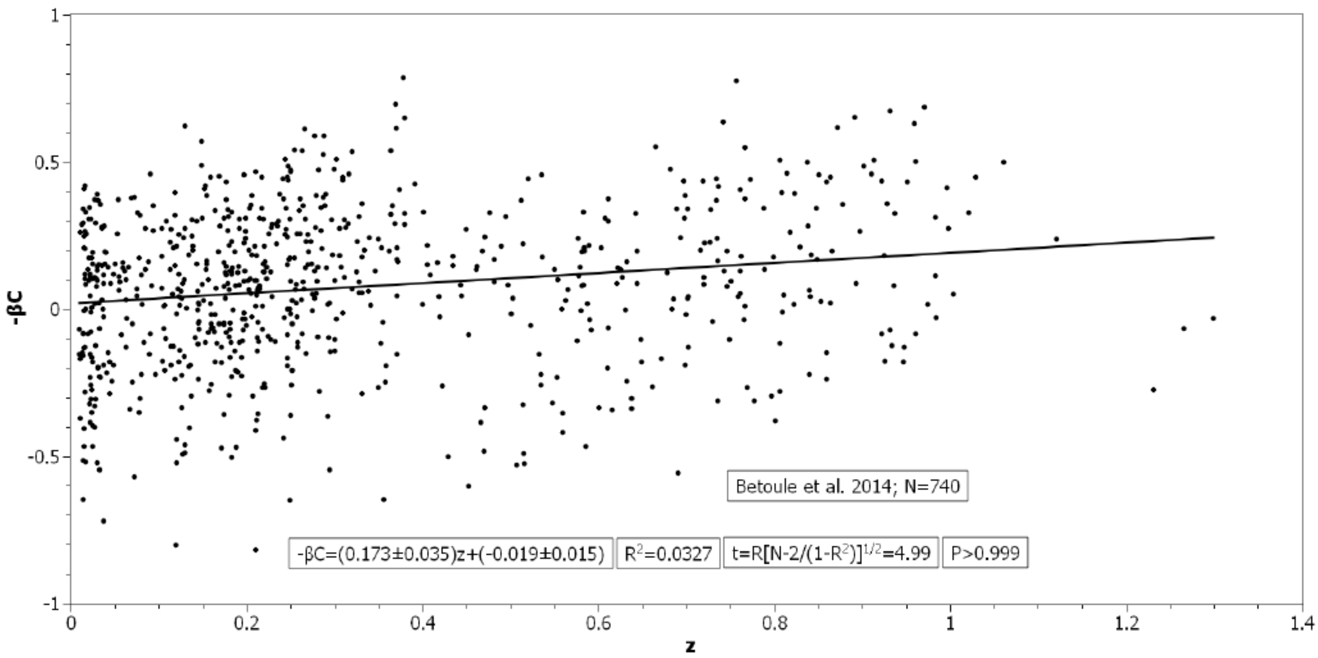

Figure 5. Dependence of the value βC introduced for standardization of luminosity's of type 1a supernovae on redshift, for the sample of Betoule & et al. (2014). Correlation significance < 0.001 (5σ).

Table 1. Values of the cosmological parameters of the ΛCDM and CDM models obtained under various assumptions about the curvature of space and the evolution of type 1a supernovae for the JLA sample (Betoule & et al. (2014)

		Received					
Supposed	Evaluated	M_0	ϵ	Ω_Λ	Ω_M	Ω_K	$< Chi^2 >$
$\Omega_K = 0, \Omega_\Lambda + \Omega_M = 1, \epsilon = 0$	$M_0, \Omega_\Lambda, \Omega_M$	-18.998	-	0.505	0.495	0	0.079493 ± 0.004761
$\Omega_K = 0, \Omega_\Lambda + \Omega_M = 1, \epsilon \neq 0$	$M_0, \epsilon, \Omega_\Lambda, \Omega_M$	-18.961	0.361	0.058	0.942	0	0.079085 ± 0.004756
$\Omega_\Lambda + \Omega_M + \Omega_K = 1, \epsilon = 0$	$M_0, \Omega_\Lambda, \Omega_M, \Omega_K$	-18.960	-	0.000	0.216	0.784	0.079046 ± 0.004755
$\Omega_\Lambda + \Omega_M + \Omega_K = 1, \epsilon \neq 0$	$M_0, \epsilon, \Omega_\Lambda, \Omega_M, \Omega_K$	-18.959	-0.044	0.000	0.146	0.854	0.079045 ± 0.004755
Supposed	Evaluated	M_0	ϵ		q_0		$< Chi^2 >$
$\Lambda = 0, \epsilon = 0$	M_0, q_0	-18.960	-		0.108		0.079046 ± 0.004755
$\Lambda = 0, \epsilon \neq 0$	M_0, ϵ, q_0	-18.959	-0.044		0.073		0.079045 ± 0.004755

evolution is small. True, if we assume evolution, then we will get a somewhat small value of Chi^2, but we cannot give preference to what.

The last two lines show the simulation results for the Universe model with zero cosmological parameter. Thus, the best approximation of the Hubble diagram for the ΛCDM model is the same as the best approximation of the CDM model. That is, the model with zero cosmological constant describes the Universe no worse than the ΛCDM model.

Let's see how good these approximations are for the entire studied redshift interval.

On Fig. 6-9 show the residuals of the observational data (the difference between the observed and theoretical apparent magnitudes) as a function of redshift.

In all figures, a horizontal line is obtained, almost indistinguishable from the line $B_{obs} - B_{th} = 0$. It means that

1. The ΛCDM model describes the Universe well.

2. The observational data have been fairly well processed by the JLA authors over the entire redshift range.

Let's try to see what happens if we take $\epsilon = -0.264$ in the formula $\mu = B_{obs} - (M_0 + \epsilon z)$ (based on the obtained dependence $\Delta M = \alpha X_1 - \beta C = 0.264z - 0.005$ in Fig. 3) and estimate the cosmological parameters.

It turns out $\Omega_\Lambda = 0.73$, $\Omega_M = 0.27$, $M = -19.013$. That is, approximately what is obtained in many studies by standardizing supernovae according to the formula $\mu = B_{obs} - (M_B - \alpha X_1 + \beta C)$.

doi: https://doi.org/10.52526/25792776-23.70.1-114

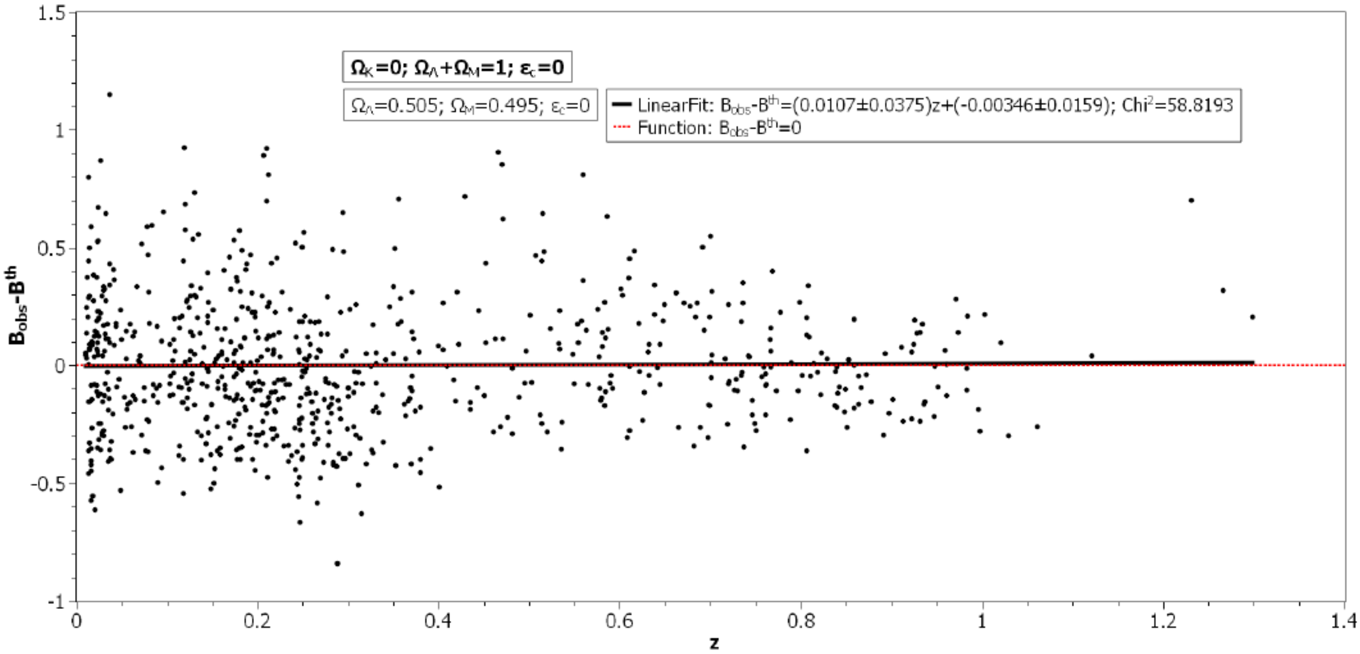

Figure 6. The difference between the observed and theoretical apparent magnitudes from the redshift for the case $\Omega_K = 0, \Omega_\Lambda + \Omega_M = 1, \epsilon = 0$.

3. Conclusion

The standardization of light curves for type 1a supernovae was invented in order to minimize the errors and bring the observational data on the Hubble diagram closer to the theoretical ones and to obtain the constraint on the cosmological parameters as accurately as possible. As a result, a close fit between observations and theory has been obtained (eg, Betoule & et al. (2014)). But, in our opinion, the authors of these works made a serious systematic error.

This leads to the fact that at large z we artificially increase the average absolute magnitude of supernovae during standardization and, therefore, for a given apparent magnitude, on average, we attribute to them a greater distance than they actually have. And so we believe that they are being receding with acceleration.

Therefore, we can conclude that such standardization is unsuitable for determining the cosmological parameters.

To determine the cosmological parameters, we study two options:

1. Do not standardize, i.e. use the apparent magnitudes of supernovae without any corrections.

2. For standardization, we assume that the absolute magnitudes of type 1a supernovae depend on the redshift and instead of the standardization relation

$$\mu = B_{obs} - (M_B - \alpha X_1 + \beta C)$$

use relation

$$\mu = B_{obs} - (M_B + \epsilon z)$$

The following results are obtained:

• Assuming a flat Universe without supernova luminosity evolution, we obtain $\Omega_\Lambda = 0.505, \Omega_M = 0.495$, but the error in this case is the largest. For a flat Universe, the case with the assumption of the evolution of supernova luminosity's is more acceptable. But then the share of dark energy in the Universe turns out to be quite small (almost 0). For the evolution coefficient, we obtain $\epsilon = 0.361$.

• If we do not impose restrictions on the curvature of space, we will get a better approximation to the Hubble diagram. In this case, both under the assumption of the absence of evolution of supernova luminosity's and under the assumption of the existence of evolution, the fraction of dark energy turns out to be exactly equal to zero, and the curvature of space turns out to be negative. In this case, the required evolution is small and can even be neglected. True, if we assume evolution, then we get a somewhat small value of Chi^2, but the difference in Chi^2 is so small that we cannot give preference to it.

In one case we get

doi: https://doi.org/10.52526/25792776-23.70.1-114

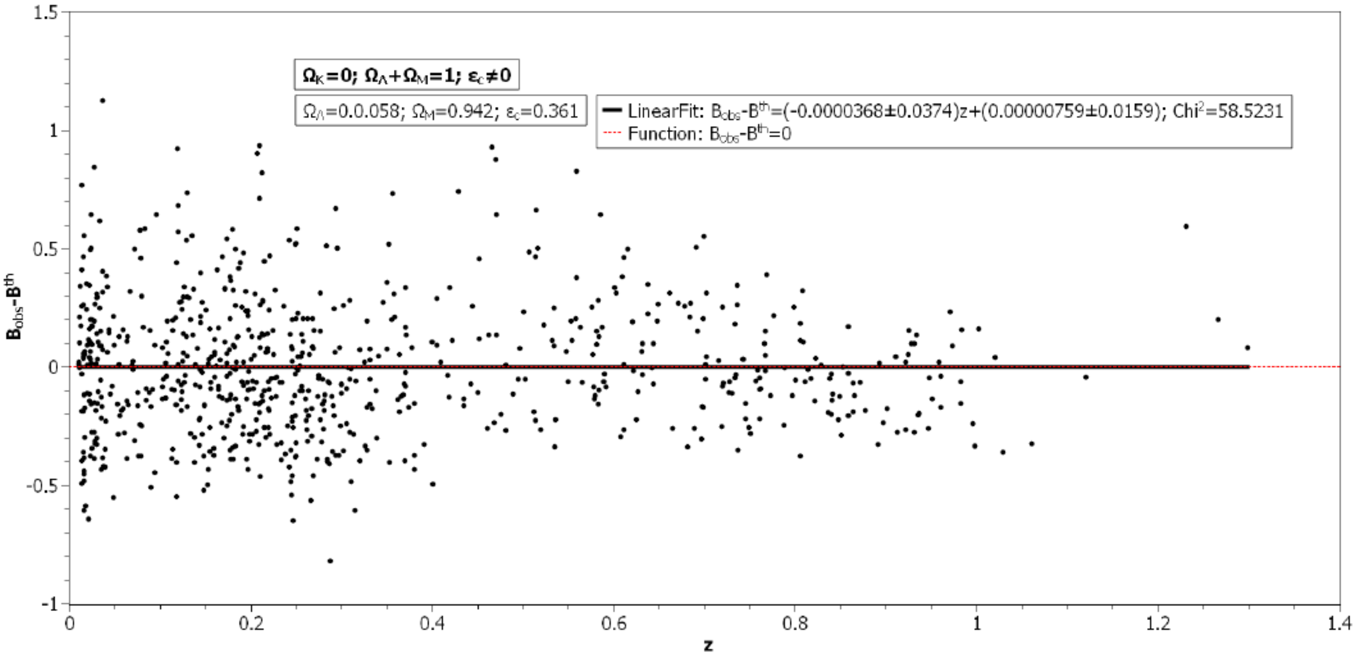

Figure 7. The difference between the observed and theoretical apparent magnitudes from the redshift for the case $\Omega_K = 0, \Omega_\Lambda + \Omega_M = 1, \epsilon \neq 0$.

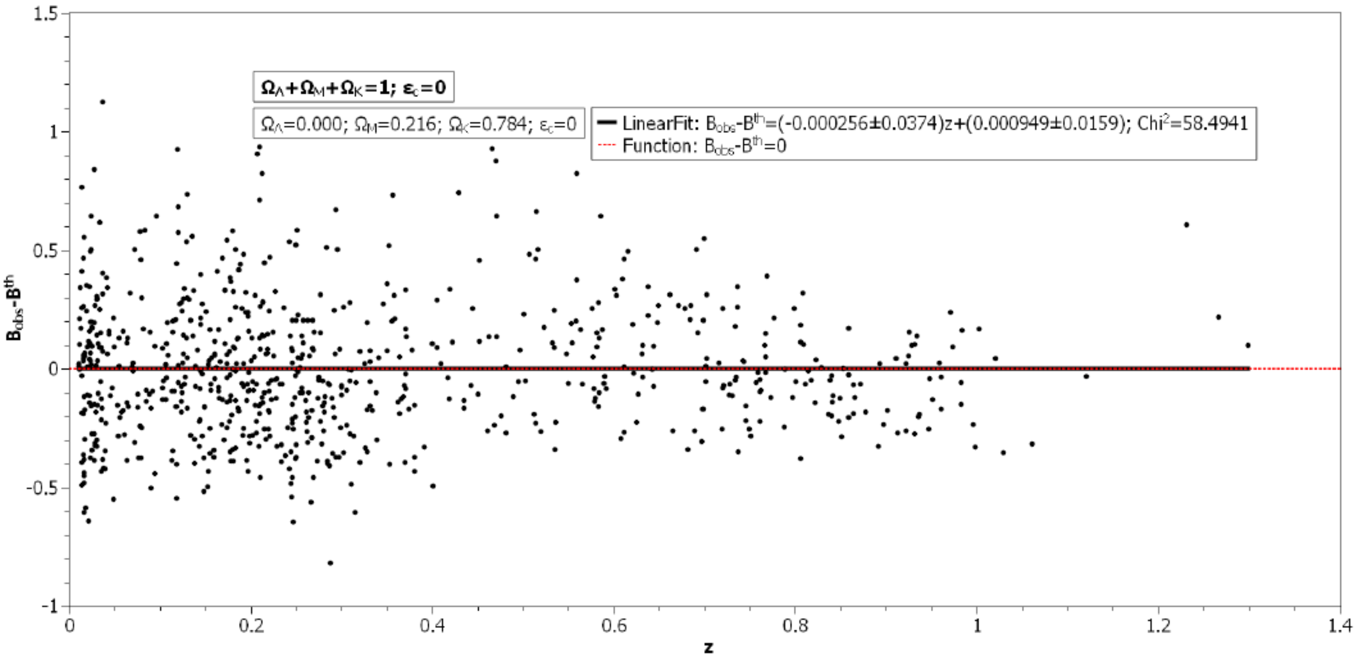

Figure 8. The difference between the observed and theoretical apparent magnitudes from the redshift for the case $\Omega_\Lambda + \Omega_M + \Omega_K = 1, \epsilon = 0$.

$\Omega_\Lambda = 0.000$, $\Omega_M = 0.216$, $\Omega_K = 0.784$, $\epsilon = 0$, (analogue for the CDM model is $q_0 = 0.108$) otherwise we get
$\Omega_\Lambda = 0.000$, $\Omega_M = 0.146$, $\Omega_K = 0.854$, $\epsilon = -0.044$, (analogue for the CDM model is $q_0 = 0.073$).

From the above analysis, we can conclude that the reason for the result about the existence of dark energy lies in the incorrect standardization of supernova luminosity's. Apparently dark energy doesn't exist.

Evidence of the evolution of the luminosity's of type 1a supernovae and the probable absence of dark energy was also obtained in our other papers and reports Mahtessian & et al. (2020), Mahtessian & et al. (2021), Mahtessian & et al. (2022), Mahtessian & et al. (2023)), as well as by other authors (for example, Kang & et al. (2020)).

doi: https://doi.org/10.52526/25792776-23.70.1-114

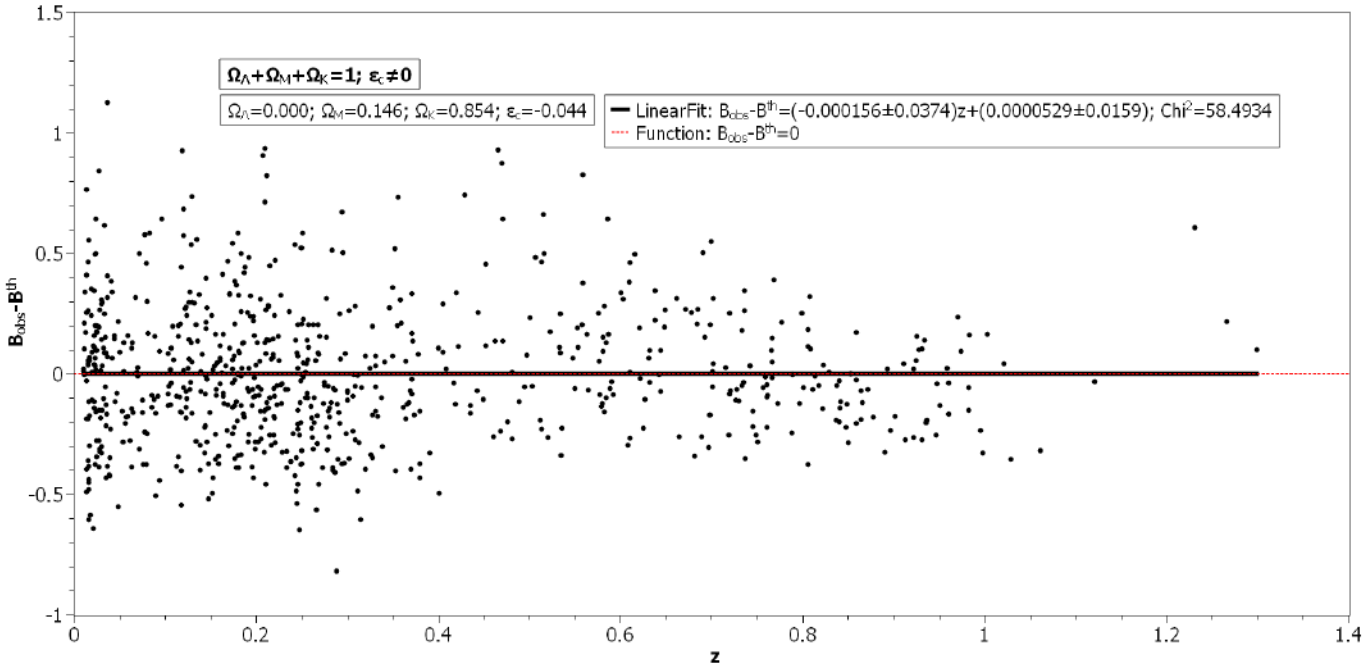

Figure 9. The difference between the observed and theoretical apparent magnitudes from the redshift for the case $\Omega_\Lambda + \Omega_M + \Omega_K = 1, \epsilon \neq 0$.

References

Amanullah R., et al. 2010, The Astrophysical Journal, 716, 712

Ashall C., et al. 2016, Monthly Notices of the Royal Astronomical Society, 460, 3529

Betoule M., et al. 2014, Astronomy and Astrophysics, 568, A22

Carroll S. M., et al. 1992, Annual Review of Astronomy and Astrophysics, 30, 499

Guy J., et al. 2007, Astronomy and Astrophysics, 466, 11

Kang J., et al. 2020, The Astrophysical Journal, 889, 8

Kowalski M., et al. 2008, The Astrophysical Journal, 686, 749

Lee Y.-W., et al. 2022, Monthly Notices of the Royal Astronomical Society, 517, 12697

Mahtessian A. P., et al. 2020, Advances in Astrophysics, 5, 18

Mahtessian A. P., et al. 2021, Communications of the Byurakan Astrophysical Observatory, 68, 484

Mahtessian A. P., et al. 2022, Communications of the Byurakan Astrophysical Observatory, 69, 280

Mahtessian A. P., et al. 2023, International Journal of Astronomy and Astrophysics, 13, 39

Mattig W., 1958, Astronomische Nachrichten, 284, 108

Perlmutter S., et al. 1999, The Astrophysical Journal, 517, 565

Riess A., et al. 1998, The Astronomical Journal, 116, 1009

Rigault M., et al. 2020, Astronomy and Astrophysics, 644, A176

Weinberg S., 2008, Cosmology. Oxford University Press, Oxford, doi:https://doi.org/10.1007/s10714-008-0728-z

doi: https://doi.org/10.52526/25792776-23.70.1-114

Evolutionary Stages of the Metagalaxy

R. Natsvlishvili *

E. Kharadze Georgian National Astrophysical Observatory, Georgia

Abstract

The matter from which the Metagalaxy is formed is constantly changing, evolving. Since the speed of propagation of the electromagnetic wave in space is not instantaneous, it is limited, within the capabilities of existing powerful telescopes, we can observe the forms of matter in different stages of the evolution of the Metagalaxy in chronological order. So, the more distant the form of matter in the Metagalaxy, the earlier, or younger, it is. In this article, we tried to characterize the stages of the Metagalaxy evolution from a dynamic point of view. In the case of such a model of the Universe, quasars are objects of earlier stage of the evolution of galaxies, and blazars are objects of an intermediate stage between quasars and galaxies.

Keywords: *Universe - Universe Structure - Metagalaxy - Evolutionary Stages of the Metagalaxy*

1. Preamble

Great persons Viktor Amazasp Ambartsumian and Eugene Kirile Kharadze established the groundwork for the bond between Georgian and Armenian astronomers and deepened friendly relations of the Georgian and Armenian people. Ludwik Vasili Mirzoyan was further continuing this connection. During a conference commemorating the 90th anniversary of his birth, I briefly characterized Mr. Ludwik Mirzoyan and referred to him as a "crystal person". Ludwik Mirzoyan was truly crystal man, he possessed strong principles and displayed generosity, showing kindness to everyone. His kind and hospitable wife, Nelly Ruben, was standing next to him, alongside their charming daughters Anait and Nune, their science and sports-loving son, Ara, with their families.

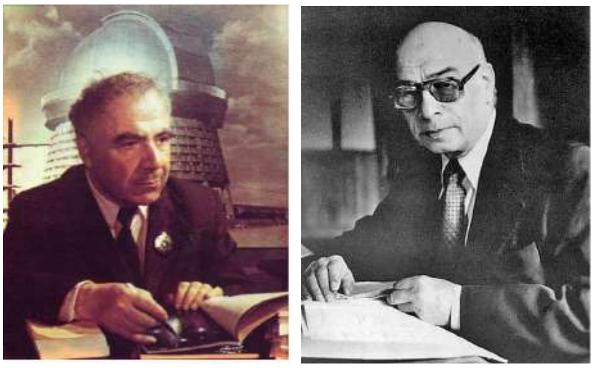

Figure 1. Viktor Amazasp Ambartsumian and Eugene Kirile Kharadze

2. Introduction

When trying to explain the energy of quasars by the accretion of matter onto a rotating massive black hole, the presence of the most massive black hole at an early stage of the Metagalaxy evolution is no less problematic. From where such a mass of matter accumulated in the Metagalaxy at an early, protoquasar stage of evolution?! We believe it is logical to assume that quasars represent an early stage in the evolution

doi:https://doi.org/10.52526/25792776-23.70.1-123

Figure 2. Ludwik Vasili Mirzoyan

of galaxies. This opinion is supported by the fact that the farther away the quasar, the brighter it is. The diagram in Fig. 3 is a clear confirmation of this.

As the redshift z increases, the apparent magnitude of quasars does not change. Therefore, it is illogical to call objects with redshift z=11 and z=13.5 (Oesch et al., 2016), (Pacucci et al., 2022) galaxies in Fig. 4 when these objects do not have any characteristics of a galaxy. These objects could be protoquasars, but not galaxies!!!

And again, when discussing the regions of the birth of stars in the Metagalaxy, for some reason there is a tendency that if an object is surrounded by a nebulous medium, then the process of accretion on the core is unambiguously assumed. Could this nebulous environment be the result of matter being ejected and flowing out of the core (Ambartsumian, 1958)? In a small encyclopedia of physics (Prokhorov et al., 1984), we read that quasars are the nuclei of distant galaxies. The word "distant" does not mean anything cosmological, it means distant galaxies, because these are objects with large redshifts. From our point of view, quasars are not the nuclei of distant galaxies, but objects of an early stage in the evolution of galaxies. Since we believe that the action of non-gravitational forces of internal repulsion has been eliminated by now, the expansion of the Universe should occur at a slower rate. Starting from the Big Bang, according to the chronological dynamic picture of the expansion and contraction of the Universe, depending on the nature of the change in time of the internal repulsive force, in the case of a pulsation of the Universe, its specific nature can be determined in principle. Large-scale Metagalactic objects appear to have formed as a result of the fragmentation of a supermassive singular body, similar to what would happen if the contents of a vessel filled with mercury were to shatter in the weightlessness of space. It would be divided into spherical fragments of different masses (see Fig. 5).

To imagine the structure of the Universe, let's try to find out how reasonable the assumption of empty space was, based on the views of Newton at that time? In our opinion, if there is at least one particle in space, it cannot have zero temperature, because it (the particle) moves and accelerates. It is also completely black radiating and the electromagnetic waves generated by it penetrate the space around the particle in all directions. The radiation flux also depends on its mass according to the mass-luminosity relation. Modern classical cosmological models always imply an accretion process. But if galaxies were formed as a result of the gravitational condensation of rarefied matter after the Big Bang, then protogalaxies should have a lower density when move from nearby galaxies to distant galaxies. In the case of such a hierarchy of the Metagalaxy, the evolutionary status of quasars due to their large mass and luminosity is unclear. Thus, Newton's empty space is unreal and non-existent, in which he needed trigger forse to set matter in motion. Sometimes the concept of empty space is such that particles are scattered in outer space in such a way that one or more particles are in one cubic meter of space. Since we know the geometric dimensions of the particles, the rest of the space may appear empty. But these particles themselves are absolutely black emitters with temperature. So the space around them is penetrated in all directions by electromagnetic radiation. The radiation flux also depends on the mass of the particle through the universal mass-luminosity relation $E = mc^2$ (Einstein, 1917). Thus, any notion of empty space is false. This idea, in turn, poses the problem of vacuum inflationary space, when an increase in the volume of space does not change its density. In this space, as it were, matter arises that violates the universal law of nature, and an a priori assumption is made about Perpetuum Mobile. According to the universal fundamental law of nature, the Perpetuum

*rezonatsvlishvili@gmail.com

doi:https://doi.org/10.52526/25792776-23.70.1-123

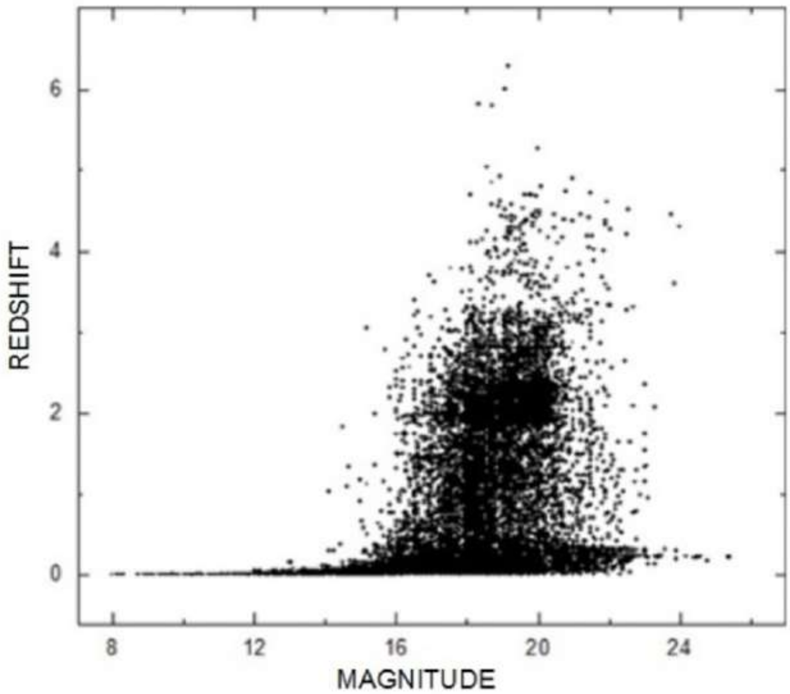

Figure 3. The dependence of redshift vs apparent magnitude for the extragalactic objects. There are objects with known redshifts (Hubble, 1929), (Huchra et al., 1996), (Veron-Cetty & Veron, 1998), (Fan et al., 2000),(Zheng et al., 2000), (Schneider et al., 2001), (Natsvlishvili, 2002), (Natsvlishvili, 2010), (Natsvlishvili & Kochiashvili, 2017) on the diagram: quasars, Lacertae objects, Seyfert galaxies and galaxies, about 36930 objects altogether

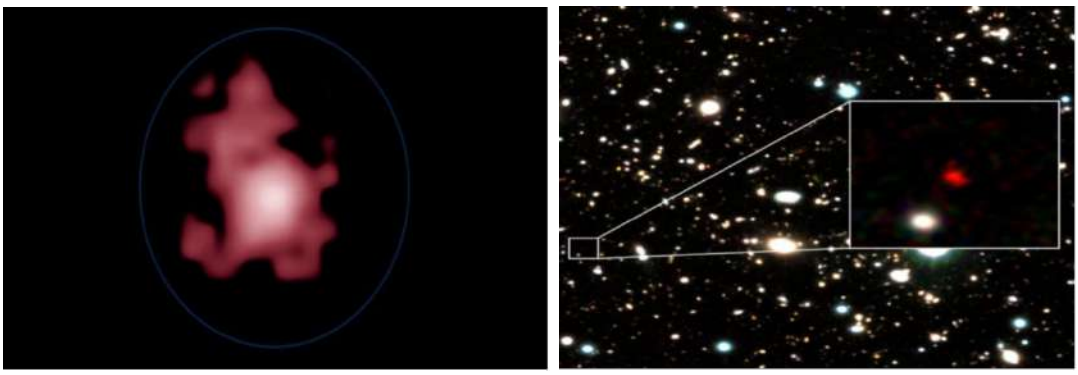

Figure 4. Galaxy GN-z11, z=11 and galaxy HD 1, z=13.5

Mobile does not exist!!!

Thus, since the zero temperature of matter does not exist, space is always penetrated by electromagnetic waves of an absolutely black emitter with a temperature of some t_k. Therefore, space is always permeated with electromagnetic waves, which means that it is not empty, as Newton imagined, and it was a problem for matter to move, which required pulling a trigger to set matter in motion. Matter does not need to be triggered because it always has a temperature above zero (Friedmann, 1922). That is, it always has radiation corresponding to the temperature that permeates the space around it, and it cannot be empty. So, there is no absolute vacuum.

3. Dynamics of the Metagalaxy Displacement

In the volume of the small encyclopedia of physics (Prokhorov et al., 1984) we read that quasars are the nuclei of distant galaxies. Here the word distant does not mean anything cosmological, the word distant refers to distant galaxies, since they are objects with large redshifts. In our opinion, quasars are not the nuclei of distant galaxies, but are objects of an earlier evolutionary stage of galaxies. Since we believe

doi:https://doi.org/10.52526/25792776-23.70.1-123

Figure 5. Spherical fragments of various masses formed when the vessel filled with mercury is destroyed.

that the action of the internal repulsion, antigravitational forces is removed, therefore, the expansion of the Universe should occur at a decreasing rate. A chronological dynamic picture of the expansion and contraction of the Universe, depending on the nature of the change in the internal repulsive force from the moment of the Big Bang for a pulsating model of the Universe, the specific form of which, in principle, can be determined.

We can ask the opposite question. If objects in the Universe have a disposable origin, which we consider logical, due to the undisputable fact that the Universe is constantly expanding, and consequently, decreasing in density after the Big Bang, then why should we assume that under conditions of different densities, events repeat analogically and of the similar objects are formed in absolutely different environments? Then what hierarchy of evolution of the Universe should we expect?

In the case of a pulsating Universe, if the cosmological constant $\Lambda = 0$, the change of Hubble's constant at the stage of contraction of the Universe should be symmetrical or quasi-symmetric with the one at the stage of the expansion stage. As the internal repulsive forces in the Universe from the moment of the Big Bang in the stage of increase of the Hubble constant, to the initial singular state, and the phase of slow expansion of the Universe, which should be caused by the gravitational action, will start from the moment when the internal repulsive forces become less than gravity. This stage of contraction will be symmetrical to the expansion stage. So there is no absolute vacuum. Thus, Newton's trigger force is not needed to set matter in motion.

Wrong interpretation of the Hubble law v=Hr can (Hubble, 1929) lead us to a paradoxical result, the law seems simple, but requires an objective perception. The form of its discovery is not connected with any process occurring in time in the Universe (Metagalaxy). The law does not contain a parameter that depends on time. It relates the spatial parameters v and r determined by the distance. The parameter v expresses the speed of an object at a distance r and cannot reflect the nature of the time shifts of this value. The Hubble law v=Hr in its original form is a formula that expresses the instantaneous state of the Universe in terms of distance and does not consider the change of the constant H over time. It would be correct to write this as H=H(r). At the same time, we a priori assume that the Hubble constant is a value that changes in time due to changes in the expansion rate of the Universe, since objects located at different distances are observed in different epochs.

The nature of the displacement of the Universe (Metagalaxy) over time will be characterized by the change of the Hubble's constant in time H=H(t) and Hubble's law will have a general form: v(t)=H(t)r i.e. H(t)=$\frac{1}{r}\frac{dr}{dt}$, therefore, the change in speed of objects at a distance r over time, and based on this, we can present a chronological picture of the displacement of the Universe (Metagalaxy).

Due to the isotropy of the Universe, it is uniform at every moment, but the observed Universe is uniform only spherically-concentrically.

Even if the Hubble constant is constant, the Universe is expanding at an accelerating rate. Thus, Hubble's law is a kinematic characteristic of the displacement of the Universe, given that the Hubble constant H is not a function that changes with time. But in general, the Hubble constant depends on time, and H=H(t)

doi:https://doi.org/10.52526/25792776-23.70.1-123

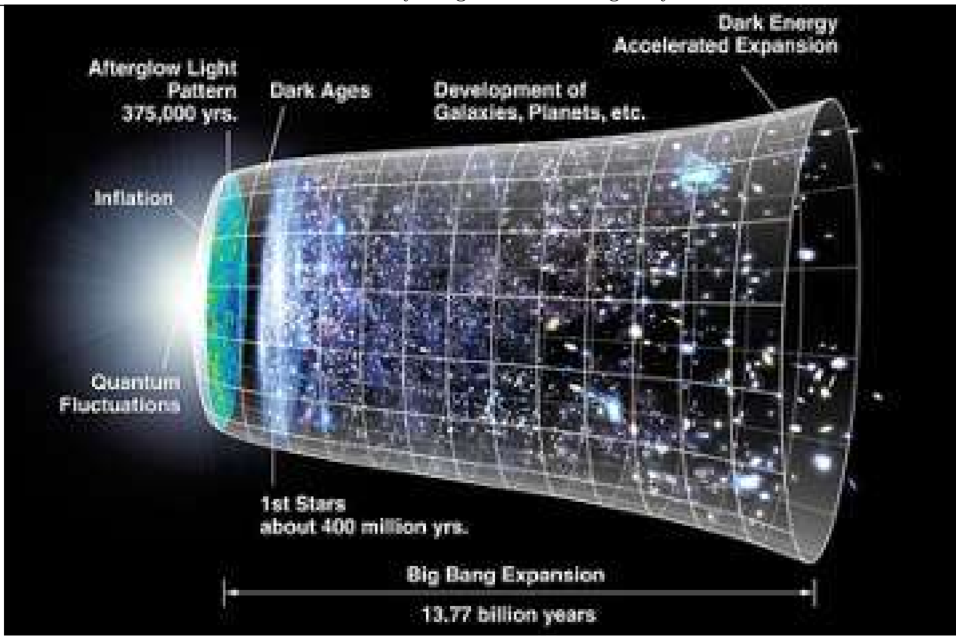

Figure 6. A graphical representation of the expansion of the universe from the Big Bang to the present day, with the inflationary epoch represented as the dramatic expansion of the metric seen on the left

is a function of time. In this case, if we give the Hubble law a general form, we will have v(t)=H(t)r, and this general Hubble law already characterizes the dynamics of the Universe.

On the other hand, if one can somehow determine the nature of the change in the speed v(t) of objects at each distance r, then the picture of the dynamic evolution of the Universe can be reconstructed from the change in time of the speed of objects at different distances. This is a theoretical perspective since it is practically impossible to determine the nature of the change in the speed of objects at large distances in a short period of time. Based on the fact that H(t)=$\frac{1}{r}\frac{dr}{dt}$ and the change in the speed of each object is relative, so it becomes more difficult to determine the nature of the change in the speed of objects if H(t)=$\frac{1}{r}\frac{dr}{dt}$ is not a very rapidly variable, i.e. the Hubble constant H(t) is not a rapidly changing function of time. It is practically impossible to notice a change in the recessional velocity of objects in a short period of time, so determining the functional form of H(t) is problematic.

When they talk about the expansion of the Universe at an accelerated rate, kind of dark energy is mentioned as the reason for this. Because the issue is about the movement of objects with acceleration, it follows that kind of repulsive, anti-gravitational force must act on these objects, the nature of which today is impossible to express any opinion, except that if we are dealing with accelerated motion, a force should act on a body moving with acceleration. This force moves apart objects, it pulls these objects away from each other. This force compensates the force of gravity and even surpasses it quantitatively, because if there were no strong pulling force, the Universe would expand more slowly, that is, the Hubble constant H=H(t) would be a decreasing function of time. And if the Universe is expanding at an accelerated rate, it turns out that the Hubble constant H=H(t) is an increasing function of time. If Hubble's constant were constant, the expansion of the universe would have to occur at a constant rate. Actually, r is a time variable, but Hubble's classical law v=Hr does not give us the nature of r's change. The variable r in the Hubble's law is not a function of time in the classical sense. It is parametric variable and equal to r for every fixed v speed. This does not show the nature of the change of r over time. Thus, the nature of the change in v is unclear.

Quasars as they were discovered in the 1960s seemed to be objects of a certain type, differing from the nearby objects only in their high radial velocities and high luminosity (Burbidge & Burbidge, 1967). So there was not even a hint that quasars represent an early evolutionary stage of galaxies. We see quasars in the distant past. If we could see the entire Universe instantly, we would notice that quasars are objects of a bygone era, and today they no longer exist, just as galaxies did not exist in the era of quasars. Because the further away a quasar is, the more absolute luminous it is, indicating that quasars are more massive objects than the galaxies. In Figure 3, Galaxies are the modern form of quasars, which in turn are evolving again. Thus, the evolutionary hierarchy of the Universe is a process of transition from high density to low density, since the observable fact is that the Universe is expanding. Since the Big Bang, the Universe has been in a state of constant expansion, as evidenced by the discovery of Hubble's law. The farther an object

doi:https://doi.org/10.52526/25792776-23.70.1-123

is, the faster it moves away from us, and wherever we are in space, it is isotropic, although the Universe we observe is not homogeneous. Instantly the Metagalaxy is only spherically concentrically homogeneous. Only the spherically concentric narrow layers of the observed Metagalaxy are homogeneous, because the rate of expansion of the Universe would be different in different epochs, so the rate included in the Hubble law and the Hubble constant are time-dependent quantities. The classical Hubble law does not tell us how the Hubble constant changes with time depending on distance. In principle, it is possible to determine the functional form of an object's speed using accurate unchanging light repers, but since there is nothing constant in the Metagalaxy and everything evolves, to determine the functional form of an object's speed in time is problematic. Without determining the dependence of speed on time, it is impossible to determine the age of the Metagalaxy and the Universe. When the age of the Universe is determined by the simple ratio $\frac{1}{H}$, this gives a very rough estimate of the age of the Universe, for a more accurate estimate, the functional form of v as a function of time is needed.

If the age of the Metagalaxy is Θ, it can be expressed through an integral and we will have:

$$\Theta = \frac{1}{c}\int_0^R \frac{dr}{v(r)}$$

where R is the radius of the Metagalaxy. If we denote by Ψ the time elapsed from the age of the objects on the border of the Metagalaxy to the moment of the Big Bang, the age of the universe, T will be $T = \Psi + \Theta$.

$$\frac{\Delta\lambda}{\lambda} = \frac{(\lambda - \lambda_0)}{\lambda} = z$$

We will have

$$v = \frac{(z+1)^2 - 1}{(z+1)+1}c$$

We will get

$$\Theta = \frac{1}{c}\int_0^R [1 + \frac{2}{z^2(r) + 2z(r)}]dr$$

At every fixed moment t_k, the age of all large-scale objects in space is the same. As for the fragmentation of matter from the Great Singularity, as we already mentioned, it should be similar to that in the weightless state of space, a vessel full of mercury is broken and fragments of different masses of mercury are scattered in space. They will all have a spherical shape and differ only in mass. So, even in the case of protoquasars, the universal dependence of mass-luminosity is preserved. An illustration of this process is in Fig. 5.

Space is always permeated with electromagnetic waves corresponding to the temperature of the matter in it with the corresponding quantitative dependence $E = mc^2$. Based on the evolutionary stages of quasars, it is not clear on what basis objects with the highest redshift z can be called galaxies. How did galaxies first exist, then quasars formed, and then galaxies again? It is logical if objects located at the corresponding redshift distance z=11 and z=13.5 can be called objects with an early evolutionary status of quasars, i.e. protoquasars. Protoquasars are objects of the early evolutionary stage of quasars. Matter of an earlier form than protoquasars is the region where the microwave background radiation of 2.7K is generated. It is not known whether this matter forms continuous layers or has a discrete structure (Penzias & Wilson, 1965), (Natsvlishvili, 2003), (Natsvlishvili, 2004). Then, as a result of evolution, quasars and, at the next stage, galaxies were formed. The objects of the next stage of protoquasars are quasars, and after quasars come the oldest large-scale intermediate objects: Seyfet galaxies, radio galaxies, galaxies with active nuclei, stationary galaxies. They can be characterized dynamically by the time change of the Hubble constant.

4. Dynamics of the Metagalaxy Motion

1. If H(t)= 0, the Metagalaxy is static.
2. If H(t)=const>0, the Metagalaxy is expanding at an increasing rate, accelerating.
3. If H(t)=const<0, the Metagalaxy is shrinking at a decreasing rate.
4. If H(t)= const > 0 and $\frac{dH(t)}{dt} > 0$, the Metagalaxy is compressible with increasing rate and acceleration.

doi:https://doi.org/10.52526/25792776-23.70.1-123

5. If H(t)>0 and $\frac{dH(t)}{dt} < 0$, then the Metagalaxy is expanding at a slower rate.

On Fig. 6 is given a picture of the evolutionary stages of the Universe. At the initial part, the inflation stage is shown, which raises many doubtful questions, since in the case of the inflationary model it turns out that matter is created, during which the volume of the medium increases, while its density remains unchanged. This indicates the formation of matter, in which the principle of the inadmissibility of Perpetuum Mobile in nature is violated.

5. Conclusion

The cosmogonic hierarchy of the Metagalaxy is a process of disposable formation of large-scale objects of the Universe. The Universe is pulsating, but it is not necessary to repeat every action exactly. The main principle of Perpetuum Mobile is excluded in nature, this universal principle must always be fulfilled. So, the assumption that the allegedly the Universe has an inflationary phase of development, we suspiciously consider, as well as an absolute vacuum. Because in the case of any volume of space, if material substance is present in it, the space around it cannot be empty, and it will be penetrated in every direction by electromagnetic waves according to the mass. Each particle or conglomerate of particles cannot be stationary, so it has electromagnetic radiation corresponding to its temperature, which penetrates the space around it in every direction.

Energy is quantified by Einstein's universal relation $E = mc^2$. Finally, we believe that quasars are the early evolutionary stage of galaxies. Objects with high z redshifts cannot be galaxies. They, in turn, are objects of the early evolutionary stage of quasars, protoquasars, from which later quasars were formed. Thus, quasars are not the nuclei of distant galaxies, but the objects of the early evolutionary stage of galaxies. At the distance of protoquasars cannot exist galaxies like at near distances – quasars. Quasars and protoquasars are objects of a bygone era and, in fact, no longer exist today, just as galaxies do not exist within the distance of quasars.

We must always keep in mind that we must distinguish between the instantaneous and the observable Universe, i.e. the state of objects and areas at any fixed moment of the Universe at any point in the Universe, from the state of objects and areas at different stages of evolution observed depending on the distance from us.

For a certain moment t_k, state of any places of the Universe must be identical to each other, which is confirmed by the isotropy of the Universe. But, in principle, it is impossible to observe them instantly. On the other hand, we simultaneously observe the state of objects and regions at different stages of the evolution of the Universe. This circumstance gives us the opportunity and perspective by observation to establish the chronological picture of the development of the Metagalaxy, from the Big Bang to the present.

References

Ambartsumian V. A., 1958, Reviews of Modern Physics, 30, 944

Burbidge G. R., Burbidge E. M., 1967, Quasi-stellar objects

Einstein A., 1917, Sitzungsberichte der Königlich Preussischen Akademie der Wissenschaften, pp 142–152

Fan X., et al., 2000, Astron. J. , 119, 1

Friedmann A., 1922, Zeitschrift fur Physik, 10, 377

Hubble E., 1929, Proceedings of the National Academy of Science, 15, 168

Huchra J. P., Geller M. J., Clemens C. M., Tokarz S. P., Michel A., 1996, VizieR Online Data Catalog, p. VII/193

Natsvlishvili R., 1997, Bulletin of the Georgian National Academy of Sciences (BNAS, 155, 51

Natsvlishvili R., 2002, Bulletin of the Georgian National Academy of Sciences (BNAS, 166, 490

Natsvlishvili R., 2003, Bulletin of the National Acadeny of Sciences, 168, 249

Natsvlishvili R., 2004, Bulletin of the Georgian National Academy of Sciences (BNAS, 170, 271

Natsvlishvili R., 2010, Bulletin of the Georgian National Academy of Sciences, 4, 42

Natsvlishvili R., Kochiashvili N., 2017, in Mickaelian A. M., Harutyunian H. A., Nikoghosyan E. H., eds, Astronomical Society of the Pacific Conference Series Vol. 511, Non-Stable Universe: Energetic Resources, Activity Phenomena, and Evolutionary Processes. p. 159

Oesch P. A., et al., 2016, Astrophys. J. , 819, 129

Pacucci F., Dayal P., Harikane Y., Inoue A. K., Loeb A., 2022, Mon. Not. R. Astron. Soc. , 514, L6

Penzias A. A., Wilson R. W., 1965, Astrophys. J. , 142, 419

Prokhorov A., Alekseev D., et al. 1984, Physical Encyclopedic Dictionary

Schneider D. P., et al., 2001, Astron. J. , 121, 1232

Veron-Cetty M. P., Veron P., 1998, VizieR Online Data Catalog, p. VII/207

Zheng W., et al., 2000, Astron. J. , 120, 1607

Communications of BAO, Vol. 70, Issue 1, 2023, pp. 131-142

Spectral lines evolution in the media illuminated by non-stationary energy sources

A. Nikoghossian*

NAS RA V.Ambartsumian Byurakan Astrophysical Observatory, Byurakan 0213, Aragatsotn Province, Armenia

Abstract

A brief review of the author's recent work on the development and application of the theory of time-dependent transfer of radiation in the spectral line is given. Various factors that influence the temporal characteristics of changes in line spectra are studied. This creates a fundamental opportunity to use them to gain insight into both external energy sources, the physical and geometrical properties of the medium itself as well as the various optical parameters of the observed spectral lines.

1. Introduction

We give a brief overview of our recent results in the theory of non-stationary radiative transfer concerning the evolution of observed line spectra that are formed under influence of time-dependent energy sources. The area is of considerable astrophysical interest, having in mind the great diversity of this kind of well-known cosmic phenomena, differing both in scale and in duration (bursts of Novas and Supernovas, flare and other activity manifestations in the Sun, Fuor-like changes, etc.).

The existing mathematical theory includes two main directions for solving time-dependent problems of radiative transfer in spectral line frequencies. They are based on the Laplace transform of derived equations (Chandrasekhar, 1948, 1950, Minin, 1964, 1965, 1967, Sobolev, 1950, 1963)and on the construction of Neumann series for desired physical quantities (Ganapol, 1979, Matsumoto, 1967, 1974, Uesugi & Irvine, 1970). Both approaches with their advantages encounter difficulties in addressing relatively more realistic model problems. Ways to overcome the difficulties encountered, both theoretical and computational, are shown in our recent papers (Nikoghossian, 2021a,b, 2022a,b).

The ultimate goal of this study is to describe the temporal variations of the observed line spectra and their dependence on various physical conditions and initial assumptions. This will make it possible to use the observed temporal characteristics of the evolution of spectral lines to interpret the observed phenomenon and to determine various optical parameters of both these lines and the medium itself.

2. Statement of the problem

In the transfer problem under consideration, the geometric and optical properties of the medium are assumed to be time-independent. Temporal changes are related only to the energy of the primary energy sources, which generally can be located both inside and outside the medium. We consider energy sources of two types of time distribution, namely, of the form of the Dirac $\delta(t)$ -function and the form of the Heaviside unit jump function $H(t)$. This choice allows us to judge the solutions of the considered problems also with a more complex temporal dependence of incident energy.

The medium is assumed to be one-dimensional and of finite optical thickness, one of boundaries of which is illuminated by non-stationary energy sources (see Fig. 1). Solution of the transfer problem for finite medium allows, in particular, to trace the asymptotical behavior of the studied time-dependent phenomenon in passing to the semi-infinite limit. Based on such considerations, the optical thickness

*nikoghoss@yahoo.com

doi: https://doi.org/10.52526/25792776-23.70.1-131

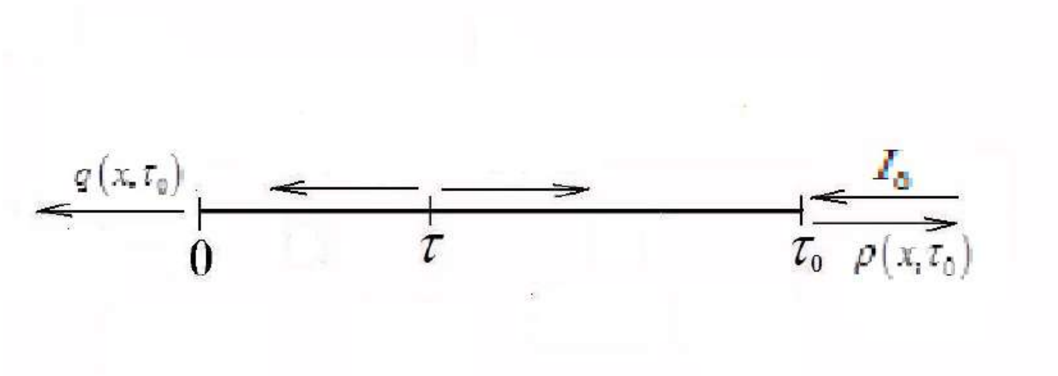

Figure 1. Schematic description of radiation transport in a one-dimensional medium of finite optical thickness

of the absorbing and scattering medium is everywhere assumed to be equal to the boundary value of $\tau_0 = 3$, above which the obtained solutions reach an asymptotic plateau. Choosing a smaller value for the thickness would make the role of multiple scattering in the medium less discernible. Some problems, we formulate under assumption that the scattering process in the medium is monochromatic, which is due to fact, that the scattering in the continuum, which influence is also of importance, is accounted for in a very simple way. The effects associated with the redistribution of radiation in spectral line frequencies we discuss separately.

3. Neumann series

The approach to the solution of time-dependent problems of the theory of radiation transfer, based on the construction of Neumann series, was developed by Matsumoto cited above). In the simplest model problems, these series are expansions of the required solutions for reflectance $\rho(x, \tau_0)$ and transmittance $q(x, \tau_0)$, in the degrees of probability of re-emission of quanta at an elementary event of scattering λ. The physical meaning of each term of the series is obviously the same as that of the sought quantity, referred, however, to a certain number of scattering events n. The latter satisfy the functional equations obtained by the well-known invariant imbedding technique (Bellman & Wing, 1973, Casti & Kalaba, 1976). In the monochromatic formulation of the problem when the medium is inhomogeneous medium, these series are of more complex nature:

$$\rho\left(x, \tau_0\right) = \sum_{n=1}^{\infty} \rho_n\left(x, \tau_0\right), \qquad q\left(x, \tau_0\right) = \sum_{n=0}^{\infty} q_n\left(x, \tau_0\right) \tag{1}$$

where x is the dimensionless frequency measured by displacement from the center of the line in Doppler units.

The essence of the method we suggest consists in constructing appropriate recurrence relations using the method of invariant imbedding, in which the first terms of the series not related to the double reflection are calculated beforehand. We have

$$\rho_1\left(x, \tau_0\right) = \frac{1}{2} \int_0^{\tau_0} \tilde{\lambda}\left(x, \tau\right) \mathrm{e}^{-2v(x)(\tau_0 - \tau)} v\left(x\right) d\tau \tag{2}$$

$$\rho_2\left(x, \tau_0\right) = \int_0^{\tau_0} \tilde{\lambda}\left(x, \tau\right) \rho_1\left(x, \tau\right) \mathrm{e}^{-2v(x)(\tau_0 - \tau)} v\left(x\right) d\tau, \tag{3}$$

$$q_0\left(x, \tau_0\right) = \mathrm{e}^{-v(x)\tau_0} \qquad q_1\left(x, \tau_0\right) = \frac{1}{2} \int_0^{\tau_0} \tilde{\lambda}\left(x, \tau\right) q_0\left(x, \tau\right) \mathrm{e}^{-v(x)(\tau_0 - \tau)} v\left(x\right) d\tau \tag{4}$$

doi: https://doi.org/10.52526/25792776-23.70.1-131

$$q_2\left(x,\tau_0\right)=\frac{1}{2}\int\limits_0^{\tau_0}\tilde{\lambda}\left(x,\tau\right)q_1\left(x,\tau\right)\mathrm{e}^{-v(x)(\tau_0-\tau)}v\left(x\right)d\tau \tag{5}$$

where the following notations are adopted: $\tilde{\lambda}\left(\tau_0\right)=\left[\lambda\left(\tau_0\right)\alpha\left(x\right)+\gamma\right]/v\left(x\right)$, $v(x)=\alpha(x)+\beta+\gamma$. We retain the commonly accepted designation $\alpha(x)$ for the profile of absorption coefficient and β and γ, correspondingly for the ratio of absorption and scattering coefficient in continuum to that in the center of the spectral line.

The above formulas have a transparent physical meaning and can be written directly. The remaining terms of the series, are expressed through auxiliary functions Φ_n and Ψ_n according to the formulas

$$\rho_n\left(x,\tau_0\right)=\int\limits_0^{\tau_0}\Phi_n\left(x,\tau\right)\mathrm{e}^{-2v(x)(\tau_0-\tau)}v\left(x\right)d\tau, \tag{6}$$

$$q_n\left(x,\tau_0\right)=\int\limits_0^{\tau_0}\Psi_n\left(x,\tau\right)\mathrm{e}^{-v(x)(\tau_0-\tau)}v\left(x\right)d\tau. \tag{7}$$

The last ones, in their turn, are expressed through the previous, already found, terms of corresponding series

$$\Phi_n\left(x,\tau_0\right)=\frac{1}{2}\tilde{\lambda}\left(x,\tau_0\right)\left[\rho_{n-1}\left(x,\tau_0\right)+\sum_{k=1}^{n-2}\rho_k\left(x,\tau_0\right)\rho_{n-k-1}\left(x,\tau_0\right)\right],\qquad n>2 \tag{8}$$

$$\Psi_n\left(x,\tau_0\right)=\frac{1}{2}\tilde{\lambda}\left(x,\tau_0\right)\left[q_{n-1}\left(x,\tau_0\right)+\sum_{k=1}^{n-2}q_k\left(x,\tau_0\right)\rho_{n-k-1}\left(x,\tau_0\right)\right],\qquad n>2 \tag{9}$$

As we see, each stage of the iterative process is accompanied by the calculation of integrals (6) and (7). The convergence of the Neumann series at a given frequency depends obviously on the optical thickness of the medium and the value of the scattering coefficient. The fastest convergence occurs in the wings of the line, where the medium is relatively transparent and the role of diffusion undergone by the quanta is small. In the problem we consider, the thickness of the medium is relatively small, so even in the central frequencies, the number of iterations, depending on the required accuracy, is about 6-8. Note that the above relations are quite general, since the possible dependence of the scattering coefficient on depth in the medium, discussed below, is taken into account. If the medium is considered homogeneous, the Neumann series turn into expansions of the corresponding physical quantities by degrees of the scattering coefficient.

4. Time-dependent problem

As is known (see, for example, Sobolev, 1963), the time spent by quanta during diffusion in the medium consists of two components: the time lost by quanta for staying in an excited state of the atom and - the time necessary for passing a path between the scattering acts undergone. In solving the time-dependent problems of radiation transfer in the line, one has most often limited ourselves to taking into account either the first of these causes or the second. The simpler first case essentially is reduced to determining the average number of scattering events. Relatively complicated is the second case, which has been considered by various authors using different methods (Minin, 1964, 1965, 1967, Sobolev, 1963), in particular, using the Laplace transform approach. Even here, however, the resulting equations, despite their resemblance to similar equations in the stationary problems, encounter considerable difficulties in their numerical solution.

Having at our disposal the solution of the stationary problem in the form of Neumann series it is not difficult to construct, as we showed in Nikoghossian (2021a,b, 2022a,b), the corresponding solutions of the non-stationary problems we consider:

doi: https://doi.org/10.52526/25792776-23.70.1-131

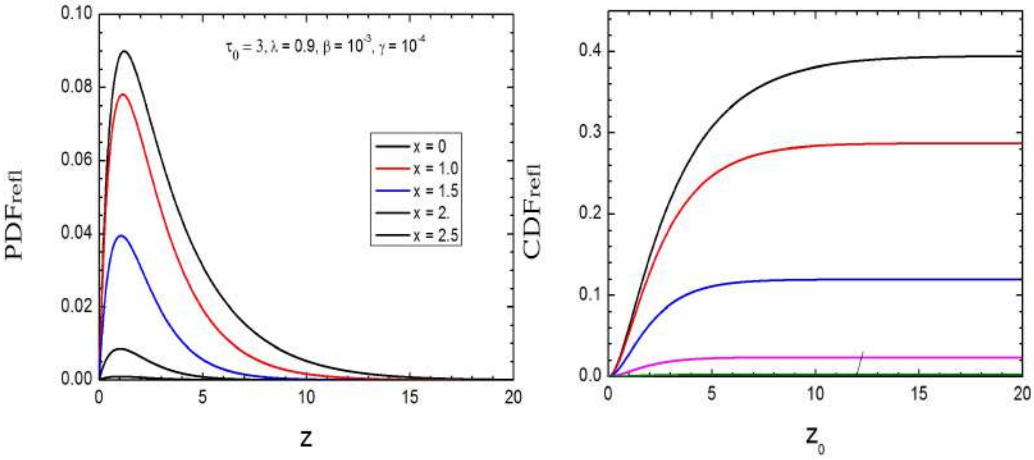

Figure 2. Probability density and cumulative distribution functions for reflected quanta for $\lambda = 0,99$.

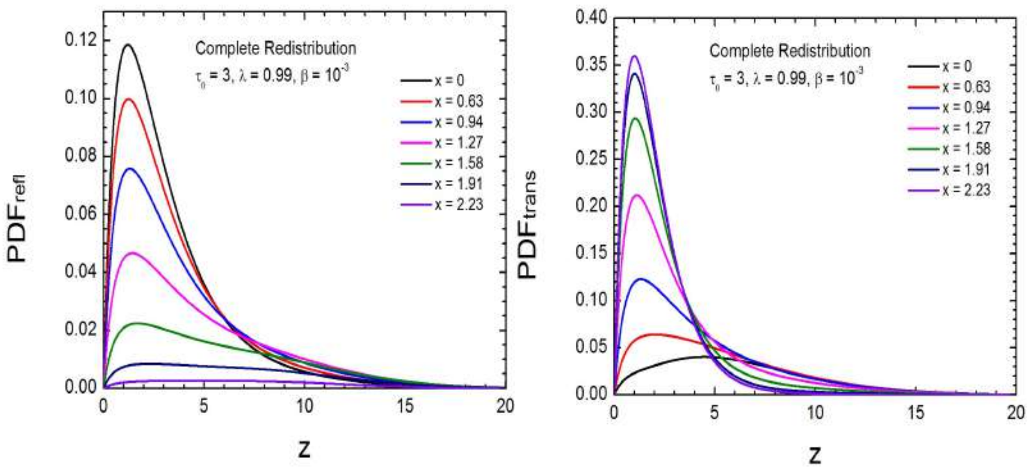

Figure 3. The same as in Fig.2. for transmitted quanta

$$\rho\left(x,\tau_0\right)=\sum_{n=1}^{\infty}\rho_n\left(x,\tau_0\right)F_n(z), \qquad q\left(x,\tau_0\right)=\sum_{n=1}^{\infty}q_n\left(x,\tau_0\right)F_n(z), \tag{10}$$

where

$$F_n(z)=\frac{z^{2n-1}}{(2n-1)!}\mathrm{e}^{-z} \qquad n=1,2,... \tag{11}$$

is the so-called Erlang-n distribution. The dimensionless temporal variable $z = t/\bar{t}$ is measured in units of $\bar{t} = t_1 t_2/\left(t_1 + t_2\right)$, where t_1 is the average time an atom stays in an excited state and t_2 is the average time it takes a quantum to travel between two successive acts of scattering. The value of t_1 in most cases is on the order of 10^{-7} -10^{-8}sec which usually is much smaller than the values of t_2 commonly found in astrophysical applications. The latter is determined by the density of absorbing atoms/ions in a given line and physical conditions in the medium.

The physical meaning of terms in the series Eq. 10 is obvious: they describe the probability density function of the quantum's escape through one of the boundaries as a result of a certain number of n scattering acts. Typical examples of probability density functions (PDF) are shown in the left panels of Fig. 2 and Fig. 3.

These functions describe the evolution of the spectral line profiles formed at the boundaries of the medium when it is illuminated by a δ-function shaped pulse. We see that all components of the Neumann series, and hence the profiles themselves, take their maximal values, as it was said, at $z = 1$ to which some real time $t = \bar{t}$ corresponds. Knowledge of $\bar{t}$ allows to estimate the value of t_2 and

doi: https://doi.org/10.52526/25792776-23.70.1-131

making then an idea about density of a given sort of atoms and on some physical characteristics of the medium such as the level of ionization. Thus, it is possible in principle to use the real-time values of when certain lines reach their maxima to estimate the relative abundance of various chemical elements

In addition, we consider also the establishment of the equilibrium state regime under prolonged illumination of the medium by a source of the unit jump form given by the Heaviside H-function. The evolution of the line profiles in this case is described by the cumulative distribution function (CDF) given by

$$C_\rho(x, \tau_0, z_0) = \mathrm{e}^{-z_0} \sum_{n=1}^{\infty} \rho_n\left(x, \tau_0\right) \sum_{k=0}^{\infty} \frac{z^{2n+k}}{(2n+k)!}, \tag{12}$$

$$C_q(x, \tau_0, z_0) = \mathrm{e}^{-z_0} \sum_{n=1}^{\infty} q_n\left(x, \tau_0\right) \sum_{k=0}^{\infty} \frac{z^{2n+k}}{(2n+k)!} \tag{13}$$

A typical example of cumulative distributions for reflected and transmitted radiation is shown in the right panels of Fig. 2 and Fig. 3. In both processes we considered it is assumed that the incident radiation has a unit intensity of continuum. The CDF curves are characterised by a plateau due to an asymptotic tendency of the line radiation towards their limiting values which are found by treating on the base of classical theory of stationary radiation transfer in spectral lines. Compared with the PDF distribution, the growth here is much slower (Δz_0 is of the order of 1), however, the steady state regime can be usually considered established in about the time interval $5 \leq z_0 \leq 10$. The illustrations above clearly show that the absorption lines formed as a result of transmission through the medium are established faster than the emission lines in the reflected spectrum. Another feature of these processes is their duration which depends for a given medium on the level of multiple scattering in the medium and increases at larger values of λ. We will return to the dynamics of changes in the spectral line profiles when the stationary mode is established in the next section.

The identification of spectral lines alongside with the dynamics and saturation rate are the power tool in interpreting the physical picture of the dynamic process under study.

5. The evolution of the line profiles

Fig. 2 and 3 show the difference between the speeds of the processes associated with the reflection of radiation from the medium and the transmission through it. The latter have a faster time course, which is due to the possibility of transmittance without scattering.

Obviously, the picture of the processes in both reflection and transmission cases depends on both the optical thickness of the medium and the value of the scattering coefficient. In particular, the duration of changes in the observed spectral lines essentially depends for a fixed value of the optical thickness on the value of the scattering coefficient. As one would expect, the greater the role of multiple scattering in the medium, the longer duration of the line evolution. For the same reason the process is comparatively short in a medium of smaller optical thickness.

A characteristic feature of the maximum value of the PDF for transmitted radiation is its weak dependence on both the optical thickness and the value of the scattering coefficient, which is associated with the asymptotic approximation of the distribution to unity in the lines wings. As a result, the maximum value of the PDF becomes approximately $\mathrm{e}^{-1} = 0.35$. This value depends only on the intensity of the primary radiation incident on the medium in the continuum, which is taken as one in the paper. Therefore, a comparison of the theoretical and observed maximum values allows us to estimate the intensity of radiation falling on the medium. This is important when comparing two spectral lines distant from each other, when the incident energy depends on the frequency.

Further, by following the evolution of the absorption line profiles arising as the result of transmittance through the medium, it is possible to gain insight into both the optical thickness of the medium and the role of diffusion in the medium in the observed spectra. This can be done by comparing the different parameters of the theoretically derived distributions and the profiles of the observed lines. For example, the relative fraction of the total energy absorbed in the line during the period up to the maximum is calculated to be weakly dependent on the scattering coefficient over the whole interval of

doi: https://doi.org/10.52526/25792776-23.70.1-131

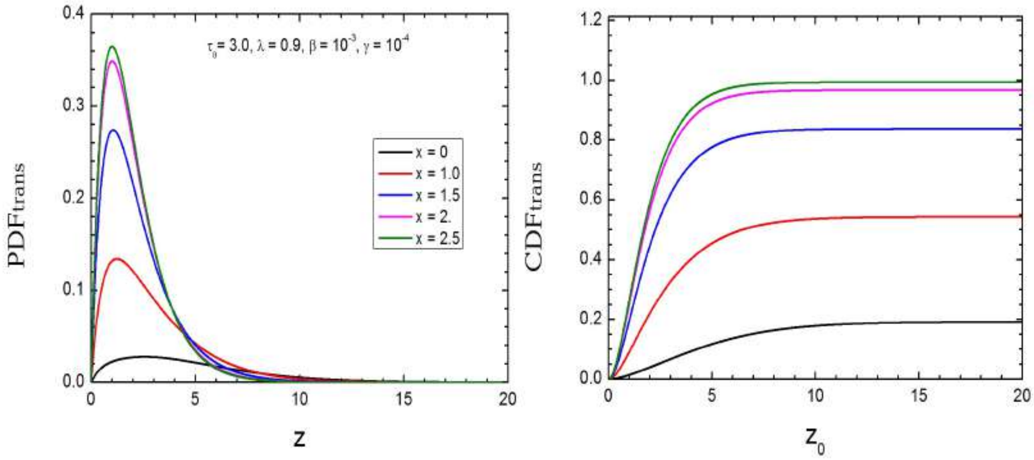

Figure 4. Probability distribution functions for reflected and transmitted quanta for $\lambda = 0,99$ in the case of completely non-coherent scattering

$0 < \lambda \leq 1$ and is accurately 22 per cent at $\tau_0 = 1$, and 19 per cent at $\tau_0 = 3$. Therefore these values can serve as an indicator of the optical thickness of the medium.

It is somewhat more difficult to estimate similar parameters when studying the evolution of the reflected emission line-spectrum. In this case, as it follows from Fig. 2 and 3, the maximum value of the reflection probability density function, as well as the duration of the whole process, are significantly dependent on the value of the scattering factor. Instead, these values for equal λ are weakly dependent on the optical thickness of the medium, what gives an indication of the value of the scattering coefficient.

For a confident interpretation of the temporal variations of the observed line-spectra, it is necessary to have data on the influence of various factors on the recorded evolution of the spectrum. Below we will consider some of these factors, the contribution of which should be considered important.

5.1. The effect of completely non-coherent scattering

In the above examples we assumed that the scattering in the spectral line is monochromatic. However, as we know, in most cases with strong lines we have to take into account the effect of redistribution of radiation over frequencies within the line. Here we consider the resulting effect for the case of completely incoherent scattering frequently used in various astrophysical problems. The corresponding PDF distributions for the reflected and transmitted radiation are depicted in Fig.4. Comparing them with the results shown in Fig. 2 and 3, we conclude that in the case of the frequency redistribution the lines evolve longer than in monochromatic scattering. It is also important the fact that, at a certain stage of the decline after the maximum, emission lines appear with double-peaked profiles at both boundaries of the medium. It may seem especially strange that an emission line can appear in the absorption spectrum after a long time (see also Fig. 6 below). Such phenomenon finds a simple physical explanation, consisting in that at a final stage of evolution, even at insignificant illumination of medium, still there is several number of diffusing quanta and the difference between radiation regimes at boundaries is reduced to a minimum.

A clearer picture of the evolution of spectral lines can be obtained from changes in their profiles over time. Fig. 5 and 6 demonstrate this evolution both before and after the PDF maximum is reached. The time variable grows with the increment $h = \Delta z$ =0.1. In the immediate vicinity of the maximum, profile changes slow down. After this, the decline begins, shown in Fig. 6. The time variable z varies here from top to bottom in ten times greater steps $h = \Delta z$=1.

Finally, let us also consider the case of prolonged illumination of the medium, as a result of which the radiation field in the medium tends to a stationary regime. Fig. 7 shows the evolution of spectral line profiles formed at the boundaries of the medium. One should pay attention to the essential differences between the evolutions of the observed profiles under the two illumination laws considered

doi: https://doi.org/10.52526/25792776-23.70.1-131

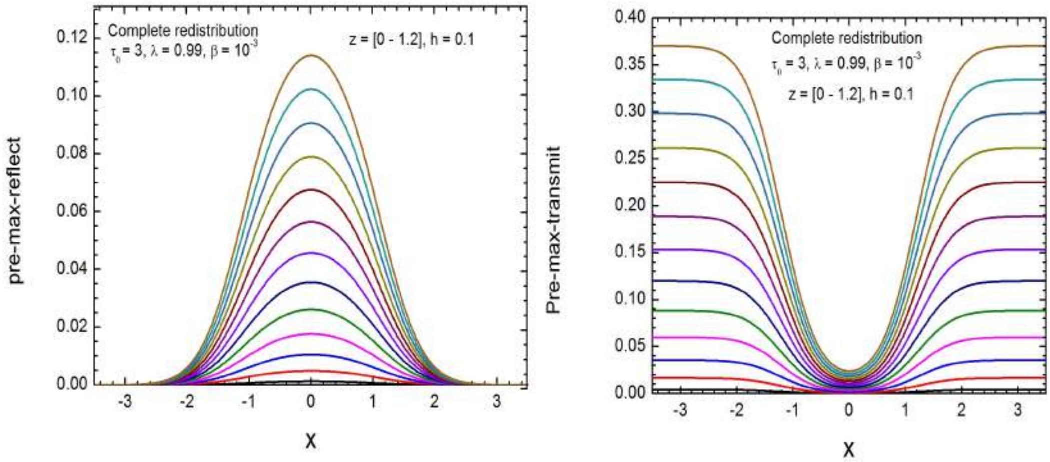

Figure 5. Evolution of the spectral line profile formed as a result of reflection (left) and transmission (right) before reaching the PDF maximum. The value of the time variable z grows from the bottom to top in increment $h = 0.1$.

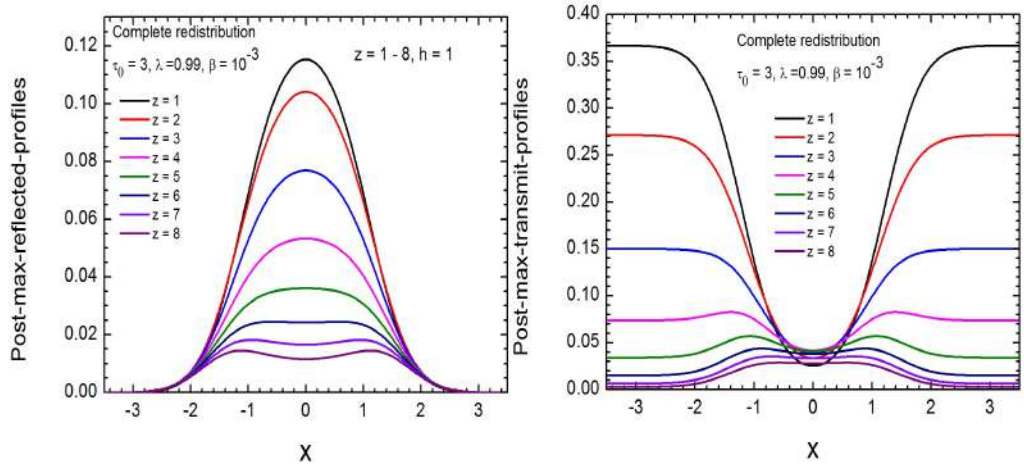

Figure 6. Evolution of the spectral lines profiles formed as a result of reflection (left) and transmission (right) after reaching the PDF maximum. The value of the time variable z grows from the top to bottom in increment $h = 1$.

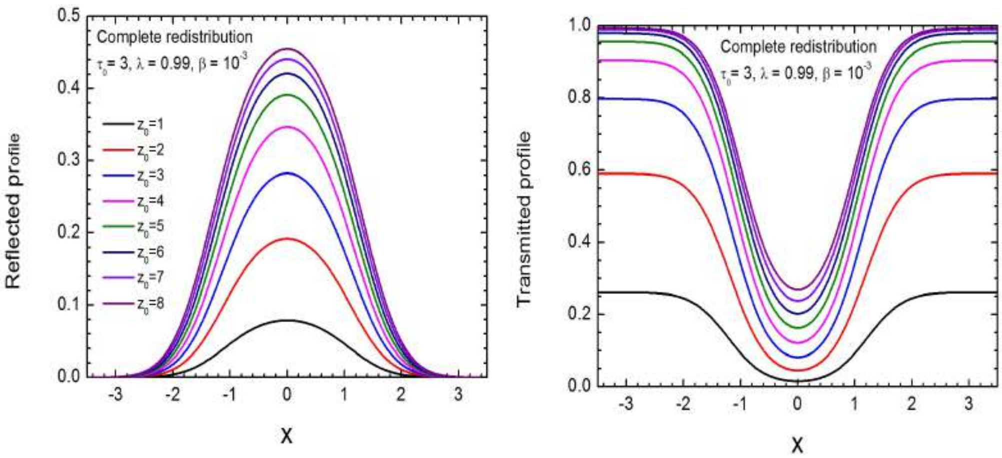

Figure 7. Evolution of the reflected (left) and transmitted (right) spectral lines profiles intending towards stationary regime during indicated time intervals.

doi: https://doi.org/10.52526/25792776-23.70.1-131

in the paper (see Fig. 5 and 7). It is of interest to compare the processes of spectral line amplification in the two types of energy sources of illumination considered in the paper. The main difference is that the specified growth in this case occurs about ten times slower. In addition, the speed of formation of the line profiles themselves are different in the line core and its wings. At a delta-shaped source, the line formed at reflection has its wings set earlier and only then the core, and the line formed after radiation passing through the medium has the opposite picture: the wings are set later than the core (Fig. 5). At the same time, as it is evident from Fig. 7, the scenario of formation of the spectral line profile is directly opposite.

5.2. The effect of inhomogeneity of the medium. The influence of the continuum scattering

Here we reveal the influence of medium inhomogeneity on the evolution of spectral lines. Obviously, in reality, each of the local optical properties of the medium can change from point to point in it. The crucial role in establishing the field of radiation in the medium plays the photon re-radiation probability in an elementary act of scattering λ, so we find it expedient to treat the effect of its probable variation with depth. Accounting for this type of medium inhomogeneity, while important, is also relatively complicated from the point of view of its theoretical implementation. For a clearer presentation of the results obtained, the characteristics of the continuous spectrum, such as the absorption and scattering coefficients, we consider here to be independent of the optical depth, despite the fact that their consideration does not lead to any fundamental difficulties.

As a simple example of the medium inhomogeneity effect, we consider a one-dimensional problem of monochromatic radiation transport, where the scattering coefficient in the line is given by the exponential law

$$\tilde{\lambda}\,(,\tau_0) = \left[1 + a(x)\mathrm{e}^{\mp v(x)\tau_0}\right]^{-1}, \tag{14}$$

where

$$a(x) = \frac{1-\tilde{\lambda}(x,0)}{\tilde{\lambda}(x,0)} = \frac{(1-\lambda\,(0))\,\alpha\,(x)+\beta}{\lambda\,(0)\,\alpha\,(x)+\gamma} \tag{15}$$

This dependence is encountered in the problems of spectral line formation within the framework of the two-level model, when, in addition to radiative transitions, collision transitions are taken into account. This takes place at relatively low temperatures and rather high concentrations of free electrons. We consider two opposite cases of exponential changes in the scattering coefficient with depth, which are either increasing or decreasing in approaching the illuminated boundary. They depend on choosing the boundary value of $\lambda(0)$ which we take, for better expository reasons, equal to $\lambda(0) = 0,5$ or 0,9 correspondingly for the negative and positive exponentials. Fig. 8 demonstrates the functions $\tilde{\lambda}(x,\tau)$ for these particular cases

We should pay attention to the dependence of the scattering coefficient in each of the cases under consideration on the frequency.

A visual representation of the differences between the two cases under consideration is given in Figs. 9, 10 which present changes in the spectral line profiles, arising from the reflection of radiation from the medium. For illustration of their evolution in the amplifying pre-maximum period, both in the absence of scattering in the continuum (left panels), and in its presence (right panels) are presented. Also for clarity, the value of the gamma parameter is assumed to be large enough, far from being always realized in astrophysical applications. The given figures allow us to make a number of important conclusions. As one might expect, accounting for scattering in the continuous spectrum leads to additional continuous emission, which weakens the lines themselves. The effect of inhomogeneity is demonstrated by Fig.10, which consists in the appearance of two-peaked profiles in the case when the level of diffusion of radiation in the medium decreases as it approaches the externally illuminated boundary. It can be also seen that as a result of additional continuous emission in this case one can observe two emission lines separated by the weak absorbtion component.

doi: https://doi.org/10.52526/25792776-23.70.1-131

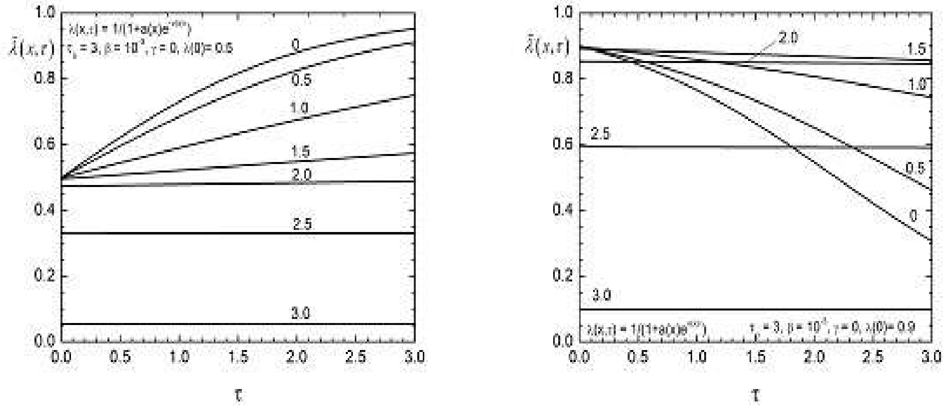

Figure 8. Functions $\tilde{\lambda}(x,\tau)$ in different frequencies for indicated values optical parameters.

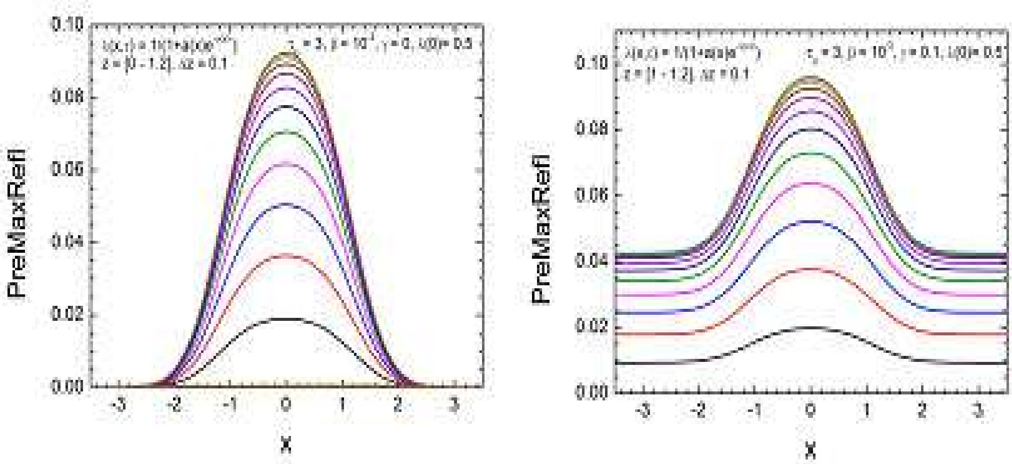

Figure 9. The evolution of the reflected pre-maximum lines profiles for $\lambda(0) = 0.5$.

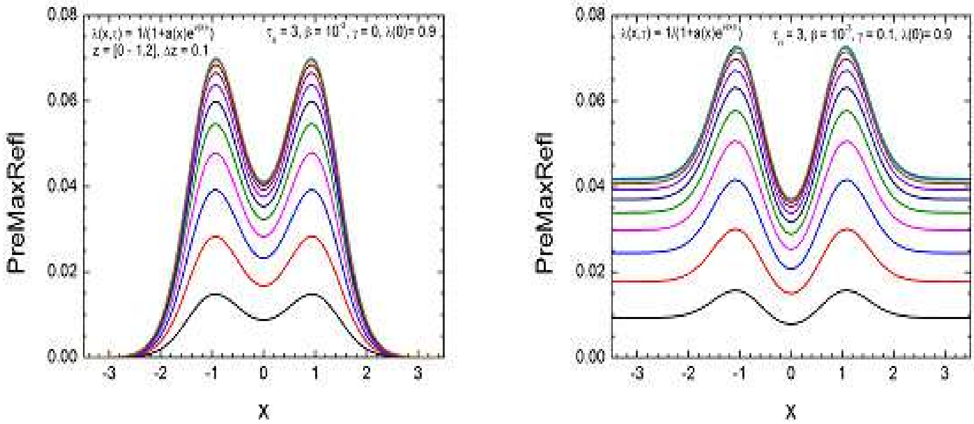

!

Figure 10. The evolution of the reflected pre-maximum lines profiles for $\lambda(0) = 0.9$.

doi: https://doi.org/10.52526/25792776-23.70.1-131

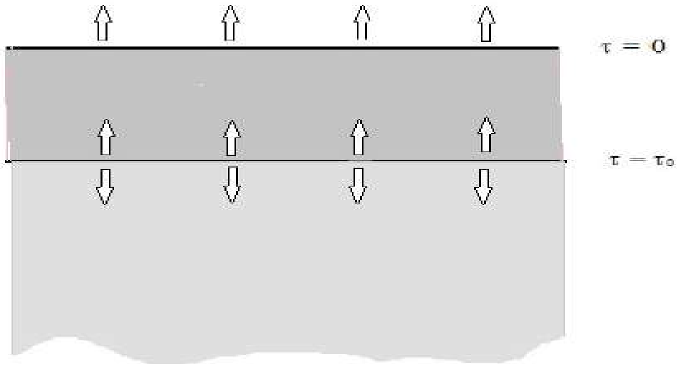

Figure 11. Schematic picture of the radiation transport in the presence of internal energy sources.

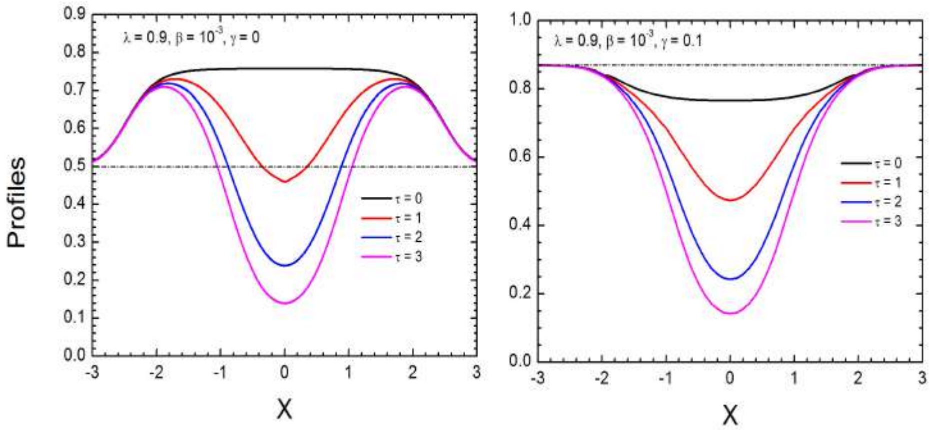

Figure 12. Profiles of spectral lines formed in the stationary regime in the semi-infinite absorbing and scattering atmosphere without (left) and with (right) continuum scattering.

5.3. Location of primary energy sources

In conclusion, let us apply the method we developed to reveal the effect of the location of the primary energy sources on the observed temporal characteristics of changes in the spectral lines. Consider this question in the simplest problem of spectral line formation in a one-dimensional semi-infinite atmosphere in the presence of an energy source at some optical depth τ_0, which radiates with the same probability of 0.5 in both directions by emission in a continuous spectrum with an intensity summarily equal to unity (Fig. 11). Fig. 12 shows the observed profiles of the lines formed by sources at different depths without considering the scattering in the continuum (left panel) and with this scattering taken into account (right panel). In both cases we obtain absorbtion profiles in spite of difference in the levels of the continuum spectrum. However in the absence of continuum scattering the lines have a specific form with emission components in the wings and absorbtion component in their core. There exists a clear correlation between the depth of the energy source location and the equivalent width and central residual intensity of lines (Nikoghossian, 2022b).

Fig. 13 demonstrates the PDF and CDF of at the center of observed spectral lines as a function of the depth of the energy source. Note that the time reading $z = z_0$ in the figure coincides with the moment of the beginning of the quanta' exit from the semi-infinite atmosphere. The strong relation between the depth of the energy source and the observed characteristics of the line allows to make an idea on the location and the some other characteristics of this source.

6. Concluding remarks

The goal we pursue is twofold: on the one hand, it is the further development of the non-stationary theory of the formation of a linear spectrum with the development of computational methods. On the

doi: https://doi.org/10.52526/25792776-23.70.1-131

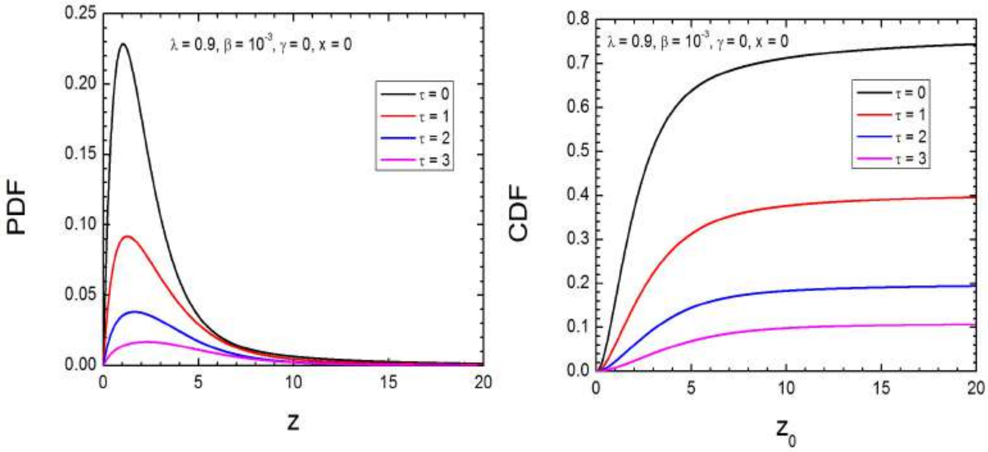

Figure 13. Typical graphs of PDF and CDF for the photons in the center of the line in the absence of continuum scattering when $\lambda = 0.9$.

other hand, it is their application in describing the evolution of spectral lines under certain physical conditions. Ultimately, the goal is how to use the information contained in the dynamic pattern of observed changes in spectra to find out the physical and optical properties of the medium in question and the chemical composition, spectrum of external and internal energy sources.

Two possible realizations of the observations are considered: spectra formed by reflection from the medium and those formed as a result of transmittance through it. Two types of primary energy sources are considered: those of the Dirac delta function and Heaviside H-functions forms. The results of numerical calculations concerning the evolution of spectral line profiles for each of the above cases are presented. The influence of various physical conditions, such as redistribution of radiation over frequencies, inhomogeneity of the medium, scattering in the continuous spectrum, location of energy sources, and various parameters of spectral lines on the shape, duration, and other characteristics of the evolution of the line spectra are described. All this provides ample opportunities for studying and interpreting, determining various physical characteristics of a large range of non-stationary processes of astrophysical interest.

References

Bellman R., Wing J., 1973, An Introduction to Invariant Imbedding. Wiley and Sons, New York

Casti J., Kalaba R., 1976, Imbedding Methods in Applied Mathematics. Mir, Moscow

Chandrasekhar S., 1948, Proceedings of the Royal Society of London Series A, 192, 508

Chandrasekhar S., 1950, Radiative Transfer. Clarendon Press, Oxford

Ganapol B. D., 1979, J. Quant. Spectrosc. Radiat. Transfer. , 22, 135

Matsumoto M., 1967, Publ. Astron. Soc. Jpn. , 19, 163

Matsumoto M., 1974, Publ. Astron. Soc. Jpn. , 26, 241

Minin I. N., 1964, Soviet Physics Doklady, 9, 114

Minin I. N., 1965, Astrophysics, 1, 104

Minin I. N., 1967, Astrophysics, 3, 154

Nikoghossian A. G., 2021a, Astrophysics, 64, 490

Nikoghossian A., 2021b, Communications of the Byurakan Astrophysical Observatory, 68, 32

Nikoghossian A., 2022a, Communications of the Byurakan Astrophysical Observatory, 69, 140

Nikoghossian A., 2022b, Communications of the Byurakan Astrophysical Observatory, 69, 25

Sobolev V., 1950, Astron. Zh., 27, 81

doi: https://doi.org/10.52526/25792776-23.70.1-131

Sobolev V. V., 1963, A treatise on radiative transfer.

Uesugi A., Irvine W. M., 1970, Astrophys. J. , 159, 127

doi: https://doi.org/10.52526/25792776-23.70.1-131

Communications of BAO, Vol. 70, Issue 1, 2023, pp. 143-151

On the new opportunity of solving the Ambartsumian's functional equation in the theory of radiative transfer

H. V. Pikichyan *

Byurakan Astrophysical Observatory, 378433, Aragatsotn District, Armenia

Abstract

A new approach to solving of the Ambartsumian's functional equation is presented. Its application is illustrated on the two classical cases: a) in the case of a plane-parallel semi-infinite medium with monochromatic anisotropic scattering and b) the simple one-dimensional problem of diffuse reflection of radiation from the scattering-absorbing semi-infinite medium in the case of the general law of redistribution of radiation by frequencies. The desired: a) azimuthal harmonics of reflection function dependent on two angular variables are explicitly expressed through the according eigenfunctions of one angle variable and b) diffuse reflection function of two frequency variables also expressed through a system of according eigenfunctions which have only one frequency variable. This does not require the use of any simplifying assumptions or special decompositions of the characteristics of elementary act of scattering: a) of scattering indicatrix and b) of the redistribution function of radiation by frequencies.

Keywords:radiative transfer, diffuse reflection problem, Ambartsumian's nonlinear functional equation, eigenfunctions and eigenvalues problem

1. Introduction and purpose of the work

The problem of diffuse reflection of radiation from a plane-parallel semi-infinite medium is one of the most important classical standard problems of theoretical astrophysics and, in particular, the theory of radiative transfer in scattering-absorbing media. It is widely used both in the interpretation of luminescence: planetary and stellar atmospheres, cosmic nebulae and various Space gas and dust complexes, and in the problems of optics of the Earth's atmosphere and ocean, the vegetation cover of the earth, as well as in the physics of nuclear reactors and radiation protection from ionizing radiation. The nonlinear integral equation for the direct determination of the diffuse reflection function from a semi-infinite medium in case of monochromatic scattering was obtained by introducing into the radiative transfer theory the so-called "Ambartsumian's principle of invariance and the method of addition of layers" (Ambartsumian, 1942b, 1943a,b, 1944). In the case of anisotropic scattering for the azimuthal harmonics of the reflection coefficient, the Ambartsumian's functional equation has the form (see, for example, Sobolev (1972) p. 51 or Yanovitskij (1995) p. 71).

$$\begin{gathered}(\mu+\mu')\,\rho^m(\mu,\mu')=\tfrac{\lambda}{4}\chi^m(-\mu,\mu')+\tfrac{\lambda}{2}\mu'\int\limits_0^1\chi^m(\mu,\mu'')\,\rho^m(\mu'',\mu')\,d\mu''\\ +\tfrac{\lambda}{2}\mu\int\limits_0^1\rho^m(\mu,\mu'')\,\chi^m(\mu'',\mu')\,d\mu''+\lambda\mu\mu'\int\limits_0^1\int\limits_0^1\rho^m(\mu,\mu''')\,\chi^m(\mu''',-\mu'')\,\rho^m(\mu'',\mu')\,d\mu''d\mu'''\end{gathered} \tag{1}$$

Here: $\rho^m(\mu,\mu')$ is the azimuthal harmonic of the desired brightness coefficient, $\chi^m(\mu,\mu')$ is the azimuthal harmonic of the scattering indicatrix, λ is the single scattering albedo of the quantum in the elementary act of scattering, μ' and μ are respectively the cosines of the angles of incidence and reflection of radiation from a semi-infinite medium with respect to the normal to its inner boundary. In the case of a one-dimensional semi-infinite medium, when there is a redistribution of radiation by frequencies, a similar equation was obtained by Sobolev (1955), which in generally accepted notations is written in the form:

$$\begin{gathered}\tfrac{2}{\lambda}\left[\alpha(x)+\alpha(x')\right]\rho(x,x')=r(x,x')+\int\limits_{-\infty}^{+\infty}r(x,\ x'')\,\rho(\ x'',\ x')\,dx''\\ +\int\limits_{-\infty}^{+\infty}\rho(x,\ x''')\,r(x''',\ \ x')\,dx'''dx'''+\int\limits_{-\infty}^{+\infty}\int\limits_{-\infty}^{+\infty}\rho(x,\ x''')\,r(x''',\ \ x'')\,\rho(x'',\ x')\,dx''dx'''\end{gathered} \tag{2}$$

*hovpik@gmail.com

doi: https://doi.org/10.52526/25792776-23.70.1-143

Here: $\rho(x, x')\,dx$ is the probability of diffuse reflection of the quantum from the medium in the $(x,\ x{+}dx)$ range of dimensionless frequencies, when entering a medium quantum had a frequency of x', $r(x''',\ x'')$ is the frequency redistribution function of radiation at an elementary act of scattering, $\alpha(x)$ is the absorption coefficient profile.

Traditionally, when solving equations (1) and (2), various expansions of the characteristics of the elementary act of scattering are used: in the case of anisotropic scattering, the scattering indicatrix is decomposed into Legendre polynomials (Ambartsumian, 1942a, 1943a, Chandrasekhar, 1950), then the m-th azimuthal harmonic of the scattering indicatrix takes the form

$$\chi^m(\mu, \mu'') = \sum_{i=m}^{N} c_i^m P_i^m(\mu)\, P_i^m(\mu'), \tag{3}$$

where $P_i^m(\mu)$ are the adjunctive Legendre functions. In the case of non-coherent scattering, for example, the bilinear decomposition of the frequency redistribution function by its eigenfunctions - $\alpha_j(x)$ (Engibaryan, 1971, Gevorkyan & Khachatryan, 1985, Gevorkyan et al., 1975, Khachatrian et al., 1991) was used

$$r(x, x') = \sum_j A_j \alpha_j(x)\, \alpha_j(x'). \tag{4}$$

Thus, the kernels of nonlinear integral equations (1) and (2) approximately became degenerate, which made it possible to obtain the solution of the main problem explicitly, through the so-called of Ambartsumian's auxiliary functions $\varphi_i^m(\mu)$ and $\varphi_j(x)$ having a smaller number of variables:

$$(\mu + \mu')\, \rho^m(\mu, \mu') = \frac{\lambda}{4} \sum_{i=m}^{N} c_i^m (-1)^{i+m} \varphi_i^m(\mu)\, \varphi_i^m(\mu'), \tag{5}$$

$$[\alpha(x) + \alpha(x')]\, \rho(x, x') = \frac{\lambda}{2} \sum_j A_j \varphi_j(x)\, \varphi_j(x'), \tag{6}$$

effectively reducing their finding to the corresponding systems of functional equations:

$$\varphi_i^m(\mu) = P_i^m(\mu) + \frac{\lambda}{4}\mu \sum_{j=m}^{N} c_j^m (-1)^{i+j} \varphi_j^m(\mu) \int_0^1 \frac{P_i^m(\mu')\, \varphi_j^m(\mu')}{\mu + \mu'} d\mu', \tag{7}$$

$$\varphi_m(x) = \alpha_m(x) + \frac{\lambda}{2} \sum_k A_k \varphi_k(x) \int_{-\infty}^{+\infty} \frac{\varphi_k(x')\, \alpha_m(x')}{\alpha(x) + \alpha(x')} dx'. \tag{8}$$

However, in cases where the representation of real or model indicatricis, as well as the functions of redistribution of radiation by frequencies, require taking into account a significantly large number of terms in expansions of types (3) and (4), the task will be significantly more complicated. Indeed, for example, with a real cloud indicatrix (Smoktiy & Anikonov, 2008), 229 is required in the decomposition (3), and with its approximate replacement by the Henyey-Greenstein phase function type model, 152 terms are required (see below, Figure 1, from the book Smoktiy & Anikonov (2008) Fig. 4.1.1).

In the case of non-coherent scattering, the construction of a general representation of the redistribution function (4), taking into account various physical factors, is already a rather time-consuming task (Arutyunyan, 1991, Gevorkyan & Khachatryan, 1985, Khachatrian et al., 1991):

$$r_V(x, x') = \begin{cases} r_{III}(x, x'), & \sigma_j = 0 \\ r_{II}(x, x'), & \sigma_i = 0 \\ r_I(x, x'), & \sigma_j = \sigma_i = 0 \end{cases}, \quad r_V(x, x') = \sum_k \frac{\beta_{2k}(x, \sigma_i, \sigma_j)\, \beta_{2k}(x', \sigma_i, \sigma_j)}{\lambda_k(\sigma_j)},$$

$$\beta_{2k}(x, \sigma_i, \sigma_j) = \sum_m \gamma_{km}(\sigma_j)\, \alpha_{2m}(x, \sigma_i), \quad \alpha_k(x, \sigma_i) = \frac{\sigma_i}{\pi} \int_{-\infty}^{+\infty} \frac{\alpha_k(t)\, dt}{(x - t)^2 + {\sigma_i}^2}, \tag{9}$$

not even to mention the number of necessary terms of the expansion to achieve a certain predetermined accuracy of the desired solution of the diffuse reflection problem. In the case of incoherent scattering, it is

doi: https://doi.org/10.52526/25792776-23.70.1-143

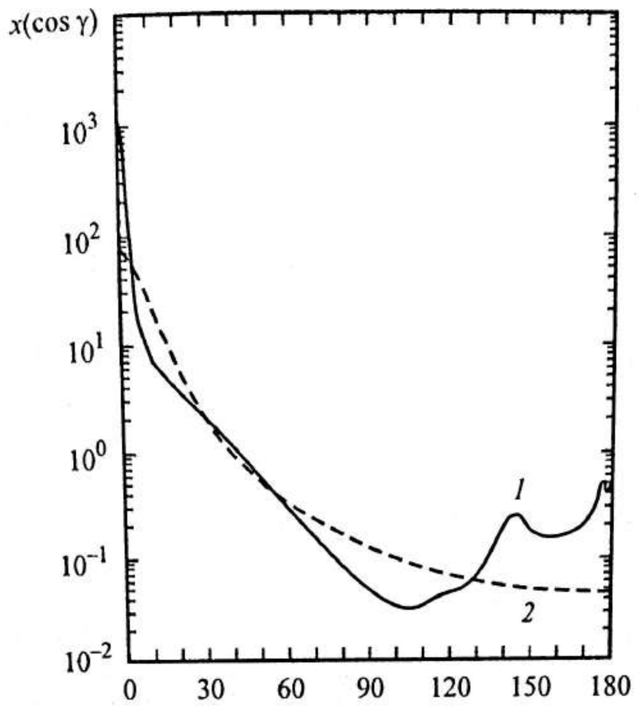

Figure 1. The scattering indicatrix - 1, $\chi\left(\cos\gamma\right)$ for the cloud model (solid line) and the model indication $\chi_{H-G}\left(\cos\gamma\right)$ Henyey-Greenstein- 2 (dashed line) approximating it. On the ordinate axis, the indicatrix $\chi(\cos\gamma)$, and on the abscissa axis, the scattering angle γ in degrees.

also important to mention the method of directly searching for the reflection function in the form Gevorkyan & Khachatryan (1985), Khachatrian et al. (1991):

$$\rho\left(x,x'\right) \quad = \sum_{i}\sum_{k}\rho_{ik}\frac{\alpha_i\left(x\right)\alpha_k\left(x'\right)}{\alpha\left(x\right)}, \quad \rho_{ik}=\int\limits_{-\infty}^{+\infty}\int\limits_{-\infty}^{+\infty}\rho\left(x,x'\right)\frac{\alpha_i\left(x\right)\alpha_k\left(x'\right)}{\alpha\left(x'\right)}dx'dx. \tag{10}$$

As we can see here, the desired solution of the problem of diffuse reflection $\rho\left(x,x'\right)$ is directly represented by a "double bilinear" series of eigenfunctions $\alpha_i\left(x\right)$ of the general frequency redistribution law $r\left(x,x'\right)$, where the coefficients ρ_{ik} are from the corresponding system of nonlinear equations. The authors of the work Gevorkyan & Khachatryan (1985) point to the effectiveness of this method of searching for $\rho\left(x,x'\right)$ in comparison with the previous one in terms of numerical calculations, motivating this by the presence here of a criterion that ensures the proper accuracy of solving the problem. However, similar to the previous method, it is also necessary to pre-construct the expansion $r\left(x,x'\right)$.

A natural question arises: is it possible to solve the problem of diffuse reflection, as before, to be reduced to finding auxiliary functions of a smaller number of variables, but at the same time to do without decomposing the characteristics of the elementary act of scattering? From the foregoing, it already follows the expediency of such a formulation of the question, since the search for the necessary decomposition of the nuclei of the elementary act of scattering is an additional and not always simple task. Moreover, the primary physical features of the characteristics of a single scattering act after each new scattering become smoother due to the next integration procedure. As a result, the final characteristics of the fields of multiple scattered radiation, of course, will have a smoother behavior, which will greatly simplify their description. Thus, from physical considerations, it follows that, in the form of corresponding expansions, it is more expedient to directly find the resulting radiation fields instead of the nuclei of the elementary scattering act. Obviously, under equal conditions, the corresponding series for $\rho^m\left(\mu,\mu'\right)$ and $\rho\left(x,x'\right)$ will be shorter than (3) and (4). The purpose of the presented work is the analytical implementation of this possibility, using the example of the above two cases described by functional equations (1) and (2).

doi: https://doi.org/10.52526/25792776-23.70.1-143

2. Formulation and solution of the problem

a) Anisotropic monochromatic scattering. On the right side of equation (1) we enter the notation

$$K^m(\mu,\mu') \equiv (\mu+\mu')\,\rho^m(\mu,\mu'), \tag{11}$$

at the same time

$$\rho^m(\mu,\mu') = \rho^m(\mu',\ \mu) \Rightarrow K^m(\mu,\mu') = K^m(\mu',\ \mu). \tag{12}$$

It is not difficult from equation (1), taking into account (11), to obtain for the introduced symmetric and positive function $K^m(\mu,\mu')$ a functional equation

$$\begin{array}{c} K^m(\mu,\mu') = \frac{\lambda}{4}\chi^m(-\mu,\mu') + \frac{\lambda}{2}\mu'\int\limits_0^1 \chi^m(\mu,\mu'')\frac{K^m(\mu'',\mu')}{\mu''+\mu'}d\mu'' + \frac{\lambda}{2}\mu\int\limits_0^1 \frac{K^m(\mu,\mu'')}{\mu+\mu''}\chi^m(\mu'',\mu')\,d\mu'' + \\ \lambda\mu\mu'\int\limits_0^1\int\limits_0^1 \frac{K^m(\mu,\mu''')}{\mu+\mu'''}\chi^m(\mu''',-\mu'')\frac{K^m(\mu'',\mu')}{\mu''+\mu'}d\mu''d\mu''' \end{array}. \tag{13}$$

Let us pose the standard problem of finding eigenvalues and eigenvectors of a symmetric integral operator $\int\limits_0^1 K^m(\mu,\mu')\ldots d\mu'$:

$$\nu_l^m\beta_l^m(\mu) = \int\limits_0^1 K^m(\mu,\mu')\,\beta_l^m(\mu')\,d\mu', \quad \int\limits_0^1 \beta_n^m(\mu)\,\beta_l^m(\mu')\,d\mu' = \delta_{ln}. \tag{14}$$

Since the unknown in (14) kernel $K^m(\mu,\mu')$ is given only by means of its nonlinear functional equation (13), then to find the appropriate eigenfunctions act with the integral operator $\int\limits_0^1 \ldots\beta_l^m(\mu')\,d\mu'$ on equation (13) and take into account (14). Then, in the subintegral expressions of the resulting ratio, we take into account the possibility of an approximate representation, with any predetermined accuracy, the desired positive and symmetric kernel $K^m(\mu,\mu')$ by means of a bilinear series of its eigenfunctions

$$K^m(\mu,\mu') = \sum_n \nu_n^m\beta_n^m(\mu)\,\beta_n^m(\mu'). \tag{15}$$

After simple calculations, we come to a system of equations:

$$\nu_l^m\beta_l^m(\mu) = \frac{\lambda}{4}Z_l^m(\mu) + \frac{\lambda}{2}\sum_n \nu_n^m D_{nl}^m(\mu) + \lambda\sum_n\sum_k \nu_n^m\nu_k^m V_{nkl}^m(\mu). \tag{16}$$

Here, the quantities $Z_l^m(\mu)$, $D_{nl}^m(\mu)$, $V_{nkl}^m(\mu)$ obviously include the desired eigenfunctions $\beta_l^m(\mu)$:

$$Z_l^m(\mu) = \int\limits_0^1 \chi^m(-\mu,\mu')\,\beta_l^m(\mu')\,d\mu', \quad w_{nl}^m(\mu'') = \beta_n^m(\mu'')\int\limits_0^1 \frac{\beta_n^m(\mu')}{\mu''+\mu'}\beta_l^m(\mu')\,\mu' d\mu',$$

$$D_{nl}^m(\mu) = \int\limits_0^1 \chi^m(\mu,\mu'')\,w_{nl}^m(\mu'')\,d\mu'' + \mu\beta_n^m(\mu)\int\limits_0^1 \frac{\beta_n^m(\mu'')}{\mu+\mu''}d\mu''\int\limits_0^1 \chi^m(\mu'',\mu')\,\beta_l^m(\mu')\,d\mu',$$

$$V_{nkl}^m(\mu) = \mu\beta_n^m(\mu)\int\limits_0^1 \frac{\beta_n^m(\mu''')}{\mu+\mu'''}d\mu'''\int\limits_0^1 \chi^m(-\mu''',\mu'')\,w_{kl}^m(\mu'')\,d\mu''. \tag{17}$$

To determine the unknown in (16) eigenvalues ν_l^m , it is not difficult from (16), taking into account (17) and the orthogonality condition (14), to obtain a system

$$\nu_l^m = \frac{\lambda}{4}b_l^m + \frac{\lambda}{2}\sum_n \nu_n^m c_{nl}^m + \lambda\sum_n\sum_k \nu_n^m\nu_k^m f_{nkl}^m, \tag{18}$$

doi: https://doi.org/10.52526/25792776-23.70.1-143

where the values b_l^m , c_{nl}^m , f_{nkl}^m in turn depend on the desired eigenfunctions:

$$b_l^m = \int_0^1 \int_0^1 \beta_l^m(\mu)\,\chi^m(-\mu,\mu')\,\beta_l^m(\mu')\,d\mu' d\mu, \quad c_{nl}^m = \int_0^1 \int_0^1 \beta_l^m(\mu)\,\chi^m(\mu,\mu'')\,w_{nl}^m(\mu'')\,d\mu'' d\mu,$$

$$f_{nkl}^m = \int_0^1 \int_0^1 w_{nl}^m(\mu''')\,\chi^m(\mu''',-\mu'')\,w_{kl}^m(\mu'')\,d\mu'' d\mu'''. \tag{19}$$

Expressions (16)-(19) together represent a system of equations for the self-consistent determination of the desired eigenfunctions and eigenvalues of the kernel $K^m(\mu,\mu')$. The solution of the initial problem of determining the azimuthal harmonics of the brightness coefficient is given by expression

$$\rho^m(\mu,\mu') = \frac{\sum_n \nu_n^m \beta_n^m(\mu)\,\beta_n^m(\mu')}{\mu+\mu'}. \tag{20}$$

b) A one-dimensional medium in the case of the general of the frequency redistribution. In equation (2) we introduce the notations:

$$K(x,x') \equiv \left[\alpha(x)+\alpha(x')\right]\rho(x,x'), \quad \varphi(x,x') \equiv \delta(x-x')+\rho(x,\ x'), \tag{21}$$

then it will take the form:

$$\frac{2}{\lambda}K(x,x') = \int_{-\infty}^{+\infty}\int_{-\infty}^{+\infty} \varphi(x,x''')\,r(x''',x'')\,\varphi(x'',x')\,dx''dx'''. \tag{22}$$

Hence, taking into account (21), for the value $K(x,x')$ we obtain a nonlinear integral equation:

$$\frac{2}{\lambda}K(x,x') = \int_{-\infty}^{+\infty}\int_{-\infty}^{+\infty}\left[\delta(x-x''')+\frac{K(x,\ x''')}{\alpha(x)+\alpha(x''')}\right] r(x''',x'')\left[\delta(x''-x')+\frac{K(x'',\ x')}{\alpha(x'')+\alpha(x')}\right] dx''dx'''. \tag{23}$$

Let us pose the problem of finding the eigenfunctions and eigenvalues of the positive and symmetric kernels $K\ (x,x')$:

$$\nu_i\beta_i(x) = \int_{-\infty}^{+\infty} K(x,x')\,\beta_i(x')\,dx', \quad \int_{-\infty}^{+\infty}\beta_i(x)\,\beta_j(x)\,dx = \delta_{ij}, \tag{24}$$

The previously unknown nucleus $K\ (x,x')$ is given by means of its nonlinear functional equation (23). By influencing this equation with the operator $\int_{-\infty}^{+\infty}\ldots\beta_j(x)\,dx$ and taking into account the possibility of an approximate representation of a symmetric positive kernel (with an arbitrary given precision) through a bilinear series of its eigenfunctions

$$K(x,x') = \sum_j \nu_j\beta_j(x)\,\beta_j(x'), \tag{25}$$

after simple calculations, it is not difficult to obtain a system of nonlinear equations for the desired eigenfunctions $\beta_k(x)$

$$\frac{2}{\lambda}\nu_k\beta_k(x) = Z_k(x) + \sum_j \nu_j D_{jk}(x) + \sum_j\sum_i \nu_i\nu_j V_{jik}(x). \tag{26}$$

The quantities $Z_k(x)$, $D_{jk}(x)$, $V_{jik}(x)$ appearing here are determined by means of the searched eigenfunctions $\beta_k(x)$:

$$Z_k(x) = \int_{-\infty}^{+\infty} r(x,x')\,\beta_k(x')\,dx', \quad w_{lk}(x'') = \beta_l(x'')\int_{-\infty}^{+\infty}\frac{\beta_l(x')}{\alpha(x'')+\alpha(x')}\beta_k(x')\,dx',$$

$$D_{jk}(x) = \beta_j(x)\int_{-\infty}^{+\infty}\frac{\beta_j(x''')}{\alpha(x)+\alpha(x''')}Z_k(x''')\,dx''' + \int_{-\infty}^{+\infty} r(x,x'')\,w_{jk}(x'')\,dx'',$$

$$V_{jik}(x) = \beta_j(x)\int_{-\infty}^{+\infty}\frac{\beta_j(x''')}{\alpha(x)+\alpha(x''')}dx'''\int_{-\infty}^{+\infty} r(x''',x'')\,w_{ik}(x'')\,dx''. \tag{27}$$

doi: https://doi.org/10.52526/25792776-23.70.1-143

In the system (26), the values of the eigenvalues ν_k are not yet known. Influencing the same integral operator $\int_{-\infty}^{+\infty} \ldots \beta_j(x)\, dx$ to the system (26), taking into account the orthogonality of eigenfunctions, we obtain a nonlinear algebraic system for determining eigenvalues ν_k :

$$\frac{2}{\lambda}\nu_k = b_k + \sum_j \nu_j c_{jk} + \sum_j \sum_i \nu_i \nu_j f_{jik}. \tag{28}$$

The quantities unknown here b_k , c_{jk} , f_{jik}, as in (26), are expressed in terms of the desired eigenfunctions $\beta_i(x)$ of the problem (24) and are represented as:

$$b_k = \int_{-\infty}^{+\infty} \int_{-\infty}^{+\infty} \beta_k(x)\, r(x,x')\, \beta_k(x')\, dx dx',$$

$$c_{jk} = 2\int_{-\infty}^{+\infty} \int_{-\infty}^{+\infty} \beta_k(x''')\, r(x''',x'')\, w_{jk}(x'')\, dx'' dx''',$$

$$f_{jik} = \int_{-\infty}^{+\infty} \int_{-\infty}^{+\infty} w_{jk}(x''')\, r(x''',x'')\, w_{ik}(x'')\, dx'' dx'''. \tag{29}$$

Thus, the one-dimensional problem of diffuse reflection of radiation from a semi-infinite scattering-absorbing medium under the general law of frequency redistribution, similar to the problem of anisotropic scattering, is reduced to a self-consistent joint solution of systems (26)-(29) for determining ν_k and $\beta_k(x)$, and then constructing the final solution in the form of

$$\rho(x,x') = \frac{\sum_j \nu_j \beta_j(x)\, \beta_j(x')}{\alpha(x) + \alpha(x')}. \tag{30}$$

3. Relationship with other methods

As mentioned above, the proposed approach to solving the problem of diffuse reflection will be more economical in comparison with the methods of decomposition of a single scattering act, since here the bilinear series is searched directly for quantities describing multiple scatterings. And the latter undoubtedly have a smoother and "integral" behavior than functions describing a single act of scattering. Due to the smoother behavior of these "resultant" radiation fields, it is natural to expect that the same accuracy in solving the original problem here will be achieved by a smaller number of terms of the bilinear expansion. That is, under equal conditions, the decomposition of the characteristics of the resulting field will be described by a smaller number of eigenfunctions than the number of auxiliary functions in the methods mentioned above. Another advantage is that it is no longer necessary to solve the additional problem of the decomposition of the characteristics of the elementary act of scattering. For a quantitative comparison of the effectiveness of the described two methods for solving the initial problem, it is very advisable to establish a two-way relationship between the quantities $\beta_i^m(\mu)$ and $\varphi_i^m(\mu)$, as well as between $\beta_i(x)$ and $\varphi_i(x)$.

a) Anisotropic monochromatic scattering. Comparison of solutions (5) and (20) gives

$$\sum_n \nu_n^m \beta_n^m(\mu)\, \beta_n^m(\mu') = \frac{\lambda}{4}\sum_i c_i^m (-1)^{i+m} \varphi_i^m(\mu)\, \varphi_i^m(\mu'). \tag{31}$$

Applying the condition of orthogonality of eigenfunctions $\beta_n^m(\mu)$, we obtain their connection with the Ambartsumian's auxiliary functions

$$\nu_n^m \beta_n^m(\mu) = \frac{\lambda}{4}\sum_i c_i^m (-1)^{i+m} \varphi_i^m(\mu)\, q_{in}^m, \quad q_{in}^m \equiv \int_0^1 \varphi_i^m(\mu')\, \beta_n^m(\mu')\, d\mu'. \tag{32}$$

The application of the condition of orthogonality of eigenfunctions in the first of the relations (32) and the subsequent consideration of the second leads to an explicit expression for determining eigenvalues ν_n^m

$$\nu_n^m = \frac{\lambda}{4}\sum_i c_i^m (-1)^{i+m} \left(q_{in}^m\right)^2. \tag{33}$$

doi: https://doi.org/10.52526/25792776-23.70.1-143

To find the unknown q_{in}^m appearing in (32) and (33), using its definition and explicit expression for $\beta_n^m(\mu)$ from (32) we obtain the relation

$$\nu_n^m q_{kn}^m = \frac{\lambda}{4}\sum_i c_i^m (-1)^{i+m} a_{ki}^m q_{in}^m, \tag{34}$$

where a_{ki}^m are given by

$$a_{ki}^m(\mu) = \int_0^1 \varphi_k^m(\mu)\,\varphi_i^m(\mu)\,d\mu. \tag{35}$$

From (34) and (33) we find the system

$$q_{kn}^m = \frac{\sum_i c_i^m (-1)^{i+m} a_{ki}^m q_{in}^m}{\sum_i c_i^m (-1)^{i+m} (q_{in}^m)^2}, \tag{36}$$

and to find the eigenfunctions $\beta_n^m(\mu)$ from (33) and (32), an explicit expression is obtained

$$\beta_n^m(\mu) = \frac{\sum_i c_i^m (-1)^{i+m} \varphi_i^m(\mu)\, q_{in}^m}{\sum_i c_i^m (-1)^{i+m} (q_{in}^m)^2}. \tag{37}$$

Feedback, i.e., the definition of $\varphi_i^m(\mu)$ when the eigenfunctions $\beta_n^m(\mu)$ are known, is obtained from the well-known definition of Ambartsumian's auxiliary functions

$$\varphi_i^m(\mu) = P_i^m(\mu) + 2\mu(-1)^{i+m}\int_0^1 P_i^m(\mu')\,\rho^m(\mu',\mu)\,d\mu'. \tag{38}$$

Substituting solution (20) here, we come to the expression

$$\varphi_i^m(\mu) = P_i^m(\mu) + 2\mu(-1)^{i+m}\sum_n \nu_n^m \beta_n^m(\mu)\, Q_{ni}^m(\mu), \tag{39}$$

where is

$$Q_{ni}^m(\mu) \equiv \int_0^1 \frac{\beta_n^m(\mu')\,P_i^m(\mu')}{\mu+\mu'}d\mu'. \tag{40}$$

b) One-dimensional medium under the general law of redistribution of radiation by frequencies. Let's compare solutions (6) and (30), similar to the previous paragraph "a", we will have

$$\sum_j \nu_j \beta_j(x)\,\beta_j(x') = \sum_k A_k \varphi_k(x)\,\varphi_k(x'), \tag{41}$$

then using the orthogonality condition of eigenfunctions $\beta_j(x)$ will give the expressions:

$$\nu_j \beta_j(x) = \sum_k A_k \varphi_k(x)\, q_{kj}, \quad q_{kj} \equiv \int_{-\infty}^{+\infty} \varphi_k(x')\,\beta_j(x')\,dx', \tag{42}$$

taking into account the orthogonality condition in the first relation (42), in turn, will give

$$\nu_j = \sum_k A_k (q_{kj})^2. \tag{43}$$

From (42) and (43) for the eigenfunctions $\beta_j(x)$, we finally get an explicit expression

$$\beta_j(x) = \frac{\sum_k A_k \varphi_k(x)\, q_{kj}}{\sum_k A_k (q_{kj})^2}. \tag{44}$$

In the ratios (42) and (43), the magnitude of q_{kj} is still unknown. To determine it, first by substituting the first ratio from (42) to the second, we get the formulas:

$$\nu_j q_{mj} = \sum_k A_k a_{mk} q_{kj}, \quad a_{mk} \equiv \int_{-\infty}^{+\infty} \varphi_m(x)\,\varphi_k(x)\,dx, \tag{45}$$

doi: https://doi.org/10.52526/25792776-23.70.1-143

and then, taking into account (43), we come to the system of equations

$$q_{mj} = \frac{\sum_k A_k a_{mk} q_{kj}}{\sum_k A_k \left(q_{kj}\right)^2}. \tag{46}$$

As a result, if the auxiliary functions of Ambartsumian are determined by the method of decomposition of the frequency redistribution function, then the transition to the eigenfunctions of the method proposed in this work is carried out by solving the system (46) and explicit expressions (43), (44). To derive the feedback-finding of auxiliary functions $\varphi_m(x)$ through the previously known eigenfunctions $\beta_j(x)$ and eigenvalues ν_j, recall their definition

$$\varphi_m(x) = \alpha_m(x) + \int_{-\infty}^{+\infty} \rho(x, x') \, \alpha_m(x') \, dx'. \tag{47}$$

After substituting in (47) the solution (30), the final expressions will be obtained

$$\varphi_m(x) = \alpha_m(x) + \frac{\lambda}{2} \sum_j \nu_j \beta_j(x) \, Q_{jm}(x), \quad Q_{jm}(x) = \int_{-\infty}^{+\infty} \frac{\beta_j(x') \, \alpha_m(x')}{\alpha(x) + \alpha(x')} dx'. \tag{48}$$

The presence of (33), (36), (37) together with (39), (40), also (43), (44), (46) together with (48) allow in both problems "a" and "b" to evaluate and compare the accuracy of the results obtained by different methods.

4. The general scheme of the organization of calculations

To calculate the desired eigenfunctions and eigenvalues above, two pairs of systems were obtained: the first pair - (16), (18) in the anisotropic scattering problem, and the second (26), (28) in the incoherent scattering problem. Each pair is to be calculated jointly, in a self-consistent manner – a certain system of orthonormal functions is taken as a zero approximation of the desired eigenfunctions (for example, in the anisotropic scattering problem, the attached Legendre functions, and in the incoherent scattering problem, Hermite polynomials). Obviously, the general structure of systems (16) and (26), as well as (18) and (28) with an accuracy of factors of type $\lambda/2$ is identical, so the scheme for their calculation is the same. In the problem of incoherent scattering, for example, the choice of the initial system of orthonormal functions will be "given" zero approximations of the desired quantities - $[\beta_k(x)]^{(0)}$.With their help, according to formulas (29), the zero approximation: $[b_k]^{(0)}$, $[c_{jk}]^{(0)}$, $[f_{jik}]^{(0)}$of the quantities is calculated. By substituting the latter in the right side of the relation (28), as well as taking here $[\nu_k]^{(0)} \equiv [b_k]^{(0)}$ as a zero approximation of eigenvalues, the subsequent first approximation - $[\nu_k]^{(1)}$ for eigennumbers in the left side of (28), will be obtained. Then, by means of formulas (27) using $[\beta_k(x)]^{(0)}$, the zero approximations of the functions $[Z_k(x)]^{(0)}$, $[D_{jk}(x)]^{(0)}$, $[V_{jik}(x)]^{(0)}$ are calculated. By substituting the values of the calculated functions in the right side (26), using the calculated first approximation - $[\nu_k]^{(1)}$, the values of the first approximation - $[\beta_k(x)]^{(1)}$of eigenfunctions are obtained. Then, the values $[\beta_k(x)]^{(n)}$ are taken as the initial approximation of the eigenfunctions and the entire described cycle is repeated. Calculations on such cycles of successive approximations $[\beta_k(x)]^{(n)}$ are repeated until the number n is reached, which gives the necessary accuracy. The same general scheme of organization of successive stages of calculations is illustrated in Fig. 2, in relation to the problem of determining the azimuthal harmonics of the brightness coefficient in the case of anisotropic scattering.

5. Conclusion

The paper presents a new possibility of solving Ambartsumian's functional equation in the problem of diffuse reflection of radiation from a semi-infinite scattering-absorbing medium. The expediency and effectiveness of the proposed approach follows from the physically obvious fact that in the process of multiple scattering of primary radiation - "diffusion" of quanta (or particles) in the medium, with each subsequent scattering act, the intensity of the formed radiation field (or the phase density of particles) becomes a mathematically smoother quantity. Therefore the problem of representing the resulting field through a bilinear series of "own" eigenfunctions is simpler and more efficient, compared to a similar problem of a single

doi: https://doi.org/10.52526/25792776-23.70.1-143

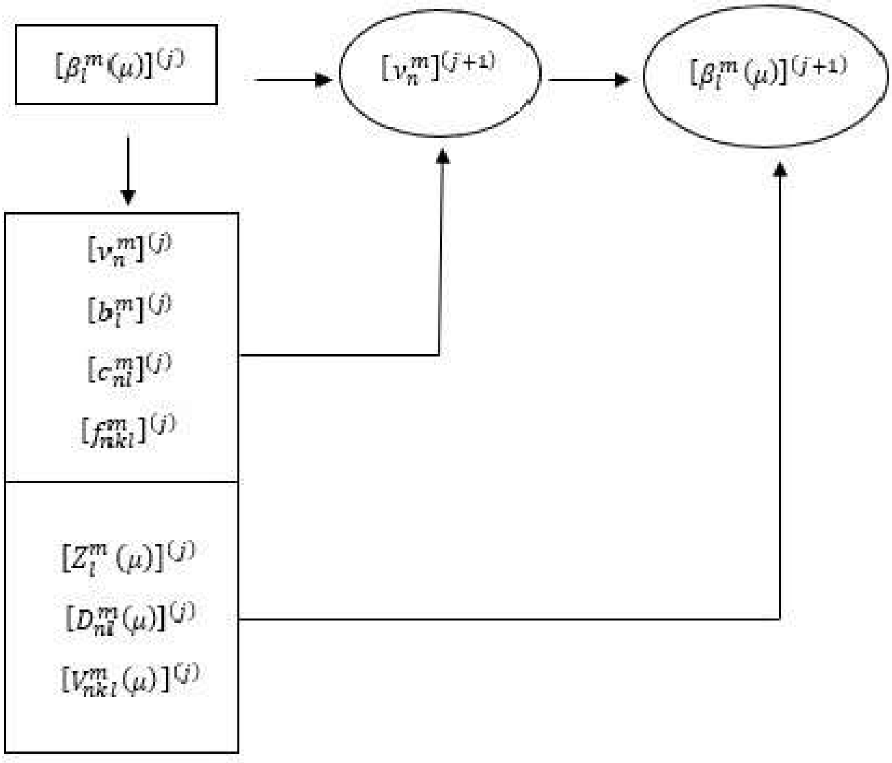

Figure 2. Diagram of sequential steps, self-consistent joint calculations of eigenvalues and eigenfunctions.

act of scattering. The method is analytically illustrated by two standard classical problems: finding the azimuthal harmonics of the reflection coefficient of monochromatic radiation from a semi-infinite medium with anisotropic scattering and diffuse reflection of radiation from a one-dimensional semi-infinite medium with the general law of frequency redistribution of radiation. Explicit expressions of solutions to the considered problems of diffuse reflection, depending on two independent variables, through the corresponding eigenfunctions of one independent variable, are obtained. To find the latter, as well as the corresponding eigenvalues in each of these cases, a pair of two systems of nonlinear equations is derived: functional and algebraic.

Acknowledgment. I express my sincere gratitude to Professor Levon Gurgen Arabadzhyan for numerous discussions and valuable mathematical consultations during the implementation of this work.

References

Ambartsumian V. A., 1942a, Izv. Academy of Sciences of the USSR, Series Geographer. and Geofiz. (in Russian), 3, 97

Ambartsumian V. A., 1942b, Astronomicheskiy Zhurnal (in Russian), 19, 30

Ambartsumian V. A., 1943a, Jurnal Teoreticheskoy i Eksperimentalnoy Fiziki (in Russian), 13, 323

Ambartsumian V. A., 1943b, DAN SSSR (in Russian), 38, 257

Ambartsumian V. A., 1944, Izvestiya. AN ArmSSR, Natural Sci. (in Russian), 1-2, 31

Arutyunyan G. A., 1991, DAN USSR (in Russian), 321, 285

Chandrasekhar S., 1950, Radiative transfer.

Engibaryan N. B., 1971, Astrophysics, 7, 340

Gevorkyan M. S., Khachatryan A. K., 1985, Astrophysics, 22, 354

Gevorkyan M. S., Engibaryan N. B., Nikogosyan A. G., 1975, Astrophysics, 11, 303

Khachatrian A. K., Akopian A. A., Melkonian E. A., 1991, J. Quant. Spectrosc. Radiat. Transfer. , 45, 367

Smoktiy O. I., Anikonov A. S., 2008, Light scattering in media of high optical thickness. St. Petersburg, Nauka Publ.

Sobolev V. V., 1955, Vestnik LGU (in Rusian), 11, 99

Sobolev V. V., 1972, Light scattering in planetary atmospheres

Yanovitskij E. G., 1995, Light scattering in inhomogeneous atmospheres

doi: https://doi.org/10.52526/25792776-23.70.1-143

The essence of onset and self-sustenance of turbulence in astrophysical shear flows

M. Kavtaradze [*1,2], G. Mamatsashvili[†1,3], and G. Chagelishvili[‡1]

[1]Abastumani Astrophysical Observatory, Abastumani 0301, Georgia
[2]Department of Physics, Faculty of Exact and Natural Sciences, Javakhishvili Tbilisi State University, Tbilisi 0179, Georgia
[3]Helmholtz-Zentrum Dresden-Rossendorf, Bautzner Landstraße 400, D-01328 Dresden, Germany

Abstract

To understand the mechanism of the self-sustenance of subcritical turbulence in spectrally stable astrophysical (constant) shear flows, we performed direct numerical simulations of turbulence in plane hydrodynamic and MHD homogeneous shear flows in the local shearing-box approximation with subsequent analysis of the dynamical processes in spectral/Fourier space. In the MHD case, we considered uniform magnetic field directed parallel to the flow. There are no exponentially growing modes in such flows and the turbulence is instead energetically supported only by the linear transient growth of Fourier harmonics of perturbations due to the shear flow non-normality. This non-normality-induced growth, also known as nonmodal growth, is anisotropic in Fourier space, which, in turn, leads to a specific anisotropy of nonlinear processes in this space. As a result, a main nonlinear process in shear flows is transverse (angular) redistribution of harmonics in Fourier space – nonlinear transverse cascade – rather than usual direct or inverse cascades. It is demonstrated that the turbulence is sustained by a subtle interplay between the linear nonmodal growth and the nonlinear transverse cascade for all considered flow configurations. The only energy supplier for the turbulence is the linear transient growth of perturbations due to the flow shear, which is mediated by Reynolds and Maxwell stresses, extracting, respectively, kinetic and magnetic energy from the background flow – the nonlinear processes do not directly change the total perturbation energy but only redistribute it among Fourier harmonics of perturbations. We propose the basic cycles of the turbulence sustenance in the considered cases, which clearly show the synergy of linear and nonlinear processes in the self-organization of the flow. Performing numerical simulations for different values of the background magnetic field, we show that with the increase of the field, the onset of turbulence occurs at larger times and the power of turbulence reduces. Finally, at definite threshold background magnetic field the flow completely stabilizes. It is significant that, there is an essential difference in the energy supply of plane and rotating/Keplerian astrophysical shear flows: in plane shear flows the leading linear process energetically supplying turbulence is due to the kinematics (Reynolds stress), while for Keplerian rotation – is due to magnetic field (Maxwell stress).

Keywords: *Astrophysical shear flows - magnetohydrodynamics - nonmodal growth - nonlinear transverse cascade - turbulence*

1. Introduction

Flows with shear velocity profile, where adjacent layers of matter move parallel to each other with different speeds, widely occur in nature and laboratory. For instance, they are observed in pipes, in the earth's atmosphere and – that is most important in the context of our study – are widespread in Astrophysics. So, the problem we study has a general and fundamental importance that can be applied to various astrophysical objects and observable phenomena, ranging from the intergalactic medium to the solar wind. Of course, these observable events are more complex and include kinematic and thermal effects, but the basic phenomena that occur there is a shearing motion of the matter.

Despite more than a century of history of research, until 1990s the reason of essence of turbulence onset and sustenance in spectrally stable shear flows (i.e., in flows without exponentially growing modes)

[*]mariami.kavtaradze986@ens.tsu.edu.ge, Corresponding author
[†]g.mamatsashvili@hzdr.de
[‡]georgech123@yahoo.com

doi: https://doi.org/10.52526/25792776-23.70.1-152

represented a puzzle. The turning point in understanding the physics of the shear flow turbulence was the 1990s, when the hydrodynamic instability community made a breakthrough rigorously revealing difficulties in the canonical spectral/modal approach of linear dynamics of perturbations in this type of flows. Specifically, it has been shown that the operators in the modal approach of linear processes in shear flows are exponentially far from normal (Reddy & Henningson, 1993, Schmid, 2007, Trefethen & Embree, 2005, Trefethen et al., 1993). Consequently, the eigenfunctions are not orthogonal to each other and, therefore, strongly interfere. As a result, even when all the eigenfunctions decrease monotonically in time, a particular solution may exhibit a large relative growth in a limited time interval, i.e., transient growth. This fact ultimately led to the change of canonical paradigm – the spectral/modal approach to, so-called, nonmodal approach (see e.g., Reddy et al., 1993, Trefethen et al., 1993).

As a result, a new, so-called bypass concept was developed for explaining the onset and self-sustenance of turbulence in spectrally stable shear flows (Baggett et al., 1995, Chapman, 2002, Eckhardt et al., 2007, Farrell & Ioannou, 1994, 2012, Gebhardt & Grossmann, 1994, Grossmann, 2000, Grue et al., 2014, Henningson & Reddy, 1994). It is based on the linear nonmodal growth of vortex mode perturbations due to the non-normality (shear), which is the only source of energy for turbulence in such flows. However, the transient growth itself is "imperfect" in the sense that it is not able to permanently provide energy for perturbations, so the role of nonlinear processes becomes crucial: they lie at the heart of self-sustenance of the turbulence which can be self-organized and self-sustained by a subtle interplay of the linear nonmodal and nonlinear processes.

The shear-induced transient growth mainly depends on the orientation of the perturbation wavevector: the spatial Fourier harmonics (SFHs) of perturbations having a certain orientation of the wavevector with respect to the shear flow, can draw flow energy and get amplified, whereas harmonics having other orientation of the wavevector give energy to the flow and decay. This anisotropy of linear processes in shear flows, in turn, leads to a specific anisotropy of nonlinear processes in Fourier (**k**-) space – even in the simplest but basic HD and MHD shear flows, the dominant nonlinear process turns out to be not direct, but, so-called, transverse cascade, that is, a transverse, or angular redistribution of perturbation harmonics in **k**-space (see e.g., Horton et al., 2010, Mamatsashvili et al., 2014).

New concepts – nonnormality, nonmodal approach, transient growth, bypass concept of subcritical turbulence – elaborated by the hydrodynamic stability community in the 1990s, was successfully adopted by atmospheric and astrophysical flow communities. The possibility of transient growth of vortex mode perturbations in hydrodynamic astrophysical/Keplerian disks was first shown by Lominadze et al. (1988). The number of studies of turbulence in astrophysical disks based on non-modal analysis has greatly increased since the 2000s (see a review Fromang & Lesur, 2019). Along this trend, in a series of recent papers Gogichaishvili et al. (2017), Gogichaishvili et al. (2018) and Mamatsashvili et al. (2020) we studied the spectral dynamics and sustenance of MHD turbulence in Keplerian flows for different magnetic field configurations. Naturally, in addition to disk flows, such an analysis is also important for plane astrophysical MHD shear flows.

In this paper, we investigate the subtle dynamic interplay of linear and nonlinear processes in subcritical MHD turbulence in shear flows. We consider three-dimensional (3D) unbounded incompressible MHD flow with a linear shear of velocity threaded by a uniform background magnetic field parallel to the flow. This flow configuration is spectrally stable in the linear regime (Ogilvie & Pringle, 1996, Stern, 1963) and therefore should be dominated by the above-mentioned shear-induced transient phenomena (Chagelishvili et al., 1997). We present the results of direct numerical simulations (DNS) in **k**-space, demonstrating the key role of the transverse cascade in the turbulence sustenance in the considered MHD shear flow.

2. Physical Model and Equations

The motion of an incompressible conducting fluid is governed by the basic MHD equations:

$$\frac{\partial \mathbf{U}}{\partial t} + (\mathbf{U}\cdot\nabla)\mathbf{U} = -\frac{1}{\rho}\nabla P + \frac{(\mathbf{B}\cdot\nabla)\mathbf{B}}{4\pi\rho} + \nu\nabla^2\mathbf{U}, \tag{1}$$

$$\frac{\partial \mathbf{B}}{\partial t} = \nabla\times(\mathbf{U}\times\mathbf{B}) + \eta\nabla^2\mathbf{B}, \tag{2}$$

$$\nabla\cdot\mathbf{U} = 0, \tag{3}$$

$$\nabla\cdot\mathbf{B} = 0, \tag{4}$$

doi: https://doi.org/10.52526/25792776-23.70.1-152

where ν is the constant kinematic viscosity, η is Ohmic resistivity, ρ is the fluid density, $\mathbf{U}$ is the velocity, $\mathbf{B}$ is the magnetic field and P is the total pressure, equal to the sum of the thermal and magnetic pressures. We use the widely accepted local shearing box approximation in astrophysical disk theory where a basic flow along the y axis has a constant shear of velocity in the x-direction, $\mathbf{U}_0 = (0, -Sx, 0)$. This flow is threaded by a uniform magnetic field along the y-axis of the flow direction, $\mathbf{B}_0 = (0, B_{0y}, 0)$. Without loss of generality, the constant shear parameter and magnetic field are chosen to be positive, $S, B_{0y} > 0$. The equilibrium density ρ_0 and total pressure P_0 are spatially constant.

Consider 3D perturbations of the velocity, total pressure and magnetic field about the equilibrium flow, $\mathbf{u} = \mathbf{U} - \mathbf{U}_0, p = P - P_0, \mathbf{b} = \mathbf{B} - \mathbf{B}_0$. Substituting them into Equations (1)-(4) and rearranging the nonlinear terms with the help of divergence-free conditions (3) and (4), we arrive to the main system of Equations (20)-(27) given in Appendix, which govern the dynamics of perturbations with arbitrary amplitude. These equations are solved numerically in a 3D cubic domain with sizes L_x, L_y, L_z and resolution $N_x \times N_y \times N_z$, respectively, in the x, y and z directions. We use standard for the shearing box boundary conditions: shearing-periodic in x and periodic in y and z.

2.1. Spectral representation of the equations

Before proceeding further, we normalize the variables by taking S^{-1} as the unit of time, ℓ as the arbitrary unit of length, $S\ell$ as the unit of velocity, $S\ell\sqrt{4\pi\rho_0}$ as the unit of magnetic field and $\rho_0 S^2 \ell^2$ as the unit of pressure and energy. Viscosity and resistivity are measured, respectively, by Reynolds number, Re, and magnetic Reynolds number, Rm, which are defined as

$$\mathrm{Re} = \frac{S\ell^2}{\nu}, \qquad \mathrm{Rm} = \frac{S\ell^2}{\eta}.$$

The strength of the imposed background magnetic field is measured by a parameter $\beta = 2S^2\ell^2/u_A^2$, where $u_A = B_{0y}/(4\pi\rho_0)^{1/2}$ is the corresponding Alfvén speed. we decompose the perturbations into spatial Fourier harmonics (SFHs):

$$f(\mathbf{r}, t) = \int \bar{f}(\mathbf{k}, t) \exp(i\mathbf{k} \cdot \mathbf{r})\, d^3\mathbf{k} \tag{5}$$

where, $f \equiv (\mathbf{u}, p, \mathbf{b})$ denotes the perturbations and $\bar{f} \equiv (\bar{\mathbf{u}}, \bar{p}, \bar{\mathbf{b}})$ is their corresponding Fourier transforms ($d^3\mathbf{k} \equiv dk_x dk_y dk_z$).

Substituting decomposition (5) into Eqs.(20)-(27) and taking into account the above normalization, we arrive at the following equations governing the dynamics of perturbation SFHs in Fourier space:

$$\frac{\partial}{\partial t}\frac{|\bar{u}_x|^2}{2} = -k_y \frac{\partial}{\partial k_x}\frac{|\bar{u}_x|^2}{2} + \mathcal{H}_x + \mathcal{I}_x^{(ub)} + \mathcal{D}_x^{(u)} + \mathcal{N}_x^{(u)}, \tag{6}$$

$$\frac{\partial}{\partial t}\frac{|\bar{u}_y|^2}{2} = -k_y \frac{\partial}{\partial k_x}\frac{|\bar{u}_y|^2}{2} + \mathcal{H}_y + \mathcal{I}_y^{(ub)} + \mathcal{D}_y^{(u)} + \mathcal{N}_y^{(u)}, \tag{7}$$

$$\frac{\partial}{\partial t}\frac{|\bar{u}_z|^2}{2} = -k_y \frac{\partial}{\partial k_x}\frac{|\bar{u}_z|^2}{2} + \mathcal{H}_z + \mathcal{I}_z^{(ub)} + \mathcal{D}_z^{(u)} + \mathcal{N}_z^{(u)}, \tag{8}$$

$$\frac{\partial}{\partial t}\frac{|\bar{b}_x|^2}{2} = -k_y \frac{\partial}{\partial k_x}\frac{|\bar{b}_x|^2}{2} + \mathcal{I}_x^{(bu)} + \mathcal{D}_x^{(b)} + \mathcal{N}_x^{(b)} \tag{9}$$

$$\frac{\partial}{\partial t}\frac{|\bar{b}_y|^2}{2} = -k_y \frac{\partial}{\partial k_x}\frac{|\bar{b}_y|^2}{2} + \mathcal{M} + \mathcal{I}_y^{(bu)} + \mathcal{D}_y^{(b)} + \mathcal{N}_y^{(b)} \tag{10}$$

$$\frac{\partial}{\partial t}\frac{|\bar{b}_z|^2}{2} = -k_y \frac{\partial}{\partial k_x}\frac{|\bar{b}_z|^2}{2} + \mathcal{I}_z^{(bu)} + \mathcal{D}_z^{(b)} + \mathcal{N}_z^{(b)}, \tag{11}$$

which are the main equations for the subsequent analysis. They serve as the mathematical basis for understanding of the interplay of the dynamical processes sustaining the subcritical turbulence in the considered shear flow. The right-hand side (rhs) terms of the above dynamical equations describe processes of linear, $\mathcal{H}_i(\mathbf{k}, t)$, $\mathcal{I}_i^{(ub)}(\mathbf{k}, t)$, $\mathcal{I}_i^{(bu)}(\mathbf{k}, t)$, $\mathcal{M}(\mathbf{k}, t)$, and nonlinear, $\mathcal{N}_i^{(u)}(\mathbf{k}, t)$, $\mathcal{N}_i^{(b)}(\mathbf{k}, t)$, origin, where the index

doi: https://doi.org/10.52526/25792776-23.70.1-152

$i = x, y, z$ henceforth. $\mathcal{D}_i^{(u)}(\mathbf{k}, t)$ and $\mathcal{D}_i^{(b)}(\mathbf{k}, t)$ terms, describing viscous and resistive dissipation, are negative definite. The linear terms are:

$$\mathcal{H}_x = -2\frac{k_x k_y}{k^2}|\bar{u}_x|^2, \quad \mathcal{H}_y = \left(\frac{1}{2} - \frac{k_y^2}{k^2}\right)(\bar{u}_x \bar{u}_y^* + \bar{u}_x^* \bar{u}_y), \quad \mathcal{H}_z = -\frac{k_y k_z}{k^2}(\bar{u}_x \bar{u}_z^* + \bar{u}_x^* \bar{u}_z),$$

$$\mathcal{M} = -\frac{1}{2}(\bar{b}_x \bar{b}_y^* + \bar{b}_x^* \bar{b}_y), \quad \mathcal{I}_i^{(ub)} = \frac{\mathrm{i}}{2} k_y B_{0y}(\bar{u}_i^* \bar{b}_i - \bar{u}_i \bar{b}_i^*), \quad \mathcal{I}_i^{(bu)} = -\mathcal{I}_i^{(ub)}$$

$$\mathcal{D}_i^{(u)} = -\frac{k^2}{\mathrm{Re}}|\bar{u}_i|^2, \qquad \mathcal{D}_i^{(b)} = -\frac{k^2}{\mathrm{Rm}}|\bar{b}_i|^2.$$

Here $\mathcal{H}_x$, $\mathcal{H}_y$, $\mathcal{H}_z$ are the energy injection terms for the corresponding velocity components, while their sum $\mathcal{H} = \mathcal{H}_x + \mathcal{H}_y + \mathcal{H}_z = (\bar{u}_x \bar{u}_y^* + \bar{u}_x^* \bar{u}_y)/2$ is Reynolds stress spectrum, $\mathcal{M}$ is the Maxwell stress spectrum, $\mathcal{I}_i^{(ub)}(\mathbf{k}, t)$, $\mathcal{I}_i^{(bu)}(\mathbf{k}, t)$ are terms that describe the linear exchange between kinetic and magnetic energies and $k^2 = k_x^2 + k_y^2 + k_z^2$. The modified nonlinear transfer functions $\mathcal{N}_i^{(u)}(\mathbf{k}, t)$ for the quadratic forms of the velocity components are:

$$\mathcal{N}_i^{(u)} = \frac{1}{2}(\bar{u}_i Q_i^* + \bar{u}_i^* Q_i). \tag{12}$$

where

$$Q_i = \mathrm{i}\sum_j k_j N_{ij}^{(u)} - \mathrm{i}k_i \sum_{m,n} \frac{k_m k_n}{k^2} N_{mn}^{(u)}, \qquad i, j, m, n = x, y, z. \tag{13}$$

and

$$N_{ij}^{(u)}(\mathbf{k}, t) = \int d^3\mathbf{k}' [\bar{b}_i(\mathbf{k}', t)\bar{b}_j(\mathbf{k} - \mathbf{k}', t) - \bar{u}_i(\mathbf{k}', t)\bar{u}_j(\mathbf{k} - \mathbf{k}', t)] \tag{14}$$

The nonlinear terms for the quadratic forms of the magnetic field components are

$$\begin{aligned} \mathcal{N}_x^{(b)} &= \frac{\mathrm{i}}{2}\bar{b}_x^*[k_y \bar{F}_z - k_z \bar{F}_y] + c.c., \\ \mathcal{N}_y^{(b)} &= \frac{\mathrm{i}}{2}\bar{b}_y^*[k_z \bar{F}_x - k_x \bar{F}_z] + c.c., \\ \mathcal{N}_z^{(b)} &= \frac{\mathrm{i}}{2}\bar{b}_z^*[k_x \bar{F}_y - k_y \bar{F}_x] + c.c. \end{aligned} \tag{15}$$

where $i, j = x, y, z$ and $\bar{F}_x, \bar{F}_y, \bar{F}_z$ are the Fourier transforms of the respective components of the perturbed electromotive force: $\boldsymbol{F} = \boldsymbol{u} \times \boldsymbol{b}$,

$$\bar{F}_x(\mathbf{k}, t) = \int d^3\mathbf{k}' [\bar{u}_y(\mathbf{k}', t)\bar{b}_z(\mathbf{k} - \mathbf{k}', t) - \bar{u}_z(\mathbf{k}', t)\bar{b}_y(\mathbf{k} - \mathbf{k}', t)], \tag{16}$$

$$\bar{F}_y(\mathbf{k}, t) = \int d^3\mathbf{k}' [\bar{u}_z(\mathbf{k}', t)\bar{b}_x(\mathbf{k} - \mathbf{k}', t) - \bar{u}_x(\mathbf{k}', t)\bar{b}_z(\mathbf{k} - \mathbf{k}', t)], \tag{17}$$

$$\bar{F}_z(\mathbf{k}, t) = \int d^3\mathbf{k}' [\bar{u}_x(\mathbf{k}', t)\bar{b}_y(\mathbf{k} - \mathbf{k}', t) - \bar{u}_y(\mathbf{k}', t)\bar{b}_x(\mathbf{k} - \mathbf{k}', t)], \tag{18}$$

One can distinguish five basic processes in Equations (6)-(11), that underlie the dynamics of perturbations:

1) The first terms on the rhs are of linear origin and describe advection, or "drift" of perturbation harmonics in Fourier space with the normalized velocity k_y. They travel along the k_x - axis for harmonics with $k_y > 0$ and opposite for $k_y < 0$ ones, the ones with $k_y = 0$ are not advected by the flow.

2) The second terms of the rhs of Equations (6)-(8) and (10), are associate with the shear, they originate from the linear terms proportional to the shear parameter and are therefore also of linear origin. They describe energy exchange between the mean flow and individual SFHs. These terms are responsible for providing energy for perturbations so that they can amplify. In the present case, such amplification is due to the shear flow non-normality. $\mathcal{H}$ and $\mathcal{M}$ are related to the volume - averaged nondimensional Reynolds and Maxwell stresses. As was mentioned above since perturbation harmonics undergo the drift in $\mathbf{k}$-space, their amplification has a transient nature (Chagelishvili et al., 2003, Farrell & Ioannou, 1993, Gustavsson, 1991, Tevzadze et al., 2003). So, these linear terms are a main source of energy for SFHs.

doi: https://doi.org/10.52526/25792776-23.70.1-152

3) The cross terms, $\mathcal{I}_i^{(ub)}$ and $\mathcal{I}_i^{(bu)}$ are also of linear origin and describe the exchange between kinetic and magnetic spectral energies. They have opposite signs and therefore cancel out in the total energy budget of SFHs. So, they do not generate new energy for harmonics, but rather exchange between kinetic and magnetic components.

4) The terms $\mathcal{D}_i^{(u)}$ and $\mathcal{D}_i^{(b)}$ are of linear origin and negative definite, they describe, respectively, the dissipation of kinetic and magnetic energies due to viscosity and resistivity. Comparing these dissipation terms with the energy-supplying terms $\mathcal{H}_i$ and $\mathcal{M}$, it is evident that dissipation is important at large wavenumbers $k \gtrsim k_D \equiv \min(\sqrt{\mathrm{Re}}, \sqrt{\mathrm{Rm}})$.

5) The nonlinear terms $\mathcal{N}_i^{(u)}$ and $\mathcal{N}_i^{(b)}$ (Equations (12) and (15)) describe nonlinear redistribution, or transfer, respectively, of kinetic and magnetic energies among SFHs with different wavenumbers in Fourier space. From the definition of these terms their sum integrated over an entire wavenumber space is zero,
$$\int [\mathcal{N}^{(u)}(\mathbf{k},t) + \mathcal{N}^{(b)}(\mathbf{k},t)] d^3\mathbf{k} = 0, \tag{19}$$
This implies that the main effect of nonlinearity is only to redistribute (scatter) the energy of perturbation harmonics, that was drawn from the background flow by the Reynolds and Maxwell stresses, over wavenumbers and among each other, while leaving the total spectral energy summed over all wavenumbers unchanged. These nonlinear transfer functions, $\mathcal{N}_i^{(u)}$ and $\mathcal{N}_i^{(b)}$ play a central role in subcritical MHD turbulence theory – they determine cascades of energies in $\mathbf{k}$-space, leading to the development of their specific spectra (Alexakis et al., 2007, Verma, 2004). These transfer functions are one of the main focuses of the present analysis. Our purpose is to explore how these functions operate in the presence of the flow shear and the background magnetic field parallel to the flow. In particular, we will demonstrate below that, similar to the cases studied in 2D HD and MHD plane, as well as in previously studied Keplerian shear flows (Gogichaishvili et al., 2017, 2018, Horton et al., 2010, Mamatsashvili et al., 2014, 2020) the energy spectra, energy injection, and nonlinear transfers are also anisotropic in the quasi-steady subcritical turbulence, resulting in the redistribution of spectral energy among wavevector angles in $\mathbf{k}$-space, which is referred to as the nonlinear transverse cascade, in contrast to the canonical direct cascade.

3. Simulations and General Characteristics

We solve Equations (20)-(27) of the Appendix using the pseudospectral code SNOOPY Lesur & Longaretti (2007), which is a general purpose code, solving HD and MHD equations, including shear, rotation, stratification, and several other physical effects. Fourier transforms are computed using the FFTW library. Nonlinear terms are computed using a pseudo-spectral algorithm and antialiasing is enforced using the 2/3 rule. Time integration is done by a standard explicit third-order Runge–Kutta scheme and for viscous and resistive terms is used an implicit scheme. The code has been tested and extensively used in a number of fluid dynamical and astrophysical contexts. The initial conditions consist of small amplitude random noise perturbations of the velocity and magnetic field with spatially uniform rms amplitudes $\langle \mathbf{u}^2 \rangle^{1/2} = \langle \mathbf{b}^2 \rangle^{1/2} = 0.6$ on top of the shear flow. The computational domain has sizes $(L_x, L_y, L_z) = (2\pi, 2\pi, 2\pi)$ and numerical resolution $(N_x, N_y, N_z) = (256, 256, 256)$. The viscous and resistive Reynolds numbers are fixed to the values $R_e = R_m = 1000$. The subsequent time-evolution with these initial conditions was followed to $t_f = 1000$ (i.e., for a total of 1000 shear times).

Figure 1 shows the time-development of the volume-averaged perturbed kinetic, E_K, and magnetic, E_M, energy densities for different initial magnetic field strengths, $B_{0y} = 0$; 0.1, 0.3; 0.35. At the early stage of evolution, the initially imposed small perturbations start to grow as a result of transient amplification, due to the flow non-normality of separate SFHs contained in the initial conditions. Then, after several orbits the perturbation amplitude becomes high enough for the nonlinearity to be triggered. After reaching the nonlinear regime, the flow eventually settles down into a sustained quasi-steady subcritical MHD turbulence that persists until the end of the simulation. It is clearly seen in Figure 1, that the kinetic energy dominates the magnetic one and as the value of the initial magnetic field increases, the kinetic as well as magnetic energy decrease in magnitude, and after reaching a critical value $B_{0y,c} \approx 0.33$ the turbulence disappears.

Figure 2 shows the time development of the volume-averaged Reynolds, $\langle u_x u_y \rangle$, and Maxwell, $\langle -b_x b_y \rangle$, stresses for different initial magnetic field strengths, $B_{0y} = 0$; 0.1, 0.3; 0.35. In all the cases, the Reynolds

doi: https://doi.org/10.52526/25792776-23.70.1-152

stress is larger than the Maxwell stress. This indicates that the energy extraction from the mean flow are dominated by the velocity perturbations in 3D MHD shear flows rather than by magnetic field ones, which actually take energy from the velocity perturbations. Similarly, we see that the increase of the background magnetic field B_{0y} leads to the decay of the turbulence. So, the Reynolds stress plays a vital role in counteracting dissipation and ensuring turbulence sustenance by continuously replenishing transiently growing modes that themselves alone would be incapable of long-term supply of turbulence.

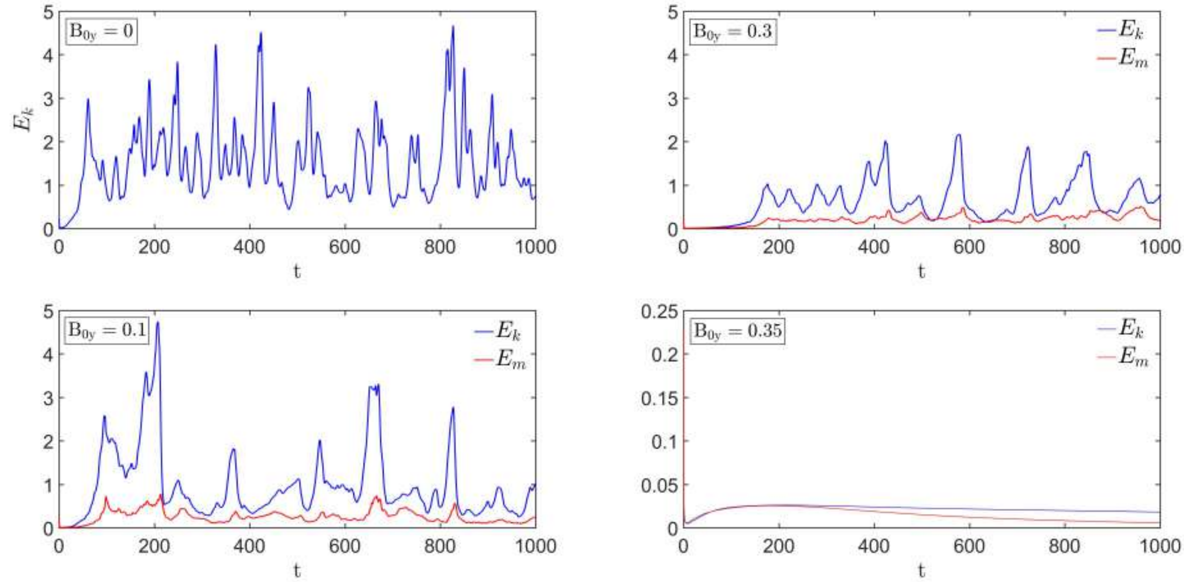

Figure 1. Evolution of the volume-averaged kinetic (blue) and magnetic (red) energy densities for different initial magnetic field strengths $B_{0y} = 0$; 0.1, 0.3; 0.35. Turbulence sets in after several orbits, with the kinetic energy dominating magnetic one. As the value of the mean magnetic field increases, turbulence decays.

.

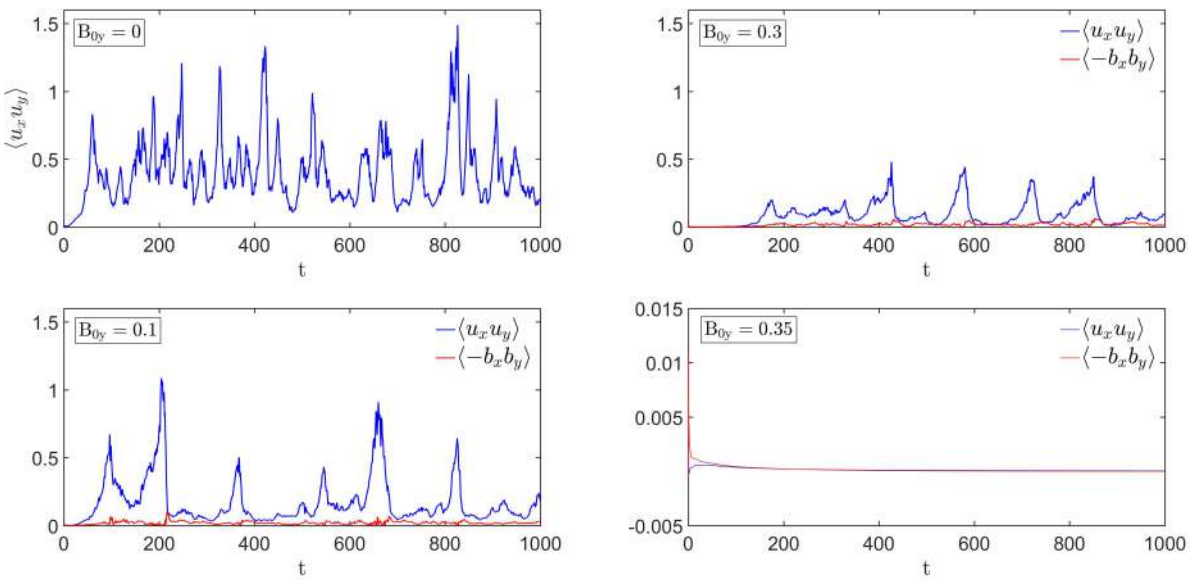

Figure 2. Evolution of the volume-averaged Reynolds (blue) and Maxwell (red) stresses for different initial magnetic field strengths $B_{0y} = 0$; 0.1, 0.3; 0.35. In all cases, Reynolds stress dominates over Maxwell stress.

In contrast to the present case with no rotation, in the 3D MHD Keplerian flow, which represents combination of rotation and shear, with an azimuthal mean magnetic field, energy extraction from the background flow is mostly due to Maxwell stress, as shown in Figure 3 (reproduced from Gogichaishvili et al., 2017). It is interesting to note that the dominance of Maxwell stress is observed in all other cases of 3D MHD turbulence with Keplerian flows and different magnetic field configurations (Gogichaishvili et al., 2018, Mamatsashvili et al., 2020). The Maxwell stress is also much larger than the Reynolds stress in the

doi: https://doi.org/10.52526/25792776-23.70.1-152

2D MHD case (Mamatsashvili et al., 2014), signifying that the energy extraction from the mean flow is dominated by the magnetic field perturbations. Moreover, this study has shown that the Reynolds stress not only has a smaller magnitude than the Maxwell stress but also has a negative sign, thereby indicating that it does not contribute to the gain in turbulent kinetic energy.

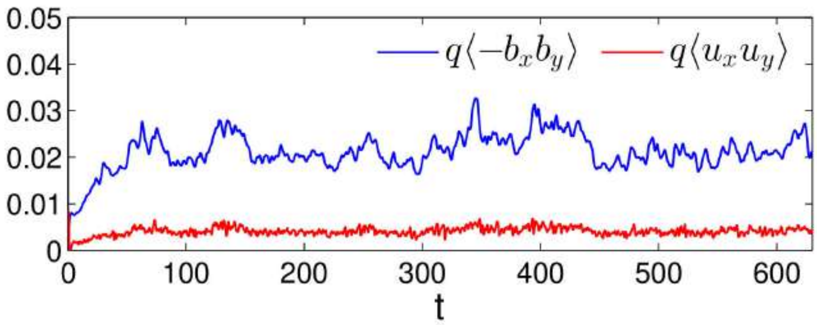

Figure 3. Evolution of the volume-averaged Reynolds (red) and Maxwell (blue) stresses for Keplerian disk with an azimuthal magnetic field (Gogichaishvili et al., 2017). Here Maxwell stress dominates Reynolds stress contrary to the 3D MHD plane case.

3.1. Analysis in Fourier Space

Deeper insight into the nature of the dynamics of the 3D MHD subcritical turbulence can be gained by performing analysis in Fourier space. In general, as demonstrated in previous works (Gogichaishvili et al., 2017, Mamatsashvili et al., 2014) to understand the dynamics of the quasi-steady turbulence state, each linear and nonlinear term of the spectral equations (6)-(11) should be calculated explicitly and visualized in Fourier space. But without a loss of generality in this proceedings paper, we will only focus on the x-component of the velocity field (Equation 6), as it was seen from the previous section, the kinetic processes prevail over magnetic ones, and since the shear is along the x-direction, the basic cycle can be closed for the $x-$component. To visualize each component of Equation (6) in Fourier space we use simulation data from The Snoopy Code and focus on the case $B_{0y} = 0.1$. Before proceeding to spectral analysis, it should be mentioned that all of the spectral quantities/terms in the above equation are averaged in time over an entire saturated/quasi-steady turbulent state, between $t = 100$ and the end of the run at $t_f = 1000$.

Certainly, three-dimensionality complicates the analysis. Therefore, we first find out which vertical wavenumbers are important. Hence, we integrate the spectral energies and stresses in the (k_x, k_y)-plane and represent as a function of k_z (figure 4). It is evident that the kinetic and magnetic energies, along with the Reynolds and Maxwell stresses, reach their maximum values at small k_z and rapidly decrease as k_z increases, implying that the turbulence-maintaining processes predominantly occur at small wavenumbers. This energy-containing area in **k**-space is called the *vital area*. So, below we will focus on the dynamics at small k_z and, specifically, show the dynamical terms at $k_z = 0, 1, 2$.

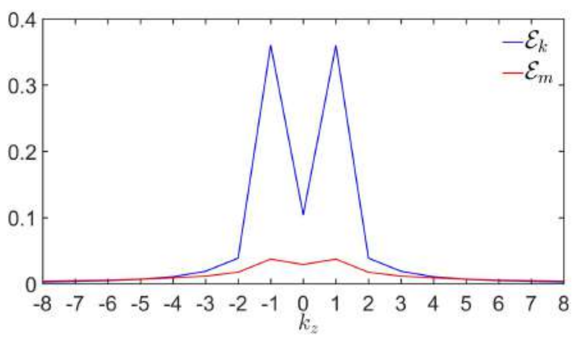

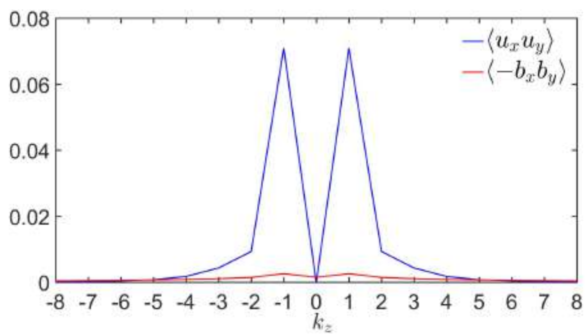

Figure 4. Time-averaged kinetic, $\mathcal{E}_k$, and magnetic, $\mathcal{E}_m$, energy spectra (left panel), also Reynolds, $\langle u_x u_y \rangle$, and Maxwell, $\langle -b_x b_y \rangle$, stresses (right panel) integrated in (k_x, k_y) plane and represented as a function of k_z.

.

We now present the distributions of time-averaged amplitude of spectral shearwise velocity $\bar{u}_x$, linear

doi: https://doi.org/10.52526/25792776-23.70.1-152

drift term along k_x, injection term, $\mathcal{H}_x$, and the nonlinear transfer term, $\mathcal{N}_x^{(u)}$, in (k_x, k_y)-plane at $k_z = 0, 1, 2$ (figure 5). It is clear from these plots that the $|\bar{u}_x|$ spectrum, as well as the linear and nonlinear terms are anisotropic, i.e., strongly depend on the wavevector angle. This specific anisotropy is due to the flow shear.

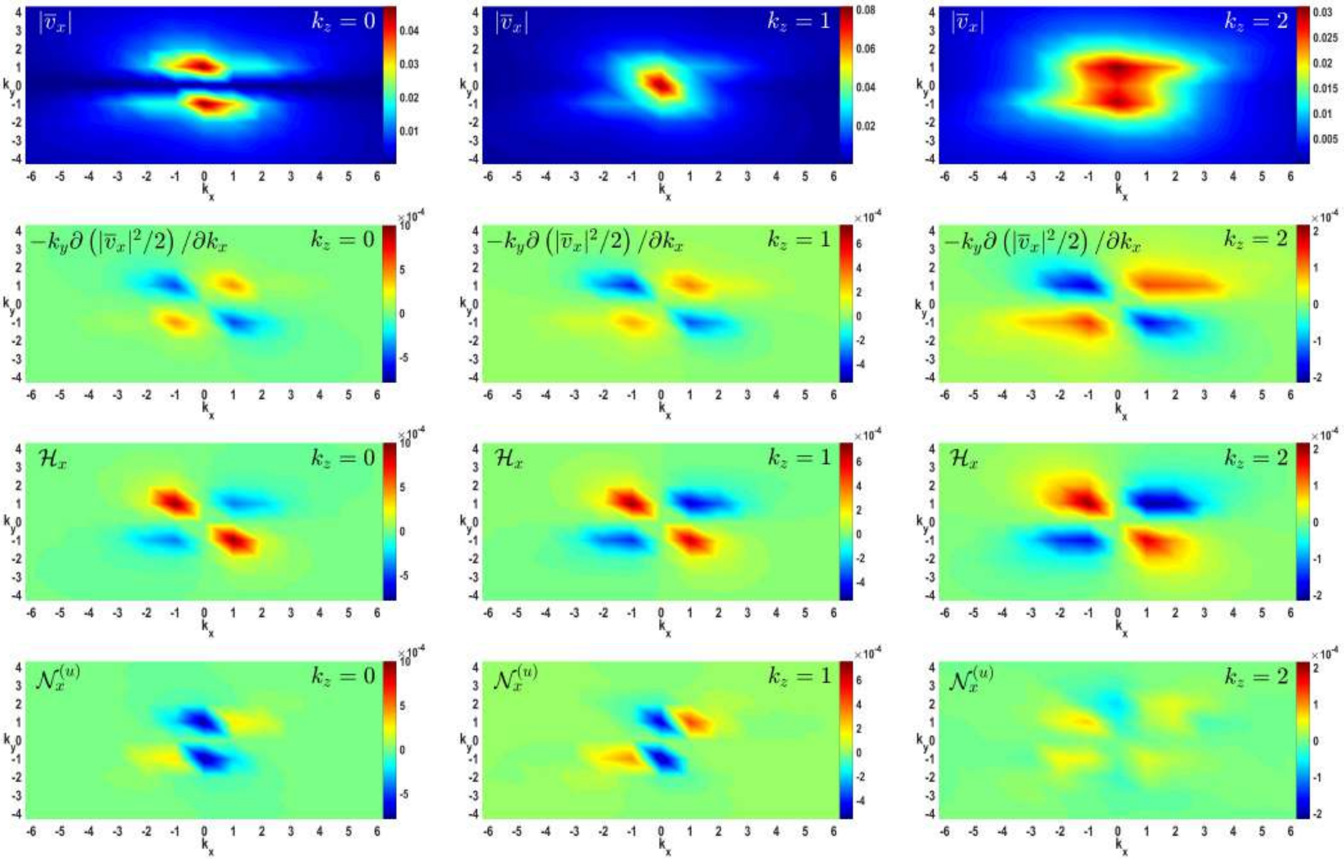

Figure 5. Spectra of $|\bar{u}_x|$ (upper row) together with the linear drift (second row), injection $\mathcal{H}_x$ (third row) and nonlinear $\mathcal{N}_x^{(u)}$ (fourth row) terms in the (k_x, k_y)-plane at k_z =0 (left), 1 (middle) and 2 (right) slices. These terms mainly operate at small wavenumbers $k \lesssim 3$. In the red and yellow regions dynamical terms are positive, in the blue and dark blue regions they are negative and in the light green regions they are small.

The dynamics of $|\bar{u}_x|$ is primarily determined by the combined action of the drift $(-k_y\partial(|\bar{u}_x|^2/2)/\partial k_x)$, injection $(\mathcal{H}_x)$, and the nonlinear $(\mathcal{N}_x^{(u)})$ terms. Here we do not show viscous term, $\mathcal{D}_i^{(u)}$, because its action is simple – it is always negative and reduces the corresponding quantities. Namely, it increases with k, but in the vital area is too small and does not influence the dynamics. The linear cross terms, $\mathcal{I}_x^{(ub)}$ and $\mathcal{I}_x^{(bu)}$, as was mentioned above, describe the exchange between kinetic and magnetic spectral energies. These terms are also small compared to other dynamical terms and do not play any notable role in the sustenance of turbulence (and hence is not shown in Figure 5).

The second row of Figure 5 shows the linear drift of SFHs. This process transfers perturbation modes with normalized velocity k_y, along the k_x-axis for $k_y > 0$ and in the opposite direction for $k_y < 0$, due to shear. Namely, harmonics drift from blue and dark blue regions (energy decrease) to red and yellow regions (energy increase). It should be mentioned that streamwise constant harmonics, with $k_y = 0$, are not affected by the drift.

The third row of Figure 5 shows the action of the injection term $\mathcal{H}_x$. As was demonstrated in the previous section, Reynolds stress is positive and larger than Maxwell stress, so it is mainly responsible for the energy supply of the turbulence, as it exchanges energy between the background shear flow and perturbations. Where the x-component of the injection term is positive (red and yellow regions in the third row of Figure 5), it increases the energy of the x component of perturbed velocity, and in the regions where it is negative (blue and dark blue regions), it takes kinetic energy from this velocity component and gives it back to the flow. Thus Reynolds stress is the main energy supplier for the turbulence. It ensures energy injection into the turbulent fluctuations.

The fourth row of Figure 5 demonstrates the action of the nonlinear transfer $\mathcal{N}_x^{(u)}$. This function redistributes the energy of the x-component of velocity $|\bar{u}_x|^2/2$ not only along the wave vector, as in the

doi: https://doi.org/10.52526/25792776-23.70.1-152

direct cascade, but also transversely to the wavevector from the blue and dark blue regions, where $\mathcal{N}_x^{(u)} < 0$, to the red and yellow regions, where $\mathcal{N}_x^{(u)} > 0$. It is apparent from Figure 5 that the dependence of this term on the polar angle is influenced by the shear, leading to a redistribution of spectral energy across wavevector angles. This relatively new process known as the nonlinear transverse cascade fundamentally differs from the canonical direct cascade, where energy is directly transferred from small wavevectors (large scales) to large ones (small scales), where it is dissipated. As we will see below, the transverse cascade is essential for the self-sustenance of the considered subcritical turbulence.

3.2. Interplay of the Linear and Nonlinear Processes

Now that we have outlined the dynamical balances in Fourier space, we can proceed to construct, based on them, the main self-sustaining scheme/cycle of 3D MHD subcritical turbulence. As was mentioned above, due to the substantial difference in magnitude and importance between the kinetic energy and Reynolds stress compared to the magnetic energy and Maxwell stress, it can be concluded that the sustenance is predominantly driven by kinematics of the flow.

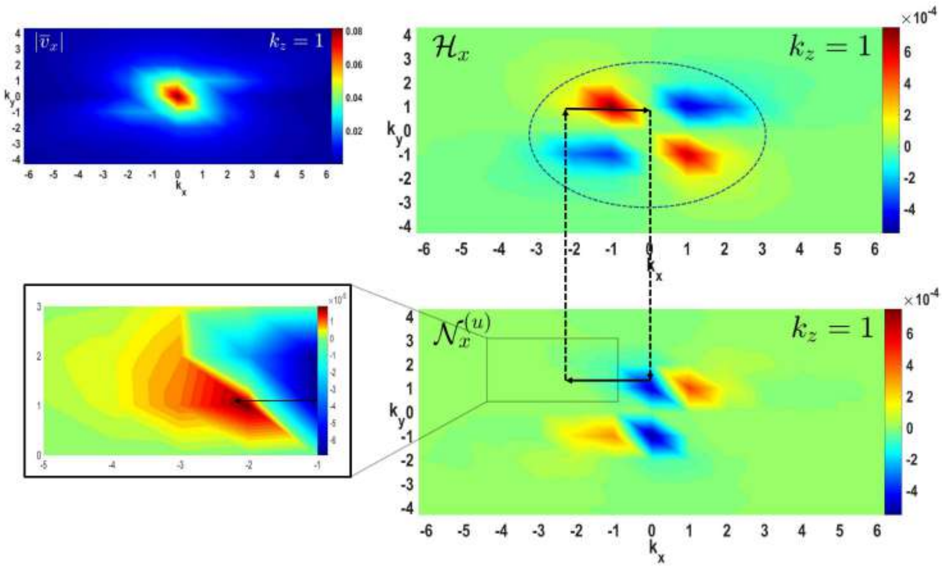

Figure 6. Scheme of the basic cycle of turbulence sustenance. In the circle, there is the vital area. The solid arrow in the plot of $\mathcal{H}_x$ represents the linear drift of perturbations from left to right. The right dashed arrow redirects the same wavevector to the $\mathcal{N}_x^{(u)}$ plot to show the processes occurring there. The solid arrow in the plot of $\mathcal{N}_x^{(u)}$ represents the nonlinear transfer (transverse cascade) of kinetic energy from right to left. The left dashed arrow redirects the same wavevector to the $\mathcal{H}_x$ plot, where, once again due to the drift, perturbations have the opportunity to pass the energy injection area and amplify and then, via $\mathcal{N}_x^{(u)}$ regenerate new modes reentering the amplification area again, thereby closing the sustenance cycle. These processes contribute to the spectra of $|\bar{u}_x|$ (shown in the top left plot).

The central aspect of this process should revolve around the dominant k_z slice ($k_z = 1$) of the x-component of the velocity field, which carries the most energy, particularly at wavenumbers where its magnitude is significant, specifically within the vital area. So, now we can construct the basic cycle of self-sustenance of turbulence based on the information presented in Figure 6. The basic cycle is as follows – harmonics located in the amplification quadrant II, in the plot of $\mathcal{H}_x$, drift along the k_x-axis from left to right due to shear, as represented by the solid arrow. The nonlinear function $\mathcal{N}_x^{(u)}$ transfers part of the kinetic energy from the amplified harmonics from right to left, represented by the solid arrow, to the amplification area, where $\mathcal{H}_x > 0$. This process regenerates harmonics having the potential of growth within the vital area, ultimately closing the cycle and realizing a positive nonlinear feedback, thereby sustaining the turbulence. So, the realization of positive feedback would not be possible without the existence of the transverse cascade,

doi: https://doi.org/10.52526/25792776-23.70.1-152

which, in this case, dominates over the nonlinear direct cascade. It transfers perturbation harmonics to the amplification part of the vital area, contrasting with the direct cascade, which takes away harmonics from the vital area and transfers them to small/dissipative scales. It is important to note that when studying anisotropic turbulence, using only the direct cascade is misleading. The presence of anisotropy introduces the existence of the transverse cascade and competition between these two nonlinear processes becomes crucial in determining whether turbulence will be sustained or not. Namely, if the transverse cascade prevails over the direct one, the turbulence will be sustained. Conversely, if the direct cascade prevails over the transverse one, the turbulence will decay.

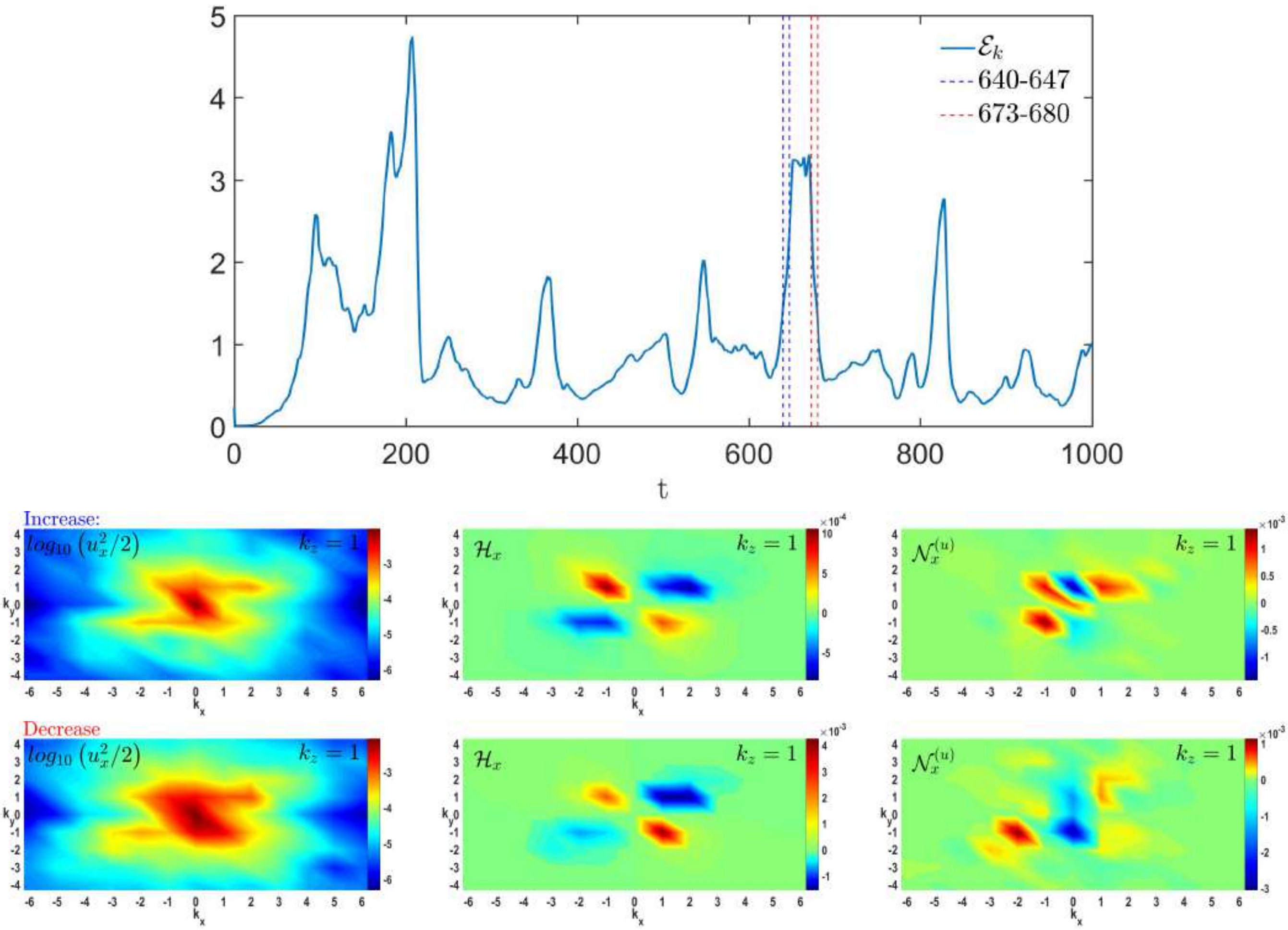

Figure 7. The upper plot shows the evolution of the volume-averaged kinetic energy, where the intervals of increase, $t = 640 - 647$, and decrease, $t = 673 - 680$, around the peak during which the spectral quantities are analyzed below are denoted with vertical dashed lines. The spectra of $|\bar{u}_x|^2/2$ (left column), injection term $\mathcal{H}_x$ (middle column) and nonlinear transfer term $\mathcal{N}_x^{(u)}$ (right column) are shown during the increase (middle row) and decrease (bottom row) phases of kinetic energy. From the right plot of the transfer term during the increase stage it is seen that mode with wavevector $\mathbf{k} = (0, 0, 1)$ gains energy ($\mathcal{N}_x^{(u)}(0, 0, 1) > 0$) whereas, during the decrease regime, energy is transferred away from this mode ($\mathcal{N}_x^{(u)}(0, 0, 1) < 0$).

So far, we have averaged the spectral quantities in time over an entire saturated turbulent state and study their dynamics and role in the sustenance of turbulence. However, it is also interesting to observe the processes that occur within small time intervals, which we have done. As we see in the first plot of the Figure 7, the turbulent field has a quite noisy nature – the energy curve has peaks/bursts in the quasi-steady state. By averaging spectral quantities/terms over the entire saturated turbulent state, we can gain an understanding of the general behavior of these terms. Still, during this procedure, a lot of essential information is lost. Therefore, we performed averaging of physical quantities within a small time interval, specifically, during the increase ($t = 640 - 647$) and during the decrease ($t = 673 - 680$) stages of the kinetic energy, as depicted in the upper plot of Figure 7. During the increasing regime, nonlinearity transfers energy to the wavevector, which is the basic mode of the turbulence $\mathbf{k} = (0, 0, 1)$, whereas during the decreasing

doi: https://doi.org/10.52526/25792776-23.70.1-152

regime, energy is transferred by nonlinearity from the harmonic $\mathbf{k} = (0, 0, 1)$. This behavior is attributed to the creation and weakening of a mode with the wavevector $\mathbf{k} = (0, 0, 1)$ and the Interplay of this process with the processes discussed above will ensure the sustenance of a turbulent state.

So, due to the injection term and the linear drift, perturbations experience transient growth as they are swept through the vital area in **k**-space. Nonlinear transverse cascade redistributes the modes over the wavevector angle, returning part of them in the amplification area. Consequently, turbulence in shear flows is sustained through positive feedback, resulting from the subtle interplay between linear transient growth and the nonlinear transverse cascade processes. Furthermore, the sustenance of turbulence is further influenced by the processes we observed during a small period of time analyzing the generation and decay of bursts.

4. Summary and Discussion

In this paper, we investigated the characteristics and self-sustaining mechanism of subcritical 3D turbulence in a spectrally stable MHD shear flow with constant shear and parallel to the flow mean magnetic field by first doing numerical simulations and then analyzing the dynamical processes in Fourier (**k**-)space. We showed that nonlinear processes are anisotropic in **k**-space. This anisotropy arises from the anisotropy of linear processes, which is caused by the shear. Describing this phenomenon within the traditional framework of direct and inverse cascades, commonly used in the classical theory of HD and MHD turbulence without shear, is inadequate, as the primary role of nonlinear processes is to transfer energy across different wavevector orientations (angles) in **k**-space, rather than along the wavevector as in direct/inverse cascades. This new type of nonlinear cascade – the nonlinear transverse cascade – is crucial for providing a positive feedback and thus maintenance of the subcritical turbulence. Indeed, we showed that turbulence is sustained by the subtle interplay of linear nonmodal growth, which injects energy via stresses, and nonlinear transverse cascade, which ensures the regeneration of transiently growing harmonics. This interplay is crucial for self-sustenance of subcritical turbulence. It should be noted that these processes operate at small wave numbers (large length scales) and are referred to as the vital area, where power-consuming processes ensuring the self-sustaining dynamics occur.

We showed that in 3D MHD subcritical turbulence, energy injection into turbulent fluctuations is due to Reynolds stress, in contrast to 2D MHD (Mamatsashvili et al., 2014) and 3D MHD Keplerian flows with different magnetic field configurations (Gogichaishvili et al., 2017, 2018, Mamatsashvili et al., 2020). Therefore, Reynolds stress is responsible for the onset of turbulence in the present case. We also performed numerical simulations for different values of the background magnetic field and demonstrated that as this field increases, the onset of turbulence occurs at larger times and the power of turbulence reduces. Finally, the flow completely stabilizes for $B_{0y} \approx 0.33$ and higher.

The turbulence exhibits a "bursty" nature, with energy increasing in some time intervals and decreasing in others. Therefore, it becomes important to explore this behavior at small time intervals rather than solely relying on the average effect over the whole saturated state, as the crucial information can be lost. One of the significant findings that we made is that by averaging over small time intervals (in the regions of both energy increase and decrease), we are able to observe dynamics that would otherwise be lost (if considering averaging over whole saturated time). Specifically, we observe the creation and weakening of the dominant large-scale modes $\mathbf{k} = (0, 0, 1)$, which plays a key role in the turbulence dynamics and contributes to the self-sustaining process.

Acknowledgements

M.K. would like to thank supervisor Prof. Nana Shatashvili for all supports, guidance and discussions.

Appendices

Appendix A Equations for perturbation components in physical space

Equations governing the evolution of the velocity, total pressure and magnetic field perturbations, $\mathbf{u}, p, \mathbf{b}$, about the equilibrium flow $\mathbf{U}_0 = (0, -Sx, 0)$ with net azimuthal field $\mathbf{B}_0 = (0, B_{0y}, 0)$ are obtained from the basic Equations (1)-(4) and componentwise have the form:

doi: https://doi.org/10.52526/25792776-23.70.1-152

$$\frac{Du_x}{Dt} = -\frac{1}{\rho_0}\frac{\partial p}{\partial x} + \frac{B_{0y}}{4\pi\rho_0}\frac{\partial b_x}{\partial y} + \frac{\partial}{\partial x}\left(\frac{b_x^2}{4\pi\rho_0} - u_x^2\right) + \frac{\partial}{\partial y}\left(\frac{b_x b_y}{4\pi\rho_0} - u_x u_y\right) + \frac{\partial}{\partial z}\left(\frac{b_x b_z}{4\pi\rho_0} - u_x u_z\right) + \nu\nabla^2 u_x, \tag{20}$$

$$\frac{Du_y}{Dt} = Su_x - \frac{1}{\rho_0}\frac{\partial p}{\partial y} + \frac{B_{0y}}{4\pi\rho_0}\frac{\partial b_y}{\partial y} + \frac{\partial}{\partial x}\left(\frac{b_x b_y}{4\pi\rho_0} - u_x u_y\right) + \frac{\partial}{\partial y}\left(\frac{b_y^2}{4\pi\rho_0} - \mathrm{u_y^2}\right) + \frac{\partial}{\partial z}\left(\frac{b_y b_z}{4\pi\rho_0} - u_y u_z\right) + \nu\nabla^2 u_y, \tag{21}$$

$$\frac{Du_z}{Dt} = -\frac{1}{\rho_0}\frac{\partial p}{\partial z} + \frac{B_{0y}}{4\pi\rho_0}\frac{\partial b_z}{\partial y} + \frac{\partial}{\partial x}\left(\frac{b_x b_z}{4\pi\rho_0} - u_x u_z\right) + \frac{\partial}{\partial y}\left(\frac{b_y b_z}{4\pi\rho_0} - u_y u_z\right) + \frac{\partial}{\partial z}\left(\frac{b_z^2}{4\pi\rho_0} - u_z^2\right) + \nu\nabla^2 u_z \tag{22}$$

$$\frac{Db_x}{Dt} = B_{0y}\frac{\partial u_x}{\partial y} + \frac{\partial}{\partial y}(u_x b_y - u_y b_x) - \frac{\partial}{\partial z}(u_z b_x - u_x b_z) + \eta\nabla^2 b_x, \tag{23}$$

$$\frac{Db_y}{Dt} = -Sb_x + B_{0y}\frac{\partial u_y}{\partial y} - \frac{\partial}{\partial x}(u_x b_y - u_y b_x) + \frac{\partial}{\partial z}(u_y b_z - u_z b_y) + \eta\nabla^2 b_y, \tag{24}$$

$$\frac{Db_z}{Dt} = B_{0y}\frac{\partial u_z}{\partial y} + \frac{\partial}{\partial x}(u_z b_x - u_x b_z) - \frac{\partial}{\partial y}(u_y b_z - u_z b_y) + \eta\nabla^2 b_z, \tag{25}$$

$$\frac{\partial u_x}{\partial x} + \frac{\partial u_y}{\partial y} + \frac{\partial u_z}{\partial z} = 0, \tag{26}$$

$$\frac{\partial b_x}{\partial x} + \frac{\partial b_y}{\partial y} + \frac{\partial b_z}{\partial z} = 0 \tag{27}$$

where $D/Dt = \partial/\partial t - Sx\partial/\partial y$ is the total derivative along the background flow.

References

Alexakis A., Mininni P. D., Pouquet A., 2007, New J. Phys., 9, 298

Baggett J. S., Driscoll T. A., Trefethen L. N., 1995, Physics of Fluids, 7, 833

Chagelishvili G. D., Chanishvili R. G., Lominadze J. G., Tevzadze A. G., 1997, Phys. Plasmas, 4, 259

Chagelishvili G., Zahn J.-P., Tevzadze A. G., Lominadze J. G., 2003, Astronomy & Astrophysics, 402, 401

Chagelishvili G., Hau J.-N., Khujadze G., Oberlack M., 2016, Phys. Rev. Fluids, 1, 043603

Chapman S. J., 2002, Journal of Fluid Mechanics, 451, 35

Eckhardt B., Schneider T. M., Hof B., Westerweel J., 2007, Annual Review of Fluid Mechanics, 39, 447

Farrell B. F., Ioannou P. J., 1993, Phys. Fluids, 5, 1390

Farrell B. F., Ioannou P. J., 1994, Phys. Rev. Lett., 72, 1188

Farrell B. F., Ioannou P. J., 2000, Phys. Fluids, 12, 3021

Farrell B. F., Ioannou P., 2012, Journal of Fluid Mechanics, 708, 149

Fromang S., Lesur G., 2019, in EAS Publications Series. pp 391–413, doi:10.1051/eas/1982035

Gebhardt T., Grossmann S., 1994, Physical review, 50, 3705

Gogichaishvili D., Mamatsashvili G., Horton W., Chagelishvili G., Bodo G., 2017, The Astrophysical Journal, 845, 70

Gogichaishvili D., Mamatsashvili G., Horton W., Chagelishvili G., 2018, The Astrophysical Journal, 866, 134

Grossmann S., 2000, Reviews of Modern Physics, 72, 603

Grue J., Kolaas J., Jensen A., 2014, European Journal of Mechanics - B/Fluids, 47, 97

Gustavsson L. H., 1991, Journal of Fluid Mechanics, 224, 241–260

Henningson D. S., Reddy S. C., 1994, Physics of Fluids, 6, 1396

Herault J., Rincon F., Cossu C., Lesur G., Ogilvie G. I., Longaretti P.-Y., 2011, , 84, 036321

Horton W., Kim J.-H., Chagelishvili G. D., Bowman J. C., Lominadze J. G., 2010, Phys. Rev. E, 81, 066304

Lesur G., Longaretti P.-Y., 2007, Monthly Notices of the Royal Astronomical Society, 378, 1471

Lesur G., Ogilvie G. I., 2008, Astronomy & Astrophysics, 488, 451

Lominadze D., Chagelishvili G., Chanishvili R., 1988, Soviet Astronomy Letters, 14, 364

Longaretti P.-Y., Lesur G., 2010, Astron. Astrophys. , 516, A51

Mamatsashvili G. R., Gogichaishvili D. Z., Chagelishvili G. D., Horton W., 2014, Phys. Rev. E, 89, 043101

doi: https://doi.org/10.52526/25792776-23.70.1-152

Mamatsashvili G., Khujadze G., Chagelishvili G., Dong S., Jiménez J., Foysi H., 2016, Phys. Rev. E, 94, 023111

Mamatsashvili G., Chagelishvili G., Pessah M. E., Stefani F., Bodo G., 2020, The Astrophysical Journal, 904, 47

Ogilvie G. I., Pringle J. E., 1996, Mon. Not. R. Astron. Soc., 279, 152

Reddy S. C., Henningson D. S., 1993, J. Fluid Mech., 252, 209

Reddy S., Schmid P., Henningson D., 1993, SIAM J. Appl. Math., 53, 15

Rempel E. L., Lesur G., Proctor M. R. E., 2010, Phys. Rev. Lett., 105, 044501

Schmid P. J., 2007, Annu. Rev. Fluid Mech., 39, 129

Stern M. E., 1963, Phys. Fluids, 6, 636

Sundar S., Verma M. K., Alexakis A., Chatterjee A. G., 2017, Physics of Plasmas, 24, 022304

Teaca B., Verma M. K., Knaepen B., Carati D., 2009, Phys. Rev. E, 79, 046312

Tevzadze A. G., Chagelishvili G., Zahn J.-P., Chanishvili R. G., Lominadze J. G., 2003, Astronomy & Astrophysics, 407, 779

Trefethen N. L., Embree M., 2005, Spectra and Pseudospectra: The Behavior of Nonnormal Matrices and Operators. Princeton University Press, Address

Trefethen L. N., Trefethen A., Reddy S. C., Driscoll T. A., 1993, Science, 261, 578

Verma M. K., 2004, Physics Reports, 401, 229

doi: https://doi.org/10.52526/25792776-23.70.1-152